



# Fluctuations in High-Energy Particle Collisions

Hanna Gronqvist

► **To cite this version:**

Hanna Gronqvist. Fluctuations in High-Energy Particle Collisions. High Energy Physics - Theory [hep-th]. Université Paris-Saclay, 2016. English. <NNT : 2016SACLS155>. <tel-01367259>

**HAL Id: tel-01367259**

**<https://tel.archives-ouvertes.fr/tel-01367259>**

Submitted on 15 Sep 2016

**HAL** is a multi-disciplinary open access archive for the deposit and dissemination of scientific research documents, whether they are published or not. The documents may come from teaching and research institutions in France or abroad, or from public or private research centers.

L'archive ouverte pluridisciplinaire **HAL**, est destinée au dépôt et à la diffusion de documents scientifiques de niveau recherche, publiés ou non, émanant des établissements d'enseignement et de recherche français ou étrangers, des laboratoires publics ou privés.



NNT : 2016SACLS155

THÈSE DE DOCTORAT  
DE  
L'UNIVERSITÉ PARIS-SACLAY  
PRÉPARÉE À  
L'UNIVERSITÉ PARIS-SUD

Institut de Physique Théorique de Saclay

ÉCOLE DOCTORALE N° 564  
École Doctorale Physique en Île de France

Spécialité de doctorat Physique

Par

**Mme Hanna Grönqvist**

Fluctuations in High-Energy Particle Collisions

**Thèse présentée et soutenue à Saclay, le 20.06.2016 :**

**Composition du Jury :**

M. Damir Becirevic	Dr, Université Paris-Saclay	Président
M. Simon Caron-Huot	Dr, Niels Bohr Institute	Rapporteur
M. Tuomas Lappi	Dr, Université de Jyväskylä	Rapporteur
Mme Ruth Britto	Dr, Trinity College Dublin	Directeur de thèse
M. Jean-Yves Ollitrault	Dr, Institut de Physique Théorique	Co-directeur de thèse



# Contents

List of Figures	v
List of Tables	v
Abstract	vii
Acknowledgements	ix
Introduction	xix
French resume – Résumé en français	xxiii

## I Fluctuations in quantum field theory: From unitarity cuts to coproducts of Feynman integrals 1

1 From unitarity cuts to coproducts of Feynman integrals	3
1.1 Introduction . . . . .	3
1.2 Mathematical and conceptual introduction . . . . .	6
1.2.1 Unitarity cuts . . . . .	6
1.2.2 Multiple polylogarithms . . . . .	9
1.2.3 Coalgebra and Hopf algebra . . . . .	10
1.2.4 The symbol map . . . . .	12
1.3 Pure functions and Feynman integrals . . . . .	12
1.4 The symbol alphabet . . . . .	13
1.5 One-loop triangles . . . . .	15
1.5.1 Feynman rules . . . . .	19
1.5.2 The generic one-loop three-point diagram . . . . .	20
1.5.3 A note on analytic continuation . . . . .	20

1.6	Computation of cut diagrams . . . . .	21
1.6.1	Cut in an external channel . . . . .	23
1.6.2	Cut in an internal mass . . . . .	27
1.6.3	Examples of cut diagrams . . . . .	28
1.7	The first entry condition . . . . .	33
1.8	Relations among discontinuities . . . . .	37
1.8.1	Discontinuities and cut diagrams . . . . .	37
1.8.2	Discontinuities and the coproduct . . . . .	40
1.8.3	Cuts and the coproduct . . . . .	43
1.9	Examples of Cut-Disc- $\delta$ relations . . . . .	43
1.9.1	Three-mass triangle with no internal masses . . . . .	44
1.9.2	$T(p_1^2; m_{12}^2, m_{23}^2)$ . . . . .	45
1.9.3	$T(p_1^2; m_{12}^2, m_{13}^2)$ . . . . .	49
1.10	Reconstruction . . . . .	53
1.10.1	Reconstruction of massive triangle integrals . . . . .	54
1.10.2	Examples of the reconstruction process . . . . .	56
1.10.3	Reconstructing the full function from the symbol . . . . .	59
1.11	Conclusions . . . . .	60
<b>II</b>	<b>Fluctuations in heavy ion collisions</b>	<b>63</b>
	<b>Introduction to heavy-ion collisions</b>	<b>65</b>
<b>2</b>	<b>Non-Gaussian eccentricity fluctuations</b>	<b>71</b>
2.1	Introduction . . . . .	71
2.1.1	Anisotropic flow . . . . .	73
2.2	Initial anisotropies . . . . .	77
2.3	Identical pointlike sources . . . . .	79
2.3.1	Gaussian distribution of sources: Exact result . . . . .	79
2.3.2	Perturbative results for the cumulants . . . . .	81
2.4	Statistical properties of local density fluctuations . . . . .	82
2.4.1	Perturbative expansion . . . . .	84
2.4.2	$n$ -point averages . . . . .	86
2.4.3	Perturbative results . . . . .	87
2.5	Monte Carlo simulations . . . . .	89
2.5.1	Negative binomial and logarithmic distributions . . . . .	89
2.5.2	Energy conservation . . . . .	93
2.5.3	Writing the program . . . . .	94

2.5.4	Numerical errors . . . . .	95
2.5.5	Results of Monte Carlo simulations . . . . .	97
2.6	Conclusions . . . . .	100
<b>3</b>	<b>Hydrodynamical noise and Gubser flow</b>	<b>101</b>
3.1	Introduction to relativistic hydrodynamics . . . . .	103
3.2	Gubser flow . . . . .	106
3.2.1	Coordinate transformations . . . . .	107
3.2.2	Christoffel symbols and the covariant derivative . . . . .	109
3.2.3	Solution to Gubser flow . . . . .	110
3.3	Noisy flow . . . . .	114
3.3.1	Introduction to noisy hydrodynamics . . . . .	114
3.3.2	Noisy Gubser flow . . . . .	117
3.3.3	Formal solution of the Green function . . . . .	120
3.4	Numerical simulations . . . . .	122
3.5	Conclusions . . . . .	127
<b>A</b>	<b>Gamma-matrix of Gubser flow</b>	<b>131</b>
<b>B</b>	<b>Details of figure 3.1</b>	<b>133</b>
B.0.1	The $q\tau = \text{constant}$ curves . . . . .	133
B.0.2	The $T = \text{constant}$ curves . . . . .	134
<b>C</b>	<b>First paper</b>	<b>137</b>
<b>D</b>	<b>Second paper</b>	<b>198</b>
<b>E</b>	<b>Third paper</b>	<b>212</b>
	<b>Bibliography</b>	<b>235</b>



# Abstract

We study fluctuations that are omnipresent in high-energy particle collisions. These fluctuations can be either of classical or quantum origin and we will study both. Firstly, we consider the type of quantum fluctuations that arise in proton-proton collisions. These are computable perturbatively in quantum field theory and we will focus on a specific class of diagrams in this set-up. Secondly, we will consider the fluctuations that are present in collisions between nuclei that can be heavier than protons. These are the quantum laws of nature that describe the positions of nucleons within a nucleus, but also the hydrodynamic fluctuations of classical, thermal origin that affect the evolution of the medium produced in heavy-ion collisions.

The fluctuations arising in proton-proton collisions can be computed analytically up to a certain order in perturbative quantum field theory. We will focus on one-loop diagrams of a fixed topology. Loop diagrams give rise to integrals that typically are hard to evaluate. We show how modern mathematical methods can be used to ease their computation. We will study the relations among unitarity cuts of a diagram, the discontinuity across the corresponding branch cut and the coproduct. We show how the original integral corresponding to a given diagram can be reconstructed from the information contained in the coproduct. We expect that these methods can be applied to solve more complicated topologies and help in the computation of new amplitudes in the future.

Finally, we study the two types of fluctuations arising in heavy-ion collisions. These are related either to the initial state or the intermediate state of matter produced in such collisions. The initial state fluctuations are experimentally observed to give rise to non-Gaussianities in the final-state spectra. We show how these non-Gaussianities can be explained by the random position and interaction energy of ‘sources’ in the colliding nuclei. Furthermore, we investigate the effect of hydrodynamical noise in the evolution of the medium produced just after a collision. This medium behaves like a fluid with a very low viscosity, and so the corresponding evolution is hydrodynamical.



# Acknowledgements

I want to start by thanking my two advisors, Ruth and Jean-Yves. If it were not for you, I would not be defending my thesis today. Your support has been immensely important for me in addition to everything you have taught me. You have both been role models for me, and given me self-confidence and advice for life.

Next I want to thank all of my collaborators. First of all, a big thank you to Li, who has maybe been the most patient and kindest collaborator ever. I have learnt so much from you! I will remember moments passed together in your office with you teaching me things by the white board, just as well as other moments over hot pot at restaurants in Japan or in Paris. Thank you for reading my manuscript, and helping me prepare my first heavy-ion talk at BNL.

Another special collaborator has been Samuel. You overwhelmed me with your confidence, and in the beginning I was a bit in awe of you even! But then I got to know you better, and discovered what a nice person you really are. I want to thank you for the warm welcome during the week spent at your home in Edinburgh, when I was visiting. Thank you also for all the discussions we had, I learned a lot from them.

Next, let me thank the referees of this manuscript, Simon and Tuomas. It was no easy task nor a quick one, I imagine, reading this manuscript. With such a mixture of topics and methods! And quite lengthy papers. Thank you for your feedback and suggestions on how to improve the manuscript, and thanks for coming here to Paris to attend my defense. I am looking forward to talking to you!

Also, I want to thank my other colleagues. Thank you especially to the whole pQCD group and the non-perturbative QCD group. I have spent numerous hours together with you over lunch, and these have often been nice moments that I will remember for long time, I am sure. I have good memories of many of the post-docs of both groups. You were people with whom I have spent time drinking coffee and discussing physics and life. You have given me so much support, with your experience and wisdom of the field. I will remember your good humor and your laughs.

Now is also the moment to thank the person who inspired me to study physics

in the first place: Leif. Thank you for your openness and warmth. Thank you for supporting me from day one forth, and showing me that girls can be good physicists, too. You have been a father figure for me and you are one of the very important people in my life.

Let me also thank all of the graduate students of the IPhT, whether already graduated or still around. Some of you, older than me, served as counsellors when I was starting my PhD. It was a pleasure to see you defend your theses with success but also very sad to have you leave. Thank you also to those students of my age, with whom I have been able to share a lot. Also, thank you to the younger students, who have successfully picked up on and continued the traditions of us students at the institute. Some of my best memories from this time at the IPhT are certainly lunch hours and coffee breaks passed together with you. You have been essential to my 'surviving' these last years. Thank you also to the students of Trinity College, Dublin, who made my stays there happy times.

Some of the most important people are still to thank: my family and friends. Thanks to my family for all your support during last years. Thank you for your visits in Paris, and for welcoming me in Helsinki. Thank you to my friends from the M2; you know how much you mean to me. Thank you also to all of my Finnish friends. A special thank you is due Pierre and his family, especially Pascale and Claude. You have been some of my closest supporters and oh-so-welcome breaths of fresh air during the last years.

Last, but certainly not least, let me thank all the staff of the IPhT.

# List of Figures

1.1	The unitarity cut of a one-loop amplitude. The two intermediate-state propagators are on shell. Here the filled circles denote the sum of all possible Feynman diagrams with the chosen configuration of external legs. . . . .	7
1.2	Triangles with one external massive leg. . . . .	16
1.3	Triangles with two external massive legs. . . . .	17
1.4	Triangles with three external massive legs. . . . .	17
1.5	Different regions in $(u, v) \equiv (u_2, u_3)$ space. The parabola represents the curve $\lambda(1, u_2, u_3) = 0$ . The variables $z, \bar{z}$ are defined in eq. (1.37). Figure from ref. [1]. . . . .	22
1.6	Example of cuts of $T(0, p_2^2, p_3^2; m_{12}^2, 0, 0)$ : (a) single cut in an external channel; (b) single cut in an internal mass; (c) double cut in external channels; (d) double cut in an external channel and an internal mass. Thin dotted lines correspond to cuts on external channels and imply complex conjugation of a region of the diagram. Thick dashed lines correspond to mass cuts and do not imply any complex conjugation. . . . .	22
1.7	All possible cut diagrams of $T(0, p_2^2, p_3^2; m_{12}^2, 0, 0)$ . A diagram in the top row and its corresponding diagram in the bottom row are associated to the same momentum channel, but opposite energy flow. . . . .	25
1.8	Double cuts of the three-mass triangle diagram with massless propagators. The vertices $v$ are labeled by all possible color sequences $(c_1(v), c_2(v))$ encoding the cuts. Energy flows from 0 to 1 for each cut, giving the theta functions listed below each diagram. Figure from ref. [2]. . . . .	26

- 1.9 The three-mass triangle integral  $T(p_1^2, p_2^2, p_3^2)$ , eq. (1.66), of the example in subsection 1.6.3. Here  $k$  denotes the loop momentum and the  $p_i^2$  are the external invariants. The colorings of the dots give the correct Feynman rules to use, see subsection 1.5.1. The external channels, denoted by thick lines, are massive, whereas the internal propagators, drawn as thin lines, are massless. . . . . 29
- 1.10 The cut three-mass triangle integral  $\text{Cut}_{p_2^2} T(p_1^2, p_2^2, p_3^2)$  of the example in subsection 1.6.3, with the single-channel cut denoted by a dashed red curve. Here  $k$  denotes the loop momentum and the  $p_i^2$  are the external invariants. The colorings of the dots give the correct Feynman rules to use, see subsection 1.5.1. . . . . 30
- 1.11 The doubly cut three-mass triangle integral  $(\text{Cut}_{p_2^2, p_3^2}) T(p_1^2, p_2^2, p_3^2)$  of the example in subsection 1.6.3, with the double-channel cuts denoted by dashed red curves. Here  $k$  denotes the loop momentum and the  $p_i^2$  are the external invariants. The colorings of the dots give the correct Feynman rules to use, see subsection 1.5.1. . . . . 32
- 1.12 Two-propagator cuts of the triangle  $T(p_1^2; m_{12}^2, m_{13}^2)$ . . . . . 39
- 1.13 The triangle  $T(p_1^2, p_2^2, p_3^2)$ . Left: the uncut triangle with all black vertices. Middle: The  $p_2^2$  channel cut  $\text{Cut}_{p_2^2} T(p_1^2, p_2^2, p_3^2)$  that complex conjugates a part of the diagram. Right: The sequential  $p_2^2$  and  $p_3^2$  channel cuts  $\text{Cut}_{p_2^2, p_3^2} T(p_1^2, p_2^2, p_3^2)$ . Figure from ref [2]. . . . . 44
- 1.14 Schematic figure of a heavy-ion collision with the two nuclei represented as circles. The impact parameter  $b \equiv |\vec{b}|$ , drawn with a red arrow, is the (transverse) distance between the centers of the two nuclei. . . . . 66
- 1.15 Stages of a heavy-ion collision. Figure from ref. [3]. . . . . 66
- 1.16 Values of pseudorapidity  $\eta$ , eq. (1.202). As the polar angle tends towards zero, the pseudorapidity tends towards infinity. Figure from Wikipedia. . . . . 67
- 1.17 The projection of  $C(\Delta\phi, \Delta\eta > 0.8)$  from figure 1.18 into  $\Delta\phi$  for a relative pseudorapidity gap of  $\Delta\eta > 0.8$  between trigger and associated particles. The Fourier harmonics  $V_{1\Delta}$  to  $V_{5\Delta}$  are superimposed and their sum is shown as a dashed curve. The ratio of the data to the sum of  $n \leq 5$  harmonics is shown in the lower panel. Figure from ref. [4] 68
- 1.18 Examples of two-particle correlations  $C(\Delta\phi, \Delta\eta)$  for lead-lead collisions at  $\sqrt{s_{NN}} = 2.76$  TeV for different centralities as measured by the CMS collaboration. Figure from ref. [5] . . . . . 69

- 2.1 The initial energy density in arbitrary units in the transverse plane for three different heavy-ion collision models: from left to right, IP-Glasma, MC-KLN and MC-Glauber models. Figure from [6]. . . . . 71
- 2.2 Figures of the flow harmonic  $v_n$  as a function of the initial eccentricity  $\varepsilon_n$  for  $n = 2$  (left) and  $n = 3$  (right). The data are taken from 0-5% central collisions. The response is linear for this class of events. Figure from [7]. . . . . 72
- 2.3  $v_2$ ,  $v_3$  and  $v_4$  integrated over the  $p_T$  range  $0.2 < p_T < 5.0$  GeV/ $c$  as a function of event centrality. Of special interest to us are the open squares, which show that  $v_3\{4\} \neq 0$ , implying that the eccentricity fluctuations are non-Gaussian. Figure from [8]. . . . . 73
- 2.4 The  $v_2\{2, \Delta\eta > 2\}$  (circles) and  $v_2\{4\}$  (squares) as a function of multiplicity for  $0.3 < p_T < 3$  GeV/ $c$  in 5.02 GeV p-Pb collisions. Of special interest to us are the squares, which show that  $v_2\{4\} \neq 0$ , meaning that eccentricity fluctuations are non-Gaussian. Figure from [9]. . . . . 74
- 2.5 Almond shaped interaction volume after a non-central collision of two nuclei. The spatial anisotropy with respect to the  $x - z$  -plane (reaction plane) translates into a momentum anisotropy of the produced particles (anisotropic flow). Figure from [10]. . . . . 75
- 2.6 Eccentricities  $\varepsilon_n$  corresponding to flow coefficients  $v_n$  for  $n = 2, 3, 4, 5, 6$ . 75
- 2.7 The distribution of nucleons in the transverse plane for a  $s_{NN} = 200$  GeV Au-Au collision event with  $\varepsilon_3 = 0.53$  from a Glauber Monte Carlo simulation. Participant nucleons *i.e.* the ones interacting (also called ‘wounded nucleons’) are drawn with solid circles, while non-interacting spectator nucleons are drawn as dotted circles. The triangular interaction region is precisely what gives rise to triangular flow. Figure from [11]. . . . . 76
- 2.8 A schematic picture of a nucleus, in which the sources are distributed according to a Gaussian distribution, eq. (2.14). The coordinates  $x$  and  $y$  span the plane transverse to the collision axis. On the right is a random event with  $N = 10$  sources, on the left  $N = 100$  sources. The red region depicts the best-fit ellipse to the distribution of sources. The shape of the ellipse has a link with  $\varepsilon_2$ : the more circular the form, the smaller the value of  $\varepsilon_2$  and the more elongated the form, the bigger the value of  $\varepsilon_2$ . Note the difference in the shape between the two figures. The fact that the right-hand side figure is more circular agrees with eqs (2.15), (2.16). . . . . 80

- 2.9 Results of a Monte Carlo simulation of the Gaussian independent-sources model. Blue circles correspond to numerical values of  $\varepsilon_2\{2\}$  and green circles correspond to numerical values of  $\varepsilon_2\{4\}$ . The dashed red line corresponds to the exact results, eq. (2.15), and the solid turquoise line to eq. (2.16). . . . . 81
- 2.10 Schematic picture of a nucleus with  $N = 100$  sources when the probability distribution of sources is uniform, eq. (2.23). The semi-transparent red region is the best-fit ellipse to this specific distribution of sources. The opaque solid red circle is the unit circle. . . . . 83
- 2.11 Results of Monte Carlo simulations of the independent-sources model with a uniform distribution, eq. (2.23). The blue circles correspond to  $\varepsilon_2\{2\}$  and the dashed red curve to the asymptotic result, eq. (2.24). The green squares correspond to  $\varepsilon_2\{4\}$  and the solid turquoise line to the asymptotic result, eq. (2.25), whereas the magenta line corresponds to the universal result, eq. (2.18). . . . . 83
- 2.12 Sketch of the probability of the energy  $E$  in a given area. The Gaussian (dashed line) extends into the forbidden region  $E < 0$ . Significant improvement is obtained by skewing the Gaussian (solid line). . . . . 84
- 2.13 The negative binomial distribution, eq. (2.47) with the parameters  $p = 0.892$ ,  $k = 100 \times 0.62$  (see the following subsection) for different values of  $w$ . . . . . 91
- 2.14 The Log Series probability distribution of the energy of a single source, corresponding to eq. (2.50) with the parameter  $p = 0.892$ . . . . . 91
- 2.15  $\langle N \rangle^3 \varepsilon_2\{4\}^4$  versus  $\langle N \rangle$  for an isotropic Gaussian distribution, eq. (2.14). Closed circles correspond to fixed  $N$  and the solid line to the exact result, eq. (2.16). Open circles correspond to  $N$  fluctuating according to a Poisson distribution, and the energy of the system *not* fixed. The dashed line corresponds to the perturbative result, eq. (2.83). . . . . 98
- 2.16  $\varepsilon_2\{2\} \varepsilon_2\{4\}$  versus  $\langle N \rangle$  for an isotropic Gaussian distribution, eq. (2.14) with and without energy conservation. Blue circles and magenta-colored squares correspond to  $\varepsilon_2\{2\}$  without and with energy conservation, respectively. Green triangles and orange stars correspond to  $\varepsilon_2\{4\}$  without and with energy conservation, respectively. Points where energy conservation is taken into account are shifted by one unit in  $N$  for better readability. . . . . 98

- 2.17  $\langle N \rangle \varepsilon_2 \{2\}^2$  versus  $\langle N \rangle$  for an isotropic Gaussian distribution, eq. (2.14). Closed circles correspond to the case with exact energy conservation and open circles to the case without energy conservation. For the sake of readability, the points are slightly shifted with respect to each other. The solid line is the leading-order result. . . . . 99
- 2.18  $\langle N \rangle^3 \varepsilon_2 \{4\}^4$  versus  $\langle N \rangle$  for an isotropic Gaussian distribution, eq. (2.14). Closed circles correspond to the case with exact energy conservation and open circles to the case without energy conservation. For the sake of readability, the points are slightly shifted with respect to each other. Solid line: perturbative result, eq. (2.53). Dashed line: eq. (2.18). 99
- 3.1 The analogue of figure 5 of ref. [12] for LHC energies: An approximate history of an ultra-central heavy-ion collision as seen in the  $dS_3 \times \mathbb{R}$  conformal space time. The blue region is not a part of  $\mathbb{R}^{3,1}$ . Hydrodynamics is applicable in a region between the correctly chosen green and red curves, according to the system under consideration (note that  $q$  varies between different systems, see table 3.4). We recall that  $q$  is a parameter whose inverse gives the approximate transverse size of the system. Note that the constant proper time and constant temperature curves are distinct and do not coincide. On the curves of constant proper time, the radial coordinate  $r$  grows as  $\theta$  grows. Looking at the intersections between a given  $q\tau$ -constant curve and the different  $qT$ -constant curves, we see that freeze-out occurs at the periphery of the medium first. See appendix B for details of how this figure was made. . . . . 113
- 3.2 Energy density  $\epsilon$  multiplied by a power of the proper time (left) and the radial flow velocity  $v_\perp \equiv u_\perp/u_\tau$  for the ideal and the viscous case at three different proper times  $\tau = 1 \text{ fm}/c, 3 \text{ fm}/c$  and  $5 \text{ fm}/c$ . Note that the peak of the energy density moves towards larger radii as times goes on, reflecting the fact that the system is expanding. Also note that, with time, the radial flow velocity tends towards the speed of light in the periphery of the QGP. . . . . 115
- 3.3 The temperature profile at a time  $\tau = 2.5 \text{ fm}$  for one random event in units of  $\text{fm}^{-1}$ . The effect of noise is reflected in the bumpiness of the figures. We see that this effect is smallest in the Pb-Pb system and biggest in the p-p system. . . . . 124

- 3.4 Effect of fluctuations on long-range correlations. The initial multipoles that were used as initial fluctuations are of the following forms: (a) elliptic (b) triangular (c) quadrangular (d) pentagonal. We note that the periodicity of each multipole is respected by the noise. We further note that the effect of noise is larger going from Pb-Pb to p-Pb and further to p-p. The biggest relative contribution from noise is to the higher multipoles. Snapshot of dynamics at  $\tau = 2.5\text{fm}/c$ . . . . . 126
- 3.5 The state of the system at  $\tau = 2.5\text{fm}$ , when the initial fluctuation has been set to a delta peak. We see a wave propagating in the positive  $r$  direction and a near-side peak forming on top of the wave. . . . . 127
- 3.6 Zooming in on the near-side peak of the previous figure. The shape and size of the peak varies from system to system: it is at its smallest and narrowest for the Pb-Pb system, then intermediate for the p-Pb system and wide and high for the p-p system. . . . . 128

# List of Tables

1.1	Symbol alphabet of the triangles with one external massive leg, fig. 1.2.	16
1.2	Symbol alphabet of the triangles with two external massive legs, fig. 1.3.	17
1.3	Symbol alphabet of the triangles with three external massive legs, fig. 1.4. . . . .	18
3.1	Experimentally measured values of the number of charged tracks per rapidity for the three systems considered and the relevant references.	122
3.2	Background temperature $\hat{T}_0$ and transverse size $q^{-1}$ of all three systems considered, and the corresponding $T$ values for chosen parameters $r = 0\text{fm}$ , $\tau=2.5\text{fm}$ , calculated according to eqs. (3.41), (3.43) and (3.46) which together give $f_*\tau T = \hat{T}$ , see eq. (3.97). Values for $\hat{T}_0$ and $q^{-1}$ from [13, 14]. . . . .	123



# General introduction

In this thesis we will consider two different cases: firstly the fluctuations in collisions between protons and in particular the quantum corrections to processes that contribute to particle production in proton-proton collisions. Secondly, we look more in general at different fluctuations in arbitrary nucleus-nucleus collisions. Even though the methods used and the motivations behind the different chapters are quite different, the salient feature of this thesis is the existence of fluctuations in different types of high-energy collisions, be it the more elementary proton-proton or the more complex nucleus-nucleus collisions.

Particle colliders have been operating for several decades now. In particular, they have been testing the standard model of particle physics. The standard model is one of the most successful theories of nature there exists, and it has been tested to an unprecedented precision at the particle colliders. It is the theory of elementary particles and their interactions. We are especially interested in one of its building blocks: the theory of strong interactions called quantum chromodynamics. This is the theory that explains the constitution of atomic nuclei. Indeed, it is precisely atomic nuclei that are made to collide at today's experimental particle physics facilities.

Computations in the standard model can be organized in a specific manner. This is called perturbation theory, and in this way the probability of a specific process taking place can be written down as a series in a rather small parameter, the coupling of the theory in question. When this coupling is small we are dealing with perturbation theory, and this is the framework in which we will be working in in the first part of this thesis. A way to present the perturbative series is by diagrams. The most important, lowest-order diagrams, are the ones at tree level, with no closed loops in them. The sub-leading terms have closed loops: one or several. Even though these diagrams are sub-leading, they are by no means negligible, as their contribution to final observable can be of the order of ten percent. We will focus on the one-loop diagrams of this expansion in part I.

All such one-loop diagrams can be written in terms of basic *scalar* loop integrals, whose integrands have trivial numerators, as shown by Passarino and Veltman [15].

Any integral of quantum chromodynamics with a complicated numerator insertion can therefore be reduced to such a scalar integral, and these scalar one-loop integrals will therefore be the focus of our studies.

The integrals of loop diagrams have a rich mathematical structure. In particular, the Feynman integrals arising in the computation of such diagrams (called ‘Feynman diagrams’) form a *Hopf algebra*. A Hopf algebra is a special structure in which we can define the ‘normal’ operations of algebras, such as addition and multiplication, but where, in particular, we can define an operation called the *coproduct*. This coproduct has the property of taking a complicated function and breaking it into simpler pieces. Interestingly, these different pieces carry explicit physical information, namely the information about the singularities of the integral. The information about the singularities from the coproduct can then be used to reconstruct the entire integral. We show this explicitly for one-loop three-point integrals. To be clear about the scope of this chapter, we will only consider scalar and planar Feynman integrals with generic configurations of internal and external masses, computed in dimensional regularization.

In part II we consider heavy-ion collisions with the specific goal of getting to know their fluctuations. Proton-proton collisions, already studied in part I, will be seen again in chapter 3, but in principle we focus on nuclei with more than one nucleon.

Chapter 2 carries a focus on the fluctuations in the shape of the interaction region in a collision between atomic nuclei. In particular, it is known that the overlap region, even in a perfectly head-on collision, is not fully symmetric but has some anisotropy. This feature of the initial state is known indirectly from measurements of the final-state particle spectrum. Notably, the *very low viscosity fluid* created in heavy-ion collisions acts a lens, faithfully transferring *initial state spatial anisotropies into final state momentum-space anisotropies*. These anisotropies are usually quantified by making a Fourier decomposition of the *flow harmonics of the final state*. We talk about *flow* because the matter produced in nucleus-nucleus collisions really does behave like a fluid that flows and expands during the first few fm/c after a collision.

The Fourier coefficients that relate to the spatial shape fluctuations of the interaction region are called *eccentricities*. In chapter 2 we will be studying eccentricity fluctuations. In particular, we will study the *non-Gaussian nature* of these fluctuations. Indeed, it has been experimentally measured that the statistics of these fluctuations does not follow from a Gaussian distribution. The relevant experimental observables are the *cumulants* of the distribution. The cumulants are a good way to test the Gaussian nature of the eccentricity fluctuations because for a Gaussian distribution all higher-order (order four and larger) cumulants vanish. Hence, the measured non-zero values of the fourth cumulants of the second and third Fourier

harmonics, called *elliptic and triangular flow*, quantify the non-Gaussianity of the fluctuations of eccentricity. We will study these fluctuations analytically in the framework of perturbation theory, and then test our analytical results with Monte Carlo simulations.

In chapter 3 we continue the study of fluctuations in nucleus-nucleus collisions. Here, however, we step away from the quantum world of the previous chapters and consider classical hydrodynamics. As already noted, the medium created in nucleus-nucleus collisions is known to behave like a fluid during the first few fm/c after the collision. This fluid is very hot and very dense, and also strongly interacting. It flows with very little dissipation, meaning that the viscosity of the fluid is small. This is why the fluid produced in nucleus-nucleus collisions is called *nearly ideal or perfect*. Due to the very high density and temperature of this fluid, it starts expanding and cooling down immediately after it has been produced. This three-dimensional expansion of a viscous fluid is quite complicated to describe. Indeed, for many years, a solution of a fluid expanding only in the longitudinal direction, that is, the direction of the beam axis, was only known to exist. In recent years, fully three-dimensional numerical simulations have been developed. Furthermore, and of great interest to us in chapter 3, an analytical solution has been published. This solution has the three-dimensional fluid expansion that we already mentioned, with the symmetry of the original one-dimensional solution taken into account as well. This three-dimensional solution relies on *conformal symmetry*, meaning scale invariance. What is typical for conformal transformations is that they preserve angles but not sizes. The fluid produced in nucleus-nucleus collisions is known to be conformal to a good approximation. Therefore, we come close to describing reality during (the beginning of) the hydrodynamic phase. What will be lacking in our analysis, however, are the stages where the fluid has already cooled down quite a bit, and the hydrodynamic description breaks down. This is the domain of hadronization and freeze-out.

The theme of this thesis, fluctuations, is covered in chapter 3 in the following way. This fully three-dimensional solution that we mentioned is thanks to Gubser, and we will call this solution the Gubser one. The Gubser solution has a high degree of symmetry, and it plays with different space times and coordinate transformations. As we will see, we will be able to place ourselves in a de Sitter type space, where the equations of motion of the fluid simplify. This de Sitter space is related by a conformal transformation to the usual Minkowski space. Thanks to the simplicity of the de Sitter solution, we are able to add an extra degree of difficulty: small perturbations in the hydrodynamic evolution. These are *the hydrodynamic fluctuations*. We will perform perturbative calculations, and study the system evolution with numerical simulations. In particular, we will be interested in the effect of these hydrodynamic

fluctuations on *small systems*, where the fluctuation-dissipation theorem predicts that the effect of noise is at its largest.

# French resume – Résumé en français

*Pour des références voir la version anglaise.*

Nous étudions des fluctuations qui sont omniprésentes dans des collisions entre particules aux hautes énergies. Ces fluctuations peuvent être de nature classique ou quantique et nous allons considérer ces deux cas. D’abord, nous étudions les fluctuations quantiques qui sont présentes dans des collisions entre protons. Celles-ci sont calculables en théorie quantique des champs, et nous allons nous concentrer sur une certaine classe de diagrammes dans ce cadre. Dans un second temps nous allons étudier des fluctuations qui sont présentes dans des collisions entre particules plus lourdes que le proton. Celles-ci sont décrites par les lois quantiques de la nature qui donnent les positions des nucléons dans le noyau, ou bien des fluctuations classiques, d’origine thermique, qui affectent l’évolution hydrodynamique du milieu produit dans une collision.

Les fluctuations dans des collisions entre protons peuvent être calculées analytiquement jusqu’à un certain ordre en théorie quantique des champs. Nous allons nous concentrer sur des diagrammes à une boucle, d’une topologie donnée. Ces diagrammes aux boucles donnent des intégrales, qui typiquement sont difficiles à calculer. Nous allons démontrer comment des outils des mathématiques modernes peuvent être utilisés pour faciliter leur évaluation. En particulier, nous allons étudier des relations entre des coupures d’un diagramme, la discontinuité à travers d’un branchement et le coproduit. Nous allons démontrer comment l’intégrale originale peut être reconstruite à partir de l’information contenue dans le coproduit. Nous nous attendons à ce que ces méthodes seront utiles pour le calcul des diagrammes avec des topologies plus difficiles et ainsi aident au calcul des nouvelles amplitudes de diffusion.

A la fin, nous étudions les deux types de fluctuations qui ont lieu dans des collisions entre ions lourds. Celles-ci sont liées soit à l’état initial de la matière, soit à l’état intermédiaire produit dans un tel collision. Les fluctuations de l’état ini-

tiale ont été mesurées expérimentalement, et on voit qu'elles donnent lieu à des non-Gaussianités dans le spectre final de particules. Nous allons démontrer comment ces non-Gaussianités peuvent être compris comme des positions et des énergies d'interaction aléatoires des 'sources' dans les noyaux entrant en collision. En plus, nous étudions le bruit hydrodynamique dans le milieu produit juste après un collision. Le comportement de ce milieu est celui d'un fluide à basse viscosité.

## Introduction générale

Dans cette thèse nous considérons deux cas : d'abord les fluctuations dans des collisions entre protons et en particulier les corrections quantiques aux processus qui contribuent à la production de particules dans des collisions entre protons. Ensuite nous étudions d'un point de vue plus général les fluctuations dans des collisions arbitraires entre noyaux lourds. Malgré le fait que la motivation de chaque chapitre est assez différente, le côté unificateur de cette thèse est l'existence des fluctuations dans des types différents de collisions aux hautes énergies, que cela soit des collisions entre protons ou des noyaux plus complexes que le proton.

Des collisionneurs de particules sont opérationnels depuis plusieurs décennies maintenant. Ils ont, en particulier, testé le modèle standard de la physique des particules. Ce modèle standard est une des théories les plus couronnées de succès du monde, et il a été étudié et testé jusqu'à une précision jamais vu précédemment. C'est la théorie des particules élémentaires et leurs interactions. Nous nous intéressons en particulier à un des théories de fond de ce modèle, c'est-à-dire le chromodynamique quantique, la théorie des interactions fortes. Cette théorie explique la constitution des noyaux atomiques qu'on fait s'entrechoquer aux collisionneurs aujourd'hui.

Les calculs du modèle standard peuvent être organisés d'une manière bien spécifique. Ceci est la théorie des perturbations. Dans ce cadre, la probabilité d'un processus peut être décrite comme une série d'un petit paramètre dit le couplage de la théorie. Lorsque ce couplage est faible, nous avons à faire avec la théorie des perturbations, et c'est précisément ce cadre que nous étudions dans la première partie de cette thèse. Cette série perturbative peut être représenté par des diagrammes. Les diagrammes les plus importants sont ceux qu'on appelle des diagrammes aux arbres, qui sont les diagrammes de l'ordre le plus bas. Les ordres suivants sont représentés par des diagrammes aux boucles fermées. Nous allons étudier les diagrammes à une boucle dans la partie I de cette thèse. C'est des diagrammes sous-dominants, mais pas du tout négligables, car leur contribution à la section efficace peut être de l'ordre de dix pour cents.

N'importe quel tel digramme à une boucle peut être écrit en terme d'intégrales

dites *scalaires*. Une intégrale scalaire a un numérateur qui est trivial. Donc, une intégrale compliquée de chromodynamique quantique avec des insertions dans le numérateur peut être réduit à une telle intégrale scalaire. Ces intégrales seront donc notre focus dans la première partie de cette thèse.

Les intégrales de diagrammes aux boucles ont une structure mathématique très riche. En particulier, ces intégrales dites *de Feynman* forment une algèbre de Hopf. Une algèbre de Hopf est une structure mathématique spéciale dans laquelle nous pouvons définir les opérations ‘normales’ d’une algèbre, telles que l’addition et la multiplication, mais aussi une opération nommée le *coproduit*. Le coproduit a la propriété de prendre une fonction complexe de l’algèbre et de la casser en morceaux plus élémentaires. Ce qui rend le coproduit intéressant est le fait que chacun de ses morceaux contient de l’information physique sur le diagramme étudié. Ceci est l’information des singularités de l’intégrale. Cette connaissance des singularités de l’intégrale peut ensuite être utilisée pour reconstruire l’intégrale entièrement. Nous démontrons ceci explicitement pour des intégrales de trois pattes externes à l’ordre d’une boucle. Pour rendre plus clair le domaine de validité de l’œuvre présentée dans cette thèse, nous allons uniquement considérer des intégrales de Feynman scalaires et planaires, avec des configurations génériques de masses internes et externes. Toutes ces intégrales seront calculées dans la régularisation dimensionnelle.

Dans la partie II de cette thèse nous étudions les collisions entre noyaux lourds afin de connaître les effets de fluctuations dans ces collisions. Les collisions entre protons, déjà étudiées dans la partie I, seront à nouveau étudiées dans le chapitre 3, mais en principe nos travaux seront focalisés sur des noyaux avec plus d’un proton.

Dans le chapitre 2 nous nous concentrons sur les fluctuations dans la région d’interaction d’une collision entre noyaux atomiques. En particulier, c’est bien connu que, même dans des collisions parfaitement centrales, cette région d’interaction n’est pas parfaitement symétrique mais qu’elle est *anisotrope*. Cette caractéristique est connue de façon indirecte depuis le spectre final des particules. Nous remarquons que le fluide de très basse viscosité créé dans des collisions entre noyaux lourds agit comme une lentille qui transfère, de manière fidèle, *les anisotropies initiales de l’espace dans des anisotropies finales de l’espace des impulsions*. Ces anisotropies sont habituellement quantifiées en faisant une transformée de Fourier des harmoniques de *écoulement* de l’état final. Souvent le mot anglais ‘flow’ est utilisé pour cet écoulement, et nous allons l’utiliser par la suite. Ici, nous parlons de ‘flow’ puisque l’état de la matière produit dans une collision d’ions lourds, et qui ‘vit’ pendant les quelques premiers fm/c après une telle collision, se comporte en effet comme un fluide avec de l’écoulement et expansion.

Les coefficients de Fourier qui sont liés aux fluctuations de la région d’interaction,

c'est-à-dire des fluctuations dans l'espace, s'appellent des *eccentricités*. Dans le chapitre 2 nous étudions les fluctuations d'eccentricité. En particulier, nous nous intéressons à la nature non-Gaussienne de ces fluctuations. En effet, les expériences aux collisionneurs ont mesuré la statistique de ces fluctuations, et c'est établi aujourd'hui que cette statistique n'est pas Gaussienne. Les quantités mesurées dans des expériences, dites 'observables', sont les *cumulants* de la distribution statistique. Les cumulants sont adaptés aux mesures des non-Gaussianités puisque pour une distribution Gaussienne tout cumulant d'un ordre supérieur ou égale à quatre disparaît. C'est ainsi que les valeurs non-nulles mesurées des cumulants d'ordre quatre des coefficients deux et trois de la série de Fourier, appelés *flow elliptique* et *flow triangulaire*, quantifient la nature non-Gaussienne de ces fluctuations. Nous allons étudier ces fluctuations analytiquement dans le cadre de la théorie des perturbations et ensuite tester ces résultats analytiques avec des simulations Monte-Carlo.

Dans le chapitre 3 nous continuons l'étude des fluctuations dans des collisions d'ions lourds. Ici, cependant, nous nous éloignons du monde quantique des chapitres précédents pour nous mettre dans le cadre de l'hydrodynamique classique. Comme nous l'avons déjà remarqué, le milieu produit dans des collisions d'ions lourds a un comportement de fluide pendant les premiers fm/ $c$  après la collision. Ce fluide est très chaud et très dense, et en plus c'est un milieu avec des fortes interactions. C'est un fluide qui s'écoule avec très peu de résistance, ce qui veut dire que la viscosité de ce fluide est petite. Ceci est la raison pour laquelle le fluide produit dans des collisions d'ions lourds est appelé *quasi idéal ou parfait*. Puisque la densité et la température de ce fluide sont extrêmement élevées, le fluide refroidit et s'étend dès qu'il est produit. Cette expansion d'un fluide visqueux en trois dimensions spatiales est difficile à décrire. C'est pour cela qu'une solution plus simple, avec expansion seulement dans la direction longitudinale (c'est-à-dire, dans le sens du faisceau) existait pendant longtemps. Lors des dernières années des simulations numériques ont été développées pour résoudre ce problème. En plus, et ce qui nous intéressera surtout dans le chapitre 3, une solution analytique en trois dimensions a été publiée. Ceci est une solution avec une expansion tridimensionnelle et qui intègre la symétrie de la première solution unidimensionnelle. Cette solution est basée sur *la symétrie conforme*, ce qui signifie invariance d'échelle. Ce qui caractérise les transformations conformes est qu'elles préservent les angles mais non pas les tailles des choses. Le fluide produit dans des collisions d'ions lourds est connu conforme à peu près. Pour cela, nous ne sommes pas loin de la réalité (du début) de la phase hydrodynamique. Ce qui va nous manquer dans notre description hydrodynamique du fluide, c'est les phases quand le fluide a déjà pas mal refroidi, et quand l'hadronisation et le 'freeze-out' ont lieu.

Le thème de cette thèse, les fluctuations, est couvert dans le chapitre 3 dans la manière suivante. Cette solution tridimensionnel dont nous avons parlé est grâce à Gubser, et nous allons l'appeler simplement 'la solution de Gubser'. La solution de Gubser possède un haut degré de symétries et c'est une solution qui joue avec des espace-temps différents et des transformées de coordonnées. Comme nous allons le voir, nous pourrons nous placer dans un espace-temps de type de-Sitter où les équations de mouvement se simplifient. Cet espace-temps de type de-Sitter est lié à l'espace-temps usuel de Minkowski par une transformation conforme. Grâce à la simplicité de la solution dans l'espace-temps de de Sitter, nous pouvons inclure un degré de difficulté en plus : des petites perturbations dans l'évolution hydrodynamique. Celles-ci sont les *fluctuations hydrodynamiques*. Nous allons faire des calculs analytiques et étudier l'évolution du système avec des simulations numériques. En particulier, nous nous intéressons à l'effet qu'ont ces fluctuations dans des petits systèmes, là où le théorème de fluctuation-dissipation prédit que l'effet du bruit est le plus fort.

## Coupures et coproduits des diagrammes triangulaires à une boucle

Le modèle standard de la physique des particules est une théorie qui est extrêmement réussi quand il s'agit de décrire les données expérimentales à très haute précision. Cette connexion entre expériences, comme aux collisionneurs de particules, et théorie, comme le modèle standard, se fait par la section efficace d'un processus. Cette section efficace est déterminé par *l'amplitude de diffusion* du processus en question, c'est-à-dire la probabilité différentielle de ce processus.

Le modèle standard est une théorie quantique des champs. Dans la théorie quantique des champs, il existe un manière astucieuse d'organiser les calculs : c'est l'expansion en diagrammes de Feynman. Dans cet expansion, on fait une développement en série dans un petit paramètre. Ce paramètre est le couplage de la théorie et il donne la force des interactions. Il est, en effet, un paramètre plutôt petit dans le cas de la chromodynamique quantique (QCD) aux hautes énergies, le cadre pour nous dans cette thèse. Les termes de l'ordre le plus bas dans l'expansion en diagrammes de Feynman s'appellent des diagrammes aux arbres, et des diagrammes d'ordres supérieurs s'appellent *des diagrammes à boucles*, puisqu'ils incluent des boucles fermées. Dû au fait que les particules virtuelles dans des boucles ne sont pas observables, on intègre sur l'impulsion de ces particules. Alors il suit qu'un calcul donnant des prédictions dans la théorie quantique des champs implique des intégrations des di-

agrammes à boucles. Ces intégrales sont souvent difficiles à calculer, et empêchent parfois l'évaluation des observables à haute précision. Au moment d'écriture de ce manuscrit, les calculs les plus pointus et poussés sont à une ou parfois deux boucles, avec l'exception de la production du boson de Higgs, pour lequel le processus de production par fusion de gluons a été calculé à trois boucles.

La difficulté de l'évaluation de ces intégrales a donné lieu aux différentes techniques d'intégration. Une méthode utilisée assez tôt était celle de l'analyse des discontinuités de l'intégrales de Feynman à travers leurs branchements. Ces discontinuités peuvent être calculés en utilisant des règles diagrammatiques. Selon ces règles, des partitions de diagrammes de Feynman sont énumérés, et les particules aux bords de ces deux régions sont restreintes à leur couches de masse. Cette operation définit un ensemble de *diagrammes coupés*. En recueillant des diagrammes avec le même flux d'impulsion entre les deux régions, nous contruisons la *coupure d'unitarité* (anglais : 'unitarity cut') qui capture la discontinuité à travers le branchement lié à cet invariant d'impulsion. Ces restrictions de couche de masse simplifient l'intégration et le résultat. L'intégrale d'origine peut ensuite être 'reconstruit', traditionnellement en utilisant des relations de dispersion. Ceci n'est, par contre, pas une tâche facile, et c'est en effet une partie de la motivation derrière les travaux présentés dans ce chapitre.

Une autre méthode, plus recente, pour l'évaluation des diagrammes aux boucles est la méthode appelé *la méthode de l'unitarité* (anglais : 'unitarity method'), dans laquelle des discontinuités d'une amplitude sont utilisées pour la projeter sur une base d'intégrales connues. On gange en efficacité en faisant des *coupures multiples* dans plusieurs canaux d'impulsion simultanément. Le fait de restreindre plusieurs propagateurs à leurs couches de masse sépare le digramme en plusieurs éléments qui sont sur leur couche de masse, et qui sont souvent plus faciles à calculer.

C'est connu qu'à l'ordre d'une boucle, toute intégrale peut être réduit aux intégrales *scalaires*, c'est-à-dire des intégrales avec numérateurs qui valent un. Nous allons donc travailler avec ces composantes de base des intégrales à une boucle, et considérer uniquement des diagrammes de Feynman scalaires. À cet ordre, c'est aussi connu que les intégrales qui apparaissent peuvent être décrites en termes des fonctions spéciales, dites polylogarithmes multiples. Aussi d'autres intégrales, aux ordres supérieurs peuvent être décrites par ces polylogarithmes, tant qu'elles ont assez peu de masses. Sinon, aux ordres supérieurs, des fonctions elliptiques peuvent apparaître. En toute généralité, lesquelles sont les fonctions produites par des intégrales de Feynman est toujours une questions sans réponse. Des développements récents portant sur la structure mathématique de cette classe de fonctions, les polylogarithmes, et en particulier leur *structure d'algèbre de Hopf* ont donc eu un grand impact sur la

communauté les dernières années.

Les polylogarithmes multiples ont une structure algébrique très riche. En particulier, ils forment une algèbre de Hopf, une structure naturelle pour analyser les discontinuités. Aujourd’hui il existe déjà beaucoup d’évidence pour le ‘first-entry condition’, la condition de la première entrée. Cette condition stipule que des termes du coproduit ayant un poids transcendantal  $1, n - 1$  peuvent être écrits comme suit

$$\sum_i \log(-s_i) \otimes f_{s_i} , \quad (1)$$

où la somme est sur tous les invariants de Mandelstam  $s_i$  et  $f_{s_i}$  est la discontinuité du diagramme par rapport à la variable  $s_i$ . Ceci est vrai pour tout diagramme avec des masses internes nulles.

La nouveauté du papier originel dans l’annexe C et des travaux présentés dans ce chapitre est l’inclusion de masses. Nous incluons les masses partout : sur les pattes externes et aussi sur les propagateurs internes. Nous considérons également des limites où certaines de ces masses disparaissent.

Nos études en présence des masses internes suggèrent que la condition de la première entrée doit être modifiée pour tenir compte des nouveaux emplacements des branchements. Les impulsions externes ont des branchements liés à leurs seuils de masse, et aussi des masses internes ont des branchements. Compte tenu de ces observations, la composante  $1, n - 1$  du coproduit s’écrit

$$\sum_i \log(m_{p_i}^2 - p_i^2) \otimes f_{p_i} + \sum_j \log(m_j^2) \otimes f_{m_j} , \quad (2)$$

où les  $f_{p_i}$  et  $f_{m_j}$  sont des discontinuités liés aux variables  $p_i^2$  et  $m_j^2$  respectivement.

Les fonctions  $f_x$  sont liés aux coupures d’unitarité dans le canal correspondant. Ceci est le cas pour des coupures simples et aussi pour des coupures multiples. Les coupures et discontinuités prises dans des canaux externes et internes sont encodées dans des termes distincts du coproduit. Ces termes sont tout simplement un ensemble des logarithmes avec les mêmes discontinuités. Les coupures dans des masses internes, *coupures dans particules uniques* (anglais : ‘single-particle cut’), correspondent aux discontinuités dans les masses internes et aux termes avec des masses comme premier cofacteur dans l’équation 2. Ces masses sont le côté neuf dans notre analyse : le cas sans masses internes a été étudié précédemment mais la généralisation aux masses internes non nulles est présenté dans ce chapitre et dans l’annexe C. Nous concentrons nos efforts sur des *triangles scalaires*, puisque ceux-ci sont assez simples pour nous donner un ‘aire des jeux’ assez simple, permettant à étudier cette nouveauté de masses internes mais dans l’attente de voir déjà à ce stade là des nouveaux problèmes apparaître.

Une autre nouvelle observation est que les fonctions qui apparaissent comme arguments des logarithmes dans le coproduit des intégrales considérées, que nous allons appeler les *lettres de l'alphabet du symbole*, sont indiquées par les coupures. Notre but est de trouver des lettres qui sont des fonctions rationnelles. Une algorithmique générale pour trouver un tel alphabet n'est pas connu, mais nos études suggèrent que le calcul des coupures peut aider à le trouver.

## Conclusions de ce chapitre

Dans ce chapitre nous avons étudié la structure analytique des diagrammes de Feynman à trois pattes et à une boucle avec des configurations différentes de masses internes et externes. Nous nous intéressons surtout aux intégrales ayant des propagateurs massifs, mais nous avons aussi brièvement considéré le triangle à une boucle dont toutes les masses internes sont nulles quand cela donne lieu aux simplifications et où cela nous a aidé à démontrer ce nous voulions. Ce cas du triangle à une boucle sans masses internes a été étudié auparavant ailleurs, dans un papier où il a été présenté, pour la première fois, des relations entre des coupures d'unitarité, des discontinuités à travers des branchements et la structure de coproduit de l'algèbre de Hopf des intégrales de Feynman. Nos études dans ce chapitre sont des généralisations de ce premier papier, et les résultats complets sont donnés dans l'annexe C de cette thèse. Les travaux de l'auteur ont principalement porté sur la reconstruction du symbole et la fonction entière à partir des coupures d'unitarité des intégrales.

Les conclusions principales de ce chapitre sont les suivantes. D'abord, nous avons vu que *la condition de la première entrée* doit être généralisée quand nous considérons des diagrammes avec des propagateurs internes massifs. Dans l'absence de ces masses internes, les premières entrées du coproduit sont simplement des logarithmes des invariants de Mandelstam du diagramme. Dans la présence des masses internes, nous devons prendre en compte les seuils de masse des invariants.

En deuxième lieu, nous avons généralisé les règles des coupures pour des diagrammes avec masses internes. Les observations faites ailleurs dans l'absence des masses internes tiennent toujours pour les discontinuités dans des canaux externes. Par contre, les masses internes donnent lieu à un nouveau type de coupure : *la coupure dans une particule unique*. Nous avons démontré comment calculer ces coupures et clarifié leur signification en terme du symbole du diagramme. Nous avons également observé que le calcul de coupures est en fait une bonne manière pour obtenir un alphabet de symbol *rationnel*. Les coupures nous indiquent la bonne direction à prendre pour trouver des variables qui rationalisent l'alphabet.

En un troisième lieu, nous avons élargi les relations 'Cut=Disc= $\delta$ ' pour tenir

compte des masses internes. Nous arrivons à le faire en liant les coupures d'unitarité 'Cut' aux discontinuités à travers les branchements 'Disc' et ensuite en reliant les discontinuités aux entrées du coproduit ' $\delta$ '. De cette façon, nous relierons Cut à  $\delta$ , ce qui est le résultat principal de ce chapitre. Les résultats présentés ici sont pour la plupart des généralisations des relations publiés par d'autres chercheurs ailleurs, sauf pour des détails subtils liés à la présence des masses internes. Un tel détail est que nous nous obligeons à faire toute coupure dans les canaux externes avant de faire des coupures dans des masses internes.

Enfin, nous avons étudié *la reconstruction* des intégrales par leurs coupures et symboles. Dans tous nos exemples il suffit de connaître une seule coupure dans un canal externe d'un diagramme donné pour arriver à reconstruire la fonction complète. Nous nous concentrons surtout sur le fait de trouver le symbole d'un diagramme à partir d'une coupure. La méthode appliquée est de construire un ansatz pour le symbole pour ensuite restreindre les paramètres numériques de cet ansatz. Pour le faire, nous utilisons des observations que nous avons été amenés à faire lors de ces études concernant les triangles massifs à une boucle. L'intégration du symbole, malgré le fait qu'elle reste un problème non résolu pour d'ordres supérieurs et plus de pattes externes, est faisable pour les triangles en utilisant des logiciels modernes.

Pour conclure, nous croyons qu'une meilleure compréhension de la structure analytique des diagrammes de Feynman est fondamentale pour le développement des méthodes de calcul pointues et plus efficaces. Compte tenu des résultats de ce chapitre de cette thèse, nous croyons que le coproduit de l'algèbre de Hopf des polylogarithmes multiples est un outil approprié pour aborder ce problème.

## Introduction aux collisions d'ions lourds

Des collisions d'ions lourds, parfois appelés des 'Little Bangs', créent des conditions proches à celles qui existaient dans l'univers pendant la première microseconde après le Big Bang. Dans ces collisions, les scientifiques créent températures qui sont les plus élevées jamais vues sur terre :  $5.5 \cdot 10^{12}$  degrés, ce qui correspond aux températures 300 000 fois supérieures à celle au centre du soleil. Le milieu produit se comporte comme un fluide, et donc on parle des gouttelettes les plus petites et chaudes jamais produites.

Ces gouttelettes sont produites à deux collisionneurs différents aujourd'hui : le Relativistic Heavy Ion Collider (RHIC) à Brookhaven, New York, et le Large Hadron Collider (LHC) près de Genève. Au RHIC des noyaux différents ont été utilisés : des protons, des deutérons, du cuivre, de l'or et de l'uranium. Au LHC on se concentre sur des protons et du plomb. Les énergies par paire des nucléons varie de 130 MeV

(début de l'utilisation du RHIC) jusqu'à 5.02 TeV (Novembre 2015 au LHC).

Dans ces collisionneurs, les particules sont accélérées jusqu'à ce qu'elles atteignent plus de 99% de la vitesse de la lumière. Ceci implique que les noyaux entrant en collision sont fortement contractés et ressemblent alors aux crêpes minuscules et très fines. En outre, la dilatation du temps de Lorentz implique que le temps se ralentit pour les noyaux, ce qui signifie que les configurations sont figées dans un état quantique bien spécifique lors de la collision. Alors une collision à haute énergie donne vraiment une image instantanée d'un noyau au moment où il heurte l'autre noyau. Cette configuration initiale des nucléons dans un noyau nous intéresse, et nous allons en parler plus dans le chapitre 2.

Une manière spécifique pour décrire l'état initial d'un noyau avec une très haute énergie et qui entre en collision, c'est le modèle de Glauber. Ce modèle donne l'interaction noyau-noyau en terme des interactions entre les nucléons avec une certaine distribution de densité. C'est un modèle semi-classique qui donne la collision nucléaire dans la représentation du paramètre d'impact et où les noyaux bougent dans le sens de la collision sur des lignes droites. Le paramètre d'impact, mentionné ici, et la distance transverse entre les centres des deux noyaux qui entrent en collision. Ceci est représenté dans la figure 1.14. Ceci est le type d'image que nous avons en tête dans le chapitre 2.

Au bout d'un certain temps après la collision, typiquement autour de 1 fm/c après la collision, le système se comporte comme un fluide. Lors de ce stade, le système est décrit par l'hydrodynamique, voir figure 1.15. Effectivement, la façon de modéliser une collision d'ions lourds aujourd'hui consiste à prendre un état initial, possiblement avec des fluctuations, et de le laisser évoluer selon l'hydrodynamique relativiste. Ici, le cadre correcte est l'hydrodynamique *visqueuse* puisque la viscosité du fluide est non nulle.

Le fait que le système se comporte comme un fluide on sait depuis des nombreux évidences liées à l'expansion forte du milieu produit dans une collision d'ions lourds. La réalisation d'un milieu chaud et dense est suggéré par plusieurs choses : parmi celles-ci sont des analyses des spectres de particules identifiées, le 'flow' elliptique (dont nous parlerons plus plus tard), l'interferométrie de Hanbury-Brown-Twiss et la suppression de particules ayant un grand impulsion transverses.

Selon les données expérimentales, la distribution finale des impulsions de particules produites est *asymétrique dans l'angle azimutal*. Ces asymétries ont une forme bien spécifique, et on peut les décrire avec une série de Fourier (voir figure 1.17)

$$E \frac{dN}{d^3p} \equiv \frac{1}{2\pi} \frac{\sqrt{m^2 + p_T^2 \cosh^2 \eta}}{p_T \cosh \eta} \frac{dN}{p_T dp_T d\eta} \left( 1 + \sum_{n=1}^{\infty} v_n \cos n(\phi - \Psi_n) \right), \quad (3)$$

où  $p_T$  est l'impulsion transverses de la particule émise et  $\eta$  est défini selon

$$\eta = -\ln\left(\tan\frac{\theta}{2}\right). \quad (4)$$

Des valeurs différentes de  $\eta$  sont montrées dans la figure 1.16.

Ceci est un phénomène qui porte le nom *flow harmonique*. Le premier harmonique est celui du ‘flow orienté’. Le deuxième et le plus dominant dans des collisions où le paramètre d’impacte est non nul est le ‘flow elliptique’. Le flow elliptique peut être simplement compris comme venant de la région de forme d’amande qui caractérise la région d’interaction de deux noyaux quand la collision n’est pas parfaite. Dû aux fluctuations quantiques, aussi des harmoniques plus élevés existent. Le plus important de ces harmoniques élevés est le flow triangulaire. Plus le harmonique est élevé, plus il est étouffé par la viscosité, alors les harmoniques dominants sont ceux de l’ordre le plus bas.

Le flow harmonique est dû à une répose du système aux anisotropies initiales. En fait, le plasma de basse viscosité transfère, grâce aux gradients de pression, la structure géométrique de la distribution initiale de densité en une anisotropie de l’état final. Ensuite ceci apparaît comme des corrélations entre des particules produites (voir figure 1.18). Dans cette figure on montre la quantité  $C(\Delta\phi, \Delta\eta)$ , qui est définie comme

$$C(\Delta\phi, \Delta\eta) \equiv \left\langle \frac{dN}{d\phi_1 d\eta_1} \frac{dN}{d\phi_2 d\eta_2} \right\rangle, \quad (5)$$

où  $\Delta\phi = \phi_1 - \phi_2$  et  $\Delta\eta = \eta_1 - \eta_2$ .

La nature des fluctuations quantiques de l’état initial est le sujet du chapitre 2. Expérimentalement il est observé que ces fluctuations ne sont pas Gaussiennes. Ceci est lié aux effets de taille finie : le système produit dans des collisions d’ions lourds ne peut pas être vu comme un système de taille infinie, dans quel cas le théorème du limite centrale s’appliquerait et les fluctuations seraient Gaussiennes.

Les fluctuations sont aussi présentes lors des phases plus tardives d’une collision, et non pas seulement dans l’état initial. Comme nous l’avons déjà dit, au bout d’un fm/c après une collision le milieu est fluide et peut être décrit par l’hydrodynamique. Dans un système thermique avec une température non nulle, des fluctuations thermiques existent. De telles fluctuations existent aussi dans l’évolution hydrodynamique du fluide, et nous les appelons *des fluctuations hydrodynamiques*. Ceci est le phénomène qui nous intéresse dans le chapitre 3.

## Fluctuations non-Gaussiennes de l’eccentricité

La méthode moderne pour modéliser des collisions d’ions lourds consiste à prendre un état initial et de le laisser évoluer selon les lois de l’hydrodynamique. Pendant longtemps, cette modélisation d’hydrodynamique utilisait des états initiaux avec des densités d’énergie lisses et symétriques. Dans la réalité, par contre, il existe des fluctuations dans les premières étapes d’une collision, venant de la structure nucléonique des noyaux qui entrent en collision. La densité d’énergie est en fait grumeleuse et asymétrique et en plus elle fluctue d’une collision à l’autre. Ceci est vrai même pour des collisions avec le même paramètre d’impact, c’est-à-dire pour des événements qui sont dans la même classe de centralité. Pour une illustration des états initiaux grumeleux et asymétriques, voir la figure 2.1.

Cette anisotropie au début de la collision, dû aux fluctuations d’un événement à l’autre, donne lieu à une anisotropie dans l’angle azimutal de la production des particules grâce à l’expansion collective. Ces asymétries dans l’angle azimutal de la production des particules est mesurée en comptant des paires des particules, c’est-à-dire en mesurant des *corrélations à deux particules*, ou alors en comptant plusieurs particules à la fois. Ces mesures ont conduit à l’image du *flow anisotropique* en termes d’une série de Fourier. L’harmonique de l’ordre  $n$  du flow,  $v_n$ , est liée à l’anisotropie spatiale  $\varepsilon_n$  de façon linéaire, au moins pour des collisions ‘ultra-centrales’, comme illustré dans la figure 2.2. Il suit qu’en mesurant des corrélations des particules de l’état final, on a de façon indirecte accès à l’état initial du noyau, décrit par des lois quantiques.

Comme nous l’avons brièvement mentionné déjà, l’état quantique initial fluctue d’un événement à l’autre. Ces fluctuations sont dans une première approximation Gaussiennes. Cependant, quand des corrélations à quatre particules ont été mesurées, comme à l’expérience ALICE (voir la figure 2.3) ou à l’expérience CMS (voir la figure 2.4), on a découvert que ces fluctuations ne sont en fait *pas Gaussiennes*. L’anisotropie de l’état initial est quantifié par son eccentricité  $\varepsilon_n$ . Voir la figure 2.5 pour une illustration de  $\varepsilon_2$ . Dans ce chapitre nous étudions précisément cette nature non-Gaussienne de ces fluctuations de l’eccentricité, en supposant une réponse linéaire  $v_n \propto \varepsilon_n$ .

### Conclusions de ce chapitre

Dans ce chapitre nous avons étudié les fluctuations de l’eccentricité et en particulier leur nature non-Gaussienne. Comme outils nous avons utilisé la théorie des perturbations et les simulations Monte Carlo. Tout résultat présenté dans ce chapitre était

pour le cas de l'ellipticité  $\varepsilon_2$ , mais nous avons vérifié que nos conclusions tiennent pour la triangularité  $\varepsilon_3$ .

D'abord, nous avons généralisé des résultats précédents pour tenir compte d'un profil de densité continu. En le faisant, nous avons supposé que les fluctuations de la densité sont locales. En plus, nous avons soutenu que la nature non-Gaussienne des fluctuations d'excentricité viennent pour une grande partie de la nature non-Gaussienne des fluctuations de densité. Le fait de demander que l'énergie d'un système soit positive génère, de manière naturelle, des non-Gaussianités sous la forme d'asymétrie et kurtosis non nuls. La magnitude de ces quantités est contrôlée par la dynamique microscopique du système.

En un deuxième lieu, nous prenons note du fait que les non-Gaussianités sont sensibles à la dynamique sous-jacente. En particulier, la signe du cumulants d'ordre quatre varie et peut être négative. Nous observons une puissance quatre de ce cumulants qui est négative en présence de grandes fluctuations de multiplicité. Nos simulations Monte Carlo suggèrent que la convergence vers cette valeur négative asymptotique est très lente. Ces simulations démontrent aussi que des résultats obtenus pour quelques centaines de 'sources', correspondant au nombre de participants dans une collision centrale d'ions lourds, peuvent varier de façon significative du résultat perturbatif.

Enfin, pour des petits systèmes nous observons que la statistique 'universelle' proposé auparavant par Yan et Ollitrault est en général une bonne approximation. Cette observation est en accord avec des données expérimentales sur le flow elliptique dans des collisions entre protons et noyaux, ce qui renforce la conclusion que le flow elliptique dans ces systèmes vient de l'excentricité initiale  $\varepsilon_2$ .

## Fluctuations hydrodynamiques et flow de Gubser

Des phénomènes collectifs sont omniprésents dans le domaine de la physique et ils sont observés dans des systèmes ayant des échelles temporaires et spatiales qui vont des noyaux atomiques et échelles biologiques jusqu'aux échelles liés à la formation des galaxies. Pour parler de manière vague, la collectivité est un comportement commun manifesté par un ensemble d'entités tels que des particules allant dans la même direction. Le phénomène de collectivité est souvent associé aux systèmes complexes de plusieurs corps, pour lesquels les interactions de base sont bien comprises. En effet, le but de ces études de collectivité est de comprendre comment les interactions microscopiques donnent lieu à un comportement macroscopique. Effectivement, l'hydrodynamique est une description s'appliquant aux longueurs d'onde longues et pour des moments tardifs, qui décrit le transport des charges ou degrés de liberté

conservées. À la théorie de l'hydrodynamique il manque plusieurs des excitations de la théorie sous-jacente, ce sont précisément les charges qui ne sont pas conservées.

Comme mentionné plus haut, le paradigme d'un plasma fortement couplé et opaque est aujourd'hui bien établi. Par contre, il a été anticipé que la magnitude de la collectivité allait diminuer en diminuant la taille du système, par exemple pour des systèmes tels que celui produit dans des collisions proton-proton. Dans des petits systèmes le libre parcours moyen des constituants s'approche de la taille typique du système, dans quel cas les effets visqueux deviennent plus importants et la validité de la modélisation hydrodynamique n'est plus certaine. Il est ainsi, parce que dans des tels systèmes minuscules la présence des gradients grands pourrait exciter des modes non-hydrodynamiques ou juste gêner l'expansion en termes de gradients. Une telle tendance de collectivité qui diminue a été mesurée dans des collisions périphériques de noyau-noyau, et on ne s'attendait à aucun flow collectif dans des collisions entre protons et noyaux ou protons et protons. Étonnamment, des phénomènes qui rassemblent à la collectivité ont été mesurés dans des collisions à haute multiplicité entre protons. Des mesures ultérieures ont démontré un comportement similaire dans des collisions à haute multiplicité entre protons et plomb et ensuite deutérons et or au LHC et au RHIC, respectivement.

La réponse à la question sur la collectivité dans les plus petits systèmes hadroniques pourra éclaircir non pas seulement la matière du modèle standard de plasma à fort couplage, mais aussi donner des nouvelles voies pour étudier la structure du proton. Si les effets de l'état final décrits par le flow de l'hydrodynamique sont à l'origine de ces corrélations alors la présence d'un fluide à basse viscosité permettrait l'étude des protons et des fluctuations sub-nucléoniques aux échelles de temps très courtes.

L'applicabilité de l'hydrodynamique dans des petits systèmes n'est pas mise en cause que par la présence possible des grands gradients mais aussi par la présence du bruit. Malgré le fait que le bruit hydrodynamique a été décrit analytiquement il y a longtemps par Landau et Lifshitz et récemment généralisé aux systèmes relativistes, le bruit est toujours souvent négligé dans des simulations modernes d'hydrodynamique. Puisque le bruit hydrodynamique est lié aux dissipations on s'attend à ce que son effet soit plus grand dans des petits systèmes et c'est pour ceci qu'il existe un besoin de clarifier le rôle du bruit dans de tels systèmes. Le but de ce chapitre est d'étudier quantitativement l'effet du bruit sur des systèmes différents. Les trois systèmes qui seront étudiés sont le système proton-proton, proton-plomb et plomb-plomb aux énergies correspondant au LHC.

Au lieu de faire des simulations purement numériques nous allons faire une étude semi-analytique. Ce qui nous permet de faire des calculs analytiques est le cadre simplifié du *flow de Gubser*. Dans ce cadre conforme, grâce aux symétries présentes,

nous allons pouvoir résoudre les équations visqueuses de l'hydrodynamique de Navier-Stokes. Comme nous l'avons mentionné déjà, il est connu qu'aux hautes températures le plasma quark-gluon est presque conforme. Nous allons ensuite ajouter des petites fluctuations en plus de la solution de Navier-Stokes. Nous étudions l'effet de ces *fluctuations hydrodynamiques* à l'évolution du système et en particulier nous étudions leur effet sur des petits systèmes.

Nous remarquons que la fonction de corrélation du tenseur de bruit peut être calculée en utilisant le théorème de fluctuation-dissipation et que dans le cas de Gubser la structure tensorielle se factorise, ce qui nous permet de déduire une expression pour le tenseur de bruit depuis son autocorrelateur. De cette manière nous trouvons que *la magnitude du bruit est essentiellement déterminée par la multiplicité* d'une collision et non pas par la taille du système, comme on aurait pu s'attendre en partant du théorème de fluctuation-dissipation.

Nous voyons comment résoudre les équations de Navier-Stokes dans la présence de bruit en faisant une décomposition en modes. Cette décomposition dépend de la symétrie rotationnelle de la solution de Gubser, et elle simplifie les calculs. De cette manière nous obtenons une équation de mouvement pour chaque mode, une équation qui ressemble à l'équation de Langevin contenant un terme de traînée et un terme de bruit. Ensuite nous choisissons un observable à analyser. Inspirés par les expériences qui mesurent des corrélations à deux particules, nous choisissons une quantité similaire, c'est-à-dire la fonction de corrélation du flow radial. Nous ne sommes pas en mesure de faire un lien direct avec les données expérimentales puisque nous ne considérons que l'hydrodynamique, donc un continuum sans particules, et par contre les expériences mesurent l'ensemble discret de particules (chargées) dans l'état final, ce qui sort de l'hydrodynamique après l'hadronisation et le 'freeze-out', comme on dit en anglais. Donc, en négligeant l'hadronization et le freeze-out, nous prenons la meilleure option et considérons la fonction de corrélation du flow radial. Nous choisissons cette fonction de corrélation en particulier puisque nous nous intéressons à l'expansion transverse du système.

## Conclusions de ce chapitre

Dans ce chapitre nous avons étudié l'effet du bruit hydrodynamique appliqué sur un système de fond de flow de Gubser en 3+1 dimensions de l'espace-temps. Plus spécifiquement, nous avons étudié l'effet qu'a le bruit hydrodynamique sur les fonctions de corrélations à deux points du flow radial, avec des fluctuations initiales soit de longue, soit de courte portée.

Les conclusions les plus importantes de ces études sont les suivantes. D'abord,

nous avons vu que la magnitude du bruit dans une collision d'ions lourds est surtout déterminée par *la multiplicité* de l'événement et non pas la taille (transverse) du système. Cette même conclusion tient pour deux cas : le flow de Bjorken dans 1+1 dimensions, et le flow de Gubser en 3+1 dimensions. Nos études répondent donc implicitement à la question 'Quelle est la gouttelette la plus petite du plasma quark-gluon qui évolue comme un fluide?'. La réponse est qu'il n'y a pas de limite, tant qu'on continue à mettre de plus en plus d'énergie dans le système, pour que la multiplicité totale reste assez élevée pour la formation d'un plasma. Ce premier point est la conclusion la plus importante de nos études.

En un second lieu nous avons étudié la fonction de corrélation à deux points du flow radial, inspirés par le fait que nous considérons que l'expansion radiale du système est d'une très grande importance. Nous avons vu que l'effet du bruit sur ce corrélateur est modeste. Pour des corrélations à longue portée, le bruit s'additionne sur l'excentricité du système, et donc ajoute une contribution dans le flow anisotropique. L'effet du bruit est le plus petit pour le système plomb-plomb et le plus grand pour le système proton-proton. Aussi, l'effet relatif du bruit par rapport à la contribution venant de la fluctuation initiale est plus important pour des harmoniques plus élevés. Ceci peut être compris comme suit. La magnitude du bruit est indépendante du degré de l'harmonique considéré, puisque l'équation de mouvement est indépendante de l'indice  $m$ . Par contre, les harmoniques plus élevés souffrent d'une atténuation plus importante que les harmoniques d'ordre bas, dû à la viscosité. Ceci implique que la puissance relative du flow radial venant du bruit hydrodynamique vis à vis les fluctuations initiales est plus importante pour les harmoniques élevés.

Finalement, nous avons étudié l'effet du bruit sur les corrélations de courte portée, initiées par des pics delta dans le plan transvers. Nos études montrent que le bruit donne lieu à la formation d'un pic étroit par dessus de la vague qui propage à partir du pic delta initial. Les caractéristiques de ce pic étroit varient d'un système à l'autre d'une manière cohérente : le pic est le plus étroit et bas pour le système plomb-plomb et le plus large et haut pour le système proton-proton. Le système proton-plomb se situe entre ces deux extrêmes.

# Part I

Fluctuations in quantum field theory:  
From unitarity cuts to coproducts of  
Feynman integrals



# Chapter 1

## From unitarity cuts to coproducts of Feynman integrals

### 1.1 Introduction

The standard model of particle physics is a theory that is extremely successful in describing experimental data at very high precision. This connection between theoretical predictions, made in quantum field theory for theories such as the standard model, and experimental measurements at collider experiments is made through the cross sections of a given process. The cross section is determined by the *scattering amplitude* of the process in question, namely the differential probability of this specific scattering process happening.

A way in which computations in quantum field theory can be organized is the so-called Feynman diagram expansion. In this method a power series expansion in a small parameter is done. This parameter is called the coupling of the theory, and it gives the strength of interactions. It is indeed a rather small parameter in the case of high-energy quantum chromodynamics (QCD), the theory of interest to us in this thesis. The terms in this Feynman diagram expansion carry names according to the order at which they appear. The lowest-order diagrams are called tree diagrams, whereas higher-order diagrams are called *loop diagrams*, because they include closed loops. Because virtual particles inside loops are unobservable, one has to integrate over the momenta of such particles. Hence the computation of physical predictions in quantum field theory necessarily involves the calculation of loop diagrams. These loop integrals are often very hard to compute, and indeed they often form a bottleneck for the evaluation of high-precision observables. At the time of writing this thesis, the state of the art is one or sometimes two-loop processes, with the notable exception

of Higgs production amplitudes where the gluon-fusion process has been computed up to three loops [16].

The difficulty of evaluating these integrals has led to various integration techniques. An early used technique has been the analysis of the discontinuities of Feynman integrals across their branch cuts. These discontinuities can be computed directly using diagrammatic rules [17, 18, 19, 20, 21]. According to these rules, partitions of Feynman diagrams into two regions are enumerated, and the particles at the boundary of the two regions are restricted to their mass shells. This operation defines the set of *cut diagrams*. Collecting the cut diagrams with the same momentum flow between the regions, we construct a *unitarity cut* which captures the discontinuity across the branch cut in that momentum invariant. The on-shell restrictions greatly simplify the integration and its result. The original uncut integral can then be reconstructed, traditionally through dispersion relations [17, 18, 19, 20, 21]. This is not an easy task, however, and indeed it is part of our motivation behind the work presented in this chapter.

Another, more recent, technique of evaluating loop diagrams is the so-called *unitarity method*, in which discontinuities of an amplitude are used to project it onto a small basis of master integrals [22, 23, 24, 25, 26, 27, 28, 29, 30, 31, 32, 33, 34, 35, 36]. One gains in efficiency when *multiple cuts* are taken in different channels simultaneously. Restricting many propagators to their mass shells separates a diagram into several on-shell elements, which are typically simpler to compute.

At one-loop order it is known that all Feynman diagrams can be reduced to *scalar integrals*, that is, integrals with unit numerators [15]. We will therefore work with these basic building blocks of one-loop integrals, and consider only scalar Feynman diagrams. At this order it is also known that the integrals arising can be written in terms of a special class of functions called multiple polylogarithms (MPLs). Even some higher-order integrals with sufficiently few masses can be written in terms of MPLs, but in general, at high loop order, elliptic functions can appear [37, 38, 39, 40, 41, 42]. (Which functions are produced by Feynman integrals in general is still an open question.) Recent developments on the mathematical structure of this class of functions, in particular their *Hopf algebraic structure* [43, 44], have thus had a big impact on the physics community over the last few years [45, 46].

Multiple polylogarithms carry a lot of algebraic structure. In particular, they form a Hopf algebra, which is a natural tool to capture discontinuities. Today there exists a lot of evidence for the so-called *first entry condition* [47], which states that the terms in the coproduct having transcendental weight  $1, n - 1$  can be written in

the form

$$\sum_i \log(-s_i) \otimes f_{s_i} , \quad (1.1)$$

where the sum is over all Mandelstam invariants  $s_i$  and  $f_{s_i}$  is the discontinuity of the diagram with respect to the variable  $s_i$ . This is true for all diagrams with vanishing internal masses.

The new feature of the original paper in the appendix C and in the work presented in this chapter is the inclusion of masses. We include masses everywhere: on the external legs and on the internal propagators, and we consider limits where some of these masses vanish.

Our studies with massive diagrams suggest that, in the presence of internal masses, the first entry condition needs to be modified to account for the new locations of branch cuts. The external momenta have branch cuts related to their mass thresholds and also the internal masses have branch cuts. Taking into account these observations, as long as the diagram has one or more massive internal propagators, the  $1, n - 1$  component of the coproduct has the form

$$\sum_i \log(m_{p_i^2}^2 - p_i^2) \otimes f_{p_i} + \sum_j \log(m_j^2) \otimes f_{m_j} , \quad (1.2)$$

where  $f_{p_i}$  and  $f_{m_j}$  are the discontinuities related to the variables  $p_i^2$  and  $m_j^2$  respectively and  $m_{p_i^2}$  is the mass threshold of the external channel  $p_i^2$ . In section 1.7 we will see a more general version of eq. (1.2) for functions that have the same branch points.

The functions  $f_x$  are related to the unitarity cut on the corresponding channel, both for single cuts [18, 19, 20], and for multiple cuts [2]. The cuts and discontinuities taken in external and internal channels are encoded in specific terms in the coproduct. These terms are just a set of logarithms with the same discontinuities. The cuts in internal channels, *single particle cuts*, correspond to discontinuities in the internal masses and to terms with the mass as a first cofactor in eq. (1.2). The masses are a new feature of our analysis: the massless case was studied in ref [2] but the extension to non zero masses is presented in this chapter and in the original paper in the appendix C. We focus our studies on *scalar triangles*, because they are simple enough to provide a nice play ground for our investigations, but on the other hand complicated enough so that we expect new issues with introducing masses already to appear at this stage.

Another new observation is that the functions appearing as arguments of the logarithms in the coproduct of the integrals considered, to be called the *letters of the symbol alphabet*, are suggested by the cuts. Our aim is to find letters that are just

rational functions. A general algorithm for finding such an alphabet is not known, but our studies suggest that computing cuts may help in finding it.

The outline of this chapter is as follows. We start with a mathematical introduction to unitarity and Hopf algebras in section 1.2. Then we talk about pure Feynman integrals and their symbol alphabets in sections 1.3 and 1.4, respectively. In section 1.5 we introduce the diagrams that we will focus on in this thesis, namely the massive scalar three-point integrals, and the Feynman rules used to evaluate them. Section 1.6 carries a focus on cut diagrams. We will cover cuts in external channels and in internal propagators. We list our cutting rules and finish with examples. Next, we focus on the first entry condition in section 1.7, and show how it generalizes to the new case studied in this chapter: the massive case. Then we present relations between discontinuities in section 1.8, the main result of this chapter, and examples of these relations in section 1.9. After this, we will talk about the main work of the author, that is, the process of reconstructing an integral from its cuts, through the coproduct. This we do in section 1.10. We finish this chapter by concluding in section 1.11.

## 1.2 Mathematical and conceptual introduction

### 1.2.1 Unitarity cuts

Our interest lies in constructing scattering amplitudes from their singularities. In the case of tree-level amplitudes, the singularities are just poles. For loop amplitudes, the singularities are branch cuts and other singularities associated with so-called generalized cuts, where different propagators or combination of propagators are put on shell. In this way, the calculation is given in terms of lower-order amplitudes instead of the sum of loop Feynman diagrams. [48]

Unitarity states that the scattering matrix  $S$  is a unitary matrix. Writing  $S$  in terms of the interaction matrix  $T$  we have  $S = 1 + iT$ . In this form  $SS^\dagger$  gives the equation  $(1 + iT)(1 - iT) = 1$ , or  $2\Im T = TT^\dagger$ , or

$$\text{Disc}T = TT^\dagger, \tag{1.3}$$

where  $\text{Disc}(x) = 2\Im(x)$  is the discontinuity across a branch cut. We see that the imaginary part of a one-loop amplitude is related to the product of two tree-level amplitudes. Expanding this relation perturbatively in the coupling constant  $g$  we

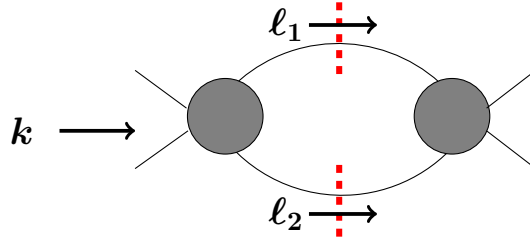


Figure 1.1: The unitarity cut of a one-loop amplitude. The two intermediate-state propagators are on shell. Here the filled circles denote the sum of all possible Feynman diagrams with the chosen configuration of external legs.

obtain, for four- and five-gluon amplitudes in QCD [49],

$$T_4 = g^2 T_4^{(0)} + g^4 T_4^{(1)} + g^6 T_4^{(2)} + \dots, \quad (1.4)$$

$$T_5 = g^3 T_5^{(0)} + g^5 T_5^{(1)} + g^7 T_5^{(2)} + \dots, \quad (1.5)$$

where  $T_n^{(L)}$  is the  $L$ -loop  $n$ -gluon amplitude. Inserting these expressions for the four-point amplitude into eq. (1.3) and collecting powers of the coupling constant, we see that

$$\text{Disc} T_4^{(0)} = 0, \quad (1.6)$$

$$\text{Disc} T_4^{(1)} = T_4^{(0) \dagger} T_4^{(0)}, \quad (1.7)$$

$$\text{Disc} T_4^{(2)} = T_4^{(0) \dagger} T_4^{(1)} + T_4^{(1) \dagger} T_4^{(0)} + T_5^{(0) \dagger} T_5^{(0)}. \quad (1.8)$$

The first one of these equations states that the tree amplitude has no branch cut, a result that generalizes to more legs. The second equation shows that discontinuities of one-loop amplitudes are given by products of tree amplitudes. In this case there is a so-called two particle cut, because there are two particles re-scattering. The last equation states that there are two types of discontinuities of two-loop amplitudes: two-particle cuts where one of the amplitudes is a tree-level amplitude and the other a one-loop level amplitude, the other types involving three-particle cuts and higher-multiplicity tree amplitudes.

A unitarity cut of a one-loop amplitude is the discontinuity of the amplitude across a branch cut, in a kinematical region associated with a chosen momentum channel. In this kinematic region one chosen momentum invariant, say  $k^2$ , is positive while all other invariants are negative. The choice of  $k$  isolates this momentum channel, and in the end we sum over all such possible choices to construct the full amplitude.

The unitarity cut of a one-loop amplitude is:

$$\text{Cut}_{k^2} A^{1\text{-loop}} \equiv \int d\mu A_{\text{Left}}^{\text{tree}} \times A_{\text{Right}}^{\dagger \text{tree}} , \quad (1.9)$$

where the Lorentz-invariant phase-space measure is defined by

$$d\mu = d^4\ell_1 d^4\ell_2 \delta^{(4)}(\ell_1 + \ell_2 - k) \delta^+(\ell_1^2) \delta^+(\ell_2^2) . \quad (1.10)$$

The superscript  $+$  on the delta functions indicates that the positive energy solution is taken. The Cutkosky rules state that eq. (1.9) is equivalent to the discontinuity in the same channel [18],

$$\text{Cut}_{k^2} A^{1\text{-loop}} = -\text{Disc}_{k^2} A^{1\text{-loop}} . \quad (1.11)$$

Now we can see that (1.7) really is an instance of (1.9). The amplitudes  $A$  are elements of the interaction matrices  $T$  (or  $S$ ). So far, we have introduced two operators ‘Disc’, one in eq. (1.3) and the second one in eq. (1.11). The difference between the two is that the one with the subscript  $k^2$  is the general one but evaluated in the specific kinematic region that singles out this chosen variable.

Now, how can the unitarity cuts be used to calculate the amplitude? First, we need to know that any four-dimensional one-loop integral can be expanded in a set of master integrals, ranging from the tadpole ( $n = 1$ ) to the box ( $n = 4$ ):

$$A^{1\text{-loop}} = \sum_n \sum_{\mathbf{k}=\{k_1, \dots, k_n\}} c_n(\mathbf{k}) I_n(\mathbf{k}) , \quad (1.12)$$

In dimensional regularization, the tadpole only contributes when internal masses are nonzero. Keeping higher-order contributions in  $\epsilon$ , the dimensional regularization parameter, also the pentagon ( $n = 5$ ) appears as an independent master integral. Eq. (1.12) implies in particular that, since the master integrals are known, the — often difficult— integration can be done once and for all, leaving it as our task to compute only the coefficients  $c_n(\mathbf{k})$ .

By now applying unitarity cuts in different channels on the one-loop amplitude, we get information about the coefficients  $c_n$ . If the unitarity cut is applied directly to eq. (1.12), then we have

$$\Delta A^{1\text{-loop}} = \sum_n \sum_{\mathbf{k}=\{k_1, \dots, k_n\}} c_n(\mathbf{k}) \Delta I_n(\mathbf{k}) , \quad (1.13)$$

because the branch cuts are located only in the master integrals, the pre factors being just rational functions. The problem of computing the one-loop integral now

reduces to the problem of isolating the coefficients  $c_n(\mathbf{k})$ . This is so because the master integrals are known functions, so, in particular, their cuts are known as well. Hence we can think of (1.13) as projecting any integral onto a basis of known master integrals thanks to the use of discontinuities.

Equation (1.13) is the starting point of the unitarity method. We see from (1.9) that it only involves tree-level quantities. Another simplification is that many of the terms on the right-hand side of (1.13) vanish, because there are only certain diagrams that have cuts in any chosen channel. We can write separate equations for every channel, summing over all possible diagrams that contribute to the chosen channel. So in fact, we started with eq. (1.12) and ended up with a set of several simpler and shorter equations. The simplicity comes from the fact that [49]

- The tree-level amplitudes can be simplified before substituting them into eq. (1.9).
- The tree-level amplitudes are often simple, because they possess an effective supersymmetry that the loop amplitude does not have.
- The on-shell condition can be used for the intermediate state particles.

Any  $D$  dimensional one-loop amplitude can be obtained from its cut: they are *cut-constructible*. This means that the branch cuts uniquely determine the amplitudes. This also implies that we will work in  $D = d - 2\epsilon$  dimensions in what follows.

### 1.2.2 Multiple polylogarithms

Many Feynman integrals can be expressed in terms of functions called multiple polylogarithms (MPLs). In fact, it is known that this is the case for all one-loop integrals, and for higher-loop integrals with sufficiently few massive legs. At higher loop orders, elliptic integrals may appear [37, 38, 39, 40, 41, 42]. In this section, we will briefly review definitions related to the multiple polylogarithms. We will follow the presentations given in refs. [46, 50].

Multiple polylogarithms are defined in a recursive manner through the iterated integral [51, 43]

$$G(a_1, \dots, a_n; z) = \int_0^z \frac{dt}{t - a_1} G(a_2, \dots, a_n; t) , \quad (1.14)$$

where  $a_i, z \in \mathbb{C}$  and  $G(z) = 1$ . In the special case where all the  $a_i$ 's are zero, we have, using the vector notation  $\vec{a}_n = \underbrace{(a, \dots, a)}_n$ :

$$G(\vec{0}_n; z) = \frac{1}{n!} \log^n z . \quad (1.15)$$

Other special cases are

$$G(\vec{a}_n; z) = \frac{1}{n!} \log^n \left(1 - \frac{z}{a}\right) \quad \text{and} \quad G(\vec{0}_{n-1}, 1; z) = -\text{Li}_n(z) . \quad (1.16)$$

The vector  $\vec{a}_n = (a_1, \dots, a_n)$  is called the *vector of singularities*. The number  $n$  of elements in  $\vec{a}_n$  is called the *weight* of the MPL. The weight  $w$  is also defined for certain transcendental numbers:  $w(\pi^n) = n$ ,  $w(\zeta^n) = n$ <sup>1</sup>.

We note the following properties of the functions of eq. (1.16)

- $G(\vec{a}_n; z) = \frac{1}{n!} \log^n \left(1 - \frac{z}{a}\right)$  has a branch cut from  $z = a$  to  $z = \infty$  in the complex  $z$  plane.
- $G(0, 1; z) = -\text{Li}_2(z)$  has a branch cut from  $z = 1$  to  $z = \infty$  in the complex  $z$  plane.

The branch cut structure of  $G(a_1, \dots, a_n; z)$  is in general complicated due to the singularities at  $z = a_i$  in the integral representation (1.14). In particular, from the integral representation it can be seen that  $G(a_1, \dots, a_n; z)$  is divergent whenever  $z = a_1$  and analytic at  $z = 0$  whenever  $a_n \neq 0$ .

### 1.2.3 Coalgebra and Hopf algebra

Let us denote by  $\overline{\mathcal{H}}$  the vector space spanned by multiple polylogarithms. Furthermore,  $\overline{\mathcal{H}}$  can be turned into an algebra. Indeed, iterated integrals form a shuffle algebra, which allows us to express the product of two multiple polylogarithms of weight  $n_1$  and  $n_2$  as a linear combination of multiple polylogarithms of weight  $n_1 + n_2$ :

$$G(\vec{a}_1; z)G(\vec{a}_2; z) = \sum_{\vec{a} \in \vec{a}_1 \amalg \vec{a}_2} G(\vec{a}; z) , \quad (1.17)$$

where  $\amalg \vec{a}_2$  denotes the set of all possible shuffles of  $\vec{a}_1$  and  $\vec{a}_2$ , meaning the set of all permutations of their union that preserve the relative orderings inside  $\vec{a}_1$  and  $\vec{a}_2$ . We note that eq. (1.17) preserves the weight. It follows that the algebra of MPLs is graded by the weight:

$$\overline{\mathcal{H}} = \bigoplus_{n=0}^{\infty} \overline{\mathcal{H}}_n , \quad \text{with} \quad (1.18)$$

$$\overline{\mathcal{H}}_{n_1} \cdot \overline{\mathcal{H}}_{n_2} \subset \overline{\mathcal{H}}_{n_1+n_2} . \quad (1.19)$$

---

<sup>1</sup>The Riemann zeta function has not been proven to be transcendental for certain odd integers  $\zeta_5, \zeta_7, \dots$

Here  $\overline{\mathcal{H}}_n$  is the vector space spanned by all MPLs of weight  $n$ , and we define  $\overline{\mathcal{H}}_0 = \mathbb{Q}$ .

In addition to the usual structure needed to define an algebra, namely a vector space equipped with a multiplication that has a unit element and is associative and distributive, we also need another algebraic structure: a *coalgebra*. A coalgebra is a vector space  $\mathcal{A}$  that has a *comultiplication*, namely a linear map  $\Delta : \mathcal{A} \rightarrow \mathcal{A} \otimes \mathcal{A}$ , which

- is *coassociative*

$$(\text{id} \otimes \Delta)\Delta = (\Delta \otimes \text{id})\Delta , \quad (1.20)$$

- respects multiplication

$$\Delta(a \cdot b) = \Delta(a) \cdot \Delta(b) , \quad (1.21)$$

- and respects the weight

$$\mathcal{A}_n \xrightarrow{\Delta} \bigoplus_{k=0}^n \mathcal{A}_k \otimes \mathcal{A}_{n-k} . \quad (1.22)$$

The meaning of the coassociativity property is the following: the coproduct assigns to every element  $a \in \mathcal{A}$  a linear combination of pairs of elements:

$$a \mapsto \Delta(a) = \sum_i a_i^{(1)} \otimes \sum_i a_i^{(2)} . \quad (1.23)$$

Now that we have a way of splitting  $a$  into two, we can iterate and split  $a$  into three. However, this second splitting can be done by applying  $\Delta$  either to  $a_i^{(1)}$  or  $a_i^{(2)}$  above. Coassociativity means that the two are equivalent; the order in which we iterate the coproduct is not important.

As examples of the coproduct, let us mention the following:

$$\Delta(\log(z)) = 1 \otimes \log(z) + \log(z) \otimes 1 , \quad (1.24)$$

$$\Delta(\text{Li}_n(z)) = 1 \otimes \text{Li}_n(z) + \text{Li}_n(z) \otimes 1 + \sum_{k=1}^{n-1} \text{Li}_{n-k}(z) \otimes \frac{\log^k(z)}{k!} , \quad (1.25)$$

and

$$\Delta(\log x \log y) = \Delta(\log x) \Delta(\log y) = [1 \otimes \log x + \log x \otimes 1] [1 \otimes \log y + \log y \otimes 1] \quad (1.26)$$

$$= 1 \otimes (\log x \log y) + \log x \otimes \log y + \log y \otimes \log x + (\log x \log y) \otimes 1 . \quad (1.27)$$

Strictly speaking, the coalgebra  $\mathcal{A}$  is not a Hopf algebra. In order for us to retrieve a Hopf algebra from the coalgebra  $\mathcal{A}$  we need to consider its specific quotient space  $\mathcal{A}$  modulo  $i\pi$ . This means that we are working modulo  $\zeta_2$  and  $i\pi$  (i.e. “ $\zeta_2 = i\pi = 0$ ”). The same holds for  $\overline{\mathcal{H}}$ , it is the quotient space  $\mathcal{H} = \overline{\mathcal{H}}/(i\pi)$  that is a Hopf algebra.

### 1.2.4 The symbol map

The coassociativity property of the coproduct implies that it can be iterated in a unique way. For the maximal iteration, corresponding to the partition  $(1, \dots, 1)$  of  $n$  there is a correspondence with the *symbol* of a transcendental function  $F$  [51] (see also refs [46, 50]):

$$\mathcal{S}(F) \equiv \Delta_{1, \dots, 1} F \pmod{i\pi} . \quad (1.28)$$

Since all the factors of the symbol are just logarithms, we follow the convention of dropping the ‘log’-signs inside the symbol, i.e. we write  $a_1 \otimes \dots \otimes a_n$  instead of  $\log a_1 \otimes \dots \otimes \log a_n$ . We refer to the entries  $a_i$  of the symbol as the *symbol alphabet*  $\mathcal{A}$  of  $F$ . The symbol map is linear and it satisfies the following properties:

$$\dots \otimes (a \cdot b) \otimes \dots = \dots \otimes a \otimes \dots + \dots \otimes b \otimes \dots \quad (1.29)$$

$$\dots \otimes a^n \otimes \dots = n(\dots \otimes a \otimes \dots) \quad (1.30)$$

$$\dots \otimes \rho \otimes \dots = 0 , \quad (1.31)$$

where  $\rho$  is a root of unity:  $\rho^n = 1$  for some  $n$ . This last property follows from the fact that we work modulo  $i\pi$ .

Not any tensor is the symbol of a function. In order for a tensor to be a symbol it has to satisfy the *integrability condition*

$$\sum_{i_1, \dots, i_n} c_{i_1, \dots, i_n} d \log x_{i_k} \wedge d \log x_{i_{k+1}} \log x_{i_1} \otimes \dots \otimes \log x_{i_{k-1}} \otimes \log x_{i_{k+2}} \otimes \dots \otimes \log x_{i_n} = 0 . \quad (1.32)$$

## 1.3 Pure functions and Feynman integrals

Here we will follow the discussion of ref. [52].

In this part of the thesis we will study connected planar Feynman integrals in dimensional regularization. When the dimension of the space time is  $D = d - 2\epsilon$ , then for  $d$  even an  $L$ -loop Feynman integral  $F^{(L)}$  defines a Laurent series

$$F^{(L)}(\epsilon) = \sum_{k=-2L}^{\infty} F_k^{(L)} \epsilon^k . \quad (1.33)$$

If the functions in  $F_k^{(L)}$  have the same transcendental weight then the integral is said to have *uniform transcendental weight*.

As we have already discussed in section 1.2.1, loop integrals can be expressed in terms of master integrals. If the coefficients of this master-integrals expansion are free from rational or algebraic functions of the external kinematic variables then the integral is called *pure*. It has been conjectured in ref. [53] that the master integrals can indeed taken to to be pure integrals, and this conjecture has been seen to hold in several nontrivial examples [54, 55, 56, 57]. (Sometimes there the pure functions have an algebraic prefactor, but this happens to be the same for all the coefficients and one can choose to normalize by this factor.) So, the computation of loop integrals boils down to the computation of pure master integrals, which justifies our choice to study this particular class of integrals.

Let us conclude this short section with a few comments. Firstly, we note that the dimensionality of the triangle integrals of interest to us in this chapter is  $d = 4$ , so that  $D = 4 - 2\epsilon$ . Secondly, we will consider scalar triangle diagrams with different mass configurations, and all our integrals evaluate to functions of uniform transcendental weight. The main interest of choosing this class of integrals is that it makes the analysis simpler, but we still expect to see new features appearing from the inclusion of massive propagators. Lastly, we treat the dimensional regularization parameter  $\epsilon$  as having a transcendental weight -1. Hence a given diagram in our analysis has a specific transcendental weight, which for the triangle diagrams we consider, is two.

## 1.4 The symbol alphabet

In this section we discuss the observations of ref. [2].

For any given integral, the most natural kinematic variables can be quite complicated functions of momentum invariants. The arguments of the polylogarithmic functions are a priori algebraic functions of the external kinematic scales. It would be more convenient to find such a parametrization of the external kinematics that the arguments of the polylogarithms were rational functions.

If a Feynman integral depends on  $n$  independent scales  $s_i$ , such as the Mandelstam invariants, then we would like to find  $n - 1$  independent variables  $z_i$  such that

$$\frac{s_i}{s_n} = f_i(z_1, \dots, z_{n-1}) , \quad (1.34)$$

where the  $f_i$  are rational functions. In this way all arguments of the polylogarithms are rational functions of the variables  $z_i$ . A general algorithm for finding such parametrizations is not known, but parametrizations (1.34) are known to exist for all

known examples where the Feynman integral can be expressed in terms of multiple polylogarithms. In particular, this is the case for all Feynman integrals studied in this thesis. We furthermore note that the inverse relations of eq. (1.34), giving the variables  $z_i$  in terms of the external invariants  $s_j$ , are algebraic functions which often involve square roots of polynomials of the invariants  $s_j$ .

In this thesis we will only study diagrams for which rational parametrizations (1.34) have been found. Let us now look at the concrete example of triangle integrals, which will be the focus of our studies and for which a convenient parametrization was found in ref. [1]. For triangle diagrams with massless propagators and three massive external legs, denoted  $p_1^2$ ,  $p_2^2$ ,  $p_3^2$ , a parametrization is found for the dimensionless ratios

$$u_i \equiv \frac{p_i^2}{p_1^2} \quad (1.35)$$

for  $i = 2, 3$ . Now a clever parametrization, leading to a rational symbol alphabet, is

$$u_2 = z\bar{z}, \quad u_3 = (1-z)(1-\bar{z}). \quad (1.36)$$

As already noted, the inverse transformation involves square roots:

$$z = \frac{1 + u_2 - u_3 + \sqrt{\lambda(1, u_2, u_3)}}{2}, \quad \bar{z} = \frac{1 + u_2 - u_3 - \sqrt{\lambda(1, u_2, u_3)}}{2}, \quad (1.37)$$

where the Källén function  $\lambda$  appears inside the square root,

$$\lambda(a, b, c) \equiv a^2 + b^2 + c^2 - 2ab - 2ac - 2bc. \quad (1.38)$$

In [58] a similar parametrization was found for triangle diagrams with massive external channels *and* massive internal propagators. Let us note by  $m_{ij}^2$  the square of the mass of the internal propagator between the two external legs  $i$  and  $j$ . We define new dimensionless ratios of these masses squared:

$$\mu_{ij} \equiv \frac{m_{ij}^2}{p_1^2} \quad (1.39)$$

for  $\{ij\} = \{12, 13, 23\}$ . Then we have two new variables  $w_1$  and  $\bar{w}_1$ , related to the  $\mu_{ij}$ :

$$\mu_{12} = w_1\bar{w}_1, \quad \mu_{13} = (1-w_1)(1-\bar{w}_1), \quad (1.40)$$

and whose inverse transformations read

$$w_1 = \frac{1 + \mu_{12} - \mu_{13} + \sqrt{\lambda_1}}{2}, \quad \bar{w}_1 = \frac{1 + \mu_{12} - \mu_{13} - \sqrt{\lambda_1}}{2}, \quad (1.41)$$

where

$$\lambda_1 \equiv \lambda(1, \mu_{12}, \mu_{13}). \quad (1.42)$$

The mass  $\mu_{23}$  is an independent variable. Similarly as in eq. (1.42), we define  $\lambda_2$  and  $\lambda_3$  as

$$\lambda_2 \equiv \lambda(z\bar{z}, w_1\bar{w}_1, \mu_{23}) , \quad \lambda_3 \equiv \lambda((1-z)(1-\bar{z}), (1-w_1)(1-\bar{w}_1), \mu_{23}) . \quad (1.43)$$

If a parametrization as in eq. (1.34) has been found for a specific Feynman integral then the entries of the symbol of this given integral will be rational functions of the  $z_i$ . In addition, due to the additivity of the symbol (it being just logarithms), we can assume that the entries of the symbol are polynomials with integer coefficients in the variables  $z_i$ . Without loss of generality we may assume that these are irreducible over  $\mathbb{Z}$ . So, once a rational parametrization (1.34) has been found, we can assign to every Feynman integral a set  $\mathcal{A} \subset \mathbb{Z}[z_1, \dots, z_{n-1}]$  of irreducible polynomials. We will call this set  $\mathcal{A}$  the *symbol alphabet*, and its elements the *letters* of the symbol alphabet.

In practice it is often an advantage if one knows the symbol alphabet of a diagram when starting to compute a diagram. Knowing the alphabet allows one to write down an ansatz for the symbol, and the parameters of the ansatz can then be fixed by a procedure that we will detail in section 1.10. Even though no general algorithm for finding the alphabet exists, a possible way of finding the letters is by computing *cut diagrams*, already discussed in section 1.2.1. For techniques applicable to our specific diagrams, see for example ref. [52]. We will consider a few examples in following sections, but first let us define the scalar one-loop three-point functions studied in this thesis.

## 1.5 One-loop triangles

In this section we present the scalar one-loop triangles studied in this first part of the thesis. We take arbitrary internal and external masses. (The case of the three-mass one-loop triangle with no internal masses was treated in [2].) See figs. 1.2, 1.3, 1.4 for the one-mass, two-mass and three-mass triangles, respectively. The symbol alphabets of these triangles are given in tables 1.1, 1.2 and 1.3.

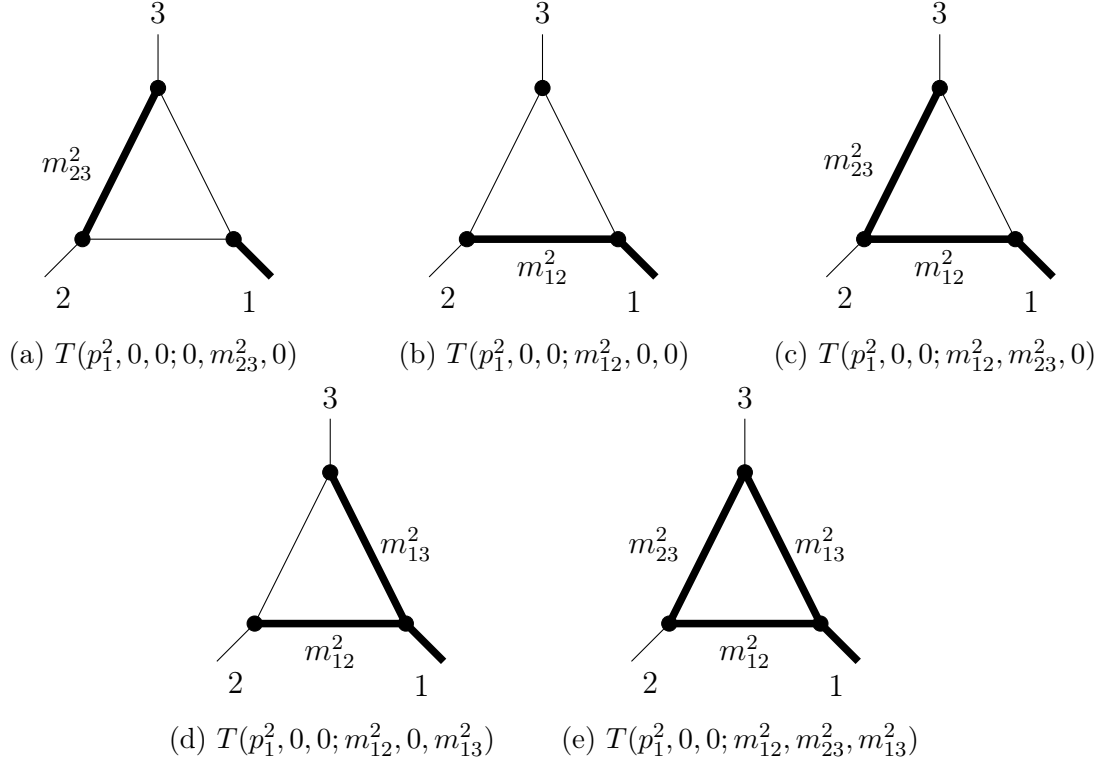


Figure 1.2: Triangles with one external massive leg.

Triangle	Symbol alphabet $\mathcal{A}$ (up to $\mathcal{O}(\epsilon^0)$ )
$T(p_1^2, 0, 0; 0, m_{23}^2, 0)$	$p_1^2, m_{23}^2, p_1^2 + m_{23}^2$
$T(p_1^2, 0, 0; m_{12}^2, 0, 0)$	$p_1^2, m_{12}^2, m_{12}^2 - p_1^2$
$T(p_1^2, 0, 0; m_{12}^2, m_{23}^2, 0)$	$p_1^2, m_{12}^2, m_{23}^2, m_{12}^2 - p_1^2, m_{12}^2 - m_{23}^2, m_{12}^2 - m_{23}^2 - p_1^2$
$T(p_1^2, 0, 0; m_{12}^2, 0, m_{13}^2)$	$w_1, \bar{w}_1, 1 - w_1, 1 - \bar{w}_1$
$T(p_1^2, 0, 0; m_{12}^2, m_{23}^2, m_{13}^2)$	$w_1, \bar{w}_1, 1 - w_1, 1 - \bar{w}_1, \mu_{23} - (1 - w_1)(1 - \bar{w}_1), \mu_{23}, \mu_{23} - w_1\bar{w}_1, \mu_{23} + w_1(1 - \bar{w}_1), \mu_{23} + \bar{w}_1(1 - w_1)$

Table 1.1: Symbol alphabet of the triangles with one external massive leg, fig. 1.2.

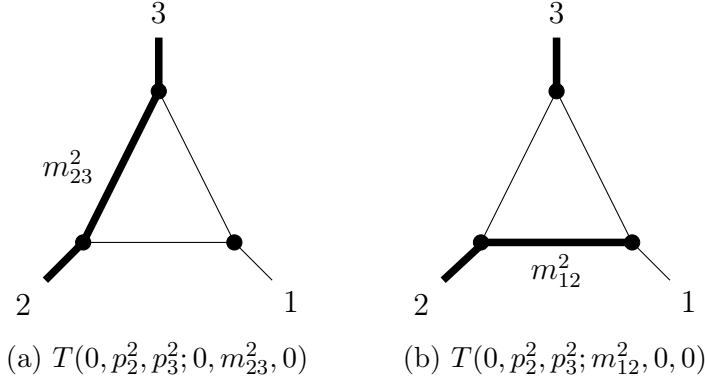


Figure 1.3: Triangles with two external massive legs.

Triangle	Symbol alphabet $\mathcal{A}$ (up to $\mathcal{O}(\epsilon^0)$ )
$T(0, p_2^2, p_3^2; 0, m_{23}^2, 0)$	$m_{23}^2, p_2^2, p_3^2, m_{23}^2 - p_2^2, m_{23}^2 - p_3^2$
$T(0, p_2^2, p_3^2; m_{12}^2, 0, 0)$	$m_{12}^2, p_2^2, p_3^2, m_{12}^2 - p_2^2, p_2^2 - m_{12}^2 - p_3^2$

Table 1.2: Symbol alphabet of the triangles with two external massive legs, fig. 1.3.

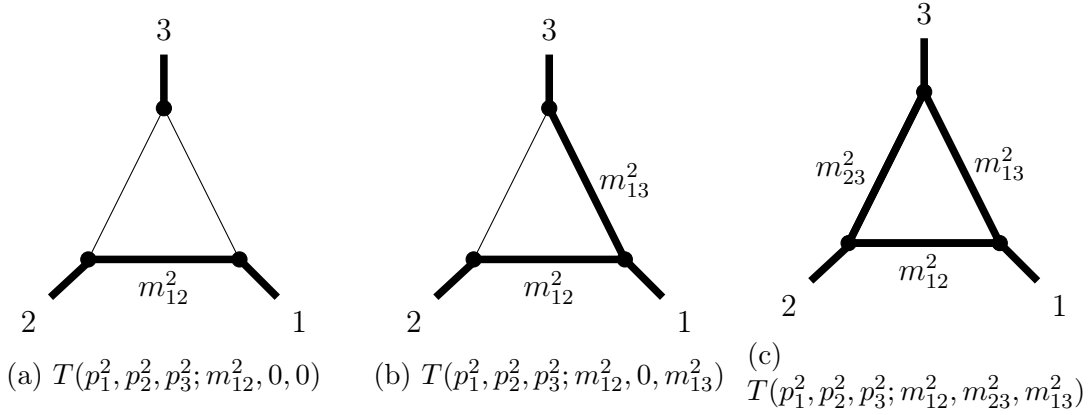


Figure 1.4: Triangles with three external massive legs.

Triangle	Symbol alphabet $\mathcal{A}$ (up to $\mathcal{O}(\epsilon^0)$ )
$T(p_1^2, p_2^2, p_3^2; m_{12}^2, 0, 0)$	$z, \bar{z}, 1 - z, 1 - \bar{z}, \mu_{12}, 1 - \mu_{12},$ $z\bar{z} - \mu_{12}, z - \mu_{12}, \bar{z} - \mu_{12}$
$T(p_1^2, p_2^2, p_3^2; m_{12}^2, 0, m_{13}^2)$	$z, \bar{z}, 1 - z, 1 - \bar{z}, w_1, \bar{w}_1, 1 - w_1, 1 - \bar{w}_1,$ $z\bar{z} - w_1\bar{w}_1, w_1 - z, w_1 - \bar{z}, \bar{w}_1 - z, \bar{w}_1 - \bar{z},$ $(1 - z)(1 - \bar{z}) - (1 - w_1)(1 - \bar{w}_1)$
$T(p_1^2, p_2^2, p_3^2; m_{12}^2, m_{23}^2, m_{13}^2)$	$z, 1 - z, w_1, \bar{w}_1, 1 - w_1, 1 - \bar{w}_1, \mu_{23},$ $w_1\bar{w}_1 - z\bar{z} + \mu_{23} - \sqrt{\lambda_2},$ $(1 - z)(1 - \bar{z}) - (1 - w_1)(1 - \bar{w}_1) - \mu_{23} + \sqrt{\lambda_3},$ $(w_1 - z)(\bar{w}_1 - \bar{z}) - \mu_{23}, (w_1 - \bar{z})(\bar{w}_1 - z) - \mu_{23},$ $(z\bar{z} + w_1\bar{w}_1 - \mu_{23})(z + \bar{z}) - 2z\bar{z}(w_1 + \bar{w}_1) \pm (z - \bar{z})\sqrt{\lambda_2},$ $z^2(1 - \bar{z}) + \bar{z}^2(1 - z) + (w_1 + \bar{w}_1)(2z\bar{z} - z - \bar{z})$ $+ (\mu_{23} - w_1\bar{w}_1)(z + \bar{z} - 2) \pm (z - \bar{z})\sqrt{\lambda_3}$

Table 1.3: Symbol alphabet of the triangles with three external massive legs, fig. 1.4.

### 1.5.1 Feynman rules

First, let us define the Feynman rules used throughout this chapter.

Our conventions for the Feynman rules of the scalar diagrams we consider are:

- Vertex:

$$\bullet = i \quad (1.44)$$

- Complex conjugated vertex:

$$\circ = -i \quad (1.45)$$

- Propagator:

$$\bullet \text{---} \bullet = \frac{i}{p^2 - m^2 + i0} \quad (1.46)$$

Massive (massless) propagators are drawn with a thick (thin) line.

- Complex conjugated propagator:

$$\circ \text{---} \circ = \frac{-i}{p^2 - m^2 - i0} \quad (1.47)$$

Massive (massless) propagators are drawn with a thick (thin) line.

- Cut propagator for cut in an external channel:

$$\circ \text{---} \bullet = \bullet \text{---} \circ = \bullet \text{---} \bullet = \circ \text{---} \circ = 2\pi \delta(p^2 - m^2) \quad (1.48)$$

There is a theta function restricting the direction of energy flow in a cut propagator. For single cuts, our convention is that energy flows from black to white. For multiple cuts, there are separate color labels for each cut—see section 1.6 for details. There can be multiple thin dotted lines indicating cuts on the same propagator without changing its value. However, each thin dotted line implies complex conjugation of a region of the diagram.

- Cut propagator for cut in an internal mass:

$$\bullet \text{---} \bullet = \circ \text{---} \circ = 2\pi \delta(p^2 - m^2) \quad (1.49)$$

- Loop factor for loop momentum  $k$ :

$$\left( \frac{e^{\gamma_E \epsilon}}{\pi^{2-\epsilon}} \right) \int d^{4-2\epsilon} k . \quad (1.50)$$

### 1.5.2 The generic one-loop three-point diagram

We denote these triangles by  $T$  and define them in  $D = d - 2\epsilon$  dimensions by

$$T(p_1^2, p_2^2, p_3^2; m_{12}^2, m_{23}^2, m_{13}^2) \equiv -e^{\gamma_E \epsilon} \int \frac{d^D k}{\pi^{D/2}} \frac{1}{[k^2 - m_{13}^2 + i0] [(k + p_1)^2 - m_{12}^2 + i0] [(k - p_3)^2 - m_{23}^2 + i0]} , \quad (1.51)$$

where  $\gamma_E = -\Gamma'(1)$  is the Euler-Mascheroni constant. We use  $p_i$  with  $i = 1, 2, 3$  to denote the external four-momenta and  $m_{ij}$  to denote the masses of the internal propagators. The mass  $m_{ij}$  is that of the propagator between the external legs  $i$  and  $j$ . Throughout this paper, the masses are assumed to be generic.

The preceding section number 1.5.1 contains a summary of our Feynman rules, used for the generic triangle in eq. (1.52). We will consider this triangle in cases where either internal or external invariants become massless, or both. We use dimensional regularization because some of our triangles are divergent. In practice we always truncate the Laurent series (see eq. (1.33)) at order  $\epsilon^0$ . We will mostly be interested in the pure function and for this purpose we define

$$T(p_1^2, p_2^2, p_3^2; m_{12}^2, m_{23}^2, m_{13}^2) \equiv ir(p_1^2, p_2^2, p_3^2) \mathcal{T}(p_1^2, p_2^2, p_3^2; m_{12}^2, m_{23}^2, m_{13}^2) , \quad (1.52)$$

with  $r$  a rational function and  $\mathcal{T}$  the pure function.

### 1.5.3 A note on analytic continuation

Let us for a moment discuss the kinematics of the one-loop three-point planar diagram, following the discussion in [1]. Let us assume that all external legs are off-shell and all internal propagators are massless. We will denote the generic one-loop triangle integral in  $D = 4 - 2\epsilon$  with external momenta  $\{p_1, p_2, p_3\}$  by  $T(p_1, p_2, p_3; \epsilon)$ . Momentum conservation and Lorentz invariance imply that  $T$  can only depend on  $\{p_1, p_2, p_3\}$  through the virtualities  $p_i^2 \neq 0$ . In dimensional regularization we can therefore write

$$T(p_1, p_2, p_3; \epsilon) = c_\Gamma (-p_1^2)^{n-\epsilon} \mathcal{T}(u_2, u_3; \epsilon) \quad (1.53)$$

without loss of generality for some integer  $n$ . (For us, in this thesis,  $n = 1$ .) Here we have defined  $u_i$  as in eq. (1.35) and the loop factor is

$$c_\Gamma = e^{\gamma_E \epsilon} \frac{\Gamma(1 + \epsilon) \Gamma(1 - \epsilon)^2}{\Gamma(1 - 2\epsilon)} , \quad (1.54)$$

with  $\gamma_E$  the Euler-Mascheroni constant, as before. The euclidean region is defined to be the region where all  $p_i^2 < 0$ , meaning that  $u_2, u_3 > 0$ . Here all invariants are below

their thresholds. The physical region where  $p_i^2 > 0$  is of phenomenological interest because *i*) it describes the decay of a heavy particle into two lighter particles and *ii*) the three-mass triangles in this region appear in the production amplitude for a pair of weak gauge bosons at higher order in perturbation theory.

This physical region  $p_i^2 > 0$  is related to the euclidean region  $p_i^2 < 0$  by analytic continuation:

$$-(p_k^2 + i\epsilon) \rightarrow e^{-i\pi} |p_k^2|. \quad (1.55)$$

The phase factors cancel in the ratios  $u_i$  so that the analytic continuation of eq. (1.53) is very simple:

$$T(p_1, p_2, p_3; \epsilon) \rightarrow (-1)^n e^{-i\pi\epsilon} c_\Gamma |p_1^2|^{n-\epsilon} \mathcal{T}(u_2, u_3; \epsilon). \quad (1.56)$$

As we have already mentioned, the kinematics of a triangle integral is most conveniently parametrized in terms of variables  $z, \bar{z}$ , defined in eq. (1.37). The appearance of the Källén function  $\lambda$  in these variables divides the  $(u_2, u_3)$  region into four different kinematic regions, shown in figure 1.5. In the regions denoted II, III and IV, the Källén function is positive, and so  $z, \bar{z}$  are real. In the region I, the Källén function is negative and  $z, \bar{z}$  are the complex conjugates of one another. The authors of ref. [1] argue that this is the fundamental domain in which all three-mass triangle integrals are defined. The other regions are related to region I by analytic continuation.

In this thesis we will mostly focus on  $z, \bar{z} \in \mathbb{R}$ .

## 1.6 Computation of cut diagrams

Feynman diagrams with massive propagators have discontinuities associated with both the external massive channels and the internal masses. These two types of discontinuities correspond to diagrammatic cuts that are slightly different. The first types of cuts are the ones in external channels [19, 20, 2] and the second types of cuts are single-propagator cuts for which we give the rules in this section. We start by reviewing cuts in external channels, then we introduce single-propagator cuts and finally we give examples on both types of cuts. In the cases of both external-channel and single-propagator cuts our cutting rules are designed to reproduce the discontinuities in the corresponding variables. This will allow us to compute all different kinds of single and double cuts considered in this thesis. In figure 1.6 we give examples of such single and double cuts.

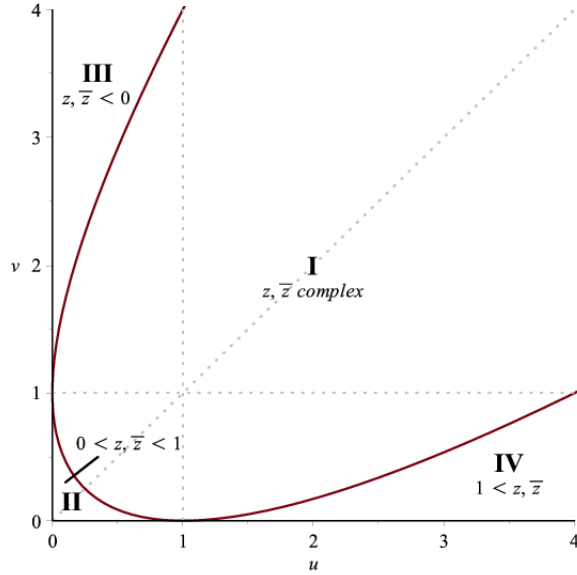


Figure 1.5: Different regions in  $(u, v) \equiv (u_2, u_3)$  space. The parabola represents the curve  $\lambda(1, u_2, u_3) = 0$ . The variables  $z, \bar{z}$  are defined in eq. (1.37). Figure from ref. [1].

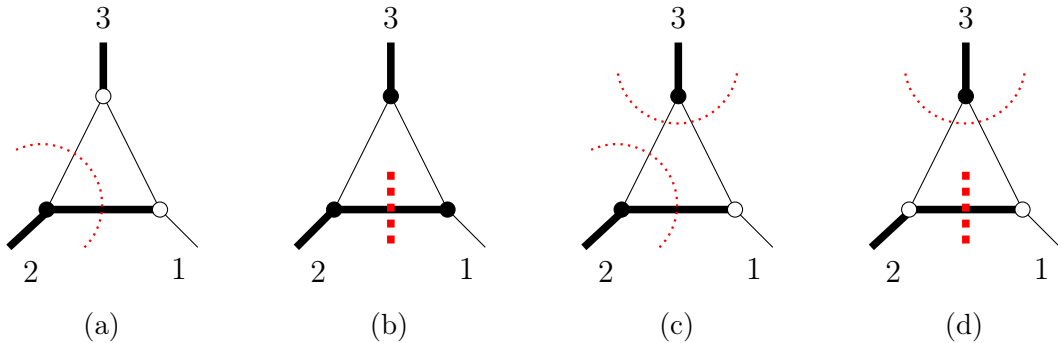


Figure 1.6: Example of cuts of  $T(0, p_2^2, p_3^2; m_{12}^2, 0, 0)$ : (a) single cut in an external channel; (b) single cut in an internal mass; (c) double cut in external channels; (d) double cut in an external channel and an internal mass. Thin dotted lines correspond to cuts on external channels and imply complex conjugation of a region of the diagram. Thick dashed lines correspond to mass cuts and do not imply any complex conjugation.

### 1.6.1 Cut in an external channel

Let us consider cuts in an external channel  $s_i$ . The operator  $\text{Cut}_{s_i}$  gives a sum of *cut* Feynman integrals, in which some propagators are replaced by Dirac delta functions. These propagators are called *cut propagators*. The sum is over all combinations of cut propagators that separate the diagram into two parts in which the momentum flowing through the cut propagators from one part to the other corresponds to the Mandelstam invariant  $s_i$ . To see this more clearly, let us take as a starting point the one-loop integrand,

$$I = \frac{N(k)}{D_0 D_1 \cdots D_k}, \quad (1.57)$$

where, in general,  $N(k)$  is a polynomial in the loop momentum  $k$ , but which for scalar integrals equals unity, and the denominator factors are

$$D_i = (k - K_i)^2 - m_i^2. \quad (1.58)$$

A single cut in  $D$  dimensions of a particular propagator  $D_i$  is then defined to act on this specific propagator  $D_i$  in the following way:

$$\text{Cut}_{D_i} [I] \equiv \int d^D k \delta^{(+)}(D_i) \left( \frac{N(k)}{D_0 \cdots D_{i-1} D_{i+1} \cdots D_k} \right), \quad (1.59)$$

see, for example, ref. [59]. So, in short, making a cut in a specific channel  $D_i$  means making the replacement

$$\frac{1}{D_i} \xrightarrow{\text{Cut}} \delta^{(+)}(D_i), \quad (1.60)$$

where the superscript  $+$  on the delta denotes the positive-energy solution. The fact that the propagator is replaced by a delta distribution often greatly simplifies the integration and its result. This simplification lies at the heart of the interest in the unitarity method.

Each cut is associated with a consistent direction of energy flow between the two parts of a given diagram. In the following we give a brief summary of the cutting rules of refs [19, 20] for single cuts, and generalized in ref. [2] for sequential cuts.

**First cut.** We enumerate all possible partitions of the vertices of a Feynman diagram into two non-empty sets, distinguished by being colored black or white; see fig. 1.7 for an example. Each diagram is evaluated according to the following rules for scalar theory. (See section 1.5.1 for a summary of our conventions.)

- Black vertices, and propagators joining two black vertices, are computed according to the usual Feynman rules.

- White vertices, and propagators joining two white vertices, are complex-conjugated with respect to the usual Feynman rules.
- Propagators joining a black and a white vertex are *cut*. They are replaced by an on-shell delta function, together with a factor of  $2\pi$  to capture the complex residue correctly, *and* a theta function restricting energy to flow in the direction *from* black *to* white. Stated precisely, when cut, a (complex conjugated) propagator is replaced according to

$$\frac{\pm i}{p^2 - m^2 \pm i0} \longrightarrow 2\pi \delta(p^2 - m^2) \theta(p_0), \quad (1.61)$$

where we assume that the momentum vector  $p$  is directed from the black to the white vertex.

The notation  $\text{Cut}_{s_i}$  stands for the sum of all diagrams that isolate the channel  $s_i$ : if  $p$  is the sum of the momenta flowing through cut propagators from black to white, then  $p^2 = s_i$ . Although cut diagrams in a given momentum channel appear in pairs that are black/white color reversals (see fig. 1.7) only one can be consistent with the energies of the fixed external momenta.

We emphasize that these rules imply that one of the two regions of the diagram — the white region in our conventions — must be computed with complex conjugated Feynman rules. In particular, this means that the  $\pm i0$  of the invariants in the white region is reversed.

**Consider a multiple-channel cut**  $\text{Cut}_{s_1, \dots, s_k} F$ . It is represented by a diagram with a color-partition of vertices for each of the cut invariants  $s_i = p_i^2$ . Assign a sequence of colors  $(c_1(v), \dots, c_k(v))$  to each vertex  $v$  of the diagram, where each  $c_i$  takes the value 0 or 1. For a given  $i$ , the colors  $c_i$  partition the vertices into two sets, such that the total momentum flowing from vertices labeled 0 to vertices labeled 1 is equal to  $p_i$ . A vertex  $v$  is finally colored according to  $c(v) \equiv \sum_{i=1}^k c_i(v)$  modulo 2, with black for  $c(v) = 0$  and white for  $c(v) = 1$ . The rules for evaluating a diagram are as follows (see section 1.5.1 for a summary of our conventions):

- Black vertices are computed according to the usual Feynman rules; white vertices are computed according to complex-conjugated Feynman rules.
- A propagator joining vertices  $u$  and  $v$  is uncut if  $c_i(u) = c_i(v)$  for all  $i$ . If the vertices are black, i.e.  $c(u) = c(v) = 0$ , then the propagator is computed according to the usual Feynman rules, and if the vertices are white, i.e.  $c(u) =$

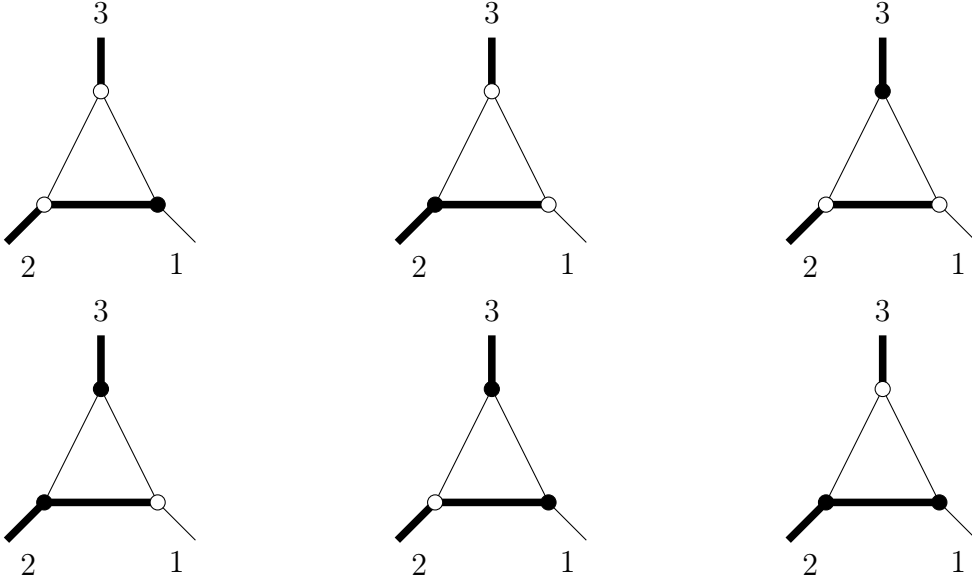


Figure 1.7: All possible cut diagrams of  $T(0, p_2^2, p_3^2; m_{12}^2, 0, 0)$ . A diagram in the top row and its corresponding diagram in the bottom row are associated to the same momentum channel, but opposite energy flow.

$c(v) = 1$ , then the propagator is computed according to complex-conjugated Feynman rules.

- A propagator joining vertices  $u$  and  $v$  is cut if  $c_i(u) \neq c_i(v)$  for any  $i$ . There is a theta function restricting the direction of energy flow from 0 to 1 for each  $i$  for which  $c_i(u) \neq c_i(v)$ . If different cuts impose conflicting energy flows, then the product of the theta functions is zero and the diagram gives no contribution. See figure 1.8 for an illustration of sequential cuts.

For more details about sequential cuts we refer the reader to ref. [2].

For the examples considered in this thesis, cut diagrams are evaluated in the region where the cut invariants are above their respective thresholds and all other Mandelstam invariants are below their thresholds. Also, the squares of all internal masses are positive when they are not cut. When a cut is done in an internal mass, the cut mass will be analytically continued to negative values.

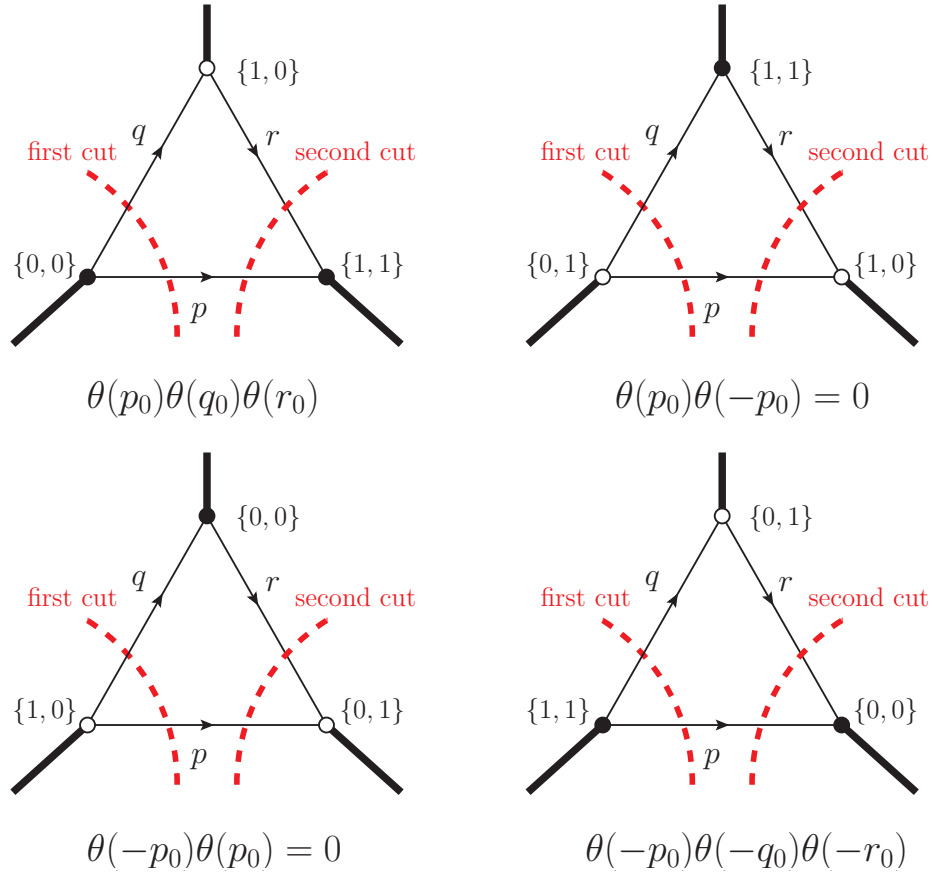


Figure 1.8: Double cuts of the three-mass triangle diagram with massless propagators. The vertices  $v$  are labeled by all possible color sequences  $(c_1(v), c_2(v))$  encoding the cuts. Energy flows from 0 to 1 for each cut, giving the theta functions listed below each diagram. Figure from ref. [2].

### 1.6.2 Cut in an internal mass

In order to give a complete description of the cuts and coproduct of diagrams with internal masses we must introduce a new type of cut: a single-propagator cut. This corresponds to the discontinuity across a branch cut related to an internal mass. For simplicity, we will only analyze the one-loop case, but the results generalize to the multi-loop case.

Let  $F$  be a one-loop planar diagram with  $n$  external legs of momentum  $p_i$ , for  $i = 1, \dots, n$ , all incoming, massive or not, and with internal masses  $m_{i,i+1}^2$  between legs  $i$  and  $i+1$ , which we assume are all distinct. Furthermore, we define  $q_j = \sum_{i=1}^j p_i$ , for  $j = 1, \dots, n$ , so that  $q_n = 0$ . Then, according to our Feynman rules,

$$F(q_i \cdot q_j; m_{1,2}^2, \dots, m_{1,n}^2) = (-1)^n e^{\gamma_E \epsilon} \int \frac{d^{4-2\epsilon} k}{\pi^{2-\epsilon}} \prod_{i=1}^n \frac{1}{(k + q_i)^2 - m_{i,i+1}^2 + i0}. \quad (1.62)$$

The integral  $F$  is evaluated away from any branch cut in the euclidean region of the Mandelstam invariants, and for all  $m_{i,i+1}^2 > 0$ . By looking at the form of the propagators, we can associate a  $-i0$  prescription to the masses:

$$m_{i,i+1}^2 \rightarrow m_{i,i+1}^2 - i0. \quad (1.63)$$

Although it does not correspond to a physical region, we can analytically continue  $F$  to a region where the square of one of the masses is negative (without loss of generality, say  $m_{1,n}^2 < 0$ ), while keeping all the other squared masses positive and the Mandelstam invariants in the euclidean region. In this region, we isolate the discontinuity associated with  $m_{1,n}^2$ :

$$\begin{aligned} \text{Disc}_{m_{1,n}^2} F &= F(q_i \cdot q_j; m_{1,2}^2, \dots, m_{1,n}^2 - i0) - F(q_i \cdot q_j; m_{1,2}^2, \dots, m_{1,n}^2 + i0) \\ &= (-1)^n e^{\gamma_E \epsilon} \int \frac{d^{4-2\epsilon} k}{\pi^{2-\epsilon}} \left( \frac{1}{k^2 - m_{1,n}^2 + i0} - \frac{1}{k^2 - m_{1,n}^2 - i0} \right) \prod_{i=1}^{n-1} \frac{1}{(k + q_i)^2 - m_{i,i+1}^2} \\ &= (-1)^{n+1} e^{\gamma_E \epsilon} \int \frac{d^{4-2\epsilon} k}{\pi^{2-\epsilon}} (2\pi i) \delta(k^2 - m_{1,n}^2) \prod_{i=1}^{n-1} \frac{1}{(k + q_i)^2 - m_{i,i+1}^2} \\ &\equiv \text{Cut}_{m_{1,n}^2} F, \end{aligned} \quad (1.64)$$

which shows that mass discontinuities do indeed correspond to single-particle cuts. We again stress that although we are discussing one-loop integrals, this is just for simplicity of the expressions. The same result holds for a multi-loop diagram.

Furthermore, we notice that  $F$  can also be a cut Feynman diagram as long as the propagator with mass  $m_{1,n}^2$  has not been cut previously. Cuts in internal masses can then be combined with cuts in external channels to compute sequential discontinuities in internal masses and external channels.

We can thus deduce the rules for single-propagator cuts, corresponding to mass discontinuities: we simply replace the cut propagator by a delta function, according to

$$\frac{\pm i}{p^2 - m^2 \pm i0} \rightarrow 2\pi\delta(p^2 - m^2), \quad (1.65)$$

without any condition on the energy flow or any further conjugation of other parts of the diagram. Unlike cuts in kinematic channels, the black and white colorings are unaffected by these cuts, as there is no notion of separation into two regions where one is complex-conjugated.

### 1.6.3 Examples of cut diagrams

Here we present examples on how to compute a cut diagram, a technique that is precious to us in our analysis throughout this chapter. These examples are based on refs. [2, 52, 60, 58].

#### Cut in an external channel

In the following we review the cut integral calculation for the case of external channel cuts, both for one cut and for two cuts. The triangle we choose to consider, written below in eq. (1.66), is fully symmetric, so it is enough to consider just one single-channel cut, fig. 1.10, and one double-channel cut, fig. 1.11. According to our conventions, summarized in section 1.5.1, our chosen triangle, depicted in fig. 1.9 reads

$$T(p_1^2, p_2^2, p_3^2) \equiv -e^{\gamma_E \epsilon} \int \frac{dk}{\pi^{D/2}} \frac{1}{k^2(p_2 - k)^2(p_1 + k)^2}. \quad (1.66)$$

**Single cut** The single cut of the diagram in eq. (1.66) and figure 1.9 is shown in fig. 1.10 and what we want to compute is

$$\text{Cut}_{p_2^2} T(p_1^2, p_2^2, p_3^2) = -(2\pi)^2 e^{\gamma_E \epsilon} \int \frac{dk}{\pi^{D/2}} \frac{\delta^+(k^2)\delta^+((p_2 - k)^2)}{(p_1 + k)^2}, \quad (1.67)$$

where

$$\delta^+(k^2) = \delta(k^2)\theta(k_0), \quad (1.68)$$

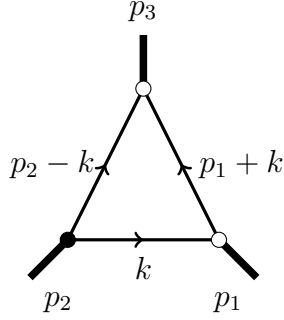


Figure 1.9: The three-mass triangle integral  $T(p_1^2, p_2^2, p_3^2)$ , eq. (1.66), of the example in subsection 1.6.3. Here  $k$  denotes the loop momentum and the  $p_i^2$  are the external invariants. The colorings of the dots give the correct Feynman rules to use, see subsection 1.5.1. The external channels, denoted by thick lines, are massive, whereas the internal propagators, drawn as thin lines, are massless.

i.e. we take the positive-energy solution. Without loss of generality, we choose to parametrize the external momenta in a specific manner that will render our calculation easier:

$$p_2 = \sqrt{p_2^2}(1, 0, \mathbf{0}_{D-2}), \quad p_3 = \sqrt{p_3^2}(\alpha, \sqrt{\alpha^2 - 1}, \mathbf{0}_{D-2}). \quad (1.69)$$

Momentum conservation fixes the value of  $\alpha$  to be

$$\begin{aligned} \alpha &= \frac{p_1^2 - p_2^2 - p_3^2}{2\sqrt{p_2^2}\sqrt{p_3^2}} \\ &= -p_1^2 \frac{1 + u_2 - u_3}{2\sqrt{p_2^2}\sqrt{p_3^2}}, \end{aligned} \quad (1.70)$$

and

$$\sqrt{\alpha^2 - 1} = -p_1^2 \frac{\sqrt{\lambda(1, u_2, u_3)}}{2\sqrt{p_1^2}\sqrt{p_2^2}}, \quad (1.71)$$

where  $\lambda$  is defined in eq. (1.38).

Likewise, we parametrize the massless loop momentum  $k$  as

$$k = k_0(1, \beta \cos \theta, \beta \sin \theta \mathbf{1}_{D-2}), \quad (1.72)$$

where  $\theta \in [0, \pi]$ ,  $k_0, \beta > 0$  and  $\mathbf{1}_{D-2}$  ranges over unit vectors in the dimensions transverse to  $p_2$  and  $p_3$ . If the propagator of momentum  $k$  is massless then  $\beta = 1$ .

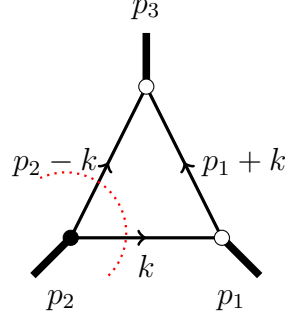


Figure 1.10: The cut three-mass triangle integral  $\text{Cut}_{p_2^2} T(p_1^2, p_2^2, p_3^2)$  of the example in subsection 1.6.3, with the single-channel cut denoted by a dashed red curve. Here  $k$  denotes the loop momentum and the  $p_i^2$  are the external invariants. The colorings of the dots give the correct Feynman rules to use, see subsection 1.5.1.

Next we choose to make a change of variables such that

$$\cos \theta = 2x - 1 , \quad (1.73)$$

for  $x \in [0, 1]$  so that, with the above parametrizations, the integration measure becomes

$$\int d^{4-2\epsilon} k \delta(k^2) \theta(k_0) = \frac{2^{1-2\epsilon} \pi^{1-\epsilon}}{\Gamma(1-\epsilon)} \int_0^\infty dk_0 |k_0|^{1-2\epsilon} \int_0^1 dx (1-x)^{-\epsilon} x^{-\epsilon} . \quad (1.74)$$

Now the  $k_0$  integral can be evaluated trivially by using the delta function  $\delta^+((p_2 - k)^2)$  in eq. (1.67). It fixes  $k_0 = \sqrt{p_2^2}/2$ .

The remaining uncut propagator in eq. (1.67) reads

$$\begin{aligned} (p_1 + k)^2 &= p_1^2 \left( \frac{1 - u_2 + u_3 - \sqrt{\lambda}}{2} + x\sqrt{\lambda} \right) \\ &= p_1^2 (1 - z) \left( 1 - \frac{x(z - \bar{z})}{z - 1} \right) , \end{aligned} \quad (1.75)$$

where  $z, \bar{z}$  have been defined in eq. (1.37). We note that these variables appear naturally in the cut computation, and that they render the kinematics parametrization rational.

The integral that remains to be computed now reads, written in the appropriate variables

$$\text{Cut}_{p_2^2} T(p_1^2, p_2^2, p_3^2) = -\frac{(2\pi)^2 e^{\gamma_E \epsilon}}{\Gamma(1-\epsilon)} \frac{(p_2^2)^{-\epsilon}}{p_1^2(1-z)} \int_0^1 dx \frac{(x(1-x))^{-\epsilon}}{\left(1 - \frac{x(z-\bar{z})}{z-1}\right)}. \quad (1.76)$$

This can easily be evaluated, for example using `Mathematica`, giving

$$\text{Cut}_{p_2^2} T(p_1^2, p_2^2, p_3^2) = -(2\pi)^2 e^{\gamma_E \epsilon} \frac{(p_2^2)^{-\epsilon}}{p_1^2(1-z)} \frac{\Gamma(1-\epsilon)}{\Gamma(2-2\epsilon)} {}_2F_1\left(1, 1-\epsilon; 2-2\epsilon; \frac{z-\bar{z}}{z-1}\right). \quad (1.77)$$

This can further be developed in a series around  $\epsilon = 0$ , giving the result in ref. [2]:

$$\text{Cut}_{p_2^2} T(p_1^2, p_2^2, p_3^2) = \frac{2\pi}{p_1^2(z-\bar{z})} \log \frac{1-z}{1-\bar{z}} + \mathcal{O}(\epsilon). \quad (1.78)$$

A remark is in order. We note that the integral in eq. (1.76) is well defined in the region where the cut invariant  $p_2^2$  is positive and the other external invariants  $p_1^2$ ,  $p_3^2$  are negative. We will get back to this when talking about the regions of the symbol letters in section 1.9.

**Double cut** The double cut of the same triangle (1.66) is computed as follows. This doubly cut integral is shown in figure 1.11. The cut triangle now reads

$$\text{Cut}_{p_2^2, p_3^2} T(p_1^2, p_2^2, p_3^2) = -\frac{4\pi^2 i e^{\gamma_E \epsilon}}{\Gamma(1-\epsilon)} \frac{(p_3^2)^{-\epsilon}}{p_1^2(z-\bar{z})} \int_0^1 dx \delta\left(x - \frac{z-1}{z-\bar{z}}\right) (x(1-x))^{-\epsilon} \quad (1.79)$$

and it evaluates to

$$\text{Cut}_{p_2^2, p_3^2} T(p_1^2, p_2^2, p_3^2) = -\frac{4\pi^2 i e^{\gamma_E \epsilon}}{\Gamma(1-\epsilon)} \frac{(p_3^2)^{-\epsilon}}{p_1^2(z-\bar{z})} \left(-\frac{(z-1)(\bar{z}-1)}{(z-\bar{z})^2}\right)^{-\epsilon} \theta\left(\frac{z-1}{z-\bar{z}}, \frac{\bar{z}-1}{\bar{z}-z}\right) \quad (1.80)$$

The integral (1.79) is well defined for  $p_2^2$ ,  $p_3^2 > 0$  and  $p_1^2 < 0$ . In this region the Heaviside theta function in eq. (1.80) equals one.

### Cut in an internal mass

Cuts in internal masses are more complicated to compute than cuts in external channels. We will present two ways of computing them: a more elegant way which does not always work, and a ‘brute force’ method that always works. Whichever method we choose depends on the configuration of internal and external masses. We have checked that the results of the two methods coincide, when both can be applied.

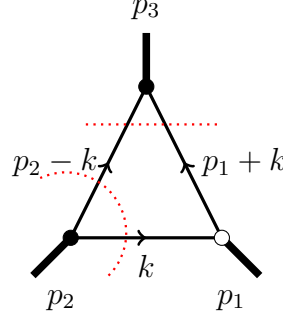


Figure 1.11: The doubly cut three-mass triangle integral  $(\text{Cut}_{p_2^2, p_3^2})T(p_1^2, p_2^2, p_3^2)$  of the example in subsection 1.6.3, with the double-channel cuts denoted by dashed red curves. Here  $k$  denotes the loop momentum and the  $p_i^2$  are the external invariants. The colorings of the dots give the correct Feynman rules to use, see subsection 1.5.1.

**The first method** This method is the more elegant way, but it only works for special configurations of internal and external masses. More precisely, if the legs of a triangle are called  $i$ ,  $j$  and  $k$  and the mass we are cutting in is  $m_{ij}^2$ , then we require  $p_k^2 \neq 0$  for this method to be applicable. This is so, because there is no sequential cut associated to the cuts in an internal mass and an external channel when these two are adjacent.

The way in which we proceed is the following. We do a triple cut on the triangle, that is, we cut all its propagators. This is equivalent to subsequently cutting in the massive external leg  $p_k^2$  and in the mass  $m_{ij}^2$ . We then perform a dispersive integral in the  $p_k^2$ -channel. This is a very convenient way to proceed, because when all the propagators of the triangle are cut then the integral is trivial to evaluate. On the other hand, there is no guarantee that there exists a dispersive representation for the  $p_k^2$ -channel, so it is not certain that we can do this last dispersive integral and recover the mass cut.

As an example, let us study  $T(p_2^2, p_3^2; m_{12}^2)$ . Its three-propagator cut in  $m_{12}^2$  and  $p_3^2$  is evaluated in the region where  $p_3^2 > 0$  and  $m_{ij}^2 < 0$  and it reads

$$\text{Cut}_{m_{12}^2, p_3^2} T(p_2^2, p_3^2; m_{12}^2) = -\frac{4\pi^2 i e^{\gamma_E \epsilon}}{\Gamma(1-\epsilon)} \frac{(p_3^2)^{-\epsilon} (-m_{12}^2)^{-\epsilon}}{(p_3^2 - p_2^2)^{1-\epsilon}} (p_3^2 + m_{12}^2 - p_2^2)^{-\epsilon} \theta(p_3^2 + m_{12}^2 - p_2^2). \quad (1.81)$$

Now, through a dispersive integral (see section 1.10), we recover the sole  $m_{ij}^2 < 0$

cut:

$$\begin{aligned} \text{Cut}_{m_{12}^2} T(p_2^2, p_3^2; m_{12}^2) &= \text{Disc}_{m_{12}^2} T(p_2^2, p_3^2; m_{12}^2) \\ &= -\frac{2\pi e^{\gamma_E \epsilon}}{\Gamma(1-\epsilon)} (-m_{12}^2)^{-\epsilon} \int_0^\infty \frac{ds}{s-p_3^2} \frac{s^{-\epsilon}}{(s-p_2^2)^{1-2\epsilon}} (s+m_{12}^2-p_2^2)^{-\epsilon}. \end{aligned} \quad (1.82)$$

This integral is computable at any order in  $\epsilon$  and gives the result in eq. (C.10) of appendix C.

**The second method** This method relies on finding a Feynman parameter representation for the diagram. Then the discontinuity across the branch cut associated with the internal mass is computed. This method is naturally valid for any configuration of internal and external masses. For the same triangle as above, we have

$$T(p_2^2, p_3^2; m_{12}^2) = i \frac{e^{\gamma_E \epsilon} \Gamma(1+\epsilon)}{\epsilon} \int_0^1 dx \frac{(1-x)^{-\epsilon}}{m_{12}^2 + x(p_3^2 - p_2^2)} \left( (-p_3^2 x)^{-\epsilon} - (m_{12}^2 - p_2^2 x)^{-\epsilon} \right), \quad (1.83)$$

which is obtained by computing the trivial and the first non-trivial Feynman parameter integrals. Then we have

$$\text{Disc}_{m_{12}^2} [(m_{12}^2 - p_2^2 \epsilon)^{-\epsilon}] = \frac{2\pi i \epsilon}{\Gamma(1-\epsilon) \Gamma(1+\epsilon)} (p_2^2 x - m_{12}^2)^{-\epsilon} \theta \left( \frac{m_{12}^2}{p_2^2} - x \right), \quad (1.84)$$

where we have used  $m_{12}^2 = m_{12}^2 - i0$  and we are in the region  $p_2^2 < m_{12}^2 < 0$ . We thus get

$$\begin{aligned} \text{Cut}_{m_{12}^2} T(p_2^2, p_3^2; m_{12}^2) &= \text{Disc}_{m_{12}^2} T(p_2^2, p_3^2; m_{12}^2) \\ &= \frac{2\pi e^{\gamma_E \epsilon}}{\Gamma(1-\epsilon)} \int_0^{m_{12}^2/p_2^2} dx (1-x)^{-\epsilon} \frac{(p_2^2 x - m_{12}^2)^{-\epsilon}}{m_{12}^2 + x(p_3^2 - p_2^2)}. \end{aligned} \quad (1.85)$$

This integral is trivial to evaluate to any order in  $\epsilon$ .

## 1.7 The first entry condition

As in [58], let us now extend the first-entry condition of ref. [47] to cases with internal masses. First, let us start with a discussion about the kinematic regions of interest in computing Feynman integrals.

Feynman integrals are most easily computed in the kinematic region where the integral is well-defined independently of the  $\pm i0$ -prescription of the propagators, see e.g. [17]. This region is called the *euclidean region* and in it we are away from any branch cut. In the most general three-mass one-loop triangle integral, this euclidean region is characterized by

$$p_1^2 < \left( \sqrt{m_{12}^2} + \sqrt{m_{13}^2} \right)^2, \quad p_2^2 < \left( \sqrt{m_{12}^2} + \sqrt{m_{23}^2} \right)^2, \quad p_3^2 < \left( \sqrt{m_{13}^2} + \sqrt{m_{23}^2} \right)^2, \\ m_{12}^2 > 0, \quad m_{23}^2 > 0, \quad m_{13}^2 > 0. \quad (1.86)$$

For all other examples considered in this thesis, the euclidean region is obtained by taking the appropriate massless limit. For example, in the case where all internal masses vanish, as in ref. [2], the euclidean region corresponds to all external invariants being negative. When departing from this region, we are sensitive to the branch cuts of the integral. Especially, the  $\pm i0$ -prescription tells us on which side of the branch cut we are on. Comparing the  $+i0$ -prescription to the  $-i0$  one gives the discontinuity across the branch cut.

The coproduct of the multiple polylogarithms provides a natural way of analyzing the discontinuities. In [46] it was argued that the discontinuity acts only on the first entry of the coproduct:

$$\Delta \text{Disc} = (\text{Disc} \otimes \text{id}) \Delta, \quad (1.87)$$

leaving the rest alone. Here, the definition of Disc is, for a Feynman integral  $F$  [2],

$$\text{Disc}_x [F(x \pm i0)] = \lim_{\varepsilon \rightarrow 0} [F(x \pm i\varepsilon) - F(x \mp i\varepsilon)] . \quad (1.88)$$

Above,  $x$  represents any kinematic variable, for example a Mandelstam invariant or an internal mass invariant. A few comments are in order: Firstly, we note that if there is no branch cut in the region under consideration, or if  $F$  does not depend on  $x$ , then the discontinuity vanishes. For example, the discontinuity in a Mandelstam invariant only exists in the region above its threshold. Secondly, we note that the choice of sign in the  $+i0$ -prescription is inherited from the prescription of the propagators of  $F$ . As a last comment, we note that a sequential discontinuity operator also can be defined

$$\text{Disc}_{x_1, \dots, x_k} F \equiv \text{Disc}_{x_k} (\text{Disc}_{x_1, \dots, x_{k-1}} F), \quad (1.89)$$

where the variables  $x_i$  are associated with internal masses or external momentum invariants.

Eq. (1.87) implies that the first entries of the coproduct of a Feynman integral must have the same branch cut structure as the Feynman integral itself. This observation is known as the *first entry condition* and it was first given for the context of

massless propagators in ref. [47]. There the first entries of the symbol were written as logarithms of Mandelstam invariants. For us, considering massive propagators, this generalizes to the fact that the first entries of the  $\Delta_{1,n-1}$  component of the coproduct must be simple logarithms with branch points at the boundaries of the euclidean region.

When massive propagators are present, we find two ways in which the first entry condition generalizes: The first one is that we no longer have logarithms of simple Mandelstam invariants but rather logarithms with branch cuts at the mass threshold of the corresponding invariant. The second one is that the squared masses of the propagators appear as first entries.

Another feature that is already present in the massless-propagators case and that is still true in the presence of internal masses is that the second entries of the coproduct correspond to the discontinuities associated with the branch cut of the first entry. A new feature in the massive-propagator case is that discontinuities associated with the internal masses are present. To summarize, the discontinuities can be associated either to Mandelstam invariants going above their thresholds or to internal masses becoming negative.

As discussed in section 1.4 we strive to work with symbol alphabets that have rational letters. If we can have such an alphabet when working with Mandelstam invariants themselves, or rather ratios of them in order to have dimensionless letters, the above properties are easy to check. In cases that are more complicated, we may want to use letters such as  $z$ ,  $\bar{z}$  defined in eq. (1.37). In such cases the situation is not as clear. However, we claim that the symbol tensor can always be rearranged in such a way that the above properties can be checked.

Let us now consider a few examples of the first entry condition.

**Example 1:** Consider the triangle  $T(p_1^2; m_{12}^2) \equiv i/p_1^2 \mathcal{T}(p_1^2; m_{12}^2)$ , whose symbol is

$$\begin{aligned} \mathcal{S}[\mathcal{T}(p_1^2; m_{12}^2)] &= \frac{1}{\epsilon} \frac{m_{12}^2 - p_1^2}{m_{12}^2} + m_{12}^2 \otimes \frac{m_{12}^2(m_{12}^2 - p_1^2)}{p_1^2} \\ &\quad + (m_{12}^2 - p_1^2) \otimes \frac{p_1^2}{(m_{12}^2 - p_1^2)^2} + \mathcal{O}(\epsilon). \end{aligned} \quad (1.90)$$

The first term of the finite part has  $\log(m_{12}^2)$  as its first entry, and the second term has  $\log(m_{12}^2 - p_1^2)$  as its first entry. The latter is written in a form in which the argument of the logarithm is positive in the euclidean region where the integral is originally evaluated.

**Example 2:** Consider the triangle  $T(p_1^2; m_{12}^2, m_{13}^2) \equiv i/p_1^2 \mathcal{T}(p_1^2; m_{12}^2, m_{13}^2)$ , whose symbol is

$$\mathcal{S}[\mathcal{T}(p_1^2; m_{12}^2, m_{13}^2)] = \left( \frac{w_1}{1-w_1} \right) \otimes \left( \frac{\bar{w}_1}{1-\bar{w}_1} \right) + \left( \frac{\bar{w}_1}{1-\bar{w}_1} \right) \otimes \left( \frac{w_1}{1-w_1} \right). \quad (1.91)$$

We have changed variables according to (1.41) to have a rational symbol alphabet. Because the new variables have a more complicated relation to the Mandelstam invariants, the first entry condition is not as transparent as in the previous example. However, as mentioned above, the symbol of  $\mathcal{T}(p_1^2, 0, 0; m_{12}^2, 0, m_{13}^2)$  can be rewritten as

$$(w_1 \bar{w}_1) \otimes \frac{w_1}{1-w_1} + ((1-w_1)(1-\bar{w}_1)) \otimes \frac{1-\bar{w}_1}{\bar{w}_1} + (w_1(1-\bar{w}_1)) \otimes \frac{\bar{w}_1(1-w_1)}{w_1(1-\bar{w}_1)}. \quad (1.92)$$

The first entry of the first term is  $\log(m_{12}^2/p_1^2)$ , and its second entry is associated with the discontinuity in the variable  $m_{12}^2$ . The first entry of the second term is  $\log(m_{13}^2/p_1^2)$ , and its second entry is associated with the discontinuity in the variable  $m_{13}^2$ . The first entry of the third term corresponds to the threshold at  $p_1^2 = (\sqrt{m_{12}^2} + \sqrt{m_{13}^2})^2$ , and its second entry is associated with the discontinuity in the variable  $p_1^2$ . The argument of the logarithm in the first entry of this term is not a direct change of variables of  $p_1^2 - (\sqrt{m_{12}^2} + \sqrt{m_{13}^2})^2$ , which would not be a rational function. Nevertheless, one can verify that the condition  $w_1(1-\bar{w}_1) > 0$  is exactly equivalent to the condition  $p_1^2 > (\sqrt{m_{12}^2} + \sqrt{m_{13}^2})^2$ , whenever  $p_1^2 > 0$ . We can understand this latter condition as a weaker prerequisite for obtaining any discontinuity in the variable  $p_1^2$ .

In the above examples, we have neglected the  $p_1^2$  that appears in the denominator of each first entry. We choose to normalize by this invariant in order to work with dimensionless quantities. However, in both the above examples  $p_1^2$  has a nonzero mass threshold associated to it, so  $p_1^2$  by itself, with a zero mass threshold, should not appear as a first entry. Indeed, summing the second entries associated to this particular first entry, we see that the sum of the second entries vanishes. So there is no contribution to the symbol from the first entry  $p_1^2$ .

We finish with a word of caution about (1.92). In this triangle, the variables  $w_1$  and  $\bar{w}_1$  are distinguished only by the choice of branch of the square root. Like the function itself, the symbol has no preferred branch, and therefore it is invariant under the exchange  $w_1 \leftrightarrow \bar{w}_1$ . This invariance is apparent in the form given in (1.91) but obscure in (1.92). Notably, the three discontinuities, as read from (1.92), are not themselves invariant under this exchange. When relating these discontinuities to cut

integrals, we will be very specific about the kinematics and insist on taking the positive branch of the square root. From that point of view, the form given in (1.92) will be necessarily preferred over its conjugate under  $w_1 \leftrightarrow \bar{w}_1$ . Whenever we make use of the first entry condition (see section 1.10), we will therefore always take  $w_1(1 - \bar{w}_1)$  for the  $p_1^2$  channel, and not  $\bar{w}_1(1 - w_1)$ . In the following, we will relate discontinuities to operations on individual symbol letters, and not particular combinations of them. Thus, while we claim that one can generally write symbols of Feynman integrals in a form such as (1.92), where the first entries are directly identified with kinematic invariants and thresholds, one should not immediately conclude that the corresponding second entries are unambiguously interpreted as discontinuities.

## 1.8 Relations among discontinuities

In this section we discuss how to relate cuts and coproduct entries. This is done via their separate relations to discontinuities across branch cuts. In this way, we get a diagrammatic interpretation of coproduct entries. We will immediately consider the general case with massive propagators [58]. The first paper on these relations is [2] where massless propagators were studied. The generalization to massive propagators is straightforward, aside from two points concerning the  $i0$ -prescription: *i*) when combining channel and mass discontinuities, the  $\pm i0$  associated to the masses is determined once all channel cuts have been taken; *ii*) the precise determination of how the  $\pm i0$  prescription propagates from invariants to symbol letters is slightly more complicated than in the absence of internal masses.

### 1.8.1 Discontinuities and cut diagrams

The original relation for a cut in a single external channel  $s$  was derived in refs [19, 20, 21] and in our notation it reads [2]

$$\text{Disc}_s F = -\text{Cut}_s F . \quad (1.93)$$

In ref [2] it was pointed out that, for sequential cuts in  $k$  external channels, the above relation generalizes:

$$\text{Cut}_{s_1, s_2, \dots, s_k} F = (-1)^k \text{Disc}_{s_1, s_2, \dots, s_k} F . \quad (1.94)$$

Here  $\text{Cut}_{s_1, s_2, \dots, s_k} F$  should be computed according to the cutting rules given in section 1.6.

Eqs. (1.93) and (1.94) are valid in specific kinematic regions, as already mentioned for cuts in the previous section 1.6. The cuts  $\text{Cut}_{s_1, s_2, \dots, s_k} F$  are valid in the kinematic region where the invariants  $s_1, s_2, \dots, s_k$  are above threshold, the other invariants are below threshold and all internal masses are positive. On the right hand side, we proceed step by step according to the definition in eq. (1.89), where each  $\text{Disc}_{s_1, s_2, \dots, s_k}$  is evaluated after analytic continuation to the same region in which  $\text{Cut}_{s_1, s_2, \dots, s_k}$  is computed.

The relation for sequential cuts in internal masses generalizes in a trivial manner from eq. (1.64) to

$$\text{Cut}_{m_1^2, m_2^2, \dots, m_k^2} F = \text{Disc}_{m_1^2, m_2^2, \dots, m_k^2} F . \quad (1.95)$$

Now sequential cuts in external channels, eq. (1.94), and in internal masses, eq. (1.95), can be combined to give

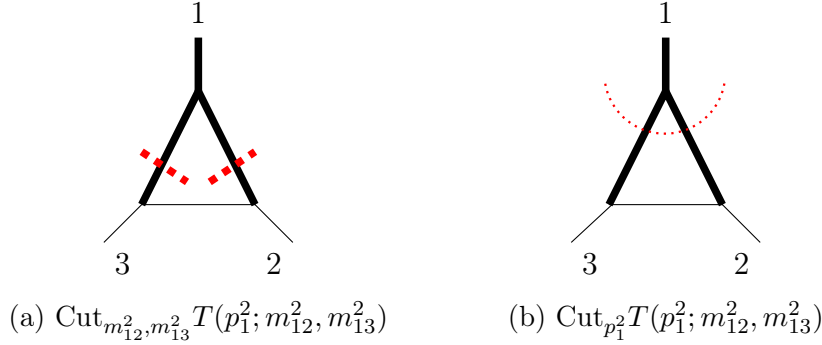
$$\text{Cut}_{s_1, \dots, s_l, m_1^2, \dots, m_k^2} F = (-1)^l \text{Disc}_{s_1, \dots, s_l, m_1^2, \dots, m_k^2} F . \quad (1.96)$$

We need to pay careful attention to the  $\pm i0$ -prescription of variables when using eq. (1.96). Indeed, in order for this equation to produce the correct signs we must first perform all cuts on external channels and only then evaluate the sign of the  $i0$ -term of the internal-mass cut. This is so, because the channel cuts always imply complex conjugation of a part of the diagram and this affects the  $\pm i0$ -prescription of the internal propagators.

We further note that, though the order in which the cuts are taken (on the left hand side of eq. (1.96)) does not matter, the order in which the discontinuities of the right hand side of the equation does matter in the sense that we may get different signs for the discontinuity when different orderings of the operations are taken. This is a prediction of our discontinuity relations. So, the right hand side takes a different form when channels and masses on the left hand side are permuted. This implies relations among the different  $\text{Disc}_{s_1, \dots, s_l, m_1^2, \dots, m_k^2} F$ . We will get back to this in section 1.8.2.

Lastly, we note that there is a restriction on the propagators being cut. The cut integrals produce sequential discontinuities through eq. (1.96) only if each additional invariant in the subscript introduces at least one new cut propagator in the diagram. For example, we do not consider the sequential cut  $\text{Cut}_{p_1^2, m_{12}^2}$ , because the  $m_{12}^2$ -propagator has already been cut when performing the cut on the external channel  $p_1^2$ .

In section 1.9 we illustrate the above definitions by giving some examples.

Figure 1.12: Two-propagator cuts of the triangle  $T(p_1^2; m_{12}^2, m_{13}^2)$ .

### A limit on multiple mass cuts

The sequential cuts in massive internal propagators will vanish if the one-loop cut diagram is equivalent to a complete cut in an external channel. To see why this is so, let us consider two massive internal propagators of masses squared  $m_{12}^2$  and  $m_{1n}^2$ , attached to the massive external leg  $p_1^2$ . (See figure 1.12 for the case of a one-mass triangle diagram.) The integral with cuts in these two masses reads

$$(-1)^n \int \frac{d^{4-2\epsilon} k}{\pi^{2-\epsilon}} (2\pi i)^2 \delta(k^2 - m_{1,n}^2) \delta((k + p_1)^2 - m_{1,2}^2) \prod_{i=2}^{n-1} \frac{1}{(k + q_i)^2 - m_{i,i+1}^2}, \quad (1.97)$$

and it can be used either as the cut integral  $\text{Cut}_{m_{1,n}^2, m_{1,2}^2} F$  or  $\text{Cut}_{p_1^2} F$ , depending on the kinematic region where it is evaluated.

If  $p_1^2 \neq 0$ , then the uncut integral  $F$  has a branch cut in  $p_1^2$ . As a consequence of the largest time equation, the integral  $\text{Cut}_{p_1^2} F$  is proportional to the discontinuity of  $F$  across this branch cut [19, 20]. In particular, the discontinuity is zero when we are below the threshold of  $p_1^2$ , which can be realized either for  $m_{1,2}^2, m_{1,n}^2 > 0$  or  $m_{1,2}^2, m_{1,n}^2 < 0$ , and in this case the integral (1.97) vanishes as well.

Now, the double-cut integral  $\text{Cut}_{m_{1,n}^2, m_{1,2}^2} F$  must be evaluated in the region where  $m_{1,2}^2, m_{1,n}^2 < 0$  and all other invariants are below their thresholds. Since  $p_1^2$ , in particular, is below its threshold, the integral vanishes by the argument given above. We will see an example of this type of vanishing double cut in  $T(p_1^2, 0, 0; m_{12}^2, 0, m_{13}^2)$  in section 1.9.3.

However, if  $p_1^2 = 0$ , then  $F$  has no branch cut associated with this external channel, and the largest time equation does not give any constraint on the result of (1.97). In this case, the double discontinuity on the masses  $m_{1,2}^2$  and  $m_{1,n}^2$  can

indeed be nonzero. We will see an example of this type of non vanishing double cut in  $T(p_1^2, 0, 0; m_{12}^2, m_{23}^2, 0)$  in section 1.9.2.

### Sequential cuts of triangle diagrams

In this thesis, where we focus our attention of triangle diagrams, we are restricted to  $k = 2$  in eq. (1.94). This is so, because after two sequential cuts in external channels all three propagators are cut. Because these diagrams vanish in dimensional regularization if all external channels are massless, we require at least one of the external channels to be massive. Therefore, the maximum value for  $k$  in eq. (1.95) is 2 as well. This is consistent with the fact that the transcendental weight of these functions is two.

## 1.8.2 Discontinuities and the coproduct

Having related diagrammatic cuts to the discontinuity operation defined in eq. (1.89) in the previous section, we now turn to a new relation: the relation between Disc and the coproduct.

Let us start by defining the operation  $\delta_{x_1, \dots, x_k}$  on the coproduct. Given the symbol alphabet  $\mathcal{A}$ , we can write the  $(1, 1, \dots, 1, n - k)$  component of the coproduct of  $F$  as

$$\underbrace{\Delta_{1,1,\dots,1,n-k}}_{k \text{ times}} F = \sum_{(x_{i_1}, \dots, x_{i_k}) \in \mathcal{A}^k} \log x_{i_1} \otimes \dots \otimes \log x_{i_k} \otimes g_{x_{i_1}, \dots, x_{i_k}}. \quad (1.98)$$

Then, our truncation operation is defined to be

$$\delta_{x_{j_1}, \dots, x_{j_k}} F \cong \sum_{(x_{i_1}, \dots, x_{i_k}) \in \mathcal{A}^k} \delta_{i_1 j_1} \dots \delta_{i_k j_k} g_{x_{i_1}, \dots, x_{i_k}}. \quad (1.99)$$

The congruence symbol indicates that  $\delta_{x_{j_1}, \dots, x_{j_k}} F$  is defined only modulo  $\pi$ ; this is an intrinsic ambiguity due to the nature of the Hopf algebra of multiple polylogarithms. If  $F$  contains overall numerical factors of  $\pi$ , they should be factored out before performing this operation and then reinstated.

In ref. [2] it was shown how the discontinuity of any element of the Hopf algebra is captured by the operation  $\delta$  defined in eq. (1.99). This relies on the relation

$$\text{Disc} F \cong \mu [(\text{Disc} \otimes \text{id})(\Delta_{1, n-1} F)], \quad (1.100)$$

where  $\mu$  is a linear map,  $\mu : \mathcal{H} \otimes \mathcal{H} \rightarrow \mathcal{H}$ , such that  $\mu(a \otimes b) = a \cdot b$ , for  $a, b \in \mathcal{H}$  and  $F$  is an element of weight  $n$  of the Hopf algebra. Eq. (1.100) is a direct consequence of

the relation between the coproduct and discontinuity operator presented in ref. [46]. Again, if  $F$  contains overall factors of  $\pi$  then these should be stripped out before performing the operation on the right hand side, and then reinstated. Since the first entries of  $\Delta_{1,n-1}F$  are of weight 1, they are just logarithms and the Disc operation on the right hand side is computing discontinuities of ordinary logarithms. In particular, this means that we pick up factors  $\pm 2\pi i$ . Whichever sign  $+$  or  $-$  we pick up depends on the  $i0$ -prescription, to be reviewed in the next section.

In eq. (1.100) we are required to choose the sign in the logarithm in such a way that the argument is positive and that the expression is real-valued in the kinematic region for which  $F$  is away from its branch cut in  $s$ . When taking Disc, the coproduct will be analytically continued to the region in which there exists a branch cut in  $s$ . In this region, the arguments of the logarithms can become negative and if the letter  $x$  in eq. (1.100) depends on  $s$  then there will be a nonzero contribution to Disc. [2]

The relation of the coproduct to sequential discontinuities of a Feynman integral  $F$  are computed by the sequential use of eq. (1.100). Explicitly, the relation reads

$$\text{Disc}_{r_1, \dots, r_k} F \cong \Theta \sum_{(x_1, \dots, x_k) \in \mathcal{A}^k} \left( \prod_{i=1}^k a_i(r_i, x_i) \right) \delta_{x_1, \dots, x_k} F, \quad (1.101)$$

where the sum is taken over ordered sequences  $(x_1, \dots, x_k)$  of  $k$  letters, and the  $r_i$  can be either internal masses or external channels. The congruence symbol in (1.101) indicates that the right-hand side only captures terms whose coproduct is non vanishing, and it therefore holds modulo  $(2\pi i)^{k+1}$ . The schematic factor  $\Theta$  expresses the restriction to the kinematic region where the left-hand side will be compared with Cut. The factors  $a_i(s_i, x_i)$  are related to the discontinuity of a real-valued logarithm after analytic continuation from  $R_{i-1}$ , the region where the  $(i-1)$ -th cut is taken, to the region  $R_i$ , the region where the  $i$ -th cut is taken:

$$a_i(r_i, x_i) = \text{Disc}_{r_i, R_i} \left[ \left[ \log(\pm x_i) \right] \right]_{R_{i-1}}, \quad (1.102)$$

where the double bracket means that the sign should be chosen so that the argument of the logarithm is positive in the region  $R_{i-1}$ .

In the simplest cases, as already mentioned, the  $a_i(r_i, x_i)$  will take on values  $\pm 2\pi i$  or 0.

Let us close this section with a few remarks. Firstly, we note that eq. (1.101) is valid no matter in which order the discontinuities are taken. However, we observe that in computing the discontinuities Disc, we need to be careful with the order in which the discontinuities are taken and this leads to the convention that we always choose to take channel cuts before internal cuts. Only in this way do we get the

correct sign in eq. (1.94). Secondly, we note that it is more complicated to identify the sign of the imaginary part of the symbol letters  $x_i$ , inherited from the  $\pm i0$ -prescription of the invariants. We will discuss this in the next section.

In section 1.9 we illuminate the above relations by examples.

### The $\pm i0$ -prescription of symbol letters

In most examples considered in this paper, it is simple to determine the sign of the  $i0$ -prescription of a given symbol letter once we know the prescription of the invariant to which it is associated and the kinematical region in which we are working. Indeed, whenever the symbol letters are linear combinations of invariants, this is a trivial problem. However, we observe that in more complicated cases there is an ambiguity in the sign of the imaginary part of some symbol letters. We need to resolve this ambiguity, because this sign is needed to obtain the correct sign in (1.101).

The simplest case where we observe this problem is the triangle with three external masses and one internal mass,  $T(p_1^2, p_2^2, p_3^2; m_{12}^2, 0, 0)$ ; see table 1.3. For instance, when considering the double cut first in  $p_2^2$  and then in  $p_1^2$ , we need to determine the sign of the imaginary part of  $\bar{z} - \mu_{12}$ , as inherited from the prescription of the second cut invariant,  $p_1^2 - i0$ . One can easily check that this sign is the same as the sign of the quantity

$$\frac{\bar{z}(1 - \bar{z}) - \mu_{12}(z - \bar{z})}{z - \bar{z}}. \quad (1.103)$$

which can be either positive or negative in the region where the double cut is computed,

$$z > 1, \quad 0 < \bar{z} < 1, \quad 0 < \mu_{12} < 1, \quad \bar{z} - \mu_{12} > 0. \quad (1.104)$$

If the imaginary part of  $\bar{z} - \mu_{12}$  is negative, then we are in the subregion

$$z > 1, \quad 0 < \bar{z} < 1, \quad \frac{\bar{z}(1 - \bar{z})}{z - \bar{z}} < \mu_{12} < \bar{z}, \quad (1.105)$$

and if it is positive, in the subregion

$$z > 1, \quad 0 < \bar{z} < 1, \quad 0 < \mu_{12} < \frac{\bar{z}(1 - \bar{z})}{z - \bar{z}}. \quad (1.106)$$

We note that if we are in the first situation we cannot smoothly take the internal mass ( $\mu_{12}$ ) to zero. However, if we are in the second situation, corresponding to a positive imaginary part of  $\bar{z} - \mu_{12}$ , we can take  $\mu_{12}$  to zero without any problem, which is naturally a desirable property. We thus associate a positive imaginary part to the symbol letter  $\bar{z} - \mu_{12}$ . We can confirm this is indeed the correct result by considering

the same double cut in the opposite order, where there are no sign ambiguities. We treat this example in detail in section 1.9.

All other cases where we have found sign ambiguities can be solved in the same way: *we always require being in a kinematic region where massless limits can be taken smoothly*. Furthermore, we have found in all of our examples of multiple cuts that there is always an ordering of the cuts where there is no ambiguity. We have then verified that any possible ambiguities were correctly lifted through the method just described.

### 1.8.3 Cuts and the coproduct

Having related cuts to discontinuities in section 1.8.1 and discontinuities to coproduct entries in section 1.8.2, it is now straightforward to relate cuts to coproduct entries. Combining the relations (1.96) and (1.101), we arrive at:

$$\text{Cut}_{s_1, \dots, s_l, m_1^2, \dots, m_k^2} F \cong \Theta \sum_{(x_1, \dots, x_l, y_1, \dots, y_k) \in \mathcal{A}^{k+l}} (-1)^l \left( \prod_{i=1}^l a_i(s_i, x_i) \prod_{j=1}^k a_j(m_j^2, y_j) \right) \delta_{x_1, \dots, x_l, y_1, \dots, y_k} F. \quad (1.107)$$

We recall that on the left-hand side the  $s_i$  and the  $m_j^2$  may be written in any order, and correspondingly permuted on the right-hand side, but we require that we act first with all the  $s_i$  and then with the  $m_j^2$ . It is not obvious that permutations of the sets  $\{s_i\}$  and  $\{m_j^2\}$  give equivalent results on the right-hand side, but this property follows from the commutativity of cuts. It implies nontrivial relations among coproduct entries.

## 1.9 Examples of Cut-Disc- $\delta$ relations

For all the examples below let us recall that the complex logarithm ‘jumps’ by  $2\pi i$  when crossing the negative real axis:

$$\lim_{\varepsilon \rightarrow 0^+} [\log(-z + i\varepsilon) - \log(-z - i\varepsilon)] = 2\pi i, \quad (1.108)$$

for  $z > 0$ .

Another important thing to note is that, since we are always considering triangles, a consistent choice for the imaginary parts is always to complex conjugate the second cut invariant in our calculations.

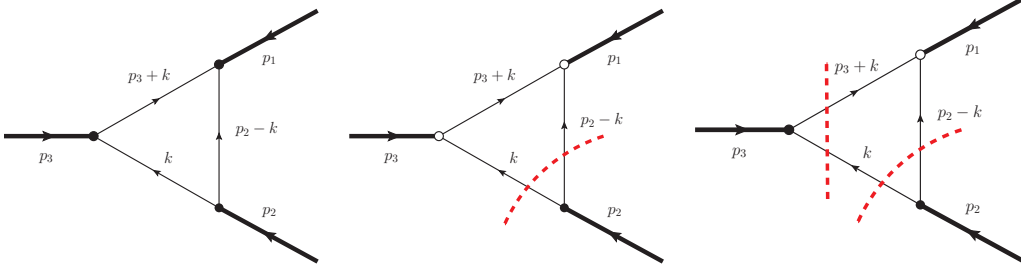


Figure 1.13: The triangle  $T(p_1^2, p_2^2, p_3^2)$ . Left: the uncut triangle with all black vertices. Middle: The  $p_2^2$  channel cut  $\text{Cut}_{p_2^2} T(p_1^2, p_2^2, p_3^2)$  that complex conjugates a part of the diagram. Right: The sequential  $p_2^2$  and  $p_3^3$  channel cuts  $\text{Cut}_{p_2^2, p_3^3} T(p_1^2, p_2^2, p_3^2)$ . Figure from ref [2].

### 1.9.1 Three-mass triangle with no internal masses

Let us start by an example from ref. [2] for a planar triangle integral with three external massive channels and no internal masses. This triangle (uncut) and the two cuts we will consider are depicted in figure 1.13.

The Feynman integral in  $D = 4$  dimensions will be a function of the dimensionless ratios:

$$F\left(\frac{p_2^2}{p_1^2}, \frac{p_3^2}{p_1^2}\right). \quad (1.109)$$

Let us define variables  $z, \bar{z}$  as in eq. (1.37) and suppose that we know that the symbol alphabet can be taken to be

$$\mathcal{A} = \{z, \bar{z}, 1 - z, 1 - \bar{z}\}. \quad (1.110)$$

$F$  is originally defined in the euclidean region where all  $p_i^2$  are negative. For real-valued  $z, \bar{z}$ , there are three distinct components of the euclidean region [1]. We choose the component  $\bar{z} < z < 0$ , which we call  $R_0$ . The relations work equally well starting from another component.

Let us take a first channel cut in the channel  $s_1 = p_2^2$ . Now  $F$  needs to be analytically continued to the region  $R_1$  of the first cut (see section 1.5.3) where  $p_2^2 > 0$  and  $p_2^2, p_3^3 < 0$ . In terms of variables  $z, \bar{z}$  this means  $R_1 = \{\bar{z} < 0, z < 1\}$  (see figure 1.5). For each symbol letter  $x_1$ , the logarithms  $\log x_1$  in the definition of  $a_1(p_2^2, x_1)$  are written with positive arguments in the region  $R_0$ . According to the usual Feynman rules (also reviewed in section 1.5.1), invariants have a positive imaginary part,  $p_2^2 + i\varepsilon$ , we can deduce the corresponding imaginary parts for  $z$  and

$\bar{z}$ . They are:  $z + i\varepsilon$ ,  $\bar{z} - i\varepsilon$ . Thus we get

$$a_1(p_2^2, z) = \text{Disc}_{p_2^2; R_1} \ln(-z - i0) = -2\pi i \quad (1.111)$$

$$a_1(p_2^2, \bar{z}) = \text{Disc}_{p_2^2; R_1} \ln(-\bar{z} + i0) = 0 \quad (1.112)$$

$$a_1(p_2^2, 1 - z) = \text{Disc}_{p_2^2; R_1} \ln(1 - z - i0) = 0 \quad (1.113)$$

$$a_1(p_2^2, 1 - \bar{z}) = \text{Disc}_{p_2^2; R_1} \ln(1 - \bar{z} + i0) = 0. \quad (1.114)$$

Here the discontinuities have been computed according to eq. (1.88). According to eqs. (1.94), (1.101) we then have the relations between the three types of discontinuities:

$$\text{Cut}_{p_2^2} F = -\text{Disc}_{p_2^2} F \cong (2\pi i) \Theta \delta_z F. \quad (1.115)$$

Let us now make a second cut in the channel  $s_2 = p_3^2$ . We analytically continue  $F$  and  $\text{Disc}_{s_1} F$  to the region  $R_2$  where  $p_2^2, p_3^2 > 0$  and  $p_1^2 < 0$ . In terms of the variables  $z$  and  $\bar{z}$  this means  $R_2 = \{\bar{z} < 0, z > 1\}$ . The  $a_1$  stay the same as before.

To evaluate the  $a_2(p_3^2, x_2)$ , we write the logarithms of the symbol letters  $x_2$  with positive arguments in the region  $R_1$ . At this point it is important to note that, consistently with our cutting rules, the imaginary part of  $p_3^2$  was conjugated in the process of applying the first cut: we have now  $p_3^2 - i\varepsilon$ . From this we deduce  $z - i\varepsilon$  and  $\bar{z} - i\varepsilon$  and therefore we have

$$a_2(p_3^2, z) = \text{Disc}_{p_3^2; R_2} \ln(z - i0) = 0 \quad (1.116)$$

$$a_2(p_3^2, \bar{z}) = \text{Disc}_{p_3^2; R_2} \ln(-\bar{z} + i0) = 0 \quad (1.117)$$

$$a_2(p_3^2, 1 - z) = \text{Disc}_{p_3^2; R_2} \ln(1 - z + i0) = 2\pi i \quad (1.118)$$

$$a_2(p_3^2, 1 - \bar{z}) = \text{Disc}_{p_3^2; R_2} \ln(1 - \bar{z} + i0) = 0. \quad (1.119)$$

The only surviving term is  $a_1(p_2^2, z)a_2(p_3^2, 1 - z) = -(2\pi i)^2$ , and the multiple cut and iterated discontinuity are then given by:

$$\text{Cut}_{p_2^2, p_3^2} F = \text{Disc}_{p_2^2, p_3^2} F \cong -(2\pi i)^2 \Theta \delta_{z, 1-z} F. \quad (1.120)$$

In ref. [2] the reader can find a complete list of the ‘Disc-Cut-Delta’ relations for all possible sequential cuts.

### 1.9.2 $T(p_1^2; m_{12}^2, m_{23}^2)$

First of all, for all the one-mass triangles in the examples below we define

$$T = \frac{i}{p_1^2} \mathcal{T}, \quad (1.121)$$

in the spirit of eq. (1.52). Then we note that the symbol alphabet and the first entries are

Alphabet:	$p_1^2, m_{12}^2, m_{23}^2, m_{12}^2 - p_1^2, m_{12}^2 - m_{23}^2, m_{12}^2 - m_{23}^2 - p_1^2$
First entries:	$m_{12}^2, m_{23}^2, m_{12}^2 - p_1^2$

### Single-cut relations

The single-cut relations are trivial because the invariants are letters of the alphabet, so we can just read off the  $\pm i0$ -prescription from the Feynman rules of section 1.5.1.

For the channel cut, we have, in the uncut region  $p_1^2 < 0$  and in the cut region  $p_1^2 > 0$ . Conventionally we take  $p_1^2 + i\varepsilon$ . Then we have to look at where the logarithm is on its branch cut, that is, when the argument of the logarithm is on the negative real axis. The logic is the same as before in section 1.9.1, except that now we are not changing variables. It follows that we pick up a factor of  $-2\pi i$ :

$$a_1(p_1^2, p_1^2) = -2\pi i . \quad (1.122)$$

For the mass cuts, in  $\text{Disc}=\delta$ , we have  $m_{ij}^2 > 0$  in the uncut region and  $m_{ij}^2 < 0$  in the cut region. By our conventions, we have  $m_{ij}^2 - i\varepsilon$ , so we pick up a factor of  $-2\pi i$ :

$$a_1(m_{12}^2, m_{12}^2) = -2\pi i \quad (1.123)$$

$$a_1(m_{23}^2, m_{23}^2) = -2\pi i . \quad (1.124)$$

For a channel cut, there is a sign change in the relation  $\text{Cut}=-\text{Disc}$ , see eq. (1.94). For a mass cut, we do not have a minus sign in the relation  $\text{Cut}=\text{Disc}$ , see eq. (1.95). Therefore the  $\text{Cut}=\delta$  relations read

$$\text{Cut}_{p_1^2} \mathcal{T} \cong (2\pi i) \Theta[\delta_{p_1^2}] \mathcal{T} \quad (1.125)$$

$$\text{Cut}_{m_{12}^2} \mathcal{T} \cong -(2\pi i) \Theta[\delta_{m_{12}^2}] \mathcal{T} \quad (1.126)$$

$$\text{Cut}_{m_{23}^2} \mathcal{T} \cong -(2\pi i) \Theta[\delta_{m_{23}^2}] \mathcal{T} . \quad (1.127)$$

### Double cut relations

**First cut  $p_1^2$ :** The only possible second cut is  $m_{23}^2$ , see the discussion in section 1.6. The first  $p_1^2$  cut complex conjugates a part of the diagram and therefore the correct imaginary part of the mass squared has a plus sign:  $m_{23}^2 + i0$ . The regions we are analyzing are:

$R_1$ and $R_2$	$p_1^2 > m_{12}^2 > 0$
$R_1$	$m_{23}^2 > 0$
$R_2$	$m_{23}^2 < 0$

The coefficients  $a_1$  stay the same as before. Our task is now to compute the  $a_2$ :

$$a_2(m_{23}^2, m_{23}^2) = 2\pi i \quad (1.128)$$

$$a_2(m_{23}^2, m_{23}^2 - m_{12}^2) = 2\pi i \theta(m_{12}^2 - m_{23}^2) \quad (1.129)$$

$$a_2(m_{23}^2, p_1^2 + m_{23}^2 - m_{12}^2) = 2\pi i \theta(m_{12}^2 - m_{23}^2 - p_1^2) . \quad (1.130)$$

We now include the factor  $(-1)^1$  for the Cut=Disc relation for the one external channel cut and thus get

$$\begin{aligned} \text{Cut}_{p_1^2, m_{23}^2} \mathcal{T} = & - (2\pi i)^2 (-1)^1 [\delta_{m_{12}^2 - p_1^2, m_{23}^2} + \theta(m_{12}^2 - m_{23}^2) \delta_{m_{12}^2 - p_1^2, m_{23}^2 - m_{12}^2} \\ & + \theta(m_{12}^2 - m_{23}^2 - p_1^2) \delta_{m_{12}^2 - p_1^2, m_{12}^2 - m_{23}^2 - p_1^2}] \mathcal{T} . \end{aligned} \quad (1.131)$$

We now need the  $\Delta_{1,1}$  coproduct i.e. the symbol of this triangle to read off the correct  $\delta_{m_{12}^2 - p_1^2, r}$ . The symbol of this triangle is computed in ref. [58] and it reads

$$\begin{aligned} \mathcal{S} [\mathcal{T}(p_1^2; m_{12}^2, m_{23}^2)] = & m_{12}^2 \otimes \left( \frac{m_{12}^2 - m_{23}^2}{m_{23}^2} \right) + m_{23}^2 \otimes \left( 1 - \frac{p_1^2}{m_{12}^2 - m_{23}^2} \right) \\ & - (m_{12}^2 - p_1^2) \otimes \left( 1 - \frac{m_{12}^2 - p_1^2}{m_{23}^2} \right) . \end{aligned} \quad (1.132)$$

Now, to read off the  $\delta_{m_{12}^2 - p_1^2, r}$  we need to look at the term of the symbol that has  $m_{12}^2 - p_1^2$  as its first entry. This is the last term. Opening up this last term we see that

$$-(m_{12}^2 - p_1^2) \otimes \left( 1 - \frac{m_{12}^2 - p_1^2}{m_{23}^2} \right) = (m_{12}^2 - p_1^2) \otimes (-m_{23}^2) - (m_{12}^2 - p_1^2) \otimes (m_{12}^2 - m_{23}^2 - p_1^2) , \quad (1.133)$$

i.e.

$$\delta_{m_{12}^2 - p_1^2, m_{23}^2} \mathcal{T} = 1 \quad (1.134)$$

$$\delta_{m_{12}^2 - p_1^2, m_{23}^2 - m_{12}^2} \mathcal{T} = 0 \quad (1.135)$$

$$\delta_{m_{12}^2 - p_1^2, m_{12}^2 - m_{23}^2 - p_1^2} \mathcal{T} = -1 , \quad (1.136)$$

so that

$$\begin{aligned} \text{Cut}_{p_1^2, m_{23}^2} \mathcal{T} = & (2\pi i)^2 [1 - \theta(m_{12}^2 - m_{23}^2 - p_1^2)] \\ = & (2\pi i)^2 \theta(m_{23}^2 + p_1^2 - m_{12}^2) . \end{aligned} \quad (1.137)$$

This confirms the cut result in ref. [58].

**First cut  $m_{12}^2$ :** The only possible second cut is the one in the other internal mass  $m_{23}^2$ , which has an imaginary part  $m_{23}^2 - i0$ , since no complex conjugation of the diagram was done for the first cut, which was also a mass cut. The cut regions are:

$R_1$	$p_1^2 < 0, m_{12}^2 < 0, m_{23}^2 > 0$
$R_2$	$p_1^2 < 0, m_{12}^2 < 0, m_{23}^2 < 0$

The coefficients  $a_2$  are now

$$a_2(m_{23}^2 - i0, m_{23}^2) = -2\pi i, \quad (1.138)$$

$$a_2(m_{23}^2 - i0, m_{23}^2 - m_{12}^2) = -2\pi i\theta(m_{12}^2 - m_{23}^2), \quad (1.139)$$

$$a_2(m_{23}^2 - i0, -m_{12}^2 + p_1^2 + m_{23}^2) = -2\pi i\theta(m_{12}^2 - m_{23}^2 - p_1^2). \quad (1.140)$$

The double cut then reads, remembering that in this case  $\text{Cut}_{m_{23}^2, m_{12}^2} = \text{Disc}_{m_{23}^2, m_{12}^2}$

$$\begin{aligned} \text{Cut}_{m_{12}^2, m_{23}^2} \mathcal{T} = & (2\pi i)^2 \left[ \delta_{m_{12}^2, m_{23}^2} + \theta(m_{12}^2 - m_{23}^2) \delta_{m_{12}^2, m_{23}^2 - m_{12}^2} \right. \\ & \left. + \theta(m_{12}^2 - m_{23}^2 - p_1^2) \delta_{m_{12}^2, p_1^2 + m_{23}^2 - m_{12}^2} \right] \mathcal{T}. \end{aligned} \quad (1.141)$$

Looking at the symbol in eq. (1.132), we can read off the coefficients  $\delta_{m_{12}^2, r}$ :

$$\delta_{m_{12}^2, m_{23}^2} \mathcal{T} = -1 \quad (1.142)$$

$$\delta_{m_{12}^2, m_{23}^2 - m_{12}^2} \mathcal{T} = 1 \quad (1.143)$$

$$\delta_{m_{12}^2, p_1^2 + m_{23}^2 - m_{12}^2} \mathcal{T} = 0, \quad (1.144)$$

and so we finally have

$$\begin{aligned} \text{Cut}_{m_{12}^2, m_{23}^2} \mathcal{T} = & (2\pi i)^2 \left[ -1 + \theta(m_{12}^2 - m_{23}^2) \right] \\ = & (2\pi i)^2 \theta(m_{23}^2 - m_{12}^2). \end{aligned} \quad (1.145)$$

Let us now check that we get the same answer when first taking the  $m_{23}^2$  cut and then the  $m_{12}^2$  cut.

**First cut  $m_{23}^2$ :**

**Second cut  $m_{12}^2$ :** The cut regions are

$R_1$	$p_1^2 < 0, m_{12}^2 > 0, m_{23}^2 < 0$
$R_2$	$p_1^2 < 0, m_{12}^2 < 0, m_{23}^2 < 0$

The coefficients  $a_2$  are computed from  $m_{12}^2 - i0$ :

$$a_2(m_{12}^2, m_{12}^2) = -2\pi i \quad (1.146)$$

$$a_2(m_{12}^2, m_{12}^2 - p_1^2) = -2\pi i \theta(p_1^2 - m_{12}^2) \quad (1.147)$$

$$a_2(m_{12}^2, m_{12}^2 - m_{23}^2 - p_1^2) = -2\pi i \theta(p_1^2 + m_{23}^2 - m_{12}^2) \quad (1.148)$$

$$a_2(m_{12}^2, m_{12}^2 - m_{23}^2) = -2\pi i \theta(m_{23}^2 - m_{12}^2) . \quad (1.149)$$

We now have

$$\begin{aligned} \text{Cut}_{m_{23}^2, m_{12}^2} \mathcal{T} = & (2\pi i)^2 [\delta_{m_{23}^2, m_{12}^2} + \theta(p_1^2 - m_{12}^2) \delta_{m_{23}^2, m_{12}^2 - p_1^2} \\ & + \theta(p_1^2 + m_{23}^2 - m_{12}^2) \delta_{m_{23}^2, m_{12}^2 - m_{23}^2 - p_1^2} + \theta(m_{23}^2 - m_{12}^2) \delta_{m_{23}^2, m_{12}^2 - m_{23}^2}] \mathcal{T} . \end{aligned} \quad (1.150)$$

Then we substitute

$$\delta_{m_{23}^2, m_{12}^2} \mathcal{T} = 0 \quad (1.151)$$

$$\delta_{m_{23}^2, m_{12}^2 - p_1^2} \mathcal{T} = 0 \quad (1.152)$$

$$\delta_{m_{23}^2, m_{12}^2 - m_{23}^2 - p_1^2} \mathcal{T} = 1 \quad (1.153)$$

$$\delta_{m_{23}^2, m_{12}^2 - m_{23}^2} \mathcal{T} = -1 , \quad (1.154)$$

which gives

$$\begin{aligned} \text{Cut}_{m_{23}^2, m_{12}^2} \mathcal{T} = & (2\pi i)^2 [\theta(p_1^2 + m_{23}^2 - m_{12}^2) - \theta(m_{23}^2 - m_{12}^2)] \\ = & (2\pi i)^2 \theta(-p_1^2 - m_{23}^2 + m_{12}^2) \theta(m_{23}^2 - m_{12}^2) . \end{aligned} \quad (1.155)$$

The two results (1.145) and (1.155) agree when we note that being in the support of  $\theta(m_{23}^2 - m_{12}^2)$  as well as being in the cut region together imply being in the support of  $\theta(-p_1^2 - m_{23}^2 + m_{12}^2)$ .

**Second cut  $p_1^2$ :** Because we always choose to do the cuts in external channels before cutting in internal masses, we will not proceed with this double cut. We require this ordering of the cuts for the definiteness of the sign in the Cut-Disc-Delta relations.

### 1.9.3 $T(p_1^2; m_{12}^2, m_{13}^2)$

In this example we wish to illustrate how the Disc=Cut= $\delta$  relations generalize when we use variables such as those defined in eq. (1.41). In particular, we wish to shed

some light on the  $i0$ -prescription of the symbol letters (see section 1.8.2) as well as to show how the double cut on the internal masses vanishes, in agreement with the discussion in section 1.8.1.

Expressions for the integral and its cuts can be found in the appendix C. We give here the expression for the symbol at order  $\epsilon^0$  for completeness, and to facilitate the reading off of the  $\delta$ 's for the Cut= $\delta$  relations:

$$\mathcal{S}[\mathcal{T}(p_1^2; m_{12}^2, m_{13}^2)] = \left( \frac{w_1}{1-w_1} \right) \otimes \left( \frac{\bar{w}_1}{1-\bar{w}_1} \right) + \left( \frac{\bar{w}_1}{1-\bar{w}_1} \right) \otimes \left( \frac{w_1}{1-w_1} \right) . \quad (1.156)$$

From this we see that there are four letters in the symbol alphabet.

The euclidean region is

$$R_0 \mid m_{12}^2 > 0, \quad m_{13}^2 > 0, \quad p_1^2 < \left( \sqrt{m_{12}^2} + \sqrt{m_{13}^2} \right)^2$$

To simplify our discussion, we will restrict the euclidean region to the subregion  $R_{0*}$ , defined by

$$R_{0*} \mid m_{12}^2 > 0, \quad m_{13}^2 > 0, \quad p_1^2 < 0 \quad \Rightarrow \quad \bar{w}_1 < 0, \quad w_1 > 1$$

### Single cuts

**Cut  $p_1^2$ :** In the cut region we have

$$R_1^{p_1^2} \mid m_{12}^2 > 0, \quad m_{13}^2 > 0, \quad p_1^2 > \left( \sqrt{m_{12}^2} + \sqrt{m_{13}^2} \right)^2 \quad \Rightarrow \quad 0 < \bar{w}_1 < w_1 < 1$$

The  $p_1^2 + i0$ -prescription implies  $w_1 + i0$  and  $\bar{w}_1 - i0$  in  $R_1^{p_1^2}$ . Out of the four letters in the alphabet only  $\bar{w}_1$  and  $1 - w_1$  change sign between  $R_{0*}$  and  $R_1^{p_1^2}$ :

$$a_1(p_1^2, w_1) = 0 \quad (1.157)$$

$$a_1(p_1^2, \bar{w}_1) = 2\pi i \quad (1.158)$$

$$a_1(p_1^2, 1 - w_1) = 2\pi i \quad (1.159)$$

$$a_1(p_1^2, 1 - \bar{w}_1) = 0 . \quad (1.160)$$

Including the minus sign that we have in the relation (1.94) for channel cuts, we have

$$\text{Cut}_{p_1^2} \mathcal{T} \cong -(2\pi i) \Theta [\delta_{\bar{w}_1} + \delta_{1-w_1}] \mathcal{T} , \quad (1.161)$$

where  $\Theta$  is inserted to keep track of the kinematic region and

$$\delta_{\bar{w}_1} \mathcal{T} = \log \frac{w_1}{1 - w_1} \quad (1.162)$$

$$\delta_{1-w_1} \mathcal{T} = -\log \frac{\bar{w}_1}{1 - \bar{w}_1} . \quad (1.163)$$

Therefore

$$\text{Cut}_{p_1^2} \mathcal{T} = -2\pi i \left( \log \frac{w_1}{1 - w_1} - \log \frac{\bar{w}_1}{1 - \bar{w}_1} \right) , \quad (1.164)$$

which agrees with the cut result in appendix C.

**Cut  $m_{12}^2$ :** The cut region is

$$\boxed{R_1^{m_{12}^2} \mid m_{12}^2 < 0, \quad m_{13}^2 > 0, \quad p_1^2 < 0 \quad \Rightarrow \quad 0 < \bar{w}_1 < 1 < w_1}$$

Imaginary parts are inherited from  $m_{12}^2 - i0$  in  $R_1^{m_{12}^2}$ :  $w_1 + i0$  and  $\bar{w}_1 + i0$ . Of the four letters, only  $\bar{w}_1$  changes sign:

$$a_1(m_{12}^2, w_1) = 0 \quad (1.165)$$

$$a_1(m_{12}^2, \bar{w}_1) = -2\pi i \quad (1.166)$$

$$a_1(m_{12}^2, 1 - w_1) = 0 \quad (1.167)$$

$$a_1(m_{12}^2, 1 - \bar{w}_1) = 0 . \quad (1.168)$$

This implies that

$$\text{Cut}_{12}^2 \mathcal{T} \cong -(2\pi i) \Theta [\delta_{\bar{w}_1}] \mathcal{T} \quad (1.169)$$

$$= -2\pi i \log \frac{w_1}{1 - w_1} , \quad (1.170)$$

which confirms the result of the cut integral, see appendix C.

**Cut  $m_{13}^2$ :** The cut region is

$$\boxed{R_1^{m_{13}^2} \mid m_{12}^2 > 0, \quad m_{13}^2 < 0, \quad p_1^2 < 0 \quad \Rightarrow \quad \bar{w}_1 < 0 < w_1 < 1}$$

Imaginary parts are inherited from  $m_{13}^2 - i0$  in  $R_1^{m_{13}^2}$ :  $w_1 - i0$  and  $\bar{w}_1 - i0$ . Of the four letters, only  $1 - w_1$  changes sign:

$$a_1(m_{13}^2, w_1) = 0 \quad (1.171)$$

$$a_1(m_{13}^2, \bar{w}_1) = 0 \quad (1.172)$$

$$a_1(m_{13}^2, 1 - w_1) = -2\pi i \quad (1.173)$$

$$a_1(m_{13}^2, 1 - \bar{w}_1) = 0 , \quad (1.174)$$

giving

$$\text{Cut}_{13}^2 \mathcal{T} \cong -(2\pi i) \Theta[\delta_{1-w_1}] \mathcal{T} \quad (1.175)$$

$$= 2\pi i \log \frac{\bar{w}_1}{1 - \bar{w}_1}, \quad (1.176)$$

which confirms the result of the cut integral, see appendix C.

### Double cuts

The cuts in  $p_1^2$  and in internal masses are not allowed, so we only have the double cut in the two internal masses to consider. Since the two internal masses  $m_{12}^2$  and  $m_{13}^2$  are connected to the same massive external leg  $p_1^2$ , the double cut should vanish according to the discussion in section 1.8.1. We will now check this claim.

**First cut  $m_{12}^2$ , second cut  $m_{13}^2$ :** The cut region is

$$R_2^{m_{12}^2, m_{13}^2} \mid m_{12}^2 < 0, \quad m_{13}^2 < 0, \quad p_1^2 < \left( \sqrt{m_{12}^2} + \sqrt{m_{13}^2} \right)^2$$

In terms of the variables  $w_1$  and  $\bar{w}_1$ , this region is split into two disconnected subregions  $R_{2a}^{m_{12}^2, m_{13}^2}$  and  $R_{2b}^{m_{12}^2, m_{13}^2}$ ,

$R_{2a}^{m_{12}^2, m_{13}^2}$	$\bar{w}_1 < w_1 < 0$
$R_{2b}^{m_{12}^2, m_{13}^2}$	$1 < \bar{w}_1 < w_1$ .

In the following, let us only focus on the nonzero coefficients.

In the subregion  $R_{2a}^{m_{12}^2, m_{13}^2}$ ,  $w_1$  and  $1 - w_1$  change sign. From  $m_{13}^2 - i0$  we get  $w_1 + i0$  and hence

$$a_2(m_{13}^2, w_1) = 2\pi i \quad (1.177)$$

$$a_2(m_{13}^2, 1 - w_1) = 2\pi i. \quad (1.178)$$

It follows that

$$\begin{aligned} \text{Cut}_{m_{12}^2, m_{13}^2} \mathcal{T} &\cong (2\pi i)^2 \Theta[\delta_{\bar{w}_1, w_1} + \delta_{\bar{w}_1, 1-w_1}] \mathcal{T} \\ &= (2\pi i)^2 \Theta[1 - 1] \mathcal{T} \\ &= 0. \end{aligned} \quad (1.179)$$

So the double cut is zero.

**First cut  $m_{13}^2$ , second cut  $m_{12}^2$ :** The cut regions are the same as in the previous example.

In  $R_{2a}^{m_{12}^2, m_{13}^2}$  none of the letters change sign so we trivially have

$$\text{Cut}_{m_{13}^2, m_{12}^2} \mathcal{T} = 0 . \quad (1.180)$$

In the subregion  $R_{2b}^{m_{12}^2, m_{13}^2}$ , the mass squared has a negative imaginary part, as usual:  $m_{12}^2 - i0$ , which implies  $\bar{w}_1 - i0$ . Both  $\bar{w}_1$  and  $1 - \bar{w}_1$  change sign:

$$a_2(m_{12}^2, \bar{w}_1) = 2\pi i \quad (1.181)$$

$$a_2(m_{12}^2, 1 - \bar{w}_1) = 2\pi i \quad (1.182)$$

giving

$$\begin{aligned} \text{Cut}_{m_{13}^2, m_{12}^2} T &\cong -(2\pi i)^2 \Theta [\delta_{1-w_1, \bar{w}_1} + \delta_{1-w_1, 1-\bar{w}_1}] \mathcal{T} \\ &= -(2\pi i)^2 \Theta [-1 + 1] \mathcal{T} \\ &= 0 . \end{aligned} \quad (1.183)$$

We verify that the two mass cuts commute.

## 1.10 Reconstruction

In this chapter we have reviewed and introduced computational tools to evaluate cut integrals. We have also shown how to relate the cut integrals to the discontinuities of an integral and its coproduct. The first paper where these so-called  $\text{Cut}=\text{Disc}=\delta$  relations were written was ref. [2] for massless propagators, and these relations were in [58] extended to triangle diagrams with massive propagators. In the following we present a way to use the knowledge of cut Feynman integrals to *reconstruct* the symbol of the integral, and then we briefly discuss the integration of this symbol, to recover the whole integral.

We will not treat the reconstruction of diagrams with massless internal propagators here, but refer the reader to refs. [2, 52].

The traditional way of evaluating a Feynman integral starting from its cuts is the method of *dispersion relations*. These give the Feynman integral as an integral of its discontinuity across a certain branch cut. A review of the subject is given for example in [2]. We will apply a more modern way of evaluating Feynman integrals starting from their cuts. This will be done in the language of the *Hopf algebra of Feynman integrals*. The process starts by evaluating a single cut in an external channel. We

then proceed to reconstruct the symbol of the integral, starting from this one cut. With modern software, the symbol, at least for the triangle diagrams considered in this thesis, can be integrated without much trouble, to recover the complete integral. We can thus get the integral without having to go through the — possibly strenuous — process of doing the integration by brute force.

### 1.10.1 Reconstruction of massive triangle integrals

In the previous section we saw how the information about the discontinuity of an integral across a branch cut and the location of that particular branch cut is sufficient to completely determine the value of the integral. With the tools reviewed and developed in the preceding sections, and in particular relying on the relations between cuts, discontinuities and the coproduct entries, we can now proceed with another kind of reconstruction process. We do this by remembering that any one of the  $\Delta_{1,n-1}$  entries of the coproduct really encode the same information as the dispersive representation. Therefore we anticipate that this coproduct structure — or the symbol — can be used to recover the whole information about an integral as well.

When working with the symbol we have to keep in mind that we lose some information. Namely, we lose knowledge of terms proportional to  $\pi$  and zeta-functions. At the end of this section we will discuss how to overcome this difficulty, and indeed, in all of our examples, we do overcome it.

#### Construction of an ansatz for the symbol

To construct an ansatz for the symbol of a given diagram, we start by noting that if the diagram is a function of  $n$  invariants, then the pure function is a function of  $n - 1$  dimensionless variables. We always choose to normalize by an external invariant. The procedure starts by the listing of possible first entries. These are fixed by the first entry condition, see section 1.7. Then we fix the second entries. This task is more difficult than the first one, but can be done starting from a single unitarity cut in an external channel. Some letters of the alphabet do not necessarily appear in the cut, and so we need some rules for finding them. Empirically, we have found such rules and we list them below.

- All letters of the symbol alphabet of the channel cut taken as the known starting point.
- Differences of internal masses, or their equivalents in terms of  $w_1$  and  $\bar{w}_1$ ; see eq. (1.40).

- For triangles with two external invariants, ratios of external invariants. In our examples, this is just  $p_2^2/p_3^2$ . For the examples with three external massive channels where we must use the variables  $z$  and  $\bar{z}$  (see (1.37)), this condition is replaced by the presence of the letters  $z, \bar{z}, (1-z)$  and  $(1-\bar{z})$ .

The above terms are added as cofactors of the first entries. Each term is multiplied by an unknown numerical coefficient. For the terms corresponding to the external channel cut, the unknown coefficients are of course fixed by the cut. For the additional first entries, they are fixed by some additional considerations, according to the following.

### Constraining the coefficients of the ansatz

We fix all coefficients according to the following steps:

1. We discard integrable terms of the form  $x \otimes x$ , as they are not needed in order to construct a minimal integrable symbol.
2. Since the first-entry condition involves the original Mandelstam invariants, the dimensionless variables appearing in the symbol should be expanded when imposing this condition. Notably, we sometimes normalize the invariants by a variable  $p_i^2$  with a nonzero mass threshold, so that  $p_i^2$  should not ultimately appear as a first entry by itself, although it shows up superficially in the expansion of the dimensionless variables. Thus, all of the second-entry cofactors of this  $p_i^2$  should combine to give zero.
3. We use the integrability condition, eq. (1.32), to fix the remaining parameters.

These three rules are already highly constraining and indeed sufficient for most examples. If they are not, in particular in cases where we use the  $z, \bar{z}, w_1$ , and  $\bar{w}_1$  variables, they can be complemented by the following:

4. Impose antisymmetry under  $z \leftrightarrow \bar{z}$  and symmetry under  $w_1 \leftrightarrow \bar{w}_1$ . Indeed, the Feynman integrals are functions of the invariants only and must thus be symmetric under these transformations. When  $z$  and  $\bar{z}$  are necessary, there is an antisymmetric rational pre factor, and so the pure function must be antisymmetric as well.
5. If there is a symmetry under the exchange of the legs with momenta  $p_2$  and  $p_3$ , impose symmetry under the simultaneous transformations  $z \rightarrow 1-\bar{z}, \bar{z} \rightarrow 1-z, w_1 \rightarrow 1-\bar{w}_1, \bar{w}_1 \rightarrow 1-w_1$ .

### 1.10.2 Examples of the reconstruction process

$T(p_1^2; m_{12}^2, m_{13}^2)$

This triangle has a symmetry under the exchange of legs 2 and 3, a constraint that we will use later.

First of all, let us consider the  $p_1^2$  cut of this triangle, at order  $\epsilon^0$ ,

$$\text{Cut}_{p_1^2} T(p_1^2; m_{12}^2, m_{13}^2) = \frac{2\pi}{p_1^2} \left( \log \left( \frac{w_1}{1-w_1} \right) - \log \left( \frac{\bar{w}_1}{1-\bar{w}_1} \right) \right), \quad (1.184)$$

and write down a general ansatz for the symbol  $\mathcal{S}$  starting from this one unitarity cut:

$$\begin{aligned} \mathcal{S} = & w(1-\bar{w}) \otimes [w - (1-w) - \bar{w} + (1-\bar{w})] \\ & + w\bar{w} \otimes [a_1 w + a_2 \bar{w} + a_3(1-w) + a_4(1-\bar{w}) + a_5(w\bar{w} - (1-w)(1-\bar{w}))] \\ & + (1-w)(1-\bar{w}) \otimes [b_1 w + b_2 \bar{w} + b_3(1-w) + b_4(1-\bar{w}) + b_5(w\bar{w} - (1-w)(1-\bar{w}))] \end{aligned} \quad (1.185)$$

Here we have used an abbreviated notation for the second entries. The letters  $a_i$  and  $b_i$  stand for the integer numbers that are the coefficients of the second entries  $\{w, \bar{w}, (1-w), (1-\bar{w}), (w\bar{w} - (1-w)(1-\bar{w}))\}$ . The second entries always come with a logarithm which we have not written explicitly here. So what we mean by an entry like  $a_1 w$  is in fact  $a_1 \log w$ .

All of the variables used are normalized by  $p_1^2$ . Since  $p_1^2$  has a mass threshold, it should always appear with its threshold, and never alone as a first entry. It follows that the second-entry cofactors of the normalization variable should combine to give zero (see discussion in section 1.10). From this we get as many relations for the coefficients  $a_i, b_i$  as there are second entries:

$$\begin{cases} 1 + a_1 + b_1 = 0 \\ -1 + a_2 + b_2 = 0 \\ -1 + a_3 + b_3 = 0 \\ 1 + a_4 + b_4 = 0 \\ a_5 + b_5 = 0 \end{cases} . \quad (1.186)$$

Solving the  $b_i$ 's in terms of the  $a_i$ 's, we can substitute these into eq. (1.185).

The first entries are also logarithms, so we may split them up using the basic rule  $\log(xy) = \log x + \log y$ . Doing so, and the above substitutions, the symbol of

eq. (1.185) reads

$$\begin{aligned}
\mathcal{S} = & w \otimes [(1 + a_1)w + (a_2 - 1)\bar{w} + (a_3 - 1)(1 - w) \\
& + (1 + a_4)(1 - \bar{w}) + a_5(w\bar{w} - (1 - w)(1 - \bar{w}))] \\
& + \bar{w} \otimes [a_1w + a_2\bar{w} + a_3(1 - w) \\
& + a_4(1 - \bar{w}) + a_5(w\bar{w} - (1 - w)(1 - \bar{w}))] \\
& + (1 - w) \otimes [(-1 - a_1)w + (1 - a_2)\bar{w} + (1 - a_3)(1 - w) \\
& + (-1 - a_4)(1 - \bar{w}) - a_5(w\bar{w} - (1 - w)(1 - \bar{w}))] \\
& + (1 - \bar{w}) \otimes [-a_1w + (-a_2)\bar{w} + (-a_3)(1 - w) \\
& + (-a_4)(1 - \bar{w}) + (-a_5)(w\bar{w} - (1 - w)(1 - \bar{w}))] . \tag{1.187}
\end{aligned}$$

Next we demand that there be no integrable terms of the form  $x \otimes x$ . Hence

$$a_1 = -1 , \quad a_2 = 0 , \quad a_3 = 1 , \quad a_4 = 0 . \tag{1.188}$$

Lastly, we use the symmetry  $2 \leftrightarrow 3$ . Specifically, this means that we have the transformations

$$w \leftrightarrow (1 - \bar{w}) \quad \& \quad \bar{w} \leftrightarrow (1 - w) . \tag{1.189}$$

Performing these substitutions in eq. (1.185) or equivalently in eq. (1.187) we see that  $a_5 = -a_5$  meaning that

$$a_5 = 0 . \tag{1.190}$$

In this way, we get an expression for the symbol:

$$\begin{aligned}
\mathcal{S} = & w \otimes [-\bar{w} + (1 - \bar{w})] \\
& + \bar{w} \otimes [-w + (1 - w)] \\
& + (1 - w) \otimes [\bar{w} - (1 - \bar{w})] \\
& + (1 - \bar{w}) \otimes [w - (1 - w)] , \tag{1.191}
\end{aligned}$$

which is exactly the same as in eq. (B.19) of appendix C.

**$T(p_1^2; m_{12}^2, m_{13}^2, m_{23}^2)$**

Let us start from the  $p_1^2$  cut:

$$\text{Cut}_{p_1^2} T(p_1^2; m_{12}^2, m_{13}^2, m_{23}^2) \frac{2\pi}{p_1^2} \log \left( \frac{\mu_{23} + w_1(1 - \bar{w}_1)}{\mu_{23} + \bar{w}_1(1 - w_1)} \right) + \mathcal{O}(\epsilon) , \tag{1.192}$$

from which we get the two letters  $\{\mu_{23} + w_1(1 - \bar{w}_1), \mu_{23} + \bar{w}_1(1 - w_1)\}$ . We know from the discussion in section 1.7 that the first entries are

$$\{w_1(1 - \bar{w}_1), w_1\bar{w}_1, (1 - w_1)(1 - \bar{w}_1), \mu_{23}\} . \quad (1.193)$$

From section 1.10 we know that differences of masses squared enter the symbol alphabet, so we add three letters  $\{\mu_{23} - w_1\bar{w}_1, \mu_{23} - (1 - w_1)(1 - \bar{w}_1), w_1\bar{w}_1 - (1 - w_1)(1 - \bar{w}_1)\}$  to the ones that we got from the cut. In this manner we have now listed all of the second entries, which we will denote by  $t_i$  in what follows:

$$\begin{aligned} & \{\mu_{23} + w_1(1 - \bar{w}_1), \mu_{23} + \bar{w}_1(1 - w_1), \\ & \mu_{23} - w_1\bar{w}_1, \mu_{23} - (1 - w_1)(1 - \bar{w}_1), w_1\bar{w}_1 - (1 - w_1)(1 - \bar{w}_1)\} \\ & \equiv \{t_1, t_2, t_3, t_4, t_5\} . \end{aligned} \quad (1.194)$$

Based on the knowledge of the  $p_1^2$  cut, the first entry condition and the second entries above, we can construct an ansatz for the symbol:

$$\begin{aligned} \mathcal{S} &= w_1(1 - \bar{w}_1) \otimes [-t_1 + t_2] \\ &+ w_1\bar{w}_1 \otimes [a_1t_1 + a_2t_2 + a_3t_3 + a_4t_4 + a_5t_5] \\ &+ (1 - w_1)(1 - \bar{w}_1) \otimes [b_1t_1 + b_2t_2 + b_3t_3 + b_4t_4 + b_5t_5] \\ &+ \mu_{23} \otimes [c_1t_1 + c_2t_2 + c_3t_3 + c_4t_4 + c_5t_5] . \end{aligned} \quad (1.195)$$

Let us ‘open up’ the first entries of this symbol into a form that is easier to manipulate:

$$\begin{aligned} \mathcal{S} &= w_1 \otimes [(a_1 - 1)t_1 + (a_2 + 1)t_2 + a_3t_3 + a_4t_4 + a_5t_5] \\ &+ \bar{w}_1 \otimes [a_1t_1 + a_2t_2 + a_3t_3 + a_4t_4 + a_5t_5] \\ &+ (1 - w_1) \otimes [b_1t_1 + b_2t_2 + b_3t_3 + b_4t_4 + b_5t_5] \\ &+ (1 - \bar{w}_1) \otimes [(b_1 - 1)t_1 + (b_2 + 1)t_2 + b_3t_3 + b_4t_4 + b_5t_5] \\ &+ \mu_{23} \otimes [c_1t_1 + c_2t_2 + c_3t_3 + c_4t_4 + c_5t_5] . \end{aligned} \quad (1.196)$$

As in the above example and as discussed in section 1.10, there is no branch cut at  $p_1^2 = 0$ . This gives us one equation for every  $t_i$ , and therefore we can eliminate each of the parameters  $c_i$  and rewrite them in terms of  $a_i$  and  $b_i$ :

$$\begin{cases} -1 + a_1 + b_1 + c_1 = 0 \\ 1 + a_2 + b_2 + c_2 = 0 \\ a_i + b_i + c_i = 0, \quad i = 3, 4, 5 \end{cases} . \quad (1.197)$$

Next we use the  $w_1 \leftrightarrow \bar{w}_1$  symmetry. Under this transformation  $t_1$  maps to  $t_2$  and vice versa. The relations we get by comparing the transformed symbol to the original one, eq. (1.196) are

$$\begin{aligned} a_2 &= a_1 - 1 , \\ b_2 &= b_1 - 1 . \end{aligned} \tag{1.198}$$

Next, let us use the  $2 \leftrightarrow 3$  symmetry, under which  $t_3 \leftrightarrow t_4$ . This gives us more constraints:

$$\begin{aligned} a_1 &= b_1 , \\ a_2 &= b_2 , \\ a_3 &= b_4 , \\ a_4 &= b_3 , \\ a_5 &= b_5 . \end{aligned} \tag{1.199}$$

Integrability, eq. (1.32), fixes the remaining coefficients.

Finally, the symbol reads:

$$\mathcal{S} = w_1 \otimes \frac{t_3}{t_1} + \bar{w}_1 \otimes \frac{t_3}{t_2} + (1 - w_1) \otimes \frac{t_4}{t_2} + (1 - \bar{w}_1) \otimes \frac{t_4}{t_1} + \mu_{23} \otimes \frac{t_1 t_2}{t_3 t_4} + \mathcal{O}(\epsilon) . \tag{1.200}$$

### 1.10.3 Reconstructing the full function from the symbol

We now explain how we integrate the symbol to get the full function. Although integrating a symbol is in general an unsolved problem, it is a simple problem for weight two functions where a complete basis is even known to exist in terms of classical polylogarithms, see e.g. [61]. Once we have found a function that matches our symbol, all that remains to be done is fixing terms that are invisible to the symbol, in our case weight one functions multiplied by  $\pi$  and a term proportional to  $\zeta_2$ .

Powers of  $\pi$  are typically generated by analytic continuation and appear multiplied by  $i$ . Working in the Euclidean region where the function is real and away from any branch cut avoids this problem.

To fix the term proportional to  $\zeta_2$ , we can use two strategies. The first, which always works, is to evaluate the integrated symbol numerically at a single point and compare it to a numerically integrated Feynman parametrization of the diagram. The difference must be a rational number multiplied by  $\zeta_2$ , which completely determines

our function. Alternatively, when possible, we can use the symmetries of the diagram to check if a term proportional to  $\zeta_2$  is allowed.

As examples, consider  $T(p_1^2; m_{23}^2)$  and  $T(p_1^2, p_2^2, p_3^2; m_{12}^2)$ . In the first case, there is no symmetry consideration to fix a term proportional to  $\zeta_2$ , and we must thus rely on numerical comparisons. In the second example, there is a rational pre factor antisymmetric under  $z \leftrightarrow \bar{z}$ , and thus the pure function must be antisymmetric under this transformation (the full function must be symmetric). This forbids the existence of a term proportional to  $\zeta_2$ .

## 1.11 Conclusions

In this chapter we have studied the analytic structure of one-loop three-point Feynman diagrams with different configurations of internal and external masses. Our interest lies mainly with integrals having massive propagators, but we have also briefly considered the one-loop triangle with massless propagators in some examples, where this has led to some simplifications and we felt that it illustrated our point the best. The case of the one-loop triangle with massless internal propagators has been studied in ref. [2], where, for the first time, relations between unitarity cuts, discontinuities across branch cuts and the coproduct structure of the Hopf algebra of Feynman integrals was presented. The studies that have carried the main focus of this chapter have been generalizations of this first paper, and the full results are given in [58] as well as in appendix C. The work of the author has principally been the study of the reconstruction of symbols and full functions from the unitarity cuts of the integrals.

The main conclusions of this chapter are the following. Firstly, we have seen that the *first entry condition* has to be generalized when we start to consider diagrams with massive internal propagators. In the absence of internal masses, as studied in [2], the first entries are just logarithms of the Mandelstam invariants of the diagram. In the presence of internal masses we have to take into account the possible mass thresholds of the invariants, and the first entries are now precisely the invariants minus their respective thresholds.

Secondly, we have generalized the cutting rules of ref. [2] to cases where the propagators can be massive. The observations of [2] still apply for discontinuities in external channels. However, the presence of internal masses leads to a new type of cut, namely the *single-propagator cut*. We have shown how to compute these cuts and clarified their meaning in terms of the symbol of the diagram. Furthermore, as already observed in [2], we have seen that cutting integrals in fact is a good way to get a rational symbol alphabet. The cuts point us in the right direction of which

variables to choose to rationalize the alphabet.

Third, we have extended the ‘Cut=Disc= $\delta$ ’-relations of [2] to include internal masses. This is done by first relating unitarity cuts (‘Cut’) to the discontinuities across branch cuts (‘Disc’), see equation (1.94). Next, the discontinuities are related to the coproduct entries (‘ $\delta$ ’), as done in equation (1.95). In this way we are able to relate Cut to  $\delta$ , equation (1.107), which is the main result of this chapter. The results presented are mostly straightforward generalizations of the results of [2], except for some subtleties arising in the presence of internal masses. Such a subtlety is that we have to do all cuts in external channels before cutting in internal masses, otherwise we end up with the wrong overall signs at the end.

Lastly, we have studied the *reconstruction* of the integrals through their cuts and symbols. We have found that, in all of our examples, the knowledge of one unitarity cut in an external channel of a given diagram is enough to reconstruct the full function. In section 1.10, we mainly focus on the reconstruction of the symbol starting from a chosen cut. We do this by building an ansatz for the symbol and then constraining the numerical parameters of the ansatz. To do so, we use empirical observations that we have found during the process of studying these massive triangle diagrams. The integration of the symbol of one-loop three-point diagrams, although an unresolved problem for higher loops and more external legs, is doable using modern software.

As an outlook, let us point out that, even though our observations hold at the level of conjectures, it would be nice to have proofs of their validity. Also, a future task is to add loops and legs to these studies.

However, more generally, we believe that a better understanding of the analytic structure of Feynman diagrams is fundamental to develop more efficient computational methods. Supported by the results of this thesis (see appendix C for the original paper), we believe that the coproduct of the Hopf algebra of multiple polylogarithms is an appropriate tool to tackle this problem.



## Part II

# Fluctuations in heavy ion collisions



# Introduction to heavy-ion collisions

Heavy-ion collisions, sometimes called Little Bangs, create conditions close to those that existed in the universe one microsecond after the Big Bang. In these collisions, scientists create the highest temperatures ever seen on earth:  $5.5 \cdot 10^{12}$  degrees, meaning temperatures of approximately 300 000 times superior to that in the center of the sun [62]. The very hot matter created is fluid like, and so we can speak about the smallest and hottest droplets of liquid ever produced.

These droplets are produced at two different colliders today: the Relativistic Heavy Ion Collider (RHIC), located at Brookhaven, New York, and the Large Hadron Collider (LHC), located near Geneva. At RHIC very different nuclei have been used: protons, deuterium, copper, gold and uranium. At the LHC the focus is on protons and lead. The energies per nucleon pair used range from 130 MeV (start of RHIC) to 5.02 TeV (November 2015 at the LHC).

At these colliders, the nuclei are accelerated to more than 99% of the speed of light. This implies that the nuclei entering a collision are highly contracted and thus look like tiny, extremely flat pancakes. Lorentz time dilatation furthermore implies that time slows down for the nuclei, meaning that their configurations are ‘frozen’ into a specific quantum state at the time of the collision. So a high-energy collision really gives a clear snapshot of the state of a nucleus at the time at which it hit the other nucleus. This initial configuration of nucleons inside a nucleus is of interest to us in this thesis, and we will discuss it more in chapter 2.

A specific way to describe the initial state of a high-energy nucleus entering a collision is with the so-called Glauber model [63](see e.g. [64] for a review). The model “gives the nucleus-nucleus interaction in terms of interaction between the constituent nucleons with a given density distribution. The model is a semiclassical model picturing the nuclear collision in the impact parameter representation where the nuclei move along the collision direction in a straight path” [65]. The impact parameter mentioned here, conventionally denoted by  $b$ , is nothing but the transverse distance between the centers of the two colliding nuclei, presented in figure 1.14. This is the type of image we will have in mind in chapter 2.

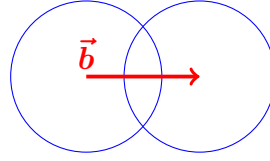


Figure 1.14: Schematic figure of a heavy-ion collision with the two nuclei represented as circles. The impact parameter  $b \equiv |\vec{b}|$ , drawn with a red arrow, is the (transverse) distance between the centers of the two nuclei.

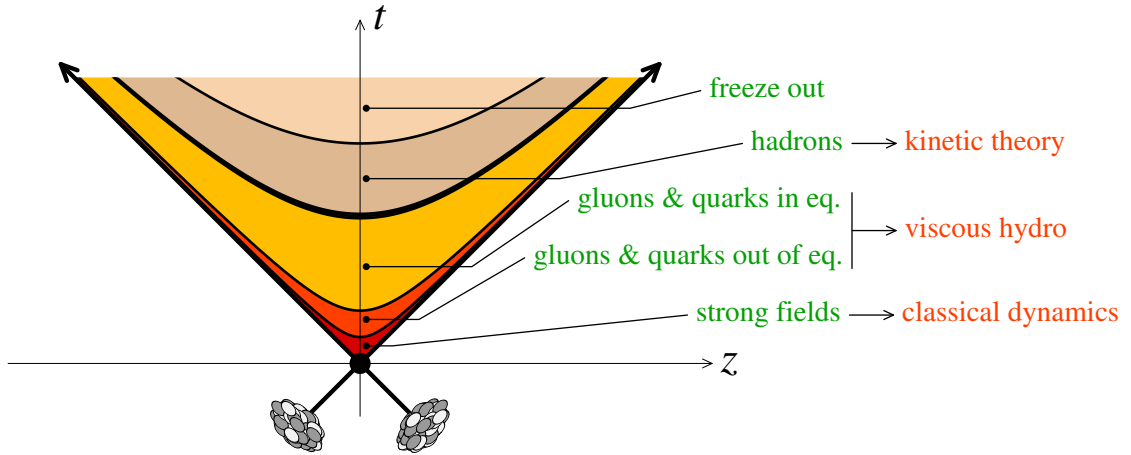


Figure 1.15: Stages of a heavy-ion collision. Figure from ref. [3].

A certain time after the collision, typically around 1 fm after it, the system is fluid like. In this phase it is thus described by hydrodynamics, see figure 1.15. Indeed, the state of the art in heavy-ion collision physics today is to take a random, possibly fluctuating initial state and let it evolve according to hydrodynamics. Here the correct framework to consider is *viscous* hydrodynamics, because, as has been argued by Kovtun, Son and Starinets in [66], the viscosity of the liquid produced in a heavy-ion collision is nonzero.

The fact that the system behaves like a fluid is known from a number of reasons related to the strong expansion of the medium produced in a heavy-ion collision. The formation of a hot and dense medium is suggested by many things: amongst these are analyses of identified particle spectra, elliptic flow (to be described below), Hanbury-Brown-Twiss (HBT) interferometry and the suppression of particles carrying high transverse momenta [67, 68, 69, 70].

It has been experimentally observed that the final distribution of momenta of

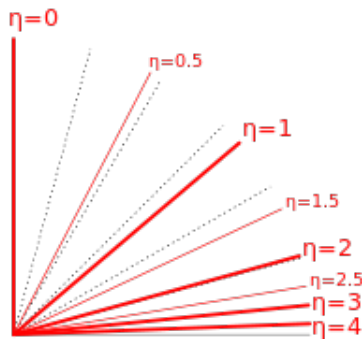


Figure 1.16: Values of pseudorapidity  $\eta$ , eq. (1.202). As the polar angle tends towards zero, the pseudorapidity tends towards infinity. Figure from Wikipedia.

the particles produced is *asymmetric in the azimuthal angle*. The asymmetries are of a very specific form, and can be quite well described by Fourier harmonics (see fig. 1.17):

$$E \frac{dN}{d^3p} \equiv \frac{1}{2\pi} \frac{\sqrt{m^2 + p_T^2 \cosh^2 \eta}}{p_T \cosh \eta} \frac{dN}{p_T dp_T d\eta} \left( 1 + \sum_{n=1}^{\infty} v_n \cos n(\phi - \Psi_n) \right), \quad (1.201)$$

where  $p_T$  is the transverse momentum of the emitted particle and  $\eta$  is defined as

$$\eta = -\ln \left( \tan \frac{\theta}{2} \right). \quad (1.202)$$

Values of  $\eta$  are shown in figure 1.16.

This is a phenomenon that is called *harmonic flow*. The first harmonic is that of directed flow. The second, and most dominant one in non-central collisions where  $b \neq 0$ , is called elliptic flow. The elliptic flow can quite simply be understood as arising from the ‘almond’-shaped overlap region between two nuclei, when they do not collide head-on. Also higher harmonics exist due to quantum fluctuations. The largest of these higher harmonics is the triangular flow, first proposed by Alver and Roland in [11]. The higher the harmonic, the stronger the viscous suppression [71], so the dominant harmonics are the lowest-order ones.

The harmonic flow, just mentioned, is due to a response of the system to initial anisotropies. In fact, the low viscosity plasma transfers the geometric structure of the initial density distributions, with their associated pressure gradients, into the final

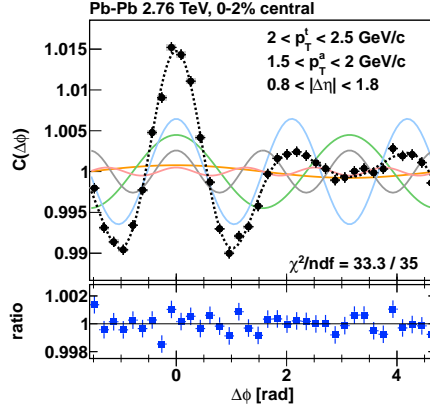


Figure 1.17: The projection of  $C(\Delta\phi, \Delta\eta > 0.8)$  from figure 1.18 into  $\Delta\phi$  for a relative pseudorapidity gap of  $\Delta\eta > 0.8$  between trigger and associated particles. The Fourier harmonics  $V_{1\Delta}$  to  $V_{5\Delta}$  are superimposed and their sum is shown as a dashed curve. The ratio of the data to the sum of  $n \leq 5$  harmonics is shown in the lower panel. Figure from ref. [4]

state. This then appears as correlations between produced particles (see fig. 1.18). In this figure is plotted  $C(\Delta\phi, \Delta\eta)$ , which is defined as

$$C(\Delta\phi, \Delta\eta) \equiv \left\langle \frac{dN}{d\phi_1 d\eta_1} \frac{dN}{d\phi_2 d\eta_2} \right\rangle, \quad (1.203)$$

where  $\Delta\phi = \phi_1 - \phi_2$  and  $\Delta\eta = \eta_1 - \eta_2$ .

The nature of the quantum fluctuations of the initial state are the subject of chapter 2. Experimentally, it is observed that these fluctuations are not Gaussian. This is related to finite-size effects: the system produced in a heavy-ion collision cannot be thought of as being of infinite extent, in which case the central limit theorem would apply and all fluctuations would be Gaussian.

Fluctuations are also present in late stages of a heavy-ion collision, not only in the initial state. As already mentioned, after a time of about 1 fm after the collision, the medium is a liquid and can hence be described by hydrodynamics. In a thermal system with non zero temperature, there exist thermal fluctuations. Such fluctuations exist also in the hydrodynamical evolution of the fluid, and we call these *hydrodynamical fluctuations*. This is a phenomenon that we study in chapter 3.

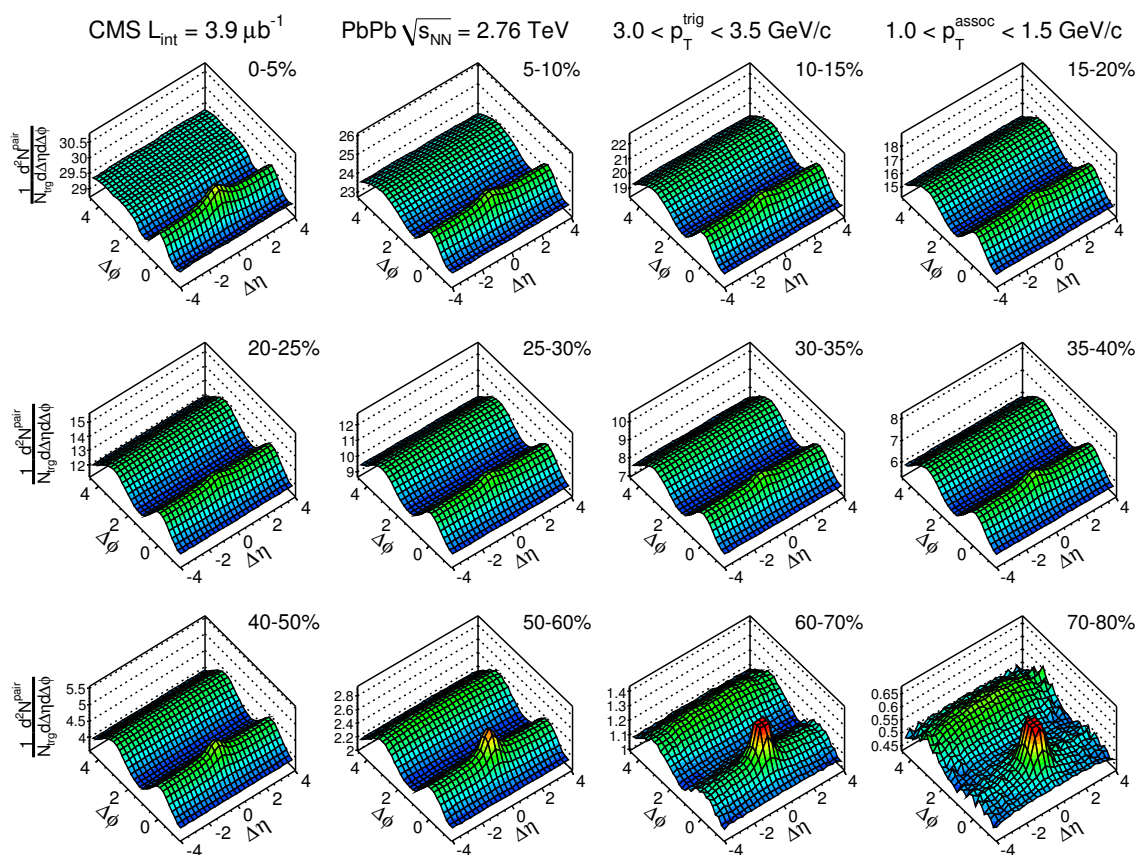


Figure 1.18: Examples of two-particle correlations  $C(\Delta\phi, \Delta\eta)$  for lead-lead collisions at  $\sqrt{s_{\text{NN}}} = 2.76 \text{ TeV}$  for different centralities as measured by the CMS collaboration. Figure from ref. [5]



# Chapter 2

## Non-Gaussian eccentricity fluctuations

### 2.1 Introduction

The state of the art modeling of heavy-ion collisions today consists of taking an initial state and letting it evolve according to hydrodynamics. For many years, this hydrodynamic modeling used smooth and symmetric initial density profiles. In reality, however, there exist fluctuations in the early stages of a heavy-ion collision that can come from the nucleonic structure of the nuclei entering the collision. The energy density at early times is in fact lumpy and asymmetric and furthermore fluctuating from one collision event to another. This is true even for events having the same impact parameter *i.e.* for events belonging to the same centrality class. For an illustration of lumpy and asymmetric initial states, see figure 2.1.

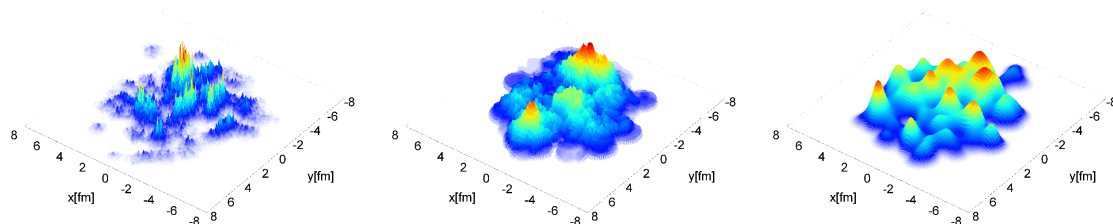


Figure 2.1: The initial energy density in arbitrary units in the transverse plane for three different heavy-ion collision models: from left to right, IP-Glasma, MC-KLN and MC-Glauber models. Figure from [6].

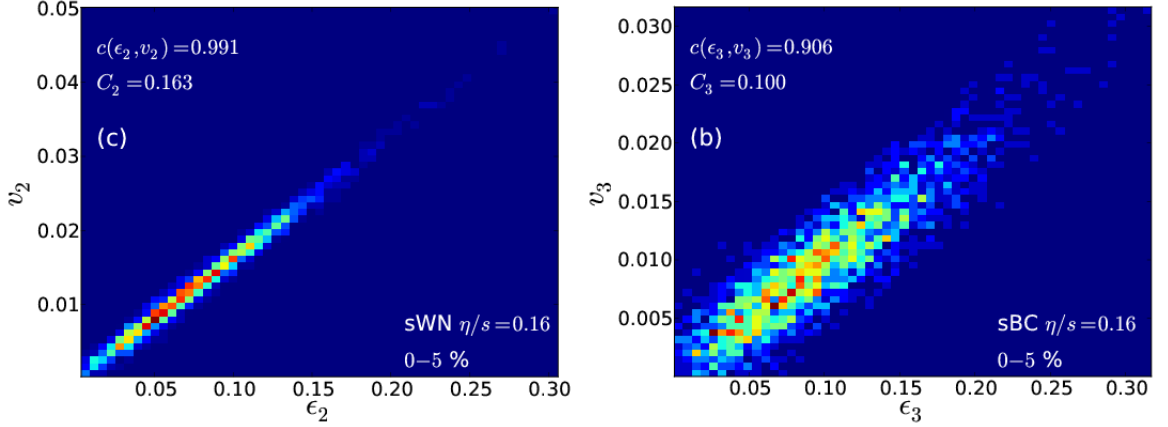


Figure 2.2: Figures of the flow harmonic  $v_n$  as a function of the initial eccentricity  $\epsilon_n$  for  $n = 2$  (left) and  $n = 3$  (right). The data are taken from 0-5% central collisions. The response is linear for this class of events. Figure from [7].

This anisotropy in the initial collision, caused by event-to-event fluctuations, leads to an anisotropy in the azimuthal particle production through the collective expansion, as already mentioned in the introduction to this section II. The azimuthal anisotropy in the final particle spectrum is measured by counting pairs of particles, that is, through *two-particle correlations*, or through correlations involving more particles. These measurements have led to the picture of the *anisotropic flow* in terms of a Fourier series. The  $n^{\text{th}}$  Fourier harmonic of flow,  $v_n$ , is related to the spatial anisotropy  $\epsilon_n$  through a linear relation (at least for ultra-central collisions), as is shown in figure 2.2. So, by measuring correlations of final-state particles, we actually indirectly access the initial state of the nucleus, described by quantum laws of nature.

As briefly mentioned already, the quantum initial state fluctuates from event to event. These fluctuations are to a first approximation Gaussian. However, when four-particle correlations have been measured, such as at ALICE (see figure 2.3) and at CMS (see figure 2.4) it was discovered that these initial-state density fluctuations are *not* Gaussian. The anisotropy of the initial state is quantified through its *eccentricity*  $\epsilon_n$ . See figure 2.5 for  $\epsilon_2$ . In this chapter we study precisely these non-Gaussian nature of these eccentricity fluctuations, assuming linear response  $v_n \propto \epsilon_n$ .

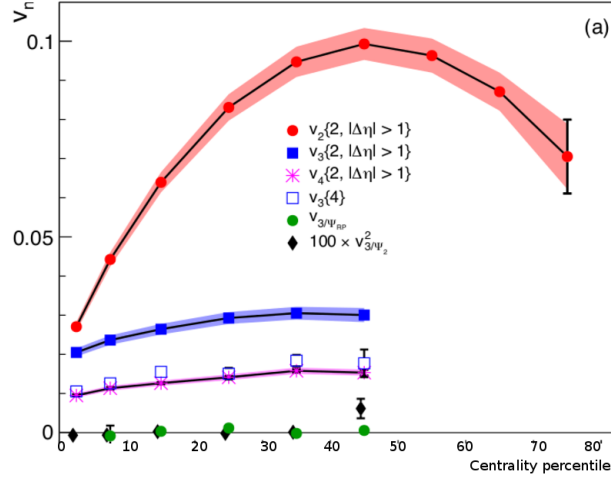


Figure 2.3:  $v_2$ ,  $v_3$  and  $v_4$  integrated over the  $p_T$  range  $0.2 < p_T < 5.0$  GeV/ $c$  as a function of event centrality. Of special interest to us are the open squares, which show that  $v_3\{4\} \neq 0$ , implying that the eccentricity fluctuations are non-Gaussian. Figure from [8].

### 2.1.1 Anisotropic flow

In collision events, experiments detect up to several thousands of different particles coming out of the collision region. We wish to analyze the properties of these particles and have observables at hand that can give insight into the dynamics of a collision and into the properties of the medium created. Let us start by defining these observables, and seeing how they relate to the underlying theory. For a review on the subject we refer the reader to ref. [72].

Anisotropic flow is one of the most prominent bulk observables in heavy-ion collisions [73]. Especially the azimuthal dependence of the emitted particles is of great interest to us and it can be written as a Fourier series in the azimuthal angle  $\phi$  as in eq. (1.201).

The coefficients  $v_n \equiv v_n(p_T, \eta)$  of equation 1.201 represent an azimuthal anisotropy in the underlying probability distribution and the angles  $\Psi(p_T, \eta)$  are defined such that all sine terms vanish. The flow vector can be written as a number in the complex plane

$$v_n e^{in\Psi_n}(p_T, \eta) \equiv \frac{\int_0^{2\pi} d\phi \frac{dN}{d\phi dp_T d\eta} e^{in\phi}}{\int_0^{2\pi} \frac{dN}{d\phi dp_T d\eta}}. \quad (2.1)$$

If the collective pressure gradients are large enough and drive the evolution of the

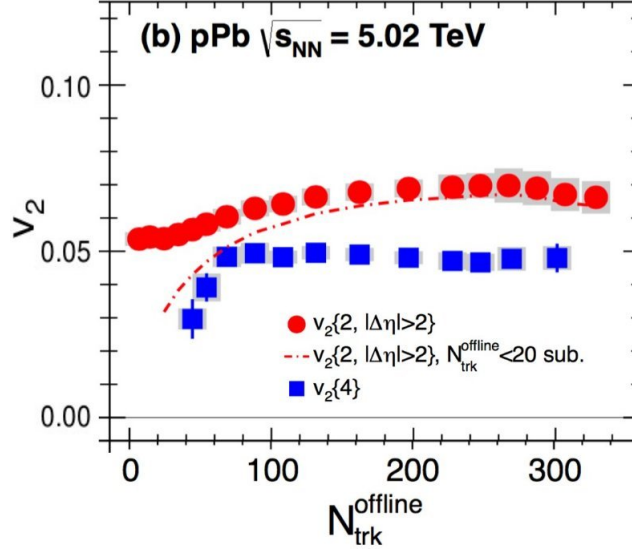


Figure 2.4: The  $v_2\{2, \Delta\eta > 2\}$  (circles) and  $v_2\{4\}$  (squares) as a function of multiplicity for  $0.3 < p_T < 3$  GeV/c in 5.02 GeV p-Pb collisions. Of special interest to us are the squares, which show that  $v_2\{4\} \neq 0$ , meaning that eccentricity fluctuations are non-Gaussian. Figure from [9].

system, then the final state momentum space anisotropy is just a reflection of the initial coordinate space anisotropy. This (complex) initial coordinate space Fourier anisotropy is defined as

$$\varepsilon_n = \frac{\int_z z^n \rho(z)}{\int_z |z|^n \rho(z)}, \quad (2.2)$$

where  $\rho$  is the energy density and

$$\int_z \equiv \iint dx dy, \quad (2.3)$$

with  $x$  and  $y$  spanning the transverse plane,  $z = x + iy$ , see figure 2.5. The typical spatial anisotropies  $\varepsilon_n$  for  $n = 2, 3, 4, 5, 6$  are shown in figure 2.6.

The flow coefficient  $v_2$  ( $v_3$ ) is called *elliptic flow* (triangular flow). For a review of elliptic flow see for example [10]. The elliptic flow is the most dominant flow component in non-central collisions (see figure 2.5), where the overlap region between the two nuclei is almond-shaped. The pressure gradients are at their largest in the direction in which the almond is at its thinnest, resulting in elliptic flow. This type

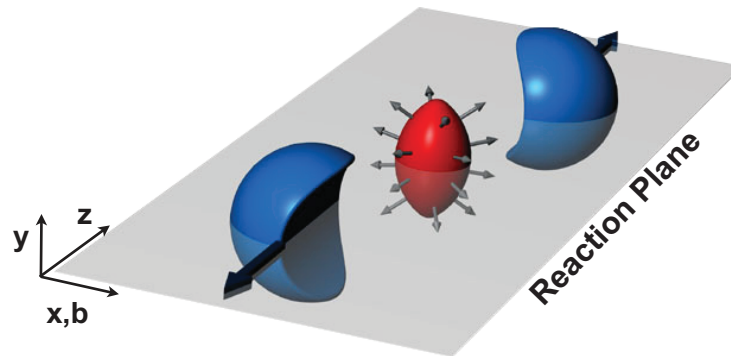


Figure 2.5: Almond shaped interaction volume after a non-central collision of two nuclei. The spatial anisotropy with respect to the  $x - z$  -plane (reaction plane) translates into a momentum anisotropy of the produced particles (anisotropic flow). Figure from [10].

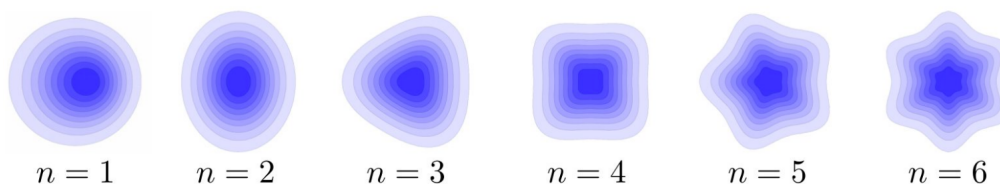


Figure 2.6: Eccentricities  $\varepsilon_n$  corresponding to flow coefficients  $v_n$  for  $n = 2, 3, 4, 5, 6$ .

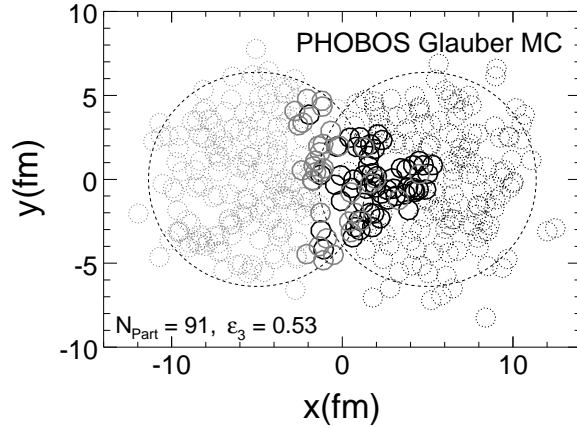


Figure 2.7: The distribution of nucleons in the transverse plane for a  $s_{NN} = 200$  GeV Au-Au collision event with  $\epsilon_3 = 0.53$  from a Glauber Monte Carlo simulation. Participant nucleons *i.e.* the ones interacting (also called ‘wounded nucleons’) are drawn with solid circles, while non-interacting spectator nucleons are drawn as dotted circles. The triangular interaction region is precisely what gives rise to triangular flow. Figure from [11].

of flow is, however, to a lesser extent also present in ultra-central collisions, where the overlap region is circular [74]. This effect arises purely from fluctuations. So is the case for triangular flow, too (see figure 2.7) [11]. This is analogous to the cosmic microwave background, where inhomogeneities in the observed power spectra are sensitive to primordial quantum fluctuations (see, for example, ref. [75]).

The two-particle correlations from which the anisotropic flow is extracted also get contributions from physical processes that are non-hydrodynamical in their origin. These phenomena are simply called ‘non-flow’ and come for example from jets, resonance decays and Bose-Einstein correlations. In order to access the pure flow signal, we want to subtract the effect of non-flow. Since the non-flow correlations typically have a small pseudorapidity gap, a large pseudorapidity interval (typically  $|\Delta\eta| > 2$ ) is applied to the data selection. Another way to suppress the effect of non-flow is to measure many-particle correlations, with the word ‘many’ referring to more than two particles. This is the method of *higher-order cumulants* (we will define the relevant cumulants below). When many-particle correlations are measured higher statistics are needed, but on the other hand, one gains in precision. Measured cumulants include 6-th and 8-th order cumulants [76].

To conclude this introductory section about anisotropic flow we note that the two-particle azimuthal correlations at large (pseudo-)rapidity gap are well described by the first three Fourier components (see *e.g.* [11]).

## 2.2 Initial anisotropies

The time scale of nucleus-nucleus collisions is so short that each of the nuclei sees the other nucleus in a frozen configuration, where nucleons are at specific positions with probabilities determined by the nuclear wave function [77]. Fluctuations in the nucleon positions result in fluctuations of the initial energy density in the transverse plane, and play an important role in the dynamics of the collision. As explained for example in [72], these fluctuations leave observable traces in the final-state particle distribution after hydrodynamical evolution of the system. As mentioned in section 2.1, the relevant phenomena and nomenclature for situations in which fluctuations of energy density become important are: *elliptic flow fluctuations* [74, 78], *triangular flow* [11, 8, 78, 79] and *higher harmonics* [5, 80] as well as *directed flow near midrapidity* [80, 81, 82, 83].

As already mentioned in section 2.1, the fluctuations of the initial anisotropy  $\varepsilon_n$  are to a first approximation Gaussian [84, 85]. When the anisotropy comes from fluctuations only, then the non-Gaussianities can be measured directly using higher-order cumulants. This is so because for a Gaussian distribution the higher-order cumulants vanish. For instance, we may consider the fourth cumulant of the distribution of  $v_n$ , denoted  $v_n\{4\}$ . We recall that for the case considered in this part of the thesis, the flow harmonic  $v_n$  is proportional to the initial spatial anisotropy  $\varepsilon_n$ :

$$v_n \propto \varepsilon_n , \quad (2.4)$$

see figure 2.2. This holds in particular for ultra-central collisions ( $b = 0$ ), where the anisotropy is solely due to fluctuations.

In order to quantitatively study the fluctuations of the initial spatial anisotropies, let us recall the definition in eq. (2.2). We note that in this equation, since the energy density  $\rho$  is positive, it follows that

$$|\varepsilon_n| \leq 1 . \quad (2.5)$$

It was argued in [86] that this condition alone generates a universal, non-Gaussian distribution, matching recent measurements of higher-order cumulants in proton-lead collisions [76]. In this chapter we seek to determine to what extent this universality holds.

We note that the standard definition of  $\varepsilon_n$  holds in a *centered* coordinate system. By definition, we call ‘centered’ a system where

$$\int_z z \rho(z) = 0 , \quad (2.6)$$

where we have used the abbreviated notation of eq. (2.3). Throughout this chapter, we use complex coordinates in the transverse plane:  $z = x + iy$ . The function  $\rho(z)$  is the energy density in a given event. The energy density in a given event is to a good approximation boost invariant but has large fluctuations in the plane transverse to the collision axis.

In this centered coordinate system, one should replace  $z^n$  by  $(z - z_0)^n$  and  $|z|^n$  by  $|z - z_0|^n$ , with the center of the distribution at

$$z_0 \equiv \frac{\int_z z \rho(z)}{\int_z \rho(z)} . \quad (2.7)$$

In our Monte Carlo simulations, to be discussed in section 2.5, we take into account this recentering correction but since its effect on cumulants is negligible, we ignore it in the perturbative computations of this section. The effect of the recentering is discussed in some detail in the appendices of the original paper, see appendix E.

Experimental observables involve even moments of the distribution of  $|\varepsilon_n|$ , combined into cumulants. The two cumulants of interest to us are defined as [87]

$$\varepsilon_n \{2\}^2 \equiv \langle |\varepsilon_n|^2 \rangle \quad (2.8)$$

$$\varepsilon_n \{4\}^4 \equiv 2 \langle |\varepsilon_n|^2 \rangle^2 - \langle |\varepsilon_n|^4 \rangle , \quad (2.9)$$

where angular brackets denote an average over events in a centrality class. As we already mentioned, higher order cumulants of a normal distribution vanish (the normal distribution is uniquely determined by its first two cumulants), so for example the fourth cumulant  $\varepsilon_n \{4\}$  is a direct measure of the non-Gaussian nature of a distribution. Other higher order cumulants, such as the sixth order one,  $\varepsilon_n \{6\}$  could be used in a similar manner as a measure of the non-Gaussianity, but this would require higher-order computations in perturbation theory. Below we will focus on next-to-leading order accuracy, and will therefore concentrate our studies on the fourth cumulant. These investigations generalize the study of [85] by including the leading corrections to the central limit.

## 2.3 Identical pointlike sources

We begin by reviewing some known analytical results obtained for the case of identical, pointlike sources. This set-up is of phenomenological interest since it is similar to Monte Carlo Glauber simulations [64]. The energy density is a sum of delta peaks,

$$\rho(z) = \sum_i^N \delta(z - z_i) , \quad (2.10)$$

where  $z_i$  for  $i = 1, \dots, N$  are independent random variables, drawn in the transverse plane according to a probability distribution  $p(z)$ , and  $N \geq 2$  is assumed. We note that

$$\int_z \rho(z) = N , \quad (2.11)$$

and

$$\langle \rho(z) \rangle = Np(z) , \quad (2.12)$$

where the second equality is a basic result for independent, identically distributed random variables. For central collisions ( $b = 0$ ),  $p(z)$  depends only on  $r \equiv |z|$ , so for very large  $N$  the distribution would be perfectly isotropic and the anisotropies  $|\varepsilon_n|$  would vanish. However, due to a finite number of ‘sources’  $N$  in a given collision event, the anisotropies are generally non zero. For large  $N$  the scaling is

$$\varepsilon_n \underset{N \gg 1}{\propto} \frac{1}{\sqrt{N}} , \quad (2.13)$$

so that small fluctuations correspond to large  $N$ .

### 2.3.1 Gaussian distribution of sources: Exact result

Let us consider a two-dimensional Gaussian density profile

$$p(z_i) \propto e^{-|z_i|^2/\sigma^2} , \quad (2.14)$$

depicted in figure 2.8, for which the probability distribution of  $\varepsilon_n$  can be computed exactly, and the first two cumulants read

$$\varepsilon_2 \{2\}^2 = \frac{2}{N} \quad (2.15)$$

$$\varepsilon_2 \{4\}^4 = \frac{16}{N^2(N+2)} . \quad (2.16)$$

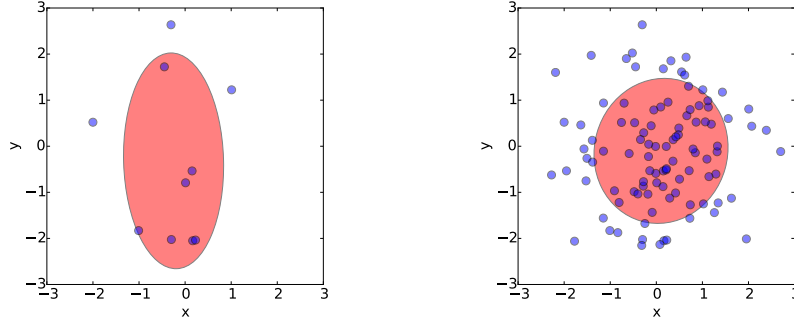


Figure 2.8: A schematic picture of a nucleus, in which the sources are distributed according to a Gaussian distribution, eq. (2.14). The coordinates  $x$  and  $y$  span the plane transverse to the collision axis. On the right is a random event with  $N = 10$  sources, on the left  $N = 100$  sources. The red region depicts the best-fit ellipse to the distribution of sources. The shape of the ellipse has a link with  $\varepsilon_2$ : the more circular the form, the smaller the value of  $\varepsilon_2$  and the more elongated the form, the bigger the value of  $\varepsilon_2$ . Note the difference in the shape between the two figures. The fact that the right-hand side figure is more circular agrees with eqs (2.15), (2.16).

A few comments are in order. Firstly, in the limit of two sources, the energy consists just of two points, and then  $|\varepsilon_2| = 1$ , which implies that  $\varepsilon_2 \{2\} = \varepsilon_2 \{4\} = 1$ . Secondly, as expected both  $\varepsilon_2 \{2\}$  and  $\varepsilon_2 \{4\}$  vanish when  $N \rightarrow \infty$ . This is as anticipated above: when  $N$  is very large the distribution of sources is isotropic and therefore the anisotropy is zero. Thirdly,  $\varepsilon_2 \{4\}$  decreases faster than  $\varepsilon_2 \{2\}$  in the limit of large  $N$ . This is to be expected, since for a large sample the central limit theorem applies and the distribution of eccentricity fluctuations becomes a Gaussian, and we recall that for a Gaussian distribution  $\varepsilon_2 \{4\} = 0$ .

We test the validity of eqs. (2.15), (2.16) with Monte Carlo simulations and the results are shown in figure 2.9. For each simulated collision event, the positions  $z_i$  in eq. (2.10) are generated randomly according to a Gaussian distribution and then the positions are shifted so, that the system is centered, i.e. it holds that

$$\sum_{i=1}^N z_i = 0. \quad (2.17)$$

When this recentering correction is not taken into account we need to replace  $N$  by  $N + 1$  in eqs. (2.15), (2.16) Looking at figure 2.9 we see that the numerical results (circles) are compatible with the analytic results (lines).

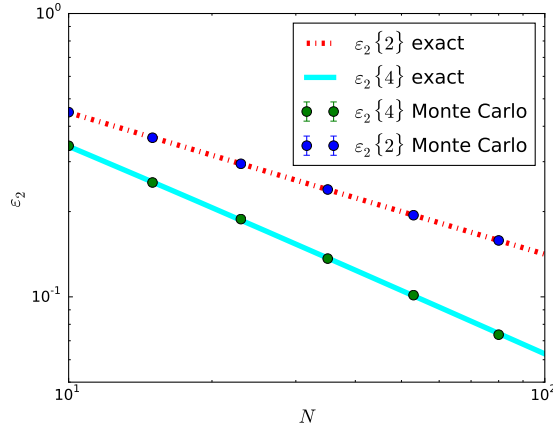


Figure 2.9: Results of a Monte Carlo simulation of the Gaussian independent-sources model. Blue circles correspond to numerical values of  $\varepsilon_2 \{2\}$  and green circles correspond to numerical values of  $\varepsilon_2 \{4\}$ . The dashed red line corresponds to the exact results, eq. (2.15), and the solid turquoise line to eq. (2.16).

**A universal relation** for the cumulants  $\varepsilon_2 \{2\}$  and  $\varepsilon_2 \{4\}$  was conjectured in ref. [86]. The relation is obtained by eliminating  $N$  between eqs. (2.15) and (2.16), and it reads

$$\varepsilon_2 \{4\}^4 = \frac{2\varepsilon_2 \{2\}^6}{1 + \varepsilon_2 \{2\}^2} \quad (2.18)$$

The statement of ref. [86] is that this relation is a good approximation for any model of initial conditions. In this chapter we study the validity of this claim.

### 2.3.2 Perturbative results for the cumulants

When considering the limit  $N \gg 1$  the fluctuations become small and they can be treated perturbatively. In this limit analytic results have been obtained to leading order in  $N^{-1}$  for  $\varepsilon_2$  [88] and  $\varepsilon_3$  [89]:

$$\varepsilon_n \{2\}^2 = \frac{\langle r^{2n} \rangle}{N \langle r^n \rangle^2} \quad (2.19)$$

$$\varepsilon_n \{4\}^4 = \frac{1}{N^3} \left( -\frac{8 \langle r^{2n} \rangle^3}{\langle r^n \rangle^6} + \frac{8 \langle r^{3n} \rangle \langle r^{2n} \rangle}{\langle r^n \rangle^5} - \frac{\langle r^{4n} \rangle}{\langle r^n \rangle^4} + \frac{2 \langle r^{2n} \rangle^2}{\langle r^n \rangle^4} \right), \quad (2.20)$$

where  $n = 2, 3$  and angular brackets denote averages taken with  $p(z)$ . We note that  $\varepsilon_n\{4\}^4$  is obtained by subtracting two terms (see eq. (2.9)), both of the order  $N^{-2}$ . The difference of the two terms is smaller by a factor of  $N^{-1}$ , so in the perturbative analysis we must push the computations of the moments to next-to-leading order in  $N^{-1}$ . We also note that  $\varepsilon_n\{4\}^4$  is a sum of two positive and two negative terms, and that typically there are large cancellations between these two. For example, for the two-dimensional Gaussian profile of eq. (2.14), we obtain for  $n = 2$ ,

$$\varepsilon_n\{2\}^2 = \frac{2}{N} \quad (2.21)$$

$$\varepsilon_n\{4\}^4 = \frac{1}{N^3} (8 - 24 + 96 - 64) = \frac{16}{N^3}, \quad (2.22)$$

in agreement with eqs. (2.15), (2.16).

In order to study in more detail the sensitivity of anisotropies on the density profile, we perform Monte Carlo simulations with a uniform density profile in the unit circle,

$$p(z) = \theta(1 - |z|), \quad (2.23)$$

see figure 2.10. For this distribution the two cumulants of interest to us are

$$\varepsilon_2\{2\}^2 = \frac{4}{3N} \quad (2.24)$$

$$\varepsilon_2\{4\}^4 = \frac{368}{135N^3}. \quad (2.25)$$

The results of the simulations are displayed in figure 2.11. We see that the numerical values of the simulations converge to the perturbative values of eq. (2.24) for large values of  $N$ . The dashed line represents the value of  $\varepsilon_2\{4\}$  of eq. (2.18). For this curve the Monte Carlo values for  $\varepsilon_2\{2\}$  are substituted into the right-hand side of eq. (2.18). The agreement between the simulations and the conjectured universal behavior is best for small  $N$  but reasonable for all values of  $N$ .

## 2.4 Statistical properties of local density fluctuations

We now derive the statistical properties of the initial energy density  $\rho(z)$  under the assumption that fluctuations are correlated only over distances much shorter than any other scale of interest [85]. Typically, the transverse scale of fluctuations is much smaller than the nuclear radius.

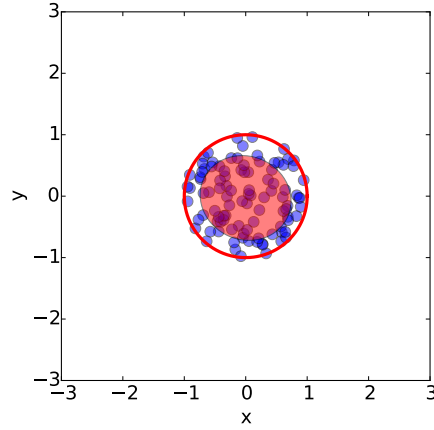


Figure 2.10: Schematic picture of a nucleus with  $N = 100$  sources when the probability distribution of sources is uniform, eq. (2.23). The semi-transparent red region is the best-fit ellipse to this specific distribution of sources. The opaque solid red circle is the unit circle.

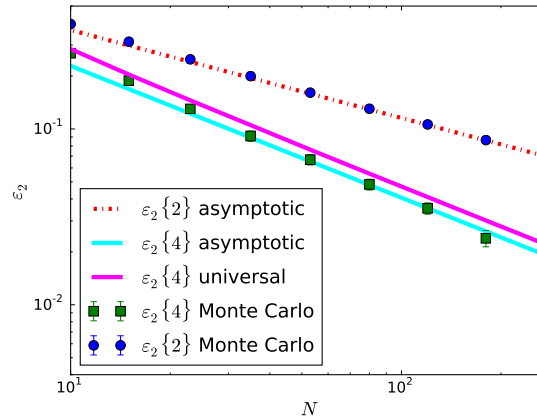


Figure 2.11: Results of Monte Carlo simulations of the independent-sources model with a uniform distribution, eq. (2.23). The blue circles correspond to  $\varepsilon_2\{2\}$  and the dashed red curve to the asymptotic result, eq. (2.24). The green squares correspond to  $\varepsilon_2\{4\}$  and the solid turquoise line to the asymptotic result, eq. (2.25), whereas the magenta line corresponds to the universal result, eq. (2.18).

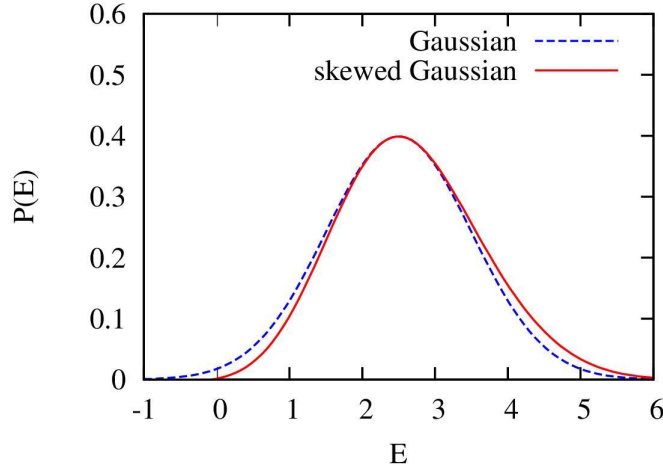


Figure 2.12: Sketch of the probability of the energy  $E$  in a given area. The Gaussian (dashed line) extends into the forbidden region  $E < 0$ . Significant improvement is obtained by skewing the Gaussian (solid line).

While this locality assumption is reasonable at a fixed impact parameter, in practice analyses are not done at a fixed impact parameter. Experiments use as a proxy for impact parameter an observable dubbed ‘centrality’ which is typically based on the multiplicity seen in a detector [90]. Since the multiplicity is an extensive quantity, it is strongly correlated with the total energy, and one can essentially consider that the total energy  $E = \int_z \rho(z)$  is fixed in a narrow centrality class. This is a global constraint which breaks locality. (Note that in the identical source model, the total energy  $N$  is fixed by construction.)

A consequence of the locality hypothesis is that the energy  $E$  contained in a given transverse area  $S$  has Gaussian fluctuations if the area is large enough. This is seen by decomposing the area  $S$  in a large number of independent subareas, and applying the central limit theorem. However, the condition that  $E > 0$  implies that there are non-Gaussianities when the relative fluctuations become sizeable. In particular, the probability is likely to have positive skew, as illustrated in Fig. 2.12. Skewness is proportional to the third cumulant of the energy distribution.

### 2.4.1 Perturbative expansion

In this chapter we assume that the system is radially symmetric. In particular, this implies that the energy density averaged over events,  $\langle \rho(z) \rangle$ , only depends on  $r \equiv |z|$ .

In this symmetric set-up, the anisotropy  $\varepsilon_n$  has its origin in density fluctuations only. We can obtain analytic results by considering small fluctuations of the density:

$$\delta\rho(z) \equiv \rho(z) - \langle\rho(z)\rangle . \quad (2.26)$$

Now the radial symmetry implies that

$$\int_z z^n \langle\rho(z)\rangle = 0 , \quad (2.27)$$

and therefore eq. (2.2) can be written as

$$\varepsilon_n = \frac{\int_z z^n \delta\rho(z)}{\langle E \rangle \langle r^n \rangle + \int_z r^n \delta\rho(z)} , \quad (2.28)$$

where  $\langle E \rangle$  is the average total energy,

$$\langle E \rangle = \int_z \langle\rho(z)\rangle , \quad (2.29)$$

and

$$\langle r^n \rangle = \frac{\int_z r^n \langle\rho(z)\rangle}{\int_z \langle\rho(z)\rangle} . \quad (2.30)$$

For future use we now define an abbreviated notation, for any function  $f$  of  $z$ ,

$$\delta f \equiv \frac{1}{\langle E \rangle} \int_z f(z) \delta\rho(z) . \quad (2.31)$$

Using this new notation, eq. (2.28) can now be rewritten as

$$\varepsilon_n = \frac{\delta z^n}{\langle r^n \rangle + \delta r^n} = \frac{\delta z^n}{\langle r^n \rangle} \left( 1 + \frac{\delta r^n}{\langle r^n \rangle} \right)^{-1} . \quad (2.32)$$

The term  $\delta r^n$  is the fluctuation in the size. It can be neglected at leading order in the fluctuations [85], but should be taken into account at next-to-leading order. Different moments of the distribution of  $|\varepsilon_n|$  can then be obtained by expanding eq. (2.32), in which case the second and fourth powers of  $|\varepsilon_n|$  read

$$|\varepsilon_n|^2 = \frac{\delta z^n \delta \bar{z}^n}{\langle r^n \rangle^2} \left( 1 - 2 \frac{\delta r^n}{\langle r^n \rangle} + 3 \frac{(\delta r^n)^2}{\langle r^n \rangle^2} + \dots \right) \quad (2.33)$$

$$|\varepsilon_n|^4 = \frac{(\delta z^n)^2 (\delta \bar{z}^n)^2}{\langle r^n \rangle^4} \left( 1 - 4 \frac{\delta r^n}{\langle r^n \rangle} + 10 \frac{(\delta r^n)^2}{\langle r^n \rangle^2} + \dots \right) \quad (2.34)$$

where  $\bar{z}$  is the complex conjugate of  $z$ . In order to compute the averages, we must know the statistics of the density fluctuation  $\delta\rho(z)$ . First, we recall results obtained for identical point like sources and then generalize these results to the case of a continuous density profile.

In this chapter, the perturbative result in eqs. (2.33) and (2.34) will be generalized to a continuous initial density profile. We arrive at a physical interpretation for each of the terms in  $\varepsilon_n\{4\}$ , eq. (2.20):

- The first term is the non-Gaussianity arising from the non-linearity of Eq. (2.2) as a function of  $\rho(z)$ . Due to this non-linearity, even if  $\rho(z)$  has a Gaussian distribution, the distribution of  $\varepsilon_n$  is non-Gaussian.
- The second and third term arise from the non-Gaussianity of the distribution of  $\rho(z)$ : more specifically, they are related to the three- and four-point functions, respectively.
- The fourth term is due to energy conservation, namely, the fact that the total energy  $N$  is exactly the same for all events.

## 2.4.2 $n$ -point averages

The first cumulant is just the average value of the energy density,

$$\kappa_1(z) = \langle \rho(z) \rangle . \quad (2.35)$$

Higher cumulants correspond to statistical properties of the density fluctuation  $\delta\rho(z)$ . In particular, the second cumulant  $\kappa_2(z)$  is just the variance of the distribution and the third cumulant  $\kappa_3(z)$  is related to the skewness of the distribution. The fourth cumulant  $\kappa_4(z)$  is related to the kurtosis of the distribution, that is, the heaviness of the tail.

To evaluate the moments of  $\varepsilon_n$  in the perturbative expansion of eqs. (2.33), (2.34) we need to evaluate average values of product of fluctuations  $\delta f$  (see eq. (2.31)). The two-point average is

$$\langle (\delta f)(\delta g) \rangle = \frac{1}{\langle E \rangle^2} \int_z f(z)g(z)\kappa_2(z) . \quad (2.36)$$

Similarly for the three-point average,

$$\langle (\delta f)(\delta g)(\delta h) \rangle = \frac{1}{\langle E \rangle^3} \int_z f(z)g(z)h(z)\kappa_3(z) . \quad (2.37)$$

The four-point averages can be written in the following way,

$$\begin{aligned}
 \langle (\delta f)(\delta g)(\delta h)(\delta k) \rangle &= \langle (\delta f)(\delta g) \rangle \langle (\delta h)(\delta k) \rangle \\
 &+ \langle (\delta f)(\delta h) \rangle \langle (\delta g)(\delta k) \rangle \\
 &+ \langle (\delta f)(\delta k) \rangle \langle (\delta g)(\delta h) \rangle \\
 &+ \langle (\delta f)(\delta g)(\delta h)(\delta k) \rangle_c,
 \end{aligned} \tag{2.38}$$

where the connected part is

$$\langle (\delta f)(\delta g)(\delta h)(\delta k) \rangle_c = \frac{1}{\langle E \rangle^4} \int_z f(z)g(z)h(z)k(z)\kappa_4(z). \tag{2.39}$$

A few comments are in order. Let us consider  $N$  pointlike sources. The integrals over  $z$  scale like the total transverse area, or equivalently as  $N$ . Hence the two-point average (2.36) scales like  $N^{-1}$ , which is in agreement with the expectation that  $\delta f$  scales like  $N^{-1/2}$ . The three-point average scales like  $N^{-2}$ . The quantity  $(\delta f)(\delta g)(\delta h)$  is of order  $N^{-3/2}$  but when averaging over events we pick up another factor  $N^{-1/2}$ . In the expression for the four-point average, eq. (2.39), the first three terms are of order  $N^{-2}$  and the last term is of order  $N^{-3}$ . *This means that the perturbative expansion can be seen as an expansion in  $N^{-1}$ .*

We further note that the third and fourth order expressions contribute at the same order ( $N^{-2}$ ) after the averages over fluctuations are performed. More generally speaking, orders  $2n - 1$  and  $2n$  both give contributions of order  $N^{-n}$ .

### 2.4.3 Perturbative results

Now we have all the tools needed for the evaluation of the moments eqs. (2.33) and (2.34). We keep terms up to next-to-leading order and we use radial symmetry to discard terms where  $\delta z$  and  $\delta \bar{z}$  do not come in like powers. Such terms are for example  $\langle (\delta z^n)(\delta r^n) \rangle$  and  $\langle (\delta z^n)^2 \rangle$ . Furthermore, we use Wick's theorem to reduce four-point functions and higher. We denote the non trivial contractions as

$$\begin{aligned}
 a &\equiv \frac{\langle \delta z^n \delta \bar{z}^n \rangle}{\langle r^n \rangle^2} = \frac{\int_z r^{2n} \kappa_2(z)}{\left( \int_z r^n \kappa_1(z) \right)^2}, \\
 a' &\equiv \frac{\langle (\delta r^n)^2 \rangle}{\langle r^n \rangle^2} \\
 b &\equiv \frac{\langle \delta z^n \delta \bar{z}^n \delta r^n \rangle}{\langle r^n \rangle^3} = \frac{\int_z r^{3n} \kappa_3(z)}{\left( \int_z r^n \kappa_1(z) \right)^3} \\
 c &\equiv \frac{\langle (\delta z^n)^2 (\delta \bar{z}^n)^2 \rangle_c}{\langle r^n \rangle^4} = \frac{\int_z r^{4n} \kappa_4(z)}{\left( \int_z r^n \kappa_1(z) \right)^4}.
 \end{aligned} \tag{2.40}$$

Here we divide by powers of  $\langle r^n \rangle$  to get dimensionless ratios. The contractions  $a$ ,  $b$  and  $c$  are of order  $N^{-1}$ ,  $N^{-2}$  and  $N^{-3}$  respectively. All of these quantities are positive. The last two contractions  $b$  and  $c$  follow from the non-Gaussian nature of the density fluctuations.

Using eq. (2.40) we can now write the moments (2.33) and (2.34) as

$$\begin{aligned} \langle |\varepsilon_n|^2 \rangle &= a - 2b + 3aa' \\ \langle |\varepsilon_n|^4 \rangle &= 2a^2 + c - 16ab + 20a^2a' , \end{aligned} \quad (2.41)$$

where the first term in both equations is the leading-order term and the subsequent terms are sub-leading corrections. The leading-order result for  $\varepsilon_n\{2\}$  was already computed in ref. [85]:

$$\varepsilon_n\{2\}^2 \equiv \langle |\varepsilon_n|^2 \rangle = a = \frac{\int_z r^{2n} \kappa_2(z)}{\left(\int_z r^n \kappa_1(z)\right)^2} . \quad (2.42)$$

The leading-order terms cancel in the fourth order cumulant:

$$\varepsilon_n\{4\}^4 = -8a^2a' + 8ab - c , \quad (2.43)$$

where we have kept the leading non trivial terms of order  $N^{-3}$ .

If the density fluctuations were Gaussian then  $b$  and  $c$  would vanish. This would result in the fourth-order cumulant being negative. The only positive contribution to the fourth-order cumulant is that of the second term, coming from the three-point function of the density fluctuations. This implies that the measurement of a positive  $v_n\{4\}$  indicates that the density field has positive skew.

**Locality** implies that in the case of identical, pointlike sources, the total number of sources  $N$  follows a Poisson distribution. In this case, all the cumulants are equal,

$$\kappa_n(z) = \langle N \rangle p(z) . \quad (2.44)$$

Eq. (2.40) then reduces to

$$\begin{aligned} a = a' &= \frac{1}{\langle N \rangle} \frac{\langle r^{2n} \rangle}{\langle r^n \rangle^2} \\ b &= \frac{1}{\langle N \rangle^2} \frac{\langle r^{3n} \rangle}{\langle r^n \rangle^3} \\ c &= \frac{1}{\langle N \rangle^3} \frac{\langle r^{4n} \rangle}{\langle r^n \rangle^4} . \end{aligned} \quad (2.45)$$

Inserting these expressions into eq. (2.43), one recovers the first three terms in eq. (2.20), if one replaces  $N$  with  $\langle N \rangle$ . The missing (fourth) term is due to energy conservation.

## 2.5 Monte Carlo simulations

In order to assess the domain of validity of the perturbative results, we perform two sets of Monte Carlo simulations:

- (i) This first case is similar to the case discussed in section 2.3.1. We generate  $N$  identical pointlike sources such that the distribution of sources in the transverse plane  $p(z)$  is isotropic and Gaussian. The only difference with respect to section 2.3.1 is that we do not take  $N$  to be fixed but let it fluctuate according to a Poisson distribution. (We note that  $\varepsilon_2$  is undefined for  $N = 0, 1$  and so we only consider values of  $\langle N \rangle$  large enough to have  $N = 0, 1$  with a probability close to zero.)
- (ii) In order to test the results of the previous section in the more general case where cumulants differ, we generalize eq. (2.10) slightly by letting the energy of each source fluctuate,

$$\rho(z) = \sum_{i=1}^N w_i \delta(z - z_i) , \quad (2.46)$$

where  $w_i$  is the energy of the source  $i$ . In this case the cumulant  $\kappa_n(z)$  scales like  $\langle w^n \rangle$ , see the following subsection. One needs simply to replace  $r^n$  by  $w r^n$  everywhere in eqs. (2.45).

We assume for simplicity that the energy of a source  $w$  and its position  $r$  are independent variables. For simplicity again, we assume that  $w$  is an integer, so that it represents a multiplicity rather than an energy. The probability distribution  $P(w)$  used in our calculations is discussed in the subsection below 2.5.1 and illustrated in figure 2.14. It is chosen in such a way that the total multiplicity  $\sum_{i=1}^N w_i$  follows a negative binomial distribution, according to the observation in high-energy physics experiments [91, 92].

Since the Monte Carlo simulations are the part of the work done by the author of this thesis, we will give quite some details about the relevant computations and the simulations performed.

### 2.5.1 Negative binomial and logarithmic distributions

In this section, we explain how to choose the weights, in an independent-source model, in such a way that the distribution of the total energy is a negative binomial.

The negative binomial distribution of fig. 2.13 is

$$P(w) = \binom{w+k-1}{w} p^w (1-p)^k, \quad (2.47)$$

where  $p$  and  $k$  are two parameters, with  $0 \leq p < 1$  and  $k > 0$ . If two variables  $w_1$  and  $w_2$  are both distributed according to  $P(w)$ , then the sum  $w_1 + w_2$  also follows a negative binomial distribution with the same  $p$  and  $k \rightarrow 2k$ . Thus  $p$  is an intensive quantity and  $k$  an extensive quantity. In the small-volume limit, defined by  $k \rightarrow 0$ , eq. (2.47) reduces to

$$\begin{aligned} P(0) &= 1 + k \ln(1-p) \\ P(w) &= k \frac{p^w}{w} \text{ for } w \geq 1. \end{aligned} \quad (2.48)$$

This distribution is easily generated within the independent source model. The probability of finding a source within the volume is defined as

$$\alpha \equiv 1 - P(0) = \sum_{w=1}^{+\infty} P(w) = -k \ln(1-p). \quad (2.49)$$

One then writes  $P(w) = \alpha P_s(w)$ , where  $P_s(w)$  is the distribution of  $w$  for a single source, with  $w \geq 1$ :

$$P_s(w) = -\frac{1}{\ln(1-p)} \frac{p^w}{w}. \quad (2.50)$$

Eq. (2.50) is a one-parameter distribution known as the logarithmic distribution, shown in figure 2.14. The larger  $p$ , the wider the distribution. Using the same parameters as in ref. [93], one obtains  $p = 0.892$ , which is the value we use throughout this paper. See the following subsection for how to extract this value from [93].

With such weights taken into account, eq. (2.45) is replaced with

$$\begin{aligned} a = a' &= \frac{1}{N_{\text{eff}}} \frac{\langle r^{2n} \rangle}{\langle r^n \rangle^2} \\ b &= \frac{(1+p) \langle r^{3n} \rangle}{N_{\text{eff}}^2 \langle r^n \rangle^3} \\ c &= \frac{(1+4p+p^2) \langle r^{4n} \rangle}{N_{\text{eff}}^3 \langle r^n \rangle^4}, \end{aligned} \quad (2.51)$$

where

$$N_{\text{eff}} \equiv \frac{p \langle N \rangle}{|\ln(1-p)|} \quad (2.52)$$

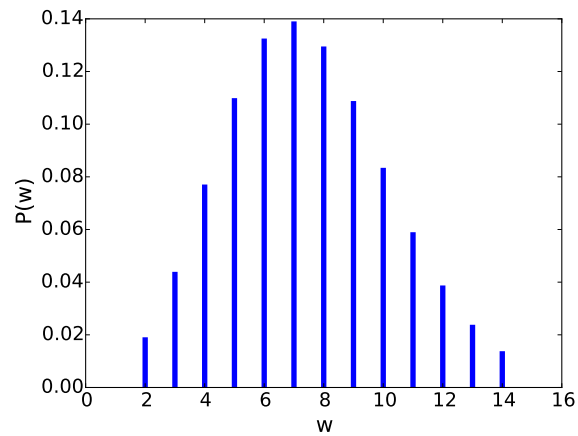


Figure 2.13: The negative binomial distribution, eq. (2.47) with the parameters  $p = 0.892$ ,  $k = 100 \times 0.62$  (see the following subsection) for different values of  $w$ .

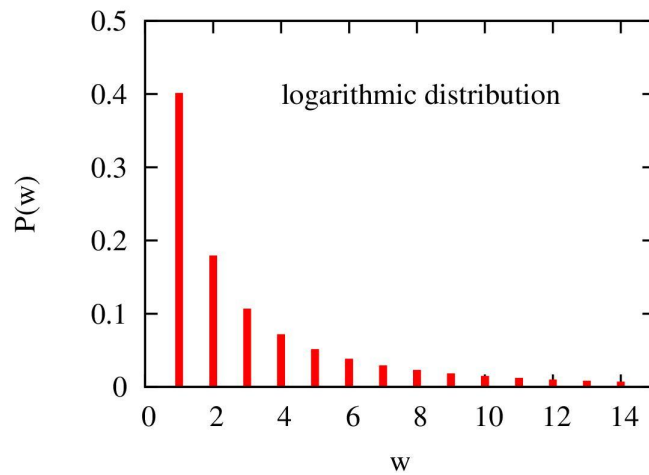


Figure 2.14: The Log Series probability distribution of the energy of a single source, corresponding to eq. (2.50) with the parameter  $p = 0.892$ .

is an effective number of sources [85].

For a Gaussian distribution of sources, eqs. 2.42 and 2.43 give

$$\begin{aligned}\langle N \rangle_{\varepsilon_2} \{2\}^2 &= \frac{2}{N_{\text{eff}}} - \frac{12p}{N_{\text{eff}}^2} \\ \langle N \rangle^3_{\varepsilon_2} \{4\}^4 &= \frac{8(1-3p^2)}{N_{\text{eff}}^3} .\end{aligned}\tag{2.53}$$

The case without fluctuations corresponds to the limit  $p \rightarrow 0$ .

### Extracting the $p$ -value from ref. [93]

The authors of ref. [93] write a negative binomial distribution (NB) as

$$P(s_i) = \frac{\Gamma(s_i - s_0\kappa)(s_0\lambda)^{s_i}(s_0\kappa)^{s_0\kappa}}{\Gamma(s_0\kappa)s_i!(s_0\lambda + s_0\kappa)^{s_i+s_0\kappa}} .\tag{2.54}$$

They further choose parameters

$$\lambda = 5.11 ,\tag{2.55}$$

$$\kappa = 0.62 .\tag{2.56}$$

The mean entropy per participant is

$$\langle s_i \rangle = s_0\lambda .\tag{2.57}$$

We can compare this to eq. (2.47) when we remember that the binomial coefficient can be rewritten as

$$\binom{w+k-1}{w} = \frac{\Gamma(w+k)}{w!\Gamma(k)} ,\tag{2.58}$$

and remembering that the mean of the negative binomial distribution reads

$$\text{mean(NB)} = \frac{kp}{1-p} .\tag{2.59}$$

Now we can equate

$$\langle s_i \rangle = s_0\lambda = \frac{kp}{1-p}\tag{2.60}$$

and furthermore, comparing eqs. (2.47) and (2.54) we see that

$$s_i = w ,\tag{2.61}$$

meaning that we arrive at

$$s_0 \kappa = k . \quad (2.62)$$

Now, combining eqs. (2.60) and (2.62) we get

$$\frac{s_0 \kappa p}{1 - p} = s_0 \lambda , \quad (2.63)$$

implying that

$$p = \frac{\lambda}{\kappa + \lambda} , \quad (2.64)$$

from which we deduce using eqs. (2.55) and (2.56) that

$$p \approx 0.892 , \quad (2.65)$$

a value that we use throughout our simulations.

### 2.5.2 Energy conservation

The condition that all events have the exact same energy,

$$E = \int_z \rho(z) , \quad (2.66)$$

implies that the fluctuation integrates to zero,

$$\int_z \delta \rho(z) = 0 . \quad (2.67)$$

This global constraint breaks locality. Energy conservation adds disconnected terms to the  $n$ -point functions which guarantee that the integral over any of the variables vanishes.

We note that the expression of  $a$  is unchanged, eq. (2.40), so that the leading order anisotropy eq. (2.42) is not affected by energy conservation.

#### Average energy

When the weight of a single source is drawn from a logarithmic distribution, figure 2.14, i.e. the sum of weights follows a negative binomial distribution, figure 2.13,

the average energy can be computed as

$$\begin{aligned}
 \langle E \rangle &= \sum_{k=0}^{\infty} p(k=w) \langle w_k \rangle \\
 &= \sum_{k=0}^{\infty} p(k=w) \sum_{i=1}^k w_i \\
 &= \langle w \rangle \sum_{k=0}^{\infty} k p(k=w) \\
 &= \langle w \rangle \langle N \rangle .
 \end{aligned} \tag{2.68}$$

Here we have

$$\begin{aligned}
 \langle w \rangle &= \sum_{k=1}^{\infty} p(k=w) p_k \\
 &= \sum_{k=1}^{\infty} k \times \frac{-p^k}{k \ln(1-p)} \\
 &= \frac{-1}{\ln(1-p)} \sum_{k=1}^{\infty} p^k \\
 &= \frac{-p}{(1-p) \ln(1-p)} ,
 \end{aligned} \tag{2.69}$$

So it follows that the average energy is

$$\begin{aligned}
 \langle E \rangle &= \langle N \rangle \times \frac{-p}{(1-p) \ln(1-p)} \\
 &= \frac{N_{\text{eff}}}{1-p} .
 \end{aligned} \tag{2.70}$$

### 2.5.3 Writing the program

We use the programming language Python to write the program for Monte Carlo simulations. This is a nice programming language, since it is high-level and does not need compilation. Furthermore, what simplifies the task of writing the program is that there are many handy functionalities in the Python libraries, notably for the generation of random numbers from different probability distributions. We now list some relevant physics notions for the writing and execution of the program.

- *Number of events*

For each point  $N_{\text{sources}}$  (or  $\langle N_{\text{sources}} \rangle$  when considering a Poisson distribution) we generate  $N_{\text{events}} = \text{factor} \times N_{\text{sources}}^2$  events over which the average is then taken. We do this in order to have approximately constant error bars, see the next subsection. We typically choose the factor in this relation to be 100, which gives errorbars  $\propto 1/\sqrt{100}$ .

- *Defining the eccentricity*

We define the eccentricity in a discretized version as

$$\text{eccentricity}(w, z, z_0, n) = \frac{\sum_{i \in \text{events}} w_i (z_i - z_0)^n}{\sum_{i \in \text{events}} w_i |z_i - z_0|^n}, \quad (2.71)$$

where

$$z_0 = \frac{\sum_{i \in \text{events}} w_i z_i}{\sum_{i \in \text{events}} w_i}. \quad (2.72)$$

The user defines whether  $w$  is the unit vector for all events, or whether it varies according to a Log Series distribution. For example, a non-recentered  $\varepsilon_2$  would be  $\text{eccentricity}(w, z, 0, 2)$ .

- *Choice of distribution*

- Gaussian distribution, eq. (2.14):

The points are generated using Python's built-in function `normal`.

- Uniform distribution, eq. (2.23):

We start by generating two points  $x_1$  and  $x_2$  on the real line between 0 and 1. Then we use these to get polar coordinates on a uniform distribution in the unit disk:

$$\begin{aligned} r &= \sqrt{x_1} \\ \phi &= 2\pi x_2, \end{aligned}$$

and then we define Cartesian coordinates

$$\begin{aligned} x &= r \cos \phi \\ y &= r \sin \phi. \end{aligned}$$

## 2.5.4 Numerical errors

Errors are calculated according to the following. Here we use the definitions in eqs (2.8), (2.9).

**Error of  $\epsilon_n\{2\}$** 

We have

$$(\delta \langle \epsilon_n^2 \rangle)^2 = \frac{\langle \epsilon_n^4 \rangle - \langle \epsilon_n^2 \rangle^2}{N_{\text{events}}} \quad (2.73)$$

and

$$\epsilon_n\{2\} = \sqrt{\langle \epsilon_n^2 \rangle}, \quad (2.74)$$

so for small errors we have

$$\delta \epsilon_n\{2\} \approx \frac{1}{2\sqrt{\langle \epsilon_n^2 \rangle}} \sqrt{\frac{\langle \epsilon_n^4 \rangle - \langle \epsilon_n^2 \rangle^2}{N_{\text{events}}}} \quad (2.75)$$

The order of magnitude of the error is

$$\delta N_{\text{sources}} \epsilon_n\{2\}^2 \approx \epsilon_n\{2\}^2 \frac{N_{\text{sources}}}{\sqrt{N_{\text{events}}}} \quad (2.76)$$

From this see that we typically want to take  $N_{\text{events}} \propto N_{\text{sources}}^2$  in order to have error bars whose magnitudes are independent of  $N_{\text{sources}}$ .

**Error of  $\epsilon_n\{4\}$** 

We will suppose that the following holds:

$$\delta \epsilon_n\{4\}^4 \approx \delta \langle \epsilon_n^4 \rangle, \quad (2.77)$$

where

$$(\delta \langle \epsilon_n^4 \rangle)^2 = \frac{\langle \epsilon_n^8 \rangle - \langle \epsilon_n^4 \rangle^2}{N_{\text{events}}}. \quad (2.78)$$

In particular, this means that the error bars of  $\epsilon_n\{4\}$  are asymmetric when considered at second order or higher orders in the error:

$$(\epsilon_n\{4\}^4 - \delta \langle \epsilon_n^4 \rangle)^{1/4} < \epsilon_n\{4\} < (\epsilon_n\{4\}^4 + \delta \langle \epsilon_n^4 \rangle)^{1/4}. \quad (2.79)$$

In particular, this means that the absolute error is

$$\delta \epsilon_n\{4\} |_{\text{abs}} \approx \frac{1}{4} \frac{\delta \langle \epsilon_n^4 \rangle}{\epsilon_n\{4\}^{4.3/4}} \quad (2.80)$$

at first order.

The error of  $N_{\text{sources}}^3 \epsilon_n \{4\}^4$  behaves as

$$N_{\text{sources}}^3 \delta \epsilon_n \{4\}^4 = N_{\text{sources}}^3 \cdot \sqrt{\frac{\langle \epsilon_n^8 \rangle - \langle \epsilon_n^4 \rangle^2}{N_{\text{events}}}} \quad (2.81)$$

$$\sim \frac{N_{\text{sources}}}{\sqrt{N_{\text{events}}}} \quad (2.82)$$

so, again, we see that we want to take  $N_{\text{events}} \propto N_{\text{sources}}^2$  in order to have error bars whose magnitudes are independent of  $N_{\text{sources}}$ .

### 2.5.5 Results of Monte Carlo simulations

We recall the two cases of interest to us in our simulations, defined above at the very beginning of this section 2.5. In the first case (i) we consider the identical, independent sources model. In the second case (ii) we include negative binomial fluctuations of energy. For the first case (i) eqs. (2.43) and (2.45) give

$$\epsilon_n \{4\}^4 = \frac{8}{\langle N \rangle^3} . \quad (2.83)$$

Comparing this with eq. (2.16) we see that the lack of energy conservation decreases  $\epsilon_n \{4\}^4$  by a factor of 2. In figure 2.15 we see that the results from the simulations rapidly converge to the perturbative result eq. (2.83) for large values of  $\langle N \rangle$ . We also note that the effect of energy conservation is small for small  $\langle N \rangle$ .

Furthermore, to study the effect of energy conservation we plot in figure 2.16 the fourth cumulant with  $N$  fluctuating according to a Poisson distribution for two cases: (i) the energy is not fixed and (ii) the energy is exactly fixed to the value in eq. (2.70). We see that the effect of energy conservation is small.

For the second case (ii) above at the very beginning of this section 2.5, figure 2.17 displays our simulation results for  $\epsilon_n \{2\}$  together with the leading-order perturbative result. Contrary to figures 2.11 and 2.15, the convergence is quite slow.

Figure 2.18 shows our result for the fourth power of the fourth cumulant,  $\epsilon_2 \{4\}^4$ . The perturbative result, eq. (2.43), is negative. Monte Carlo results, on the contrary, are positive for  $\langle N \rangle$  up to 256. This shows that the convergence of the perturbative expansion is very slow. For small values  $\langle N \rangle \lesssim 50$  the universal result, eq. (2.18), is quite accurate.

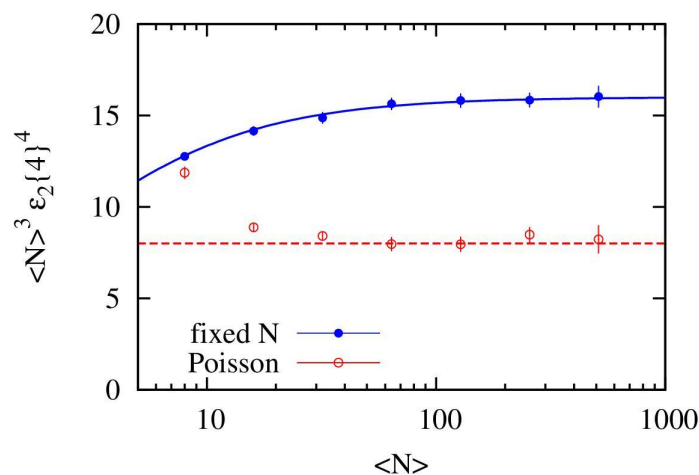


Figure 2.15:  $\langle N \rangle^3 \varepsilon_2\{4\}^4$  versus  $\langle N \rangle$  for an isotropic Gaussian distribution, eq. (2.14). Closed circles correspond to fixed  $N$  and the solid line to the exact result, eq. (2.16). Open circles correspond to  $N$  fluctuating according to a Poisson distribution, and the energy of the system *not* fixed. The dashed line corresponds to the perturbative result, eq. (2.83).

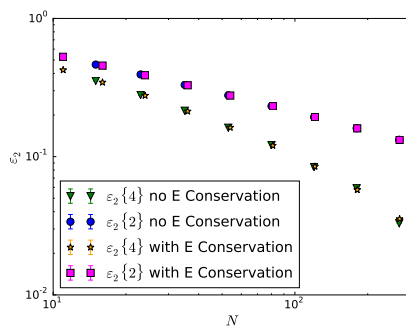


Figure 2.16:  $\varepsilon_2\{2\} \varepsilon_2\{4\}$  versus  $\langle N \rangle$  for an isotropic Gaussian distribution, eq. (2.14) with and without energy conservation. Blue circles and magenta-colored squares correspond to  $\varepsilon_2\{2\}$  without and with energy conservation, respectively. Green triangles and orange stars correspond to  $\varepsilon_2\{4\}$  without and with energy conservation, respectively. Points where energy conservation is taken into account are shifted by one unit in  $N$  for better readability.

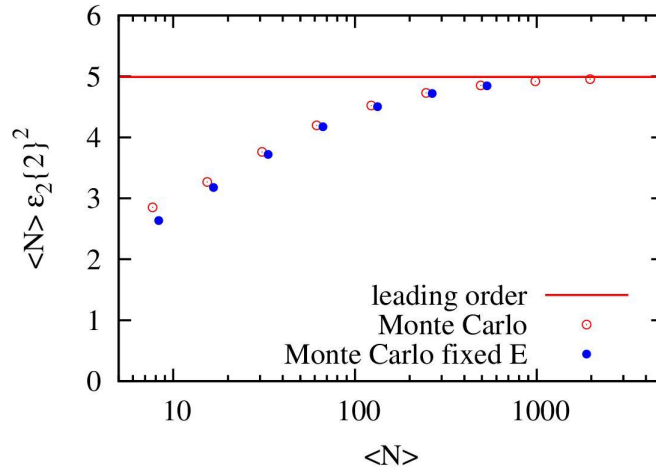


Figure 2.17:  $\langle N \rangle \varepsilon_2\{2\}^2$  versus  $\langle N \rangle$  for an isotropic Gaussian distribution, eq. (2.14). Closed circles correspond to the case with exact energy conservation and open circles to the case without energy conservation. For the sake of readability, the points are slightly shifted with respect to each other. The solid line is the leading-order result.

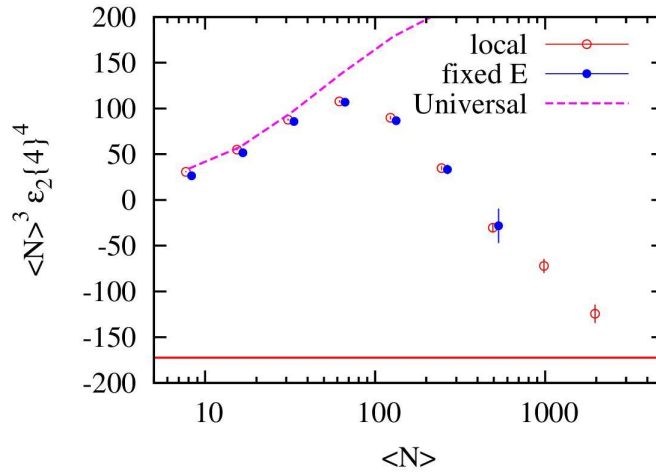


Figure 2.18:  $\langle N \rangle^3 \varepsilon_2\{4\}^4$  versus  $\langle N \rangle$  for an isotropic Gaussian distribution, eq. (2.14). Closed circles correspond to the case with exact energy conservation and open circles to the case without energy conservation. For the sake of readability, the points are slightly shifted with respect to each other. Solid line: perturbative result, eq. (2.53). Dashed line: eq. (2.18).

## 2.6 Conclusions

In this chapter we have studied eccentricity fluctuations and in particular their non-Gaussian nature. As tools in our investigations we have used perturbation theory and Monte Carlo simulations. All the Monte Carlo results presented in this chapter have been for the case of the ellipticity  $\varepsilon_2$ , but we have also checked that the conclusions hold for the triangularity  $\varepsilon_3$ . Our main observations are as follows.

First, we have generalized the results of ref. [88] to a continuous density profile. In doing so, we have assumed that density fluctuations are local. Furthermore, we have argued that the non-Gaussian nature of eccentricity fluctuations comes to a large extent from the non-Gaussianity of density fluctuations. The requirement that the energy of a system be positive naturally generates non-Gaussianities in the form of non zero skewness and kurtosis. The magnitude of these quantities is controlled by the microscopic dynamics of the system.

Secondly, we note that the non-Gaussianities are sensitive to the underlying dynamics. Especially, the sign of the fourth cumulant  $\varepsilon_n\{4\}^4$  varies and it can be negative. We observe a negative fourth power of this fourth cumulant in particular in the presence of large fluctuations in the multiplicity. Monte Carlo simulations suggest that the convergence to this negative value is very slow. They also suggest that results obtained for a few hundred sources, corresponding to the number of participants in a central nucleus-nucleus collision [85], can vary significantly from the perturbative result.

Thirdly, for small systems we observe that the universal statistics proposed in ref. [86] is in general a good approximation. The finding that this universal statistics also is compatible with experimental results on elliptic flow in proton-nucleus collisions [76] further supports the conclusion that elliptic flow in these systems originates from the initial eccentricity  $\varepsilon_2$ .

## Chapter 3

# Hydrodynamical noise and Gubser flow

Collective phenomena are omnipresent in physics and observed in systems that have different temporal and spatial scales ranging from atomic nuclei and biological systems to cosmological scales involving galaxy formation. Loosely speaking, collectivity refers to a common behavior exhibited by a collection of entities such as particles moving with a common direction. The phenomenon of collectivity is often associated with complex many-body systems, for which the basic interactions are well understood. Indeed, a goal of the studies of collectivity is to see how macroscopic behavior arises from microscopic interactions [94]. Indeed, hydrodynamics is a long wavelength late time description of the transport of conserved charges or degrees of freedom. The theory of hydrodynamics lacks many of the excitations of the underlying quantum theory, the excitations that are not conserved [95].

As discussed in the introduction to this part, the paradigm of a strongly coupled, opaque quark-gluon plasma is firmly established for the case of nucleus-nucleus collisions. However, it has been generally expected that the magnitude of collectivity would diminish as the system size decreases, for example for such systems as produced in proton-nucleus collisions. In small systems, the mean free path of constituents can approach the typical size of the system in which case viscous effects become more important and the validity of the hydrodynamical modeling is no longer certain. This is so, because in such tiny systems the presence of large gradients could excite nonhydrodynamic modes or just otherwise spoil the gradient expansion. Such a trend of decreasing collectivity has been measured in peripheral A-A collisions, and no collective flow was anticipated in p-p or p-A collisions. Surprisingly, phenomena that resemble collectivity have recently been measured in high multiplicity

p-p collisions [96]. Subsequent measurements have revealed similar behavior in high multiplicity p-Pb [97, 98, 99] and d-Au [100] collisions at the LHC and at RHIC, respectively.

As stated in [101], addressing the question on collectivity in the smallest hadronic systems will play an important role not only in completing the standard model of strongly coupled quark-gluon plasma matter, but it also provides new opportunities to probe the structure of protons. If the final-state effects described by hydrodynamic flow really are proven to be the dominant source of correlations then the presence of a low viscosity fluid would enable the study of protons and sub-nucleonic fluctuations at very short time scales [102, 103, 104].

The applicability of hydrodynamics in small systems is challenged by more than the presence of possible large gradients: it is also challenged by the presence of noise. Although hydrodynamical noise was introduced a long time ago by Landau and Lifshitz [105, 106] and recently generalized to relativistic systems in [107], it is still mostly neglected in modern hydrodynamic simulations. Since hydrodynamic noise is related to dissipations, it is expected to be larger in small systems and therefore its role in these systems needs to be clarified. The purpose of this chapter is to quantitatively study the effects of thermal noise on different systems. The three systems we will consider are Pb-Pb, p-Pb and p-p at the energies attained at the LHC.

Instead of performing purely numerical computations we will do a semi-analytical study. This we are able to do thanks to the simplified set-up of *Gubser flow* [13, 12]. In this conformal framework one can solve viscous Navier-Stokes fluid dynamics thanks to symmetry simplifications. Indeed, as already mentioned, it is known that at high temperatures, the quark-gluon plasma is nearly conformal. We then add, on top of the Navier-Stokes solution, small perturbations to the flow. We study the effect of these *hydrodynamic fluctuations* on the evolution of the system, and in particular we are interested in the effect the fluctuations have on small systems.

This chapter is organized as follows. Firstly, the theoretical framework of relativistic fluid dynamics is discussed in section 3.1. Secondly, we discuss Gubser flow in section 3.2 and its noisy analogue in section 3.3. Lastly, we finish by numerical results (section 3.4) and conclusions (section 3.5).

Our main observations can be summarized as follows.

We note that the correlation of the noise tensor can be computed thanks to the fluctuation-dissipation theorem and in the Gubser case the tensor structure of the correlator factorizes, leading us to deduce the form of the tensor itself from its auto-correlator. In this way we find that the *magnitude of noise is essentially determined by the multiplicity* of a given collision, and not the size of the system, as one could

have expected from the fluctuation-dissipation theorem.

We solve the Navier-Stokes equations in the presence of noise by doing a mode decomposition. This decomposition is dependent upon the rotational symmetry of the Gubser solution and it simplifies the calculations. In this manner, we get an equation of motion for each mode. The equation of motion resembles a Langevin equation, with a drag and a noise term. We then choose an observable to analyse. Because experiments measure two-particle correlators, we choose to look at a similar quantity: the correlator of radial flow. We are not able to make direct contact with experiments because hydrodynamics describes a continuum with no particles, whereas experiments measure the discrete set of (charged) final state particles, that have come out of hydrodynamics after hadronization and freeze-out. Therefore, not taking into account hadronization or freeze-out, we do the next best thing and choose as an observable the correlator of radial flow. We choose specifically this correlator because we are interested in the transverse expansion of the system.

Throughout this chapter we will use the metric convention  $(-+++)$ .

### 3.1 Introduction to relativistic hydrodynamics

In this section we give an brief introduction of the tools of relativistic hydrodynamics needed for the rest of this chapter. Our main reference is [108] but we also refer the interested reader to refs [109, 110]. We will only focus on aspects necessary for the chapter to follow.

Landau [111] was the first to propose using hydrodynamics for high-energy physics. This is an interesting possibility because relativistic hydrodynamics is simple and general. The simplicity comes from the fact that information about the system is contained in its thermodynamic properties, in the equation of state. The generality comes from the fact that hydrodynamics is based upon only one assumption, though a strong one, that of local thermodynamic equilibrium.

The basic equations of relativistic hydrodynamics are (i) the conservation of energy and momentum and (ii) the equation of state. The first of these reads

$$d_\mu T^{\mu\nu} = 0 . \quad (3.1)$$

where  $T^{\mu\nu}$  is the energy-momentum tensor, whose general form *in the ideal case* is

$$T_{\text{ideal}}^{\mu\nu} = \begin{pmatrix} \epsilon & 0 & 0 & 0 \\ 0 & \mathcal{P} & 0 & 0 \\ 0 & 0 & \mathcal{P} & 0 \\ 0 & 0 & 0 & \mathcal{P} \end{pmatrix} , \quad (3.2)$$

with  $\epsilon$  the energy density and  $\mathcal{P}$  the pressure. Without loss of generality, the derivative  $d_\mu$  is taken to be the covariant one. In flat space the connection coefficients vanish and it just becomes the partial derivative. We will, however, work in curved space time for reasons that will be explained shortly, and therefore one needs to keep track of the connection coefficients  $\Gamma_{\mu\nu}^\lambda$ , when letting the covariant derivative act on an arbitrary tensor  $t_{\mu_1 \dots \mu_q}^{\lambda_1 \dots \lambda_p}$ :

$$d_\nu t_{\mu_1 \mu_2}^{\lambda_1 \lambda_2} = \partial_\nu t_{\mu_1 \mu_2}^{\lambda_1 \lambda_2} + \Gamma_{\nu\kappa}^{\lambda_1} t_{\mu_1 \mu_2}^{\kappa \lambda_2} + \Gamma_{\nu\kappa}^{\lambda_2} t_{\mu_1 \mu_2}^{\lambda_1 \kappa} - \Gamma_{\nu\mu_1}^\kappa t_{\kappa \mu_2}^{\lambda_1 \lambda_2} - \Gamma_{\nu\mu_2}^\kappa t_{\mu_1 \kappa}^{\lambda_1 \lambda_2} , \quad (3.3)$$

as the reader can verify, for example, in Nakahara's book [112].

The equation of state is usually determined from lattice QCD calculations. For a review on the topic see e.g. [113]. However, we do not take a lattice equation of state, which comes close to describing the 'real thing', but use a conformal one:

$$\epsilon = 3\mathcal{P} . \quad (3.4)$$

Note that for this equation of state the energy-momentum tensor is traceless — the hallmark of conformal symmetry. We choose a conformal equation of state because it is required for our analysis in the case of the Gubser flow. This is not a bad assumption to make, in fact, because at high energies conformal symmetry is a good approximation for the QCD matter [114, 115]. By 'high temperatures' here we mean temperatures well above the critical temperature  $\sim 160$  MeV.

In relativistic and viscous hydrodynamics, the energy-momentum tensor can be written as follows,

$$T^{\mu\nu} = \epsilon u^\mu u^\nu + \mathcal{P} \Delta^{\mu\nu} + \Pi^{\mu\nu} , \quad (3.5)$$

with  $u^\mu$  the flow velocity,  $\Delta^{\mu\nu}$  a projection operator,

$$\Delta^{\mu\nu} = u^\mu u^\nu + g^{\mu\nu} , \quad (3.6)$$

and  $\Pi^{\mu\nu}$  the stress tensor encoding dissipative effects. Above  $g_{\mu\nu}$  is the Minkowski metric tensor, for which we use the convention  $(- + + +)$ . The normalization of the flow velocity is:

$$u^\mu u_\mu = -1 . \quad (3.7)$$

With the help of the tensors  $u^\mu$  and  $\Delta^{\mu\nu}$ , we can decompose any vector into directions perpendicular and parallel to the flow velocity, i.e. for a vector  $A^\mu$ ,

$$A^\mu = \Delta^{\mu\alpha} A_\alpha - u^\mu u^\alpha A_\alpha . \quad (3.8)$$

In particular, this can be done for the covariant derivative

$$d_\mu = -u_\mu D + \nabla_\mu , \quad (3.9)$$

where

$$D = u^\mu d_\mu \quad \text{and} \quad \nabla_\mu = \Delta_{\mu\nu} d^\nu . \quad (3.10)$$

For the hydrodynamic equation of motion, eq. (3.1), a similar decomposition gives

$$D u^\mu (\epsilon + \mathcal{P}) + \nabla^\mu \mathcal{P} - \Delta_{\nu}^{\mu} d_{\alpha} \Pi^{\alpha\nu} = 0 \quad (3.11)$$

$$u^\alpha (D\epsilon + (\epsilon + \mathcal{P})\nabla \cdot u + \nabla_{(\mu} u_{\nu)} \Pi^{\mu\nu}) = 0 , \quad (3.12)$$

where the first equation is perpendicular to  $u^\mu$  and the second is parallel to  $u^\alpha$ . Parentheses around indices means that the indices are symmetrized. These are the relativistic versions of Euler's equation and of the continuity equation.

At first order in gradients, the theory is called Navier-Stokes hydrodynamics. In this framework, the shear and the bulk parts of the stress tensor read

$$\Pi^{\mu\nu} = -\eta\sigma^{\mu\nu} - \zeta\Delta^{\mu\nu}\nabla^\alpha u_\alpha , \quad (3.13)$$

where

$$\sigma_{\mu\nu} = 2\nabla_{\langle\mu} u_{\nu\rangle} . \quad (3.14)$$

Here  $\eta$  is the shear viscosity and  $\zeta$  is the bulk viscosity, which in the following we will neglect [116], because we are dealing with a conformally symmetric system. Angular brackets around indices indicate that the tensor is symmetric, traceless and transverse with respect to  $u^\mu$ . The definition of a tensor having such brackets is the following:

$$A^{\langle\mu\nu\rangle} \equiv \frac{1}{2}\Delta^{\mu\alpha}\Delta^{\nu\beta}(A_{\alpha\beta} + A_{\beta\alpha}) - \frac{1}{3}\Delta^{\mu\nu}\Delta^{\alpha\beta}A_{\alpha\beta} . \quad (3.15)$$

Navier-Stokes hydro has the drawback of being acausal [117, 118]. Short wave length perturbation modes, outside of the validity range of the gradient expansion in any case, grow exponentially due to superluminal signal propagation. This leads to physical and numerical instabilities, as explained e.g. in [110]. Any numerical implementation of relativistic viscous hydrodynamics must thus include second order terms in the gradient expansion. The most widely used such frameworks are the Israel-Stewart theory [119, 120] and the BRSSS theory [121]. In BRSSS hydrodynamics, the expression found for the stress tensor is computed using conformal symmetry, and it can be found to depend upon the curvature of the manifold considered. Since we will work in the framework of Navier-Stokes hydrodynamics, we will not go into more detail here. Working at this first-order level is acceptable because we only consider a finite number of hydrodynamic modes, in which case the issue of causality is less significant.

To solve hydrodynamics in practice one needs to solve eq. (3.1). Symmetries can simplify the solution, and indeed there are two cases with a high degree of symmetry

where the hydrodynamical equations of motion are known analytically. These are the Bjorken and Gubser solutions. The Bjorken solution is well known since a long time back, so in what follows we will focus on the more recent Gubser solution.

## 3.2 Gubser flow

### Goal

Our goal is to solve the hydrodynamic equations of motion, eq. (3.1), in a 3+1D set-up mimicking a heavy-ion collision.

### Prerequisites

An important feature that any model of heavy-ion collisions should involve is *medium collective expansion*. The flow is three-dimensional: it is both longitudinal (1D) and transverse (2D). The case with longitudinal flow assuming boost invariance) has been treated long ago by Bjorken [122]. More recently, an idealised 3D version, building upon the Bjorken flow, has been solved by Gubser [12, 13]. This case is idealized because it has *conformal symmetry*. As we have already mentioned, the quark-gluon plasma is to a good approximation conformal in the early stages of a heavy-ion collision, so the Gubser solution is of phenomenological interest. The Gubser solution furthermore assumes a rotational symmetry around the beam axis, which means that it is applicable for proton-proton, proton-nucleus and ultra-central nucleus-nucleus collisions. Therefore, as a natural continuation of chapter 2, we continue to assume that this symmetry holds.

### Method

Conformal invariance is a key feature of the Gubser solution, because it relates the Minkowski, the de Sitter (dS) and the anti-de Sitter (AdS) metrics. Conformal invariance means that the dynamics of the system is invariant under Weyl rescalings of the metric:

$$g_{\mu\nu} \rightarrow \Omega^{-2} g_{\mu\nu} , \quad (3.16)$$

where the parameter  $\Omega$  may vary in space and time. This is of importance to us because, in fact, *the fluid that is expanding in all three spatial dimensions in Minkowski space actually is a fluid at rest in de Sitter space time*. We will therefore choose to work in this de Sitter space, where thanks to the fact that the flow is static, the equations of motion (see eq. (3.1)) simplify. Then, through a coordinate transformation,

we are able to map this static de Sitter flow onto Minkowski space, and recover a flow that is much like the one observed in heavy-ion collisions. Thanks to the symmetry of the Gubser solution, the solution of eq. (3.1) simplifies and we are able to add a supplementary degree of difficulty: we will add small hydrodynamical perturbations on top of the flow. We then study in detail the effect that these perturbations have on the evolution of the system, and in particular we study small systems, where a priori the effect of thermal noise is expected to be at its strongest.

### 3.2.1 Coordinate transformations

First of all, let us see how the Minkowski and de Sitter spaces are related. Once we have the correct coordinate transformation relating the two manifolds, we can write down the metric on the de Sitter space. From this metric we read off the symmetries, and this directly gives us the flow velocity, from which we solve the equation of motion, eq. (3.1).

The original Minkowskian manifold  $\mathbb{R}^{3,1}$  has the metric

$$ds^2 = -d\tau^2 + \tau^2 d\xi^2 + d\vec{x}_\perp^2, \quad (3.17)$$

where  $\tau$  is the proper time and  $\xi$  is the spatial rapidity, defined as

$$\tau = \sqrt{t^2 - z^2}, \quad (3.18)$$

$$\xi = \frac{1}{2} \ln \frac{t+z}{t-z}, \quad (3.19)$$

and  $\vec{x}_\perp = (x^1, x^2)$  parametrizes the transverse plane. Now we make a Weyl rescaling 3.16 such that

$$g_{\mu\nu} \rightarrow \tilde{g}_{\mu\nu} = \tau^{-2} g_{\mu\nu} \quad (3.20)$$

so that the metric 3.17 reads

$$d\tilde{s}^2 = \underbrace{\frac{1}{\tau^2} [-d\tau^2 + d\vec{x}_\perp^2]}_{\text{like 3D de Sitter}} + \underbrace{d\xi^2}_{\mathbb{R}^1}. \quad (3.21)$$

At this point, in order to motivate the comment ‘like 3D de Sitter’ in the equation above, we note that the de Sitter space  $dS_3$  corresponds to the equation

$$-(X^0)^2 + \sum_{m=1}^3 (X^m)^2 = 1, \quad (3.22)$$

with the line element

$$ds^2 = \frac{1}{t^2} [-dt^2 + dy_\perp^2] . \quad (3.23)$$

Wanting to go to the conformal manifold  $dS_3 \times \mathbb{R}^1$  from the manifold in eq. (3.21), we see that the terms in the brackets of (3.21) look like the  $dS_3$  line element, eq. (3.23), and we can obtain the  $dS_3$  space if we do the following coordinate transformations:

$$\begin{aligned} X^0 &= -\frac{1 - q^2\tau^2 + q^2\vec{x}_\perp^2}{2q\tau} = \sinh \rho , \\ X^1 &= \frac{x_\perp^1}{\tau} = \cosh \rho \sin \theta \cos \phi , \\ X^2 &= \frac{x_\perp^2}{\tau} = \cosh \rho \sin \theta \sin \phi , \\ X^3 &= \frac{1 + q^2\tau^2 - q^2\vec{x}_\perp^2}{2q\tau} = \cosh \rho \cos \theta . \end{aligned} \quad (3.24)$$

Now we have the metric

$$d\hat{s}^2 = \underbrace{-d\rho^2 + d\xi^2}_{SO(1,1) \times \mathcal{Z}_2} + \underbrace{\cosh^2 \rho (d\theta^2 + \sin^2 \theta d\phi^2)}_{SO(3)} , \quad (3.25)$$

where we write quantities in this new coordinate system with hats. In particular, we denote the metric giving rise to the line-element in eq. (3.25) by  $\hat{g}_{\mu\nu}$ . In eq. (3.25) we have also written down the symmetries that this metric has. The full symmetry of this Gubser solution is thus

$$SO(1,1) \times \mathcal{Z}_2 \times SO(3) . \quad (3.26)$$

The complete symmetry, eq. (3.26), of the Gubser solution implies that *any* hydrodynamic quantity in the ‘hat’ system only depends on the de Sitter time  $\rho$ .

In order to satisfy the  $SO(3)$  symmetry we choose a flow velocity that is independent of the angles  $\theta$  and  $\phi$  on the sphere. Furthermore, to satisfy the  $SO(1,1) \times \mathcal{Z}_2$  boost invariance of the solution, we choose the flow velocity such that it is independent of the spatial rapidity  $\xi$ . We are thus left with only one nonzero component, that is the de Sitter-time component  $\hat{u}_\rho$ , which is fixed by the normalization constraint (3.7):

$$\hat{u}_\rho = -1 , \quad \hat{u}_\xi = \hat{u}_\theta = \hat{u}_\phi = 0 . \quad (3.27)$$

So, the idea of Gubser is the following. Let us work in this de Sitter space  $dS_3 \times \mathbb{R}^1$  where the flow has this nice, static form. Then, once we have solved the equations of motion, eq. (3.1), we make a coordinate transformation back to Minkowski

space, according to eqs (3.24), and find a fluid that is expanding in all three spatial directions.

Now we have the flow velocity, eq. (3.27), and the equation of state, eq. (3.4), we can proceed to compute the equations of motion, eq. (3.1). To do so, we need to evaluate covariant derivatives of the flow velocity, see eqs. (3.11), (3.12). To this end, we therefore evaluate the connection coefficients, also known as Christoffel symbols, of the metric (3.25). Once we have the Christoffel symbols, we can evaluate the effect of dissipation, eq. (3.13).

### 3.2.2 Christoffel symbols and the covariant derivative

At this stage, let us define the spatial projection operator  $\hat{\Delta}^{\mu\nu}$ :

$$\hat{\Delta}_{\rho\rho} = \hat{\Delta}^{\rho\rho} = 0, \quad \text{otherwise} \quad \hat{\Delta}_{\mu\nu} = \hat{g}_{\mu\nu}. \quad (3.28)$$

In 4-dimensional Minkowski space with our metric convention this projection operator will simply be

$$\hat{\Delta}^{\mu\nu} = \text{diag}[0, 1, 1, 1]. \quad (3.29)$$

We now list the nonzero Christoffel symbols of the metric (3.25),

$$\begin{aligned} \hat{\Gamma}_{\theta\theta}^{\rho} &= \cosh \rho \sinh \rho, & \hat{\Gamma}_{\phi\phi}^{\rho} &= \cosh \rho \sinh \rho \sin^2 \theta \sin^2 \phi, \\ \hat{\Gamma}_{\rho\theta}^{\theta} &= \hat{\Gamma}_{\theta\rho}^{\theta} = \tanh \rho, & \hat{\Gamma}_{\phi\phi}^{\theta} &= \sin \theta \cos \theta, \\ \hat{\Gamma}_{\rho\phi}^{\phi} &= \hat{\Gamma}_{\phi\rho}^{\phi} = \tanh \rho, & \hat{\Gamma}_{\theta\phi}^{\phi} &= \hat{\Gamma}_{\phi\theta}^{\phi} = \cot \theta. \end{aligned} \quad (3.30)$$

Using these symbols we can now compute the derivatives of the flow velocity, needed for  $\sigma^{\mu\nu}$ , eq (3.14):

$$d_{\theta}\hat{u}^{\theta} = \tanh \rho, \quad d_{\phi}\hat{u}^{\phi} = \tanh \rho, \quad \text{zero otherwise}, \quad (3.31)$$

and

$$\begin{aligned} \nabla_{\theta}\hat{u}_{\theta} &= \cosh \rho \sinh \rho = \hat{\Delta}_{\theta\theta} \tanh \rho, \\ \nabla^{\theta}\hat{u}^{\theta} &= \hat{\Delta}^{\theta\theta} \tanh \rho, \\ \nabla_{\phi}\hat{u}_{\phi} &= \hat{\Delta}_{\phi\phi} \tanh \rho, \\ \nabla^{\phi}\hat{u}^{\phi} &= \hat{\Delta}^{\phi\phi} \tanh \rho, \\ \nabla \cdot \hat{u} &= 2 \tanh \rho. \end{aligned} \quad (3.32)$$

From these we can now read off the tensor structure of the shear stress tensor:

$$\sigma^{\theta\theta} = \frac{2}{3}\hat{\Delta}^{\theta\theta} \tanh \rho, \quad \sigma^{\phi\phi} = \frac{2}{3}\hat{\Delta}^{\phi\phi} \quad \text{and} \quad \sigma^{\xi\xi} = -\frac{4}{3}\hat{\Delta}^{\xi\xi} \tanh \rho. \quad (3.33)$$

Now we have all the information needed for solving the equations of motion (3.11) and (3.12). Let us proceed to doing just that.

### 3.2.3 Solution to Gubser flow

#### Inviscid case

The symmetry  $SO(3) \times SO(1,1) \times \mathcal{Z}_2$  forces all other components of the equation of motion (3.1) to vanish except for the  $\rho$  component:

$$d_\mu \hat{T}_0^{\mu\rho} = 0, \quad (3.34)$$

where we already anticipate the solution that includes noise by denoting  $\hat{T}_0^{\mu\rho}$  with a subscript ‘0’, meaning that this is the event averaged, noise-less part of the energy-momentum tensor. At this point we also recall that all quantities living on the manifold parametrized by the metric (3.25) are denoted by hats. Therefore,  $\hat{T}^{\mu\rho}$  is just the energy-momentum tensor in the dS space time and in the following  $\hat{\epsilon}$  is the energy density in that same space time. Eq. (3.34) turns out to be the continuity equation,

$$\begin{aligned} \hat{u}^\alpha \partial_\alpha \hat{\epsilon} &= -(\hat{\epsilon} + \hat{\mathcal{P}}) \hat{d}_\mu \hat{u}^\mu \\ \partial_\rho \hat{\epsilon} &= -2(\hat{\epsilon} + \hat{\mathcal{P}}) \tanh \rho. \end{aligned} \quad (3.35)$$

Taking into account the conformal symmetry,  $\hat{\epsilon} = 3\hat{\mathcal{P}}$ , this gives

$$\hat{\epsilon}(\rho) = \hat{\epsilon}_0 (\cosh \rho)^{-\frac{8}{3}}. \quad (3.36)$$

#### Viscous case: Navier-Stokes hydrodynamics

Now the equation of motion (3.1) gives

$$D\hat{\epsilon} + (\hat{\epsilon} + \hat{\mathcal{P}}) \hat{d}_\mu \hat{u}^\mu + \nabla_{(\mu} \hat{u}_{\nu)} \hat{\Pi}^{\mu\nu} = 0. \quad (3.37)$$

Using eqs. (3.32), (3.33) and (3.13), the viscous correction to the eq. (3.37) reads

$$\begin{aligned} \nabla_{(\mu} \hat{u}_{\nu)} \hat{\Pi}^{\mu\nu} &= \nabla_\theta \hat{u}_\theta (-\hat{\eta} \sigma^{\theta\theta}) + \nabla_\phi \hat{u}_\phi (-\hat{\eta} \sigma^{\phi\phi}) \\ &= -\frac{2\hat{\eta}}{3} \tanh^2 \rho \left( \hat{\Delta}_{\theta\theta} \hat{\Delta}^{\theta\theta} + \hat{\Delta}_{\phi\phi} \hat{\Delta}^{\phi\phi} \right) \\ &= -\frac{4}{3} \hat{\eta} \tanh^2 \rho. \end{aligned} \quad (3.38)$$

Here the sum in the square brackets is not very hard to do when one realizes that the trace of  $\hat{\Delta}^{\mu\nu}$  is Lorentz invariant and equal to 3 and  $\hat{\Delta}^{\xi\xi}\hat{\Delta}_{\xi\xi} = 1$ . Substituting eq. (3.38) into eq. (3.37) we get

$$\partial_\rho \hat{\epsilon} + 2(\hat{\epsilon} + \hat{\mathcal{P}}) \tanh \rho - \frac{4}{3} \hat{\eta} \tanh^2 \rho = 0 . \quad (3.39)$$

To solve this equation we proceed by doing two changes of variables. First, we rewrite the viscosity as

$$\hat{\eta} = H_0 \hat{T}^3 . \quad (3.40)$$

Second, we note that the energy density is defined with respect to the temperature in the hatted coordinate system as

$$\hat{\epsilon} = \hat{T}^4 . \quad (3.41)$$

When making these changes of variables, eq. (3.39) reduces to

$$4\partial_\rho \hat{T}(\rho) + \frac{4}{3} \tanh \rho \cdot \hat{T}(\rho) - \frac{4}{3} H_0 \tanh^2 \rho = 0 . \quad (3.42)$$

Thanks to the fact that we know the solution to the ideal equation of motion eq. (3.36), that is, we know the solution to the homogeneous partial differential equation, we can now solve eq. (3.42) and the solution reads

$$\hat{T}(\rho) = (\cosh \rho)^{-\frac{2}{3}} \left( \hat{T}_0 + \frac{1}{3} H_0 F_d(\rho) \right) . \quad (3.43)$$

Here the function  $F_d$  is

$$F_d(\rho) = \int_0^\rho dr (\cosh r)^{\frac{2}{3}} \tanh^2 r = \frac{1}{3} \sinh^3 \rho {}_2F_1 \left( \frac{3}{2}, \frac{7}{6}; \frac{5}{2}; -\sinh^2 \rho \right) \quad (3.44)$$

### Solution in Minkowski space-time

To see what the solution eq. (3.43) looks like in 4D Minkowski space  $\mathcal{M}_4$  we need to know how the coordinates transform between the hatted ones and those of  $\mathcal{M}_4$ . We note that the transformation of the azimuthal angle and the spatial rapidity is trivial. The coordinates  $(\rho, \theta)$ , however, have more interesting transformations, see eq. (3.24):

$$\begin{aligned} \sinh \rho &= -\frac{1 - q^2 \tau^2 + q^2 r^2}{2q\tau} , \\ \tan \theta &= \frac{2qr}{1 + q^2 \tau^2 - q^2 r^2} . \end{aligned} \quad (3.45)$$

The relevant phase space in terms of coordinates  $(\theta, \rho)$  is depicted in figure 3.1.

In eq. (3.45) there is one dimensionful parameter specifying the coordinate transformations. This is the momentum scale  $q$ , whose inverse specifies the approximate transverse size of the system.

The Gubser solution has another parameter  $\hat{T}_0$ , which together with  $q$ , determines the system completely.  $\hat{T}_0$  is the background temperature.

The energy density and velocity fields transform as follows:

$$\begin{aligned} \epsilon &= \tau^{-d} \hat{\epsilon} \\ u_\tau &= \tau \left( \frac{\partial \rho}{\partial \tau} \hat{u}_\rho + \frac{\partial \theta}{\partial \tau} \hat{u}_\theta \right) \\ u_\perp &= \tau \left( \frac{\partial \rho}{\partial \vec{x}_\perp} \hat{u}_\rho + \frac{\partial \theta}{\partial \vec{x}_\perp} \hat{u}_\theta \right) \\ u_{\phi_i} &= \tau \hat{u}_{\phi_i} \\ u_\xi &= \tau \hat{u}_\xi . \end{aligned} \tag{3.46}$$

In particular, the first of these relations implies that  $T = \tau^{-1} \hat{T}$ . Since  $\hat{T}$  is dimensionless, as we will see, this means that  $T$  has the dimension of  $\text{fm}^{-1}$ .

From the above relations we can now get the velocity fields in Minkowski space, by first noting that

$$\cosh \rho = \frac{[1 + 2q^2(\tau^2 + r^2) + q^4(\tau^2 + r^2)^2]^{1/2}}{2q\tau}, \tag{3.47}$$

$$\cos \theta = \frac{1 + q^2\tau^2 - q^2r^2}{[1 + 2q^2(\tau^2 + r^2) + q^4(\tau^2 + r^2)^2]^{1/2}}, \tag{3.48}$$

and

$$d\rho = \frac{1}{2q\tau \cosh \rho} [-2q^2\tau r dr + (1 + q^2\tau^2 + q^2r^2)d\tau], \tag{3.49}$$

$$d\theta = \frac{2q \cos^2 \theta}{(1 - q^2\tau^2 + q^2r^2)} [(1 - q^2\tau^2 - q^2r^2)dr + 2q^2\tau r d\tau], \tag{3.50}$$

one finds the flow velocities

$$u_\tau = -\frac{(1 + q^2\tau^2 + q^2r^2)}{[1 + 2q^2(\tau^2 + r^2) + q^4(\tau^2 - r^2)^2]^{1/2}}, \tag{3.51}$$

$$u_\perp = \frac{2q^2r\tau}{[1 + 2q^2(\tau^2 + r^2) + q^4(\tau^2 - r^2)^2]^{1/2}}. \tag{3.52}$$

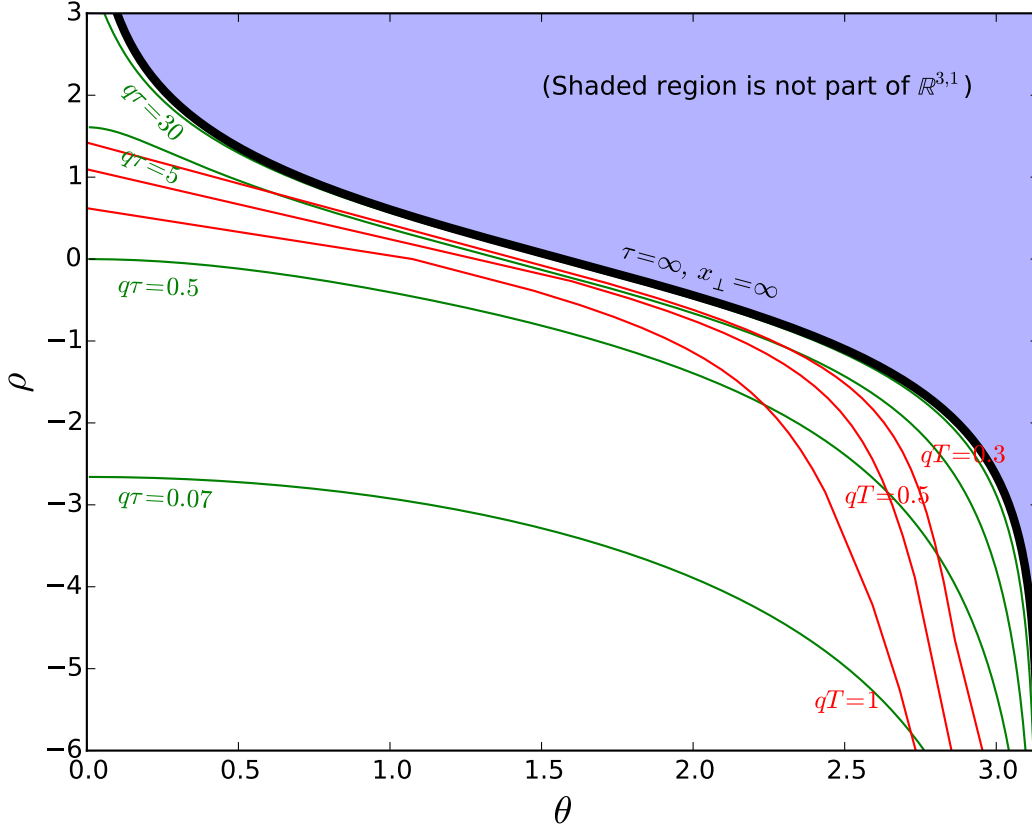


Figure 3.1: The analogue of figure 5 of ref. [12] for LHC energies: An approximate history of an ultra-central heavy-ion collision as seen in the  $dS_3 \times \mathbb{R}$  conformal space time. The blue region is not a part of  $\mathbb{R}^{3,1}$ . Hydrodynamics is applicable in a region between the correctly chosen green and red curves, according to the system under consideration (note that  $q$  varies between different systems, see table 3.4). We recall that  $q$  is a parameter whose inverse gives the approximate transverse size of the system. Note that the constant proper time and constant temperature curves are distinct and do not coincide. On the curves of constant proper time, the radial coordinate  $r$  grows as  $\theta$  grows. Looking at the intersections between a given  $q\tau=\text{constant}$  curve and the different  $qT=\text{constant}$  curves, we see that freeze-out occurs at the periphery of the medium first. See appendix B for details of how this figure was made.

From eqs. (3.43), (3.46), (3.45) we can find the energy density as

$$\epsilon(\tau, r) = \tau^{-d} \hat{\epsilon}(\rho \rightarrow (\tau, r)) \quad \text{and} \quad \hat{\epsilon}(\rho) = \hat{T}^4(\rho) . \quad (3.53)$$

The behavior of the energy density and the radial flow velocity in the transverse plane are shown in figure 3.2.

### 3.3 Noisy flow

In previous sections we have solved the equations of motion for the Gubser flow. We thus know the expressions for the flow velocity (3.27), the temperature (3.43) or equivalently the energy density (3.41). The formal solution of these equations was done in a de Sitter type space time because there the relevant equations simplify immensely, thanks to the fact that the expanding flow of Minkowski space time is static in this  $dS_3 \times \mathbb{R}^1$  space time. We have also seen what the flow velocity and energy density look like in Minkowski space, eqs (3.51), (3.52) and (3.53), see also figure 3.2.

Having this background solution written down, we can now proceed to adding a degree of difficulty to the equations: we will add small perturbations on top of this background. These perturbations are *hydrodynamic fluctuations*, present in any system with a positive temperature. We will take these perturbations to be small and solve the equations of motion (3.1) once more, but now in the presence of small fluctuations. In the following we will first review some tools needed in section 3.3.1, and then proceed to computing the perturbed Gubser flow in section 3.3.2. One of our main interests in doing so is to figure out the effect of noise in small systems, where the well-known fluctuation-dissipation theorem predicts a strong influence of noise, thus possibly invalidating the application of hydrodynamics on such small systems.

#### 3.3.1 Introduction to noisy hydrodynamics

This section is based on ref. [107], which generalizes the discussion of ref. [105, 106] to the relativistic set-up. For simplicity, we will assume explicit conformal symmetry (see the conformal equation of state, eq. (3.4)) and work in the Landau-Lifshitz frame, where

$$u_\mu T^{\mu\nu} = -u^\nu \epsilon , \quad (3.54)$$

and

$$u_\mu \Pi^{\mu\nu} = 0 . \quad (3.55)$$

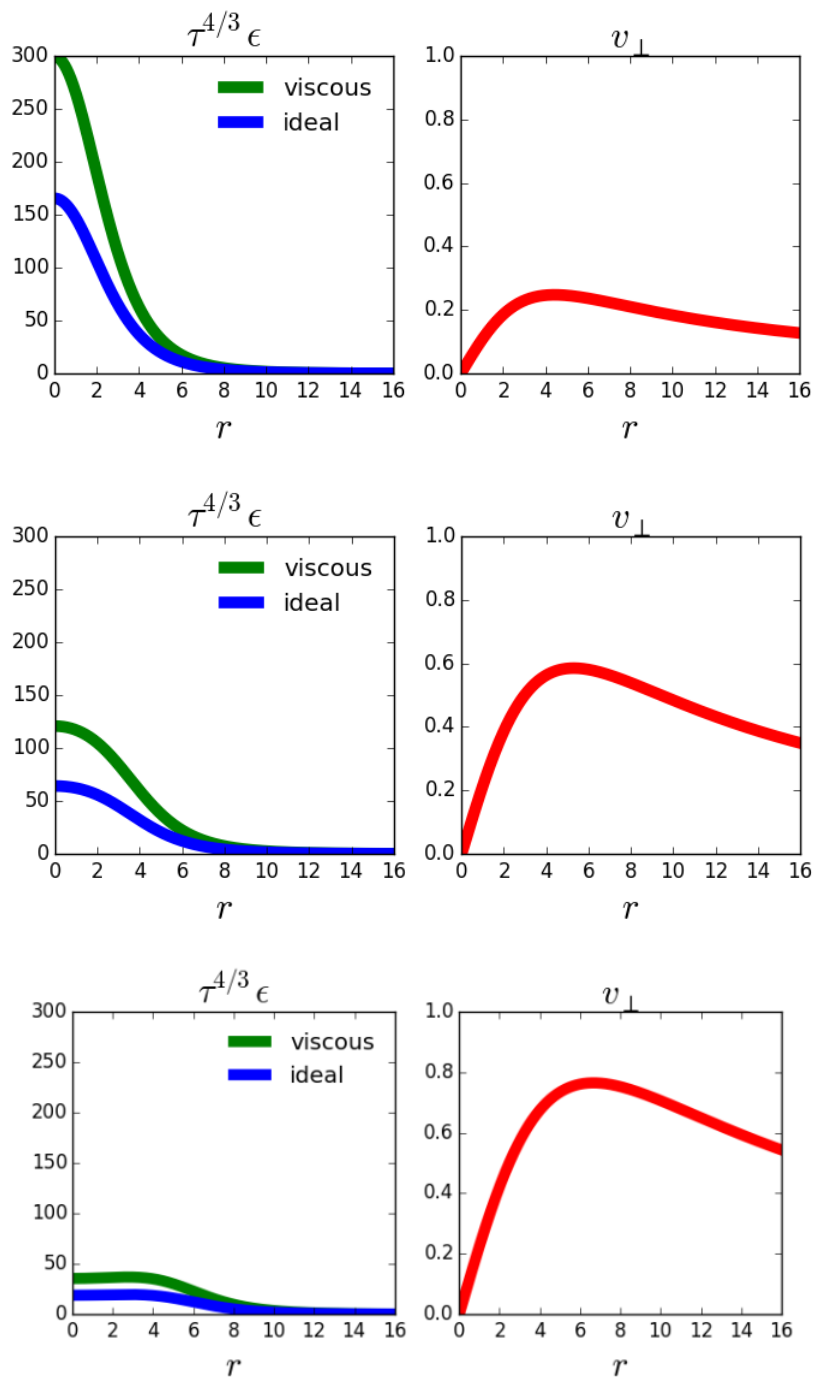


Figure 3.2: Energy density  $\epsilon$  multiplied by a power of the proper time (left) and the radial flow velocity  $v_{\perp} \equiv u_{\perp}/u_{\tau}$  for the ideal and the viscous case at three different proper times  $\tau = 1$  fm/c, 3 fm/c and 5 fm/c. Note that the peak of the energy density moves towards larger radii as times goes on, reflecting the fact that the system is expanding. Also note that, with time, the radial flow velocity tends towards the speed of light in the periphery of the QGP.

We then add fluctuations to the hydrodynamic variables:

$$\begin{aligned} T(x) &= T_0(x) + \delta T(x) \\ \epsilon(x) &= \epsilon_0(x) + \delta\epsilon(x) \end{aligned} \quad (3.56)$$

$$\mathcal{P}(x) = \mathcal{P}_0(x) + \delta\mathcal{P}(x) . \quad (3.57)$$

These fluctuations imply that also the dynamical quantities fluctuate,

$$\begin{aligned} u^\mu(x) &= u_0^\mu(x) + \delta u^\mu(x) \\ \Pi^{\mu\nu} &= \Pi_0^{\mu\nu} + S^{\mu\nu} . \end{aligned} \quad (3.58)$$

We note that the hydrodynamical noise term  $S^{\mu\nu}$  is introduced with respect to  $\Pi^{\mu\nu}$ . Taking into account these fluctuations, we arrive at a new expression for the energy-momentum tensor,

$$T^{\mu\nu} = T_0^{\mu\nu} + \delta T^{\mu\nu} . \quad (3.59)$$

Here, as before,  $T_0^{\mu\nu}$  denotes an event-averaged quantity, the ‘background’ temperature, and now  $\delta T^{\mu\nu}$  is determined by thermal fluctuations. We will treat  $\delta T^{\mu\nu}$  as a small quantity and do perturbation theory, which is valid as long as we are far away from a phase transition [123].

We note that the fluctuating thermal quantities eqs (3.56) are related through the equation of state,

$$\delta\epsilon = \bar{c}_v \delta T , \quad \delta s = \frac{\bar{c}_v}{T} \delta T , \quad \delta\mathcal{P} = s(T) \delta T \quad (3.60)$$

and further related to  $S^{\mu\nu}$  through the hydrodynamic equation of motion,

$$d_\mu(\delta T^{\mu\nu}) = 0 , \quad (3.61)$$

where  $\delta T^{\mu\nu}$  has two parts: (i) terms induced by thermal fluctuations of hydro variables and (ii)  $S^{\mu\nu}$ . This equation, in the decomposition ‘perpendicular and parallel to the flow velocity’, eqs. (3.11) and (3.12), gives the following two equations,

$$[\delta w D u_\alpha + w \delta u^\mu d_\mu u_\alpha + (D w + w \partial \cdot u) \delta u_\alpha + \nabla \delta \mathcal{P} + w D \delta u_\alpha + d_\mu (\delta \Pi_\alpha^\mu + S_\alpha^\mu)] \Delta^{\nu\alpha} = 0 \quad (3.62)$$

$$[D \delta \epsilon + \delta w \partial \cdot u + d_\mu (w \delta u^\mu) + w \delta u^\alpha D u_\alpha - u^\alpha d_\mu (\delta \Pi_\alpha^\mu + S_\alpha^\mu)] u^\nu = 0 . \quad (3.63)$$

Here we have neglected the subscript ‘0’ for the event-averaged quantities for the sake of simplifying the notation. Note that the transversality of the first equation can be seen when noting that

$$u^\mu \delta u_\mu = 0 , \quad (3.64)$$

which follows directly from the normalization constraint eq. (3.7),

$$(u + \delta u)^2 = -1 . \quad (3.65)$$

For Navier-Stokes hydrodynamics, to linear order in thermal fluctuations, we can write (see eq. (3.13))

$$\delta \Pi^{\mu\nu} = -\delta \eta \sigma^{\mu\nu} - \eta \delta \sigma^{\mu\nu} , \quad (3.66)$$

where

$$\delta \sigma^{\mu\nu} = 2 \nabla^{\langle \mu} \delta u^{\nu \rangle} + 2 \left[ \delta u^\alpha \nabla^{\langle \mu} u_{\alpha} u^{\nu \rangle} + d_\alpha u^{\langle \mu} \delta(u^{\nu \rangle} u^\alpha) - \frac{1}{3} \partial \cdot u \delta(u^\mu u^\nu) \right] . \quad (3.67)$$

The auto-correlator of noise is given by the fluctuation-dissipation theorem,

$$\langle S^{\mu\nu}(x_1) S^{\alpha\beta}(x_2) \rangle = 4T \eta \Lambda^{\mu\nu\alpha\beta} \delta(x_1 - x_2) \quad (3.68)$$

while  $\langle S^{\mu\nu}(x) \rangle = 0$ . The brackets here indicate an ensemble average and the tensor structure of  $\Lambda^{\mu\nu\alpha\beta}$ , constrained by the form of the shear tensor  $\pi^{\mu\nu}$ , can in general be involved. However, for Navier-Stokes hydrodynamics one finds that

$$\Lambda^{\mu\nu\alpha\beta} = \Delta^{\mu\nu\alpha\beta} , \quad (3.69)$$

where

$$\Delta^{\mu\nu\alpha\beta} = \frac{1}{2} [\Delta^{\mu\alpha} \Delta^{\nu\beta} + \Delta^{\mu\beta} \Delta^{\nu\alpha}] - \frac{1}{3} \Delta^{\mu\nu} \Delta^{\alpha\beta} . \quad (3.70)$$

### 3.3.2 Noisy Gubser flow

The symmetry of the Gubser solution leads to simplifications in the treatment of noise, as it did in the treatment of the background. In particular, the tensor to which the noise-noise correlator is proportional factorizes,

$$\hat{\Delta}^{\mu\nu\alpha\beta} \propto \hat{P}^{\mu\nu} \hat{P}^{\alpha\beta} , \quad (3.71)$$

where we continue to use the notation where quantities in the de Sitter space time are denoted by hats and  $\hat{P}^{\mu\nu}$  is just a diagonal tensor:

$$\hat{P}^{\mu\nu} = \text{diag} [0, 1, 1, -2] . \quad (3.72)$$

This factorization is due to the fact that the flow is static in the hatted frame. Therefore, the noise-noise auto-correlator reads,

$$\begin{aligned} \left\langle \hat{S}^{\mu\nu}(\rho_1, \theta_1, \phi_1, \xi_1) \hat{S}^{\alpha\beta}(\rho_2, \theta_2, \phi_2, \xi_2) \right\rangle &= \frac{2\nu \hat{T} \hat{s}}{\cosh^2 \rho_1 \sin \theta_1} \hat{P}^{\mu\nu} \hat{P}^{\alpha\beta} \delta(\rho_1 - \rho_2) \times \\ &\times \delta(\theta_1 - \theta_2) \delta(\phi_1 - \phi_2) \delta(\xi_1 - \xi_2) , \end{aligned} \quad (3.73)$$

so we can write

$$\hat{S}^{\mu\nu}(\rho, \theta, \phi, \xi) = \hat{w}(\rho) \hat{f}(\rho, \theta, \phi, \xi) \hat{P}^{\mu\nu} . \quad (3.74)$$

We note that, as a consequence of the factorization of the tensor structure in eq. (3.73), the hydrodynamical noise only affects scalar modes. This is a particularity of the Gubser solution and is not true in general, when the tensor structure of eq. (3.73) is more complicated, leading to fluctuations in both vector and scalar modes.

The interesting fluctuating part of (3.74) is now encoded in the scalar function  $\hat{f}$ , whose auto-correlator is

$$\begin{aligned} \left\langle \hat{f}(\rho_1, \theta_1, \phi_1, \xi_1) \hat{f}(\rho_2, \theta_2, \phi_2, \xi_2) \right\rangle &= \frac{2\nu}{\hat{w} \cosh^2 \rho_1 \sin \theta_1} \delta(\rho_1 - \rho_2) \times \\ &\times \delta(\theta_1 - \theta_2) \delta(\phi_1 - \phi_2) \delta(\xi_1 - \xi_2) . \end{aligned} \quad (3.75)$$

Here the enthalpy density  $\hat{w}$  is used to saturate the conformal dimension, even though quantities in the hatted system are dimensionless by construction.

Considering in particular the  $SO(3)$  part of the symmetry of the Gubser solution, we note that a mode decomposition can be done in terms of spherical harmonics. Decomposing the scalar function  $\hat{f}(\rho, \theta, \phi, \xi)$  in this manner, we have

$$\hat{f}(\rho, \theta, \phi, \xi) = \sum_{\ell=0}^{\infty} \sum_{m=-\ell}^{\ell} \int \frac{dk_{\xi}}{2\pi} h_{\ell m}(\rho, k_{\xi}) Y_{\ell m}(\theta, \phi) e^{ik_{\xi}\xi} , \quad (3.76)$$

where we have used the following convention for the spherical harmonics:

$$Y_{\ell m}(\theta, \phi) = \sqrt{\frac{2\ell+1}{4\pi} \frac{(\ell-m)!}{(\ell+m)!}} P_{\ell m}(\cos \theta) e^{im\phi} . \quad (3.77)$$

Now the two-point auto-correlator of each mode can be written down

$$\left\langle h_{\ell_1 m_1}(\rho_1, k_{\xi_1}) h_{\ell_2 m_2}(\rho_2, k_{\xi_2}) \right\rangle = \frac{\pi\nu}{\hat{w} \cosh^2 \rho_1} \delta(\rho_1 - \rho_2) \delta_{\ell_1 \ell_2} \delta_{m_1, -m_2} (-1)^{m_1} \delta(k_{\xi_1}, k_{\xi_2}) \quad (3.78)$$

The effect of noise can be parametrically estimated by inspecting the pre factor in eq. (3.78). We note that this factor depends on both  $\hat{w}$  and  $\nu \propto \eta/s$ . In the Gubser solution,  $\hat{w}$  only depends on  $\hat{T}_0$ , which is determined by *the total multiplicity and not the system size*.

Also the other fluctuations can be decomposed into modes, but now we also need to take vector modes into account. The decomposition of each independent fluctuating thermodynamical quantity is thus made in terms of spherical harmonics  $Y_{\ell m}$  and vector spherical harmonics  $\Phi_{\ell m}^i$ :

$$\delta\hat{T}(\rho, \theta, \phi, \xi) = \hat{T}(\rho) \sum_{\ell, m} \int \frac{dk_\xi}{2\pi} \delta_{\ell m}(\rho, k_\xi) Y_{\ell m}(\theta, \phi) e^{ik_\xi \xi} , \quad (3.79)$$

$$\delta\hat{u}_i(\rho, \theta, \phi, \xi) = \sum_{\ell, m} \int \frac{dk_\xi}{2\pi} [v_{\ell m}^s(\rho, k_\xi) \partial_i Y_{\ell m}(\theta, \phi) + v_{\ell m}^v(\rho, k_\xi) \Phi_{i(\ell m)}(\theta, \phi)] e^{ik_\xi \xi} , \quad (3.80)$$

$$\delta\hat{u}_\xi(\rho, \theta, \phi, \xi) = \sum_{\ell, m} \int \frac{dk_\xi}{2\pi} v_{\ell m}^\xi(\rho, k_\xi) Y_{\ell m}(\theta, \phi) e^{ik_\xi \xi} . \quad (3.81)$$

Here  $i = \theta, \phi$  denotes directions in the transverse plane and the  $m$  summation runs from  $-l$  to  $l$ . Composing a four-vector out of the modes in eq. (3.81) as

$$\tilde{\mathcal{V}}_{\ell m}(\rho, k_\xi) \equiv \begin{pmatrix} \delta_{\ell m}(\rho, k_\xi) \\ v_{\ell m}^s(\rho, k_\xi) \\ v_{\ell m}^\xi(\rho, k_\xi) \\ v_{\ell m}^v(\rho, k_\xi) \end{pmatrix} \quad (3.82)$$

we can then write the equation of motion for each mode, coming from  $d_\mu \hat{T}^{\mu\nu} = 0$

$$\tilde{\mathcal{V}}'_\ell(\rho) = -\tilde{\Gamma}(\rho, \ell, k_\xi) \tilde{\mathcal{V}}_\ell(\rho) + \tilde{\mathcal{K}}(\rho, k_\xi) . \quad (3.83)$$

Here the prime denotes differentiation with respect to  $\rho$ . The indices in eq. (3.83) indicate that there is a dependence on the transverse directions. The 4 by 4 matrix  $\tilde{\Gamma}(\rho, \ell, k_\xi)$  has a block-diagonal form as follows:

$$\begin{pmatrix} \tilde{\Gamma}_{11} & \tilde{\Gamma}_{12} & \tilde{\Gamma}_{13} & 0 \\ \tilde{\Gamma}_{21} & \tilde{\Gamma}_{22} & \tilde{\Gamma}_{23} & 0 \\ \tilde{\Gamma}_{31} & \tilde{\Gamma}_{32} & \tilde{\Gamma}_{33} & 0 \\ 0 & 0 & 0 & \tilde{\Gamma}_{44} \end{pmatrix} , \quad (3.84)$$

so we can see that vector and scalar modes are decoupled, as they should be according to parity. The explicit forms of the elements of the  $\tilde{\Gamma}(\rho, \ell, k_\xi)$  matrix are given in the

appendix A. The noise term of eq. (3.83) depends on the scalar function  $h_{\ell m}$  of the hydrodynamical noise

$$\tilde{\mathcal{K}} = \begin{pmatrix} -\frac{2}{3} \tanh \rho h_{\ell m}(\rho) \\ \frac{2\hat{T}}{3\hat{T}'} \tanh \rho h_{\ell m}(\rho) \\ -\frac{i4k_\xi \hat{T}}{\hat{T} + H_0 \tanh \rho} h_{\ell m}(\rho) \\ 0 \end{pmatrix}. \quad (3.85)$$

As noted before, noise only contributes to the scalar modes. In the explicit form of  $\tilde{\mathcal{K}}$  we see that this is indeed the case, since the fourth component that normally would contribute to the vector modes vanishes. In  $\tilde{\mathcal{K}}$  we also see non-trivial denominators appearing, a possible source of instabilities. These possible instabilities, discussed at length in [12], do not affect our analysis because they are present at times earlier or later than those considered in this work. We also note that these instabilities already occur in the matrix  $\tilde{\Gamma}(\rho, l, k_\xi)$ , so their presence in  $\tilde{\mathcal{K}}$  is not a source of any new instability.

### 3.3.3 Formal solution of the Green function

Before solving eq. (3.83) let us study quantitatively the behaviour and evolution of hydrodynamical noise. We do the derivation with respect to a background flow given by Gubser's solution.

Formally, we can write a general solution of eq. (3.83) as

$$\tilde{\mathcal{V}}(\rho, K) = \int_{\rho_0}^{\rho} d\rho' \tilde{\mathcal{G}}(\rho - \rho', K) \tilde{\mathcal{K}}(\rho', K) + \tilde{\mathcal{G}}(\rho - \rho_0, K) \tilde{\mathcal{V}}(\rho_0, K), \quad (3.86)$$

where  $K$  is a shorthand for the variables specifying the modes:  $K = (\ell, m, k_\xi)$ . The right hand side has two distinct pieces: the first term, proportional to  $\tilde{\mathcal{K}}$ , comes from hydrodynamical fluctuations whereas the second term, dependent on  $\rho_0$  is the contribution from the initial state fluctuations, discussed more at length in chapter 2.

The Green function  $\tilde{\mathcal{G}}$  in eq. (3.86) is determined from its equation of motion

$$\partial_\rho \tilde{\mathcal{G}}(\rho - \rho', K) = -\tilde{\Gamma}(\rho, K) \tilde{\mathcal{G}}(\rho - \rho', K), \quad (3.87)$$

together with the initial condition

$$\tilde{\mathcal{G}}(0, K) = 1. \quad (3.88)$$

Formally, then, we have

$$\tilde{\mathcal{G}}(\rho - \rho', K) = \mathcal{T} \exp \left[ - \int_{\rho'}^{\rho} d\rho'' \tilde{\Gamma}(\rho'', K) \right], \quad (3.89)$$

where the operator  $\mathcal{T}$  stands for time ordering with respect to  $\rho$ . In general the explicit form of  $\tilde{\mathcal{G}}$  is not known, but it can be computed in some specific limits.

The one-point function of the noise vanishes:

$$\langle \tilde{\mathcal{K}}(\rho, K) \rangle = 0 . \quad (3.90)$$

From this together with eq. (3.86) we see that the one-point functions are solely determined by hydrodynamic response to the initial fluctuations and that the hydrodynamical noise does not play a role:

$$\langle \tilde{\mathcal{V}}(\rho, K) \rangle = \tilde{\mathcal{G}}(\rho - \rho_0, K) \langle \tilde{\mathcal{V}}(\rho_0, K) \rangle \quad (3.91)$$

The situation for the two-point function is different. This gives us a play ground for investigating the effect of hydrodynamical noise. The equal time two-point correlator of  $\mathcal{V}(\rho, K)$  from eq. (3.86) reads

$$\begin{aligned} \langle \tilde{\mathcal{V}}_i(\rho, K) \tilde{\mathcal{V}}_j(\rho, K') \rangle &= \int_{\rho_0}^{\rho} d\rho' \left( \tilde{\mathcal{G}}(\rho - \rho', K) \Lambda_{\text{thermal}}(\rho') \tilde{\mathcal{G}}^T(\rho - \rho', -K) \right)_{ij} \delta(K + K') \\ &+ \left( \tilde{\mathcal{G}}(\rho - \rho_0, K) \Lambda_{\text{initial}}(\rho_0, K, K') \tilde{\mathcal{G}}^T(\rho - \rho_0, K') \right)_{ij} , \quad (3.92) \end{aligned}$$

where the index  $i$  denotes the component of the four-vector of modes ( $\tilde{\mathcal{V}}$ ), indices  $ij$  a matrix element, and

$$\delta(K + K') \equiv \delta_{\ell_1 \ell_2} \delta_{m_1, -m_2} (-1)^{m_1} \delta(k_{\xi_1} + k_{\xi_2}) . \quad (3.93)$$

We note that in eq. (3.92) we have only two terms because the cross-term vanishes thanks to the fact that the two contributions factorize due to different statistics and also due to the vanishing of the one-point function (3.90), namely

$$\begin{aligned} \langle \tilde{\mathcal{K}}(\rho, K) \tilde{\mathcal{V}}(\rho_0, K') \rangle &= \langle \mathcal{K}(\rho, K) \rangle \langle \mathcal{V}(\rho_0, K') \rangle \\ &= 0 . \quad (3.94) \end{aligned}$$

In computing eq. (3.92) we must specify the type of average we take. We take this average to be that over a specific centrality class of events. Thus the total multiplicity is fixed and our average contains a sum over collision events in this centrality class as well as ensemble average over each collision event. This means explicitly that

$$\langle \dots \rangle = \frac{1}{N_{\text{collisions}}} \sum [\langle \dots \rangle_{\text{ensemble}}] . \quad (3.95)$$

The form of  $\Lambda_{\text{thermal}}$  is specified once  $\tilde{\mathcal{K}}(\rho, K)$  and the fluctuation-dissipation theorem are known. As to  $\Lambda_{\text{initial}}$ , we will consider two different set-ups. The first is inspired by the independent-sources model and initial fluctuations are taken to be local. The second one is found keeping in mind the  $SO(2)$  axial symmetry. Indeed, we can choose the initial fluctuation to be an axially symmetric deformation of the initial energy density. Details of both types of initial fluctuations will be given in the next section.

### 3.4 Numerical simulations

We solve the two coupled equations for  $\delta_\ell$  and  $v_\ell^s$  numerically in a background given by the Gubser solution for energies corresponding to the ones attained at the LHC. The background is completely determined by specifying two parameters:  $\hat{T}_0$  and  $q^{-1}$ , the background temperature and the transverse size of the system. The former parameter is determined from the multiplicity of an event in the following manner, following [13, 14]. First we take

$$\hat{T}_0 = \frac{1}{f_*^{1/12}} \left( \frac{3}{16\pi} \frac{dS}{d\xi} \right)^{1/3}, \quad (3.96)$$

where the pre factor

$$f_* = \epsilon/T^4 = 11 \quad (3.97)$$

is the effective number of degrees of freedom obtained from lattice QCD calculations and the entropy production per unit spatial rapidity is

$$\frac{dS}{d\xi} = 7.5 \frac{dN_{\text{ch}}}{dy}. \quad (3.98)$$

The number of charged particles per rapidity for the three different systems at different energies are taken from the literature:

	<b>Pb-Pb</b>	<b>p-Pb</b>	<b>p-p</b>
$\sqrt{s_{NN}}$ (TeV)	2.76	5.02	13
$dN_{\text{ch}}/d\mathbf{y}$	$\sim 1600$	$\sim 150$	$\gtrsim 20$
Ref.	[14]	[9]	[124]

Table 3.1: Experimentally measured values of the number of charged tracks per rapidity for the three systems considered and the relevant references.

Using the multiplicities of table 3.1 in eqs. (3.96), (3.98) we obtain the following values for the background temperature:

	Pb-Pb	p-Pb	p-p
$\hat{T}_0$	7.3	3.1	2.0
$q^{-1}$ [fm]	4.3	1.1	1.1
$T(r = 0\text{fm}, \tau = 2.5\text{fm})$ [fm $^{-1}$ ]	0.24	0.09	0.06

Table 3.2: Background temperature  $\hat{T}_0$  and transverse size  $q^{-1}$  of all three systems considered, and the corresponding  $T$  values for chosen parameters  $r = 0\text{fm}$ ,  $\tau = 2.5\text{fm}$ , calculated according to eqs. (3.41), (3.43) and (3.46) which together give  $f_*\tau T = \hat{T}$ , see eq. (3.97). Values for  $\hat{T}_0$  and  $q^{-1}$  from [13, 14].

In all computations we take the parameter  $H_0 = 0.33$ , meaning that the viscosity over entropy density ratio is  $\eta/s = 0.134$  [125, 66].

**The temperature profile for one random event** is shown in fig. 3.3. In all of our studies we focus on three different systems: lead-lead collisions, proton-lead collisions and proton-proton collisions, such as they are experimentally measured at the LHC. We break conformal symmetry by introducing a scale into the problem. This scale is the time at which the snapshots in fig. 3.3 are taken, namely  $\tau = 2.5$  fm/ $c$ . We choose this time because all systems should be safely hydrodynamical at this stage. From the figures we see that the qualitative effect of the hydrodynamical noise is the appearance of a bumpy or spiky structure. The importance of the bumpiness is largest for the system with the lowest multiplicity, that is, in a proton-proton event, whereas it is the least significant in the lead-lead system. The intermediate system, proton-lead, has a behaviour of somewhere in between these two extremes. This is precisely as expected from eq. (3.78): *the lower the multiplicity the more important the effect of hydrodynamical noise.*

For a quantitative estimate of the effect of hydrodynamical noise, we resort to the two-point correlators of hydrodynamical variables. Because we are interested in the transverse expansion of the system, we choose to study the auto-correlator of radial flow. For the sake of simplicity, we consider these correlators at equal times and equal radii. This radial flow auto-correlator  $\langle u_r u_r \rangle$  only depends on  $\langle v_\ell^s v_\ell^s \rangle$ . We define

$$C_{u_r u_r}(\tau, r, \phi, \Delta\phi) = \langle u_r(\tau, r, \phi) u_r(\tau, r, \phi + \Delta\phi) \rangle - \langle u_b(r) \rangle \langle u_b(r) \rangle, \quad (3.99)$$

where we subtract the effect of the background. We then choose to integrate out the variables  $r$  and  $\phi$  in order to get an insight into the system at a specific proper time

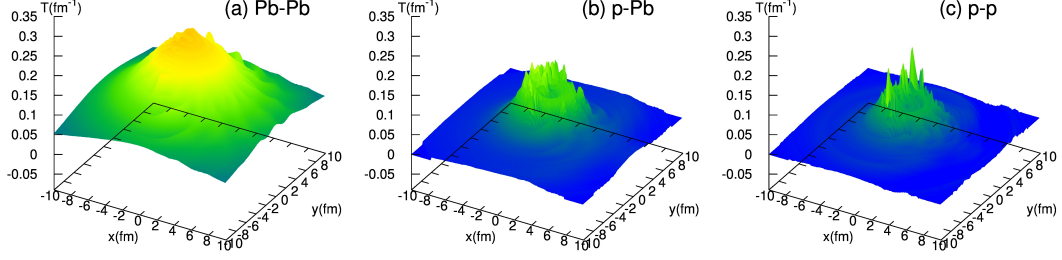


Figure 3.3: The temperature profile at a time  $\tau = 2.5$  fm for one random event in units of  $\text{fm}^{-1}$ . The effect of noise is reflected in the bumpiness of the figures. We see that this effect is smallest in the Pb-Pb system and biggest in the p-p system.

and difference in azimuthal angle. To do so, we note that the invariant integration measure is  $\tau r dr d\phi$ , and we get

$$C_{u_r u_r}(\tau, \Delta\phi) = \int \frac{\tau r dr d\phi}{2\pi} \langle u_r(\tau, r, \phi) u_r(\tau, r, \phi + \Delta\phi) \rangle - \int \frac{\tau r dr d\phi}{2\pi} \langle u_r^{\text{bkg}}(\tau, r)^2 \rangle \quad (3.100)$$

This correlator  $C_{u_r u_r}(\tau, \Delta\phi)$  now consists of two distinct parts, one coming from the hydrodynamical fluctuations and the other coming from the initial fluctuations:

$$C_{u_r u_r}(\tau, \Delta\phi) = C_{u_r u_r}^T(\tau, \Delta\phi) + C_{u_r u_r}^I(\tau, \Delta\phi), \quad (3.101)$$

where the superscripts  $T$  and  $I$  stand for ‘thermal’ and ‘initial’, respectively. To quantify the effect of hydrodynamic noise on top of the initial state fluctuation, we will investigate the relative value of these two contributions, namely  $C_{u_r u_r}^T(\tau, \Delta\phi)/C_{u_r u_r}^I(\tau, \Delta\phi)$ . This we will do in the following.

**The effect of hydrodynamic noise on long-range correlations** Long-range correlations are of utmost importance in heavy-ion collisions. From these correlations we know of the existence of *harmonic flow*, a phenomenon originating in the azimuthal anisotropies of the colliding system. The harmonic flow originates in eccentric initial distributions of density. It is thus interesting to consider initial fluctuations that mimic these density profiles. Keeping in mind the rotational symmetry in the transverse plane, we consider initial fluctuations that have a symmetry under azimuthal rotations of  $2\pi/m$ , with  $m$  an integer from 1 to 5. Inspired by the discussion in ref. [13], we initialize the system by the following fluctuations

$$\frac{\delta \hat{T}(\theta, \phi, \rho_0, \xi)}{\hat{T}(\rho_0)} = -\sqrt{\Lambda_{\text{initial}}} \left[ (-1)^m \frac{1}{\sqrt{2}} Y_{m,m}(\theta, \phi) + \frac{1}{\sqrt{2}} Y_{m,-m}(\theta, \phi) \right]. \quad (3.102)$$

This is precisely a density profile with a non zero  $\varepsilon_m$ .

The results of the radial flow correlations with the initialization eq. (3.102) are shown in figure 3.4 for three different systems (proton-proton, proton-lead and lead-lead) and four different initial eccentricities ( $\varepsilon_2$ ,  $\varepsilon_3$ ,  $\varepsilon_4$  and  $\varepsilon_5$ ). In this figure we plot the relative contribution of hydrodynamical noise  $C_{u_r u_r}^T(\tau, \Delta\phi)$  to the strength of the initial fluctuation  $C_{u_r u_r}^I(\tau, \Delta\phi = 0)$  as a function of the relative azimuthal angle  $\Delta\phi$  at a proper time  $\tau = 2.5\text{fm}$ .

Our observations are as follows. First of all, we see that the noise has always its biggest relative strength in proton-proton collisions. This is depicted by the red solid curve that always has the biggest amplitude out of the three curves in any given subfigure. Secondly, we note that the relative strength of the hydrodynamical noise increases when going from lower harmonics to higher ones. This can be explained by the following reasoning. The strength of the noise is independent of the harmonic considered, because we can see that the equation of motion, eq. (3.83), is independent of the index  $m$ . Furthermore, the higher modes die off faster than the lower modes due to viscosity. This means that higher modes of the initial fluctuations are suppressed with respect to the lower modes. So, from all our plots in fig. 3.4 the mode  $\ell = 5$  corresponding to the eccentricity  $\varepsilon_5$  has the smallest magnitude:

$$C_{u_r u_r}^I(\tau, 0) |_{m=5} < C_{u_r u_r}^I(\tau, 0) |_{m=4} < \dots < C_{u_r u_r}^I(\tau, 0) |_{m=1} . \quad (3.103)$$

This implies that

$$\frac{C_{u_r u_r}^T(\tau, \Delta\phi)}{C_{u_r u_r}^I(\tau, 0)} |_{m=5} > \frac{C_{u_r u_r}^T(\tau, \Delta\phi)}{C_{u_r u_r}^I(\tau, 0)} |_{m=4} > \dots > \frac{C_{u_r u_r}^T(\tau, \Delta\phi)}{C_{u_r u_r}^I(\tau, 0)} |_{m=1} . \quad (3.104)$$

Lastly, we note that the relative effect of the hydrodynamic noise is not significant in any of the systems we study. Indeed, for lead-lead collisions this effect is of the order of 3%.

**The effect of hydrodynamic noise on short-range correlations** Next we study short-range correlations, initialized by a peak in the transverse plane:

$$\frac{\delta\hat{T}(\theta, \phi, \rho_0, \xi)}{\hat{T}(\rho_0)} = \frac{\sqrt{\Lambda_{\text{initial}}}}{\cosh \rho_0 \sin \theta} \delta(\theta - \theta_0) \delta(\phi - \phi_0) . \quad (3.105)$$

This gives rise to the situation shown in fig. 3.5 at a proper time  $\tau = 2.5 \text{ fm}$ .

From this figure we can see that the initial perturbation propagates outward, meaning in the  $r$  increasing direction. In the upper panel of the figure we see sub

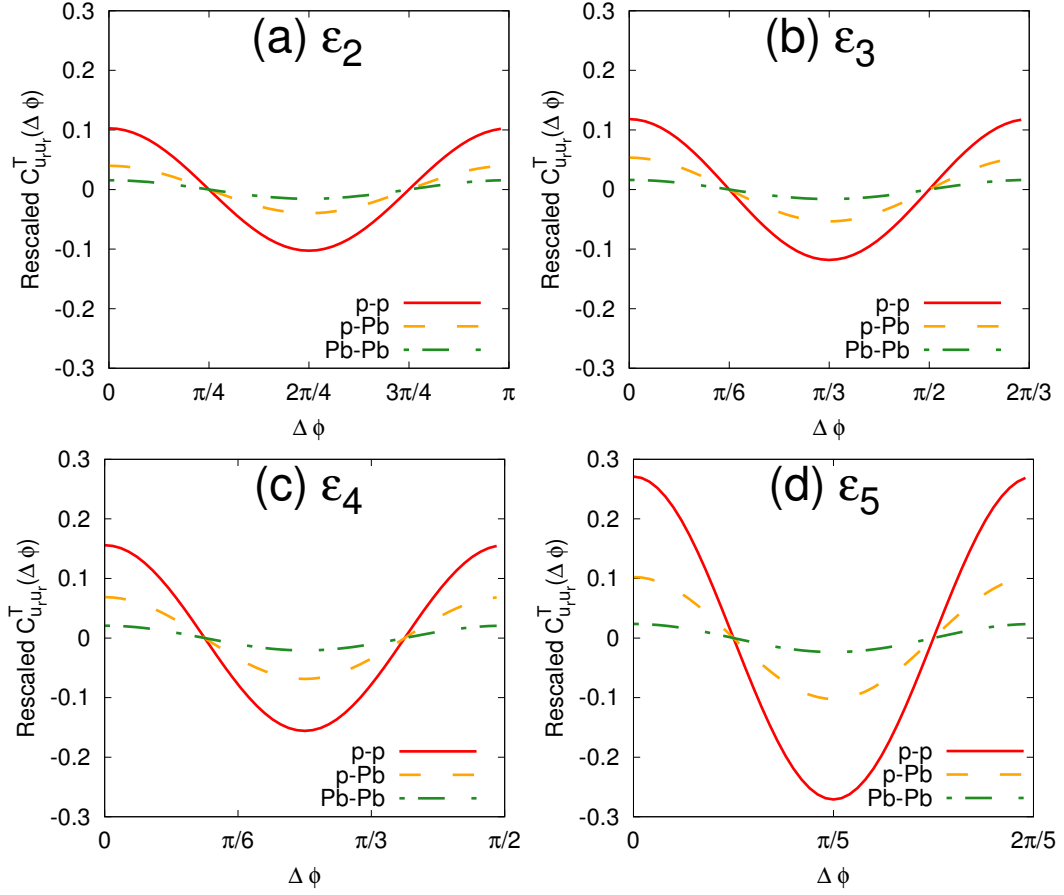


Figure 3.4: Effect of fluctuations on long-range correlations. The initial multipoles that were used as initial fluctuations are of the following forms: (a) elliptic (b) triangular (c) quadrangular (d) pentagonal. We note that the periodicity of each multipole is respected by the noise. We further note that the effect of noise is larger going from Pb-Pb to p-Pb and further to p-p. The biggest relative contribution from noise is to the higher multipoles. Snapshot of dynamics at  $\tau = 2.5\text{fm}/c$ .

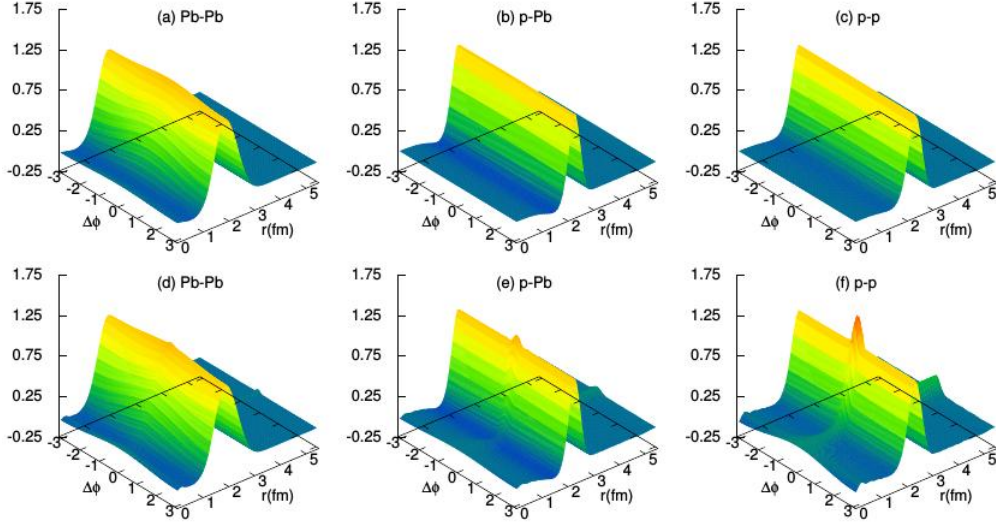


Figure 3.5: The state of the system at  $\tau = 2.5 \text{ fm}$ , when the initial fluctuation has been set to a delta peak. We see a wave propagating in the positive  $r$  direction and a near-side peak forming on top of the wave.

plots where noise has not been included into the computation. On the other hand, in the lower panel we include noise effects. We see that these contribute to the formation of a short-range peak on top of the propagating wave. In the following figure 3.6 we show details of this peak. This figure 3.6 is nothing but the figure 3.5 integrated over the radial coordinate  $r$ .

## 3.5 Conclusions

In this section we have studied the effect of hydrodynamical noise on a background of Gubser flow in 3+1 space-time dimensions. More specifically, we have investigated the effect of hydrodynamical noise on two-point correlation functions of radial flow, with initial fluctuations introduced with respect to a late-stage short-range or a long-range correlation structure.

The main conclusions from these studies are the following. First, we have seen that the magnitude of the noise in a heavy-ion collision is mostly determined by the *multiplicity* of the event, and not by the (transverse) size of the system. This same conclusion has been seen to hold both for the Bjorken (1+1D) and Gubser (3+1D) cases. Our study thus implicitly answers the question ‘What is the smallest droplet

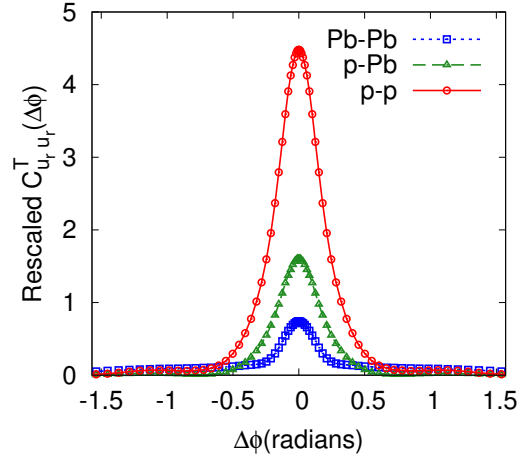


Figure 3.6: Zooming in on the near-side peak of the previous figure. The shape and size of the peak varies from system to system: it is at its smallest and narrowest for the Pb-Pb system, then intermediate for the p-Pb system and wide and high for the p-p system.

of quark-gluon plasma that evolves like a fluid’. The answer is that there is no limit, as long as one keeps on putting more and more energy into the system, so that the total multiplicity remains large enough for the formation of a plasma. This first point is the main conclusion of our investigations.

Secondly, we have studied the two-point auto-correlation function of the radial flow, inspired by the fact that we consider the transverse expansion of the system to be of utmost importance. We have seen that the effect of noise on this correlator is modest. For the long-range correlations, initialized by eq. (3.102), the noise has an additive effect onto the eccentricity of the system, and thus adds a contribution to anisotropic flow. The effect of noise is at its smallest for the Pb-Pb system and at its biggest for the p-p system. Also, the relative effect of noise with respect to the contribution coming from the initial-state fluctuations grows for higher harmonics. This can be understood as follows. The magnitude of noise is independent of the degree of the harmonic considered, because the equation of motion, eq. (3.83) is independent of the index  $m$ . However, the high harmonics suffer a higher degree of attenuation than the low-order ones. This effect is due to viscosity. This implies that the relative strength of the radial flow resulting from hydrodynamical noise as opposed to initial-state fluctuations is stronger for high harmonics.

Finally, we have considered the effect of noise on short-range correlations, as

initiated by a delta-peak in the transverse plane. Our studies show that the noise leads to a narrow peak on top of the wave front which propagates from the initial peak. The characteristics of this narrow peak vary from system to system in a consistent way: the peak is at its narrowest and shortest for the Pb-Pb system, whereas it is at its widest and highest for the p-p system. The p-Pb system lies in between these two extremes.

We have been working in the framework of Gubser flow. In particular this means that we are restricted to systems with conformal symmetry. This is a possible source of improvement, because QCD is known to be only *nearly* conformal at energies well below the critical temperature. Also, direct contact with experimental data is lacking due to the fact that we do not consider hadronization or freeze-out. We have thus focused our studies on a quantity similar to what is currently experimentally measured, that is, the two-point correlator of radial flow, similar to the two-particle correlators measured in experiments. Furthermore, the analysis could be improved by going to second-order hydrodynamics. We also look forward to extending the analysis in a way that includes non zero modes in the Fourier decomposition of the fluctuating thermal quantities.



# Appendix A

## Gamma-matrix of Gubser flow

The following results are from [12]. The contribution to the scalar modes is encoded in the left-upper  $3 \times 3$  part of  $\tilde{\Gamma}(\rho, \ell, k_\xi)$ . The first two rows read:

$$\begin{aligned}
 \tilde{\Gamma}_{11} &= \frac{H_0 \tanh^2 \rho}{3\hat{T}_b} \\
 \tilde{\Gamma}_{12} &= \frac{\ell(\ell+1)\text{sech}^2 \rho \left[ H_0 \tanh \rho - \hat{T}_b \right]}{3\hat{T}_b} \\
 \tilde{\Gamma}_{13} &= \frac{ik_\xi \left[ 2H_0 \tanh \rho + \hat{T}_b \right]}{3\hat{T}_b} \\
 \tilde{\Gamma}_{21} &= \frac{2H_0 \tanh \rho}{H_0 \tanh \rho - 2\hat{T}_b} + 1 \\
 \tilde{\Gamma}_{22} &= \frac{H_0 \hat{T}_b \left[ -4(3\ell(\ell+1) - 10)\text{sech}^2 \rho - 9k_\xi^2 - 16 \right] + 6H_0^2 \tanh^3 \rho + 8\hat{T}_b^2 \tanh \rho}{6\hat{T}_b \left[ H_0 \tanh \rho - 2\hat{T}_b \right]} \\
 \tilde{\Gamma}_{23} &= \frac{iH_0 k_\xi}{2H_0 \tanh \rho - 4\hat{T}_b}
 \end{aligned} \tag{A.1}$$

and the last row is

$$\begin{aligned}
\tilde{\Gamma}_{31} &= \frac{ik_\xi \left[ 3H_0 \tanh \rho + \hat{T}_b \right]}{H_0 \tanh \rho + \hat{T}_b} \\
\tilde{\Gamma}_{32} &= \frac{i\ell(\ell+1)H_0 k_\xi \operatorname{sech}^2 \rho}{4 \left[ H_0 \tanh \rho + \hat{T}_b \right]} \\
\tilde{\Gamma}_{33} &= \frac{\hat{T}_b \left[ (9\ell(\ell+1) - 4)H_0 \operatorname{sech}^2 \rho + 4H_0 \left[ 3k_\xi^2 + 4 \right] - 8\hat{T}_b \tanh \rho \right] + 12H_0^2 \tanh^3 \rho}{12\hat{T}_b \left[ H_0 \tanh \rho + \hat{T}_b \right]} .
\end{aligned} \tag{A.2}$$

The vector part  $\tilde{\Gamma}_{44}$  is more complicated. We give its expression in certain limits: (i) the inviscid case, (ii) the low viscosity case and (iii) the late time limit:

$$\begin{aligned}
\text{(i)} \quad \tilde{\Gamma}_{44} &= -\frac{2}{3} \tanh \rho , \\
\text{(ii)} \quad \tilde{\Gamma}_{44} &= -\frac{2}{3} \tanh \rho + \frac{3H_0(\ell^2 + k_\xi^2 \cosh^2 \rho)}{4\hat{T}_0(\cosh \rho)^{4/3}} + \dots , \\
\text{(iii)} \quad \tilde{\Gamma}_{44} &= \frac{3}{2^{5/3}} \frac{k_\xi^2 H_0}{2\hat{T}_0 + H_0 \frac{\sqrt{\pi}\Gamma(-1/2)}{\Gamma(1/6)}} e^{2\rho/3} + \frac{4}{3} + \mathcal{O}(e^{-2\rho/3}) .
\end{aligned} \tag{A.3}$$

# Appendix B

## Details of figure 3.1

In this section we give some details about the computations needed for the figure 3.1.

### B.0.1 The $q\tau = \text{constant}$ curves

First, take the mapping (3.45) and use it to rewrite  $r$  and  $\tau$  in terms of  $\rho$ ,  $\theta$  [12]

$$q\tau = \frac{\text{sech}\rho}{\cos\theta - \tanh\rho}, \quad qr = \frac{\sin\theta}{\cos\theta - \tanh\rho}. \quad (\text{B.1})$$

There are two real solutions to  $\rho(r, \tau)$ . We choose the one corresponding to the domain

$$-1 < \cos(\theta) < 1 \wedge \tilde{\tau} > 0, \quad (\text{B.2})$$

giving

$$\rho(r, \tau) = \frac{1 - \sqrt{\tilde{\tau}^2 (-\cos^2(\theta)) + \tilde{\tau}^2 + 1}}{\tilde{\tau}(\cos(\theta) - 1)}, \quad (\text{B.3})$$

where we have written  $\tilde{\tau} \equiv q\tau$ .

Now for any given  $\tilde{\tau} = \text{const.}$  we have  $\rho$  purely as a function of  $\theta$ , and we can plot this  $\rho(\theta)$  for  $\tilde{\tau} = 0.07 \text{ fm}$ ,  $0.5 \text{ fm}$ ,  $5 \text{ fm}$ ,  $30 \text{ fm}$ . We have chosen the first of these values because, for p-A collisions the transverse size of the system is approximately  $q^{-1} = 4.3 \text{ fm}$  and the thermalization time is somewhere after  $\tau = 0.3 \text{ fm}$ .

### B.0.2 The $T = \text{constant}$ curves

First of all we note that there is some maximal value of  $\rho$  corresponding to  $\theta = 0$ . This value  $\theta = 0$  is obtained at  $r = 0$ , as we can see from eq. (B.1). This means that

$$\sinh \rho_{\max} = -\frac{1 - \tilde{\tau}_{\max}^2}{2\tilde{\tau}_{\max}} , \quad (\text{B.4})$$

which we get from eq. (3.45).

Next, let us consider Gubser's solution to ideal hydro, eq. (3.36). The transformation of the temperature  $T$  between the Minkowski and de Sitter space times follows from eq. (3.46): We have  $\hat{T} = \tau T$  and furthermore

$$\tau T = \frac{1}{q} q \tau T = \tilde{\tau} T R \equiv \tilde{T} . \quad (\text{B.5})$$

Here we have remembered that  $q$  gives the inverse transverse size of the system. From eq. (3.36) we now get

$$\begin{aligned} \tilde{T} &= \frac{\hat{T}_0}{\tilde{\tau}} (\cosh \rho)^{-2/3} \\ &= \frac{\hat{T}_0}{\tilde{\tau}} (1 + \sinh^2 \rho)^{-1/3} , \end{aligned} \quad (\text{B.6})$$

where  $\rho < \rho_{\max}$ .

From this we can now solve  $\tilde{\tau}_{\max}$  as follows. We substitute eq. (B.4) into eq. (B.6) to get

$$\tilde{T} = \frac{\hat{T}_0}{\tilde{\tau}} \left( 1 + \left[ \frac{1 - \tilde{\tau}_{\max}^2}{2\tilde{\tau}_{\max}} \right]^2 \right)^{-1/3} . \quad (\text{B.7})$$

From the equation above we can solve  $\tilde{\tau}_{\max}$  for given freeze-out temperature  $\tilde{T}$  and  $\hat{T}_0$ . To do so, we need to take care of dimensions, so we need to insert  $\hbar c = 197.3269631$  MeV fm accordingly [126].

Once we have  $\tilde{\tau}_{\max}$  we get  $\rho_{\max}$  from eq. (B.4). Then we take discrete time steps  $\Delta\tilde{\tau}$  such that

$$\tilde{\tau} = \tilde{\tau}_{\max} - i\Delta\tilde{\tau} , \quad (\text{B.8})$$

where  $i = 1, 2, 3, \dots$ . For each  $\tilde{\tau}$  and  $\tilde{T}$  we solve  $\rho$  from eq. (B.6). In this way we get discrete lists

$$\begin{aligned} \tilde{\tau} &= [\tilde{\tau}_{\max}, \tilde{\tau}_{\max} - 1 \cdot \Delta\tilde{\tau}, \dots] \\ \rho &= \left[ \rho_{\max}, \rho(\tilde{T}, \tilde{\tau}_{\max} - 1 \cdot \Delta\tilde{\tau}), \dots \right] . \end{aligned} \quad (\text{B.9})$$

These lists or vectors can now be substituted into the first equation in (B.1), and we solve for  $\theta$  as

$$\theta = \cos^{-1} \left( \frac{\operatorname{sech}(\rho)}{\tilde{\tau}} + \tanh(\rho) \right) . \quad (\text{B.10})$$

At this point we have vectors  $\theta$  and  $\rho$  and we can plot points corresponding to pairs of these.



# Appendix C

## First paper

## Cuts and coproducts of massive triangle diagrams

---

**Samuel Abreu,<sup>a,b</sup> Ruth Britto,<sup>b,c,d</sup> and Hanna Grönqvist<sup>b</sup>**

<sup>a</sup>*Higgs Centre for Theoretical Physics, School of Physics and Astronomy,  
The University of Edinburgh, Edinburgh EH9 3JZ, Scotland, UK*

<sup>b</sup>*Institut de Physique Théorique, Université Paris Saclay, CEA, CNRS, F-91191 Gif-sur-Yvette*

<sup>c</sup>*School of Mathematics, Trinity College, Dublin 2, Ireland*

<sup>d</sup>*Hamilton Mathematical Institute, Trinity College, Dublin 2, Ireland*

*E-mail:* [abreu.samuel@ed.ac.uk](mailto:abreu.samuel@ed.ac.uk), [ruth.britto@cea.fr](mailto:ruth.britto@cea.fr),  
[hanna.gronqvist@cea.fr](mailto:hanna.gronqvist@cea.fr)

**ABSTRACT:** Relations between multiple unitarity cuts and coproducts of Feynman integrals are extended to allow for internal masses. These masses introduce new branch cuts, whose discontinuities can be derived by placing single propagators on shell and identified as particular entries of the coproduct. First entries of the coproduct are then seen to include mass invariants alone, as well as threshold corrections for external momentum channels. As in the massless case, the original integral can possibly be recovered from its cuts by starting with the known part of the coproduct and imposing integrability constraints. We formulate precise rules for cuts of diagrams, and we gather evidence for the relations to coproducts through a detailed study of one-loop triangle integrals with various combinations of external and internal masses.

**KEYWORDS:** Feynman integrals, unitarity cuts.

---

## Contents

<b>1</b>	<b>Introduction</b>	<b>1</b>
1.1	The Hopf algebra for Feynman integrals	3
<b>2</b>	<b>One-loop triangles</b>	<b>5</b>
<b>3</b>	<b>The first-entry condition</b>	<b>9</b>
<b>4</b>	<b>Two types of cuts</b>	<b>11</b>
4.1	Cut in a kinematic channel	12
4.2	Cut in an internal mass	14
4.3	Calculation of cut diagrams	15
<b>5</b>	<b>Relations among discontinuities</b>	<b>18</b>
5.1	Cut diagrams and discontinuities	18
5.1.1	A limit on sequential mass cuts	19
5.1.2	Sequential cuts of triangle diagrams	19
5.2	Coproduct and discontinuities	20
5.2.1	$\pm i0$ -prescription of symbol letters	21
5.3	Cuts and coproduct	22
5.4	Examples	22
5.4.1	$T(p_1^2, 0, 0; m_{12}^2, m_{23}^2, 0)$	22
5.4.2	$T(0, p_2^2, p_3^2; m_{12}^2, 0, 0)$	25
5.4.3	$T(p_1^2, 0, 0; m_{12}^2, 0, m_{13}^2)$	26
5.4.4	$T(p_1^2, p_2^2, p_3^2; m_{12}^2, 0, 0)$	28
<b>6</b>	<b>Reconstruction of Feynman integrals via the coproduct</b>	<b>30</b>
6.1	Constructing and constraining an ansatz for the symbol	31
6.2	Reconstructing the full function from the symbol	33
<b>7</b>	<b>Discussion</b>	<b>34</b>
<b>A</b>	<b>Feynman rules and definitions</b>	<b>36</b>
<b>B</b>	<b>One-mass triangles</b>	<b>37</b>
B.1	$T(p_1^2, 0, 0; 0, m_{23}^2, 0)$	37
B.1.1	Single cuts	38
B.1.2	Double cuts	38
B.2	$T(p_1^2, 0, 0; m_{12}^2, 0, 0)$	38
B.2.1	Single cuts	38
B.2.2	Double cuts	39
B.3	$T(p_1^2, 0, 0; m_{12}^2, m_{23}^2, 0)$	39

B.3.1	Single cuts	39
B.3.2	Double cuts	40
B.4	$T(p_1^2, 0, 0; m_{12}^2, 0, m_{13}^2)$	41
B.4.1	Single cuts	41
B.4.2	Double cuts	42
B.5	$T(p_1^2, 0, 0; m_{12}^2, m_{23}^2, m_{13}^2)$	42
B.5.1	Single cuts	43
B.5.2	Double cuts	44
<b>C</b>	<b>Two-mass triangles</b>	<b>45</b>
C.1	$T(0, p_2^2, p_3^2; 0, m_{23}^2, 0)$	45
C.1.1	Single cuts	46
C.1.2	Double cuts	46
C.2	$T(0, p_2^2, p_3^2; m_{12}^2, 0, 0)$	46
C.2.1	Single cuts	47
C.2.2	Double cuts	47
<b>D</b>	<b>Three-mass triangles</b>	<b>48</b>
D.1	Computation of $T(p_1^2, p_2^2, p_3^2; m_{12}^2, 0, 0)$ and $T(p_1^2, p_2^2, p_3^2; m_{12}^2, 0, m_{13}^2)$	48
D.2	$T(p_1^2, p_2^2, p_3^2; m_{12}^2, 0, 0)$	49
D.2.1	Single cuts	49
D.2.2	Double cuts	50
D.3	$T(p_1^2, p_2^2, p_3^2; m_{12}^2, 0, m_{13}^2)$	50
D.3.1	Single cuts	51
D.3.2	Double cuts	52
D.4	$T(p_1^2, p_2^2, p_3^2; m_{12}^2, m_{23}^2, m_{13}^2)$	52
D.4.1	Single cuts	53
D.4.2	Double cuts	55

---

## 1 Introduction

The evaluation of Feynman integrals is a necessary ingredient for the precise determination of physical observables in perturbative quantum field theories. The notorious difficulty of evaluating these integrals has led to the development of various integration techniques.

One family of these techniques relies on the study of the discontinuities of Feynman integrals across their branch cuts, a topic that goes back to the early days of perturbative quantum field theory. It is based on the fact that these discontinuities can be computed directly by specific diagrammatic rules [1–5]. According to these rules, partitions of Feynman diagrams into two regions are enumerated, and the particles at the boundary of the

two regions are restricted to their mass shells. This operation defines the set of *cut diagrams*. Collecting the cut diagrams with the same momentum flow between the regions, we construct a *unitarity cut* which captures the discontinuity across the branch cut in that momentum invariant. The on-shell restrictions greatly simplify the integration and its result. The original uncut integral can then be reconstructed, traditionally through dispersion relations [1–5]. More recently, modern unitarity methods use discontinuities to project an amplitude onto a basis of known master integrals [6–20]. For increased efficiency, the latter techniques can incorporate *multiple cuts* in different channels simultaneously, and even further generalizations of cut operations. Restricting many propagators to their mass shells separates a diagram into several on-shell elements, which are typically simpler to compute.

In order to find yet more efficient computational tools, it is useful to study the types of functions produced by Feynman integrals. Although it is still in general an open question to determine what functions are needed, it is known that all one-loop integrals, and a large number of higher-loop integrals with a sufficiently small number of masses, can be written in terms of the transcendental functions called multiple polylogarithms. (At higher loop order, elliptic functions can appear [21–26].) Recent developments on the mathematical structure of this class of functions, in particular their *Hopf algebraic structure* [27, 28], have thus had a big impact on the physics community over the last few years [29, 30].

In [31], cuts of Feynman diagrams without internal masses were studied in the light of these modern mathematical tools. One of the results of that paper was the establishment of a relation between (multiple) cuts of diagrams and the coproduct of the corresponding Feynman integral. Indeed, the coproduct, which is an operator defined in the Hopf algebra of multiple polylogarithms, is particularly useful in capturing their discontinuities. The coproduct breaks the original function down into lower-weight functions, such that discontinuities are perfectly captured by the so-called *first entries*, a statement known as the *first-entry condition*. The result of [31] was to extend this property to a correspondence of subsequent entries of the coproduct and multiple cuts. The strategy employed was to find a relation between cuts and the coproduct by independently relating cuts to discontinuities, and coproduct entries to discontinuities. The conjectured relations were checked in several one-loop examples and a non-trivial two-loop example.

The *first-entry condition* was observed in [32] and explained mathematically in [30], but these works were restricted to integrals with massless propagators. In these cases, the integral is a function of Mandelstam invariants constructed from the external momenta. When we include massive propagators, there are also branch cuts in the internal mass variables. Thus we would expect the masses to appear plainly among the first entries of the coproduct, and in more intricate ways in subsequent entries. In the present paper, we find this to be true. We generalize the relations between (multiple) cuts and the coproduct to diagrams with internal masses, gathering supporting evidence from a close study of triangle diagrams. The generalization requires modification of the first entry condition: along with including the mass variables among first entries, the familiar Mandelstam invariants must now be accompanied by their thresholds. The discontinuities in mass variables correspond to *single-propagator* cuts of the propagator with the same mass. We formulate cutting

rules that include these single-propagator cuts, reproducing the discontinuities precisely.<sup>1</sup> We then find generalized relations and check them on scalar one-loop three-point functions with various configurations of internal and external masses. While it will be important to extend this investigation to integrals with more loops and legs, we believe that our starting point of triangle integrals already illustrates the most essential features.

It was also shown in [31] that the original Feynman integral could be reconstructed from the knowledge of a single cut through purely algebraic manipulations on the coproduct tensor. In this paper, we provide evidence that the same kind of reconstruction procedure can be applied when internal masses are present.

The paper is organized as follows. We close the introduction with a brief review of the Hopf algebra of multiple polylogarithms, as applied to Feynman integrals. In section 2, we present the Feynman integrals that we study as examples, define the variables used for each diagram and present their symbol alphabets. In section 3, we generalize the first entry condition to diagrams with internal massive propagators. In section 4, we present the rules for calculating the two different kinds of cuts considered in this paper: the familiar channel cuts, also used in [31], and the new single-propagator cuts corresponding to mass discontinuities. We explain how these cuts can be applied iteratively to reproduce multiple discontinuities. Finally, we also comment on our strategy to explicitly compute cut diagrams. Section 5 concerns the relations among discontinuities, coproducts, and cuts. We extend the relations of [31] to diagrams with internal masses and comment on several subtleties that arise in the presence of massive internal propagators. In section 6 we discuss how, starting from a single channel cut, we can reconstruct first the symbol of a Feynman integral and then the whole integral itself. Finally, we discuss our conclusions in section 7.

In appendix A we give our conventions for the calculation of Feynman diagrams. In appendices B, C and D we present results for triangle integrals with several configurations of internal and external masses in terms of multiple polylogarithms. We also present analytical results for their (multiple) cuts and symbols. We do not write all possible configurations of masses, because we believe the examples we give are enough to illustrate and check all our relations. We have, however, checked that the remaining cases do indeed behave in the expected way.

## 1.1 The Hopf algebra for Feynman integrals

We finish this introduction with a brief review of the Hopf algebra of multiple polylogarithms in the context of Feynman integrals. For a more detailed review, we refer the reader to the literature, e.g. [27–30, 33–37] and references therein. Here, we focus on introducing the concepts used in this paper.

**Multiple polylogarithms for Feynman integrals.** As mentioned above, a large class of Feynman integrals may be expressed in terms of the transcendental functions called

---

<sup>1</sup>In contrast to most applications of multiple cuts in the literature, we are concerned here only with diagrammatic cuts that have clear interpretations as discontinuities.

*multiple polylogarithms.* These functions are defined by the iterated integrals

$$G(a_1, \dots, a_n; z) = \int_0^z \frac{dt}{t - a_1} G(a_2, \dots, a_n; t), \quad (1.1)$$

with  $a_i, z \in \mathbb{C}$  and the base case defined to be  $G(z) = 1$ . As simple special cases, we find for example

$$\begin{aligned} G(0; z) &= \log z, & G(a; z) &= \log\left(1 - \frac{z}{a}\right), & G(0, a; z) &= -\text{Li}_2\left(\frac{z}{a}\right), \\ G(a, b; z) &= \text{Li}_2\left(\frac{b-z}{b-a}\right) - \text{Li}_2\left(\frac{b}{b-a}\right) + \log\left(1 - \frac{z}{b}\right) \log\left(\frac{z-a}{z-b}\right), \end{aligned} \quad (1.2)$$

where the last equality holds for  $a$  and  $b$  different and nonzero. The transcendental *weight* of the multiple polylogarithm is defined to be  $n$  for  $G(a_1, \dots, a_n; z)$ .

Here, we study Feynman integrals evaluated in dimensional regularization, with dimensionality  $D = 4 - 2\epsilon$ . We normalize by rational functions (the leading singularities) in order to obtain *pure* functions: when expanded in a Laurent series around  $\epsilon = 0$ , each term in the expansion has uniform weight and no factors of rational or algebraic functions of external kinematic variables. It has been conjectured [38], and observed in many nontrivial examples [39–47], that such pure functions can suffice to characterize master integrals.

**Hopf algebra, coproduct, and symbol.** The space of multiple polylogarithms has the structure of a Hopf algebra, although one must take care with factors of  $\pi$ . Specifically, if  $\overline{\mathcal{H}}_n$  is the  $\mathbb{Q}$ -vector space spanned by all multiple polylogarithms of weight  $n$ , then it is the quotient space  $\mathcal{H} = \overline{\mathcal{H}}/(\pi \overline{\mathcal{H}})$  that is a Hopf algebra [27, 28]. The quotient space  $\mathcal{H}$  is hence endowed with a coproduct  $\Delta : \mathcal{H} \rightarrow \mathcal{H} \otimes \mathcal{H}$ . The coproduct can be iterated and graded in a manner compatible with weight, so that we can write

$$\Delta_{n_1, \dots, n_k} : \mathcal{H}_n \rightarrow \mathcal{H}_{n_1} \otimes \dots \otimes \mathcal{H}_{n_k}. \quad (1.3)$$

The maximal iteration of the coproduct, which corresponds to the partition  $(1, \dots, 1)$ , agrees<sup>2</sup> with the symbol of a transcendental function  $F$  [29, 33, 35, 36, 48]:

$$\mathcal{S}(F) \cong \Delta_{1, \dots, 1}(F) \in \mathcal{H}_1 \otimes \dots \otimes \mathcal{H}_1. \quad (1.4)$$

Since every polylogarithm of weight 1 is an ordinary logarithm, the ‘log’ sign is conventionally dropped when talking about the symbol of a function.

We remark that there is an *integrability condition*, necessary and sufficient for an element of  $\mathcal{H}_1 \otimes \dots \otimes \mathcal{H}_1$  to be the symbol of some function, which is that

$$\sum_{i_1, \dots, i_n} c_{i_1, \dots, i_n} d \log x_{i_k} \wedge d \log x_{i_{k+1}} \log x_{i_1} \otimes \dots \otimes \log x_{i_{k-1}} \otimes \log x_{i_{k+2}} \otimes \dots \otimes \log x_{i_n} = 0, \quad (1.5)$$

where  $\wedge$  denotes the usual wedge product on differential forms.

<sup>2</sup>The congruence symbol is used because this relation is valid modulo factors of  $\pi$  that can appear in the first entry of the coproduct tensor, see e.g. [36]. In this paper, we will often use the terms symbol and coproduct interchangeably: indeed, we will be mostly dealing with weight 2 functions, and at this weight there is little difference between these two operators.

**The symbol alphabet.** We refer to the set of entries of the symbol of a pure Feynman integral as the letters in the *symbol alphabet*  $\mathcal{A}$ .<sup>3</sup> The number of independent dimensionless variables appearing in the symbol alphabet (i.e., the number of variables on which the pure function depends) is one fewer than the number of scales in the problem. These letters are in general not simple ratios of the Mandelstam invariants, and our general goal is to find a minimal set of variables in terms of which the letters are rational functions. In the following section, we present the alphabets used for each of the triangles we study. We were able to obtain rational symbol alphabets in every case except for the triangle with three internal and three external masses. For this case, we discuss the choice of letters, and the obstacles to making them all rational, in section 2 and more fully in appendix D.4.

## 2 One-loop triangles

In this section we present the one-loop triangles studied in this paper. We consider the scalar one-loop three-point function with arbitrary mass configurations. In  $D = 4 - 2\epsilon$  dimensions, it is defined by

$$T(p_1^2, p_2^2, p_3^2; m_{12}^2, m_{23}^2, m_{13}^2) \equiv -e^{\gamma_E \epsilon} \int \frac{d^D k}{\pi^{D/2}} \frac{1}{[k^2 - m_{13}^2 + i0] [(k + p_1)^2 - m_{12}^2 + i0] [(k - p_3)^2 - m_{23}^2 + i0]}, \quad (2.1)$$

where  $\gamma_E = -\Gamma'(1)$  is the Euler-Mascheroni constant. We use  $p_i$  with  $i = 1, 2, 3$  to denote the external four-momenta and  $m_{ij}$  to denote the masses of the internal propagators. The mass  $m_{ij}$  is that of the propagator between the external legs  $i$  and  $j$ . Throughout this paper, the masses are assumed to be generic.

Because the focus of the paper lies in the computation of cut integrals, it is important to keep track of the imaginary parts. Our conventions are the following: before any cuts are made, vertices are proportional to  $i$  and propagators have a factor  $i$  in the numerator, and the usual Feynman  $+i0$  prescription is used. No factors of  $i^{-1}$  are included for loops. Appendix A contains a summary of our conventions.

We consider this triangle in cases in which either external invariants or internal masses, or both, may become massless. See figs. 1, 2, 3. Dimensional regularization is employed because of divergences in some of these cases, but in this paper we truncate the expansion at order  $\epsilon^0$ . In appendices B, C and D, we give results for several of these functions. It is not an exhaustive list, but rather a compilation of examples that illustrates all the points we make in this paper. We have checked that the configurations we have not listed also satisfy the expected relations. In this section, we list the different triangles considered, define variables convenient for their analysis, and present their symbol alphabets in terms of these variables.

Our goal is to choose variables in terms of which we have a rational symbol alphabet. In cases with sufficiently few scales, we can use the invariants themselves as variables.

---

<sup>3</sup>The letters of the symbol alphabet should be multiplicatively independent. Note that the choice of symbol alphabet is not unique.

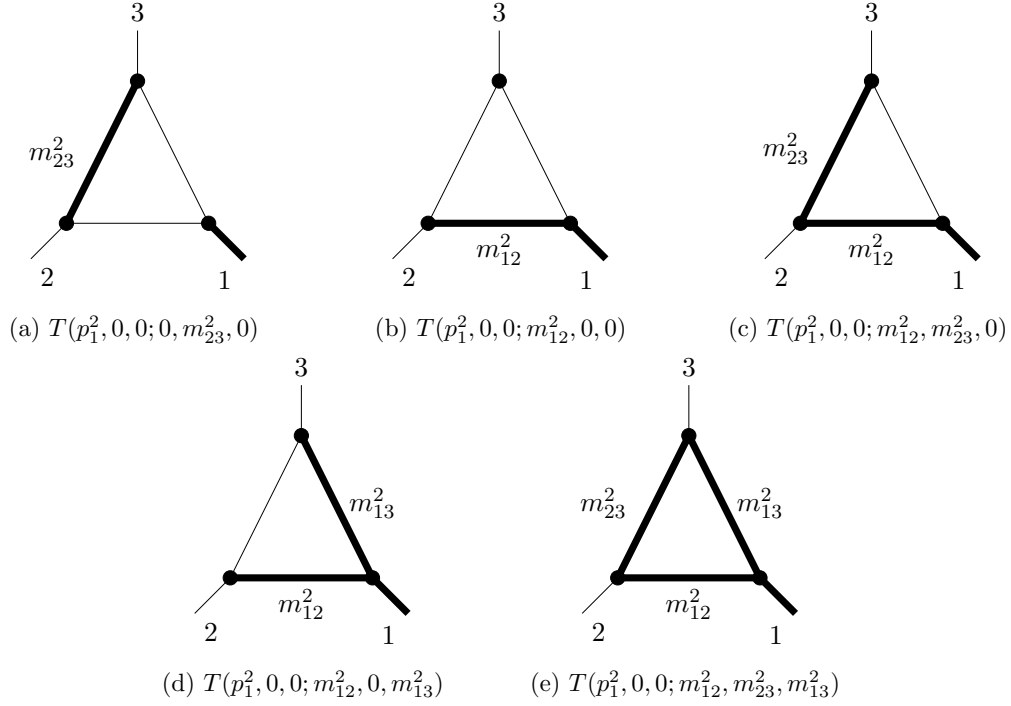


**Figure 1:** Triangles with one external massive leg.

Triangle	Symbol alphabet $\mathcal{A}$ (up to $\mathcal{O}(\epsilon^0)$ )
$T(p_1^2, 0, 0; 0, m_{23}^2, 0)$	$p_1^2, m_{23}^2, p_1^2 + m_{23}^2$
$T(p_1^2, 0, 0; m_{12}^2, 0, 0)$	$p_1^2, m_{12}^2, m_{12}^2 - p_1^2$
$T(p_1^2, 0, 0; m_{12}^2, m_{23}^2, 0)$	$p_1^2, m_{12}^2, m_{23}^2, m_{12}^2 - p_1^2, m_{12}^2 - m_{23}^2, m_{12}^2 - m_{23}^2 - p_1^2$
$T(p_1^2, 0, 0; m_{12}^2, 0, m_{13}^2)$	$w_1, \bar{w}_1, 1 - w_1, 1 - \bar{w}_1$
$T(p_1^2, 0, 0; m_{12}^2, m_{23}^2, m_{13}^2)$	$w_1, \bar{w}_1, 1 - w_1, 1 - \bar{w}_1, \mu_{23} - (1 - w_1)(1 - \bar{w}_1), \mu_{23}, \mu_{23} - w_1 \bar{w}_1, \mu_{23} + w_1(1 - \bar{w}_1), \mu_{23} + \bar{w}_1(1 - w_1)$

**Table 1:** Symbol alphabet of the triangles with one external massive leg, fig. 1.

Although the transcendental functions are only functions of ratios of the invariants, we will in general write the results explicitly in terms of the invariants. In this form, it is easy to then rewrite the result in terms of whichever dimensionless ratios are more convenient for a specific application.

In more complicated cases, invariants often appear in a specific combination, the well-known Källén function, which we denote as

$$\lambda(a, b, c) = a^2 + b^2 + c^2 - 2(ab + bc + ac). \quad (2.2)$$

In one-loop triangle integrals, it arises whenever three massive legs have momenta

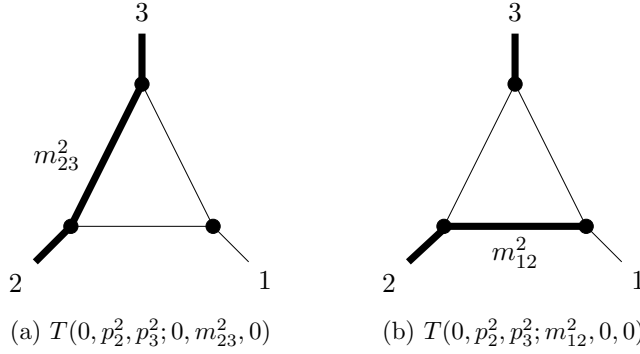


**Figure 2:** Triangles with two external massive legs.

Triangle	Symbol alphabet $\mathcal{A}$ (up to $\mathcal{O}(\epsilon^0)$ )
$T(0, p_2^2, p_3^2; 0, m_{23}^2, 0)$	$m_{23}^2, p_2^2, p_3^2, m_{23}^2 - p_2^2, m_{23}^2 - p_3^2$
$T(0, p_2^2, p_3^2; m_{12}^2, 0, 0)$	$m_{12}^2, p_2^2, p_3^2, m_{12}^2 - p_2^2, p_2^2 - m_{12}^2 - p_3^2$

**Table 2:** Symbol alphabet of the triangles with two external massive legs, fig. 2.

that sum to zero. More specifically, this occurs either when all three external legs are massive, or when three massive legs meet at one of the vertices. For these cases, the symbol letters cannot be written as rational functions of the invariants themselves, and we must thus define a different type of variable. By convention, we will always name our external momenta so that  $p_1^2$  is one of the invariants appearing as the argument of the Källén function. Then, we define the dimensionless ratios:

$$u_i = \frac{p_i^2}{p_1^2}, \quad \mu_{ij} = \frac{m_{ij}^2}{p_1^2}. \quad (2.3)$$

In terms of these dimensionless ratios, we define the following useful variables [49]:

$$z = \frac{1 + u_2 - u_3 + \sqrt{\lambda_z}}{2}, \quad \bar{z} = \frac{1 + u_2 - u_3 - \sqrt{\lambda_z}}{2}, \quad (2.4)$$

where

$$\lambda_z \equiv \lambda(1, u_2, u_3). \quad (2.5)$$

These satisfy

$$z\bar{z} = u_2, \quad (1 - z)(1 - \bar{z}) = u_3. \quad (2.6)$$

This set of variables is useful when there are three massive external legs.

Similarly, when three massive legs meet at one vertex, we define:

$$w_1 = \frac{1 + \mu_{12} - \mu_{13} + \sqrt{\lambda_1}}{2}, \quad \bar{w}_1 = \frac{1 + \mu_{12} - \mu_{13} - \sqrt{\lambda_1}}{2}, \quad (2.7)$$

where

$$\lambda_1 \equiv \lambda(1, \mu_{12}, \mu_{13}). \quad (2.8)$$

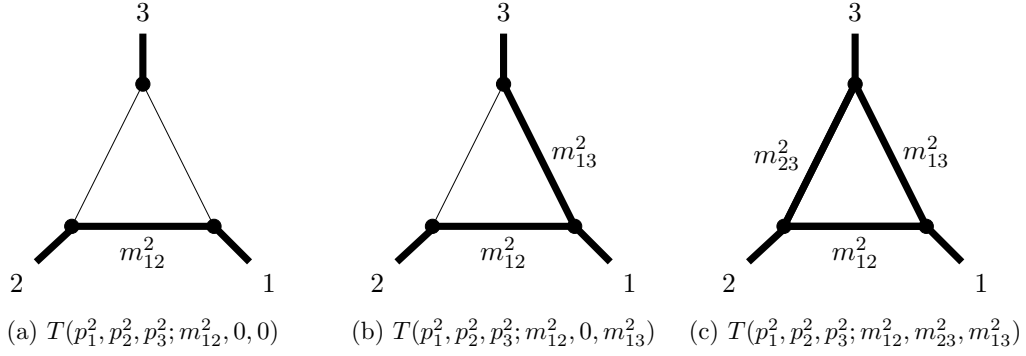


**Figure 3:** Triangles with three external massive legs.

Triangle	Symbol alphabet $\mathcal{A}$ (up to $\mathcal{O}(\epsilon^0)$ )
$T(p_1^2, p_2^2, p_3^2; m_{12}^2, 0, 0)$	$z, \bar{z}, 1 - z, 1 - \bar{z}, \mu_{12}, 1 - \mu_{12},$ $z\bar{z} - \mu_{12}, z - \mu_{12}, \bar{z} - \mu_{12}$
$T(p_1^2, p_2^2, p_3^2; m_{12}^2, 0, m_{13}^2)$	$z, \bar{z}, 1 - z, 1 - \bar{z}, w_1, \bar{w}_1, 1 - w_1, 1 - \bar{w}_1,$ $z\bar{z} - w_1\bar{w}_1, w_1 - z, w_1 - \bar{z}, \bar{w}_1 - z, \bar{w}_1 - \bar{z},$ $(1 - z)(1 - \bar{z}) - (1 - w_1)(1 - \bar{w}_1)$
$T(p_1^2, p_2^2, p_3^2; m_{12}^2, m_{23}^2, m_{13}^2)$	$z, 1 - z, w_1, \bar{w}_1, 1 - w_1, 1 - \bar{w}_1, \mu_{23},$ $w_1\bar{w}_1 - z\bar{z} + \mu_{23} - \sqrt{\lambda_2},$ $(1 - z)(1 - \bar{z}) - (1 - w_1)(1 - \bar{w}_1) - \mu_{23} + \sqrt{\lambda_3},$ $(w_1 - z)(\bar{w}_1 - \bar{z}) - \mu_{23}, (w_1 - \bar{z})(\bar{w}_1 - z) - \mu_{23},$ $(z\bar{z} + w_1\bar{w}_1 - \mu_{23})(z + \bar{z}) - 2z\bar{z}(w_1 + \bar{w}_1) \pm (z - \bar{z})\sqrt{\lambda_2},$ $z^2(1 - \bar{z}) + \bar{z}^2(1 - z) + (w_1 + \bar{w}_1)(2z\bar{z} - z - \bar{z})$ $+ (\mu_{23} - w_1\bar{w}_1)(z + \bar{z} - 2) \pm (z - \bar{z})\sqrt{\lambda_3}$

**Table 3:** Symbol alphabet of the triangles with three external massive legs, fig. 3.

These satisfy

$$w_1\bar{w}_1 = \mu_{12}, \quad (1 - w_1)(1 - \bar{w}_1) = \mu_{13}. \quad (2.9)$$

In terms of these variables, we find rational symbols for all triangles except the triangle with three internal and three external masses,  $T(p_1^2, p_2^2, p_3^2; m_{12}^2, m_{23}^2, m_{13}^2)$ , for which we fail to find a parametrization leading to a rational symbol alphabet.<sup>4</sup> Indeed, if we use a minimal set of 5 independent dimensionless variables given by  $z, \bar{z}, w_1, \bar{w}_1, \mu_{23}$ , as defined above, the symbol alphabet includes square roots of the Källén functions,

$$\lambda_2 \equiv \lambda(z\bar{z}, w_1\bar{w}_1, \mu_{23}), \quad \lambda_3 \equiv \lambda((1 - z)(1 - \bar{z}), (1 - w_1)(1 - \bar{w}_1), \mu_{23}). \quad (2.10)$$

The variables above are appropriate for the cut in  $p_1^2$ , which explains the absence of non-rational factors in the first term of eq. (D.20), and the presence of square roots in the

<sup>4</sup>The case  $T(p_1^2, p_2^2, 0; m_{12}^2, m_{23}^2, m_{13}^2)$ , not given as an example, requires a simple generalization of the variables presented here in order to produce a rational symbol alphabet.

remaining terms. Interestingly, as we show in section D.4, any given cut integral computation suggests natural variables giving a rational result. The difficulty is that each cut will suggest a different set of variables, and the variables of one cut are not rational in terms of the variables of another.

We draw the diagrams for our examples in figures 1, 2 and 3, and we give a minimal symbol alphabet of each of these examples in tables 1, 2 and 3.

### 3 The first-entry condition

We now extend the first-entry condition [32] to cases with internal masses. Our observations suggest that the coproduct can always be written in such a form where: *i*) the first entries of the coproduct component  $\Delta_{1,n-1}$  are either consistent with the thresholds of Mandelstam invariants or are internal masses themselves; *ii*) the corresponding second entry is the discontinuity across the branch point in the first entry, as is the case for diagrams with no internal masses [31].

Feynman integrals are most easily computed in the kinematic region of the invariants where the integral is well-defined independently of the  $\pm i0$ -prescription of the propagators, see e.g. [1]. In this region, the *euclidean region*, we are away from any branch cut. In the most general case considered in this paper, eq. (2.1), the euclidean region is characterized by the following conditions:

$$p_1^2 < \left(\sqrt{m_{12}^2} + \sqrt{m_{13}^2}\right)^2, \quad p_2^2 < \left(\sqrt{m_{12}^2} + \sqrt{m_{23}^2}\right)^2, \quad p_3^2 < \left(\sqrt{m_{13}^2} + \sqrt{m_{23}^2}\right)^2, \quad (3.1)$$

$$m_{12}^2 > 0, \quad m_{23}^2 > 0, \quad m_{13}^2 > 0.$$

For all of our other examples, it can be obtained from the above by taking the appropriate limit. For instance, in the absence of internal masses, the euclidean region is the region where all external invariants are negative. As we depart from this region, we are sensitive to branch cuts of the integral. The  $\pm i0$ -prescription indicates which side of the branch cut we are on. Comparing results computed with different prescriptions gives the discontinuities across the branch cuts.

The coproduct structure of multiple polylogarithms provides a natural framework for analyzing their discontinuities. Specifically, it was argued in [30] that the discontinuity acts only on the first entry of the coproduct, leaving the rest alone:

$$\Delta \text{Disc} = (\text{Disc} \otimes \text{id}) \Delta. \quad (3.2)$$

To be concrete, our precise definition of Disc is

$$\text{Disc}_x [F(x \pm i0)] = \lim_{\varepsilon \rightarrow 0} [F(x \pm i\varepsilon) - F(x \mp i\varepsilon)]. \quad (3.3)$$

Here,  $x$  represents either a Mandelstam invariant or an internal mass invariant (or indeed, any other kinematic variable). If there is no branch cut in the kinematic region being considered, or if  $F$  does not depend on  $x$ , then the discontinuity is zero. For instance,

the discontinuity in a Mandelstam invariant exists only in the region above its threshold. The choice of the sign in  $\pm i0$  is inherited from the prescription of the propagators of the Feynman integral. Finally, for later use, we also define a sequential discontinuity operator  $\text{Disc}_{x_1, \dots, x_k}$  as:

$$\text{Disc}_{x_1, \dots, x_k} F \equiv \text{Disc}_{x_k} (\text{Disc}_{x_1, \dots, x_{k-1}} F), \quad (3.4)$$

where the  $x_i$  are associated either with internal masses or with external momentum invariants.

We note that eq. (3.2) implies that the first entries of the coproduct tensor of a Feynman diagram must have the same branch cut structure as the Feynman diagram itself. In particular, when looking at the  $\Delta_{1, n-1}$  component, the first entries must be simple logarithms with branch points at the boundaries of the euclidean region.

This observation, known as the *first entry condition*, was first formulated in the context of integrals with massless propagators, where the first entries of their symbol can be written as logarithms of Mandelstam invariants [32].

In the presence of massive propagators, we find two ways in which the first entry condition generalizes. The first is that we no longer have logarithms of Mandelstam invariants themselves, but instead logarithms with branch cuts at the mass threshold for the corresponding invariant. The second is that the squared masses of the propagators themselves appear as first entries. Both modifications are consistent with our observations above.

As predicted by eq. (3.2) and already observed in the absence of internal masses [31], the second entries correspond to the discontinuities associated to the branch cut identified in the corresponding first entry. We observe the same behavior when internal masses are present, the new feature being the existence of discontinuities associated to the internal masses themselves.

In the context of the examples of this paper, we observe that when we use the Mandelstam invariants themselves (or ratios of them, if we want to work with dimensionless quantities) as variables, the above properties are very easy to check. In more complicated cases where we need to change variables to have a rational symbol alphabet, the situation is not as clear: even though the simplest expression for the symbol (or, equivalently, the coproduct) does not satisfy these properties, we can always rearrange the different terms of the symbol tensor so that they are in the form described above.

**Example 1:** Consider the triangle  $T(p_1^2, 0, 0; m_{12}^2, 0, 0)$ , whose symbol is given in eq. (B.8). The first term has  $\log(m_{12}^2)$  as its first entry, and the second term has  $\log(m_{12}^2 - p_1^2)$  as its first entry. The latter is written in a form in which the argument of the logarithm is positive in the euclidean region where the integral is originally evaluated.

**Example 2:** As another example, consider the triangle  $T(p_1^2, 0, 0; m_{12}^2, 0, m_{13}^2)$ , whose symbol is given in eq. (B.19). We have changed variables according to eq. (2.7) to have a rational symbol alphabet. Because the new variables have a more complicated relation to the Mandelstam invariants, the first entry condition is not as transparent as in the previous example. However, as mentioned above, the symbol of  $\mathcal{T}(p_1^2, 0, 0; m_{12}^2, 0, m_{13}^2)$  can

be rewritten as

$$(w_1 \bar{w}_1) \otimes \frac{w_1}{1-w_1} + ((1-w_1)(1-\bar{w}_1)) \otimes \frac{1-\bar{w}_1}{\bar{w}_1} + (w_1(1-\bar{w}_1)) \otimes \frac{\bar{w}_1(1-w_1)}{w_1(1-\bar{w}_1)}. \quad (3.5)$$

The first entry of the first term is  $\log(m_{12}^2/p_1^2)$ , and its second entry is associated with the discontinuity in the variable  $m_{12}^2$ . The first entry of the second term is  $\log(m_{13}^2/p_1^2)$ , and its second entry is associated with the discontinuity in the variable  $m_{13}^2$ . The first entry of the third term corresponds to the threshold at  $p_1^2 = (\sqrt{m_{12}^2} + \sqrt{m_{13}^2})^2$ , and its second entry is associated with the discontinuity in the variable  $p_1^2$ . The argument of the logarithm in the first entry of this term is not a direct change of variables of  $p_1^2 - (\sqrt{m_{12}^2} + \sqrt{m_{13}^2})^2$ , which would not be a rational function. Nevertheless, one can verify that the condition  $w_1(1-\bar{w}_1) > 0$  is exactly equivalent to the condition  $p_1^2 > (\sqrt{m_{12}^2} + \sqrt{m_{13}^2})^2$ , whenever  $p_1^2 > 0$ . We can understand this latter condition as a weaker prerequisite for obtaining any discontinuity in the variable  $p_1^2$ .

In this analysis, we have neglected the denominators  $p_1^2$  in each of the first entries of eq. (3.5). We did this because the denominators are simply used to normalize the variables to be dimensionless: as we know, the physically meaningful first entry is the one including the mass threshold, which is nonzero for the  $p_1^2$  channel. Indeed, since the three second entries sum to zero, we see that the term whose first entry would be  $p_1^2$  has zero as its second entry.

We finish with a word of caution about eq. (3.5). In this triangle, the variables  $w_1$  and  $\bar{w}_1$  are distinguished only by the choice of branch of the square root. Like the function itself, the symbol has no preferred branch, and therefore it is invariant under the exchange  $w_1 \leftrightarrow \bar{w}_1$ . This invariance is apparent in the form given in eq. (B.19) but obscure in eq. (3.5). Notably, the three discontinuities, as read from eq. (3.5), are not themselves invariant under this exchange. When relating these discontinuities to cut integrals, we will be very specific about the kinematics and insist on taking the positive branch of the square root. From that point of view, the form given in eq. (3.5) will be necessarily preferred over its conjugate under  $w_1 \leftrightarrow \bar{w}_1$ .<sup>5</sup> In the following, we will relate discontinuities to operations on individual symbol letters, and not particular combinations of them. Thus, while we claim that one can generally write symbols of Feynman integrals in a form such as eq. (3.5), where the first entries are directly identified with kinematic invariants and thresholds, one should not immediately conclude that the corresponding second entries are unambiguously interpreted as discontinuities.

## 4 Two types of cuts

Feynman diagrams with internal masses have discontinuities associated with both the external massive channels and the internal masses. These two types of discontinuities correspond to two slightly different types of diagrammatic cuts. The first type are the well-known cuts in external channels [3, 4, 31], and the second type are single-propagator

---

<sup>5</sup>Whenever we make use of the first entry condition (see section 6), we will therefore always take  $w_1(1-\bar{w}_1)$  for the  $p_1^2$  channel, and not  $\bar{w}_1(1-w_1)$ .

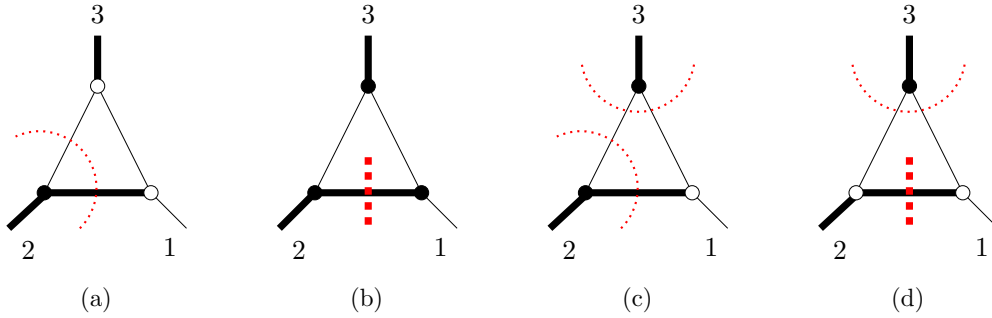


**Figure 4:** Example of cuts of  $T(0, p_2^2, p_3^2; m_{12}^2, 0, 0)$ : (a) single cut in an external channel; (b) single cut in an internal mass; (c) double cut in external channels; (d) double cut in an external channel and an internal mass. Thin dotted lines correspond to cuts on external channels and imply complex conjugation of a region of the diagram. Thick dashed lines correspond to mass cuts and do not imply any complex conjugation.

cuts for which we give the rules in this paper. We start by reviewing the rules for cuts in external channels, then introduce single-propagator cuts, and finally explain our strategy to compute the cut diagrams for our examples. In both cases, our cutting rules are designed to reproduce the discontinuities in the corresponding variables. This will allow us to compute all types of single and double cuts considered in this paper. See fig. 4 for examples.

#### 4.1 Cut in a kinematic channel

We start by discussing cuts in external channels  $s_i$ . The operator  $\text{Cut}_{s_i}$  gives a *cut* Feynman integral, in which some propagators, the *cut propagators*, are replaced by Dirac delta functions. The cut separates the diagram into two parts, with the momentum flowing through the cut propagators from one part to the other corresponding to the Mandelstam invariant  $s_i$ . Each cut is associated with a consistent direction of energy flow between the two parts of the diagram, in each of the cut propagators. We briefly review the rules established in refs. [3, 4] for single cuts, and generalized in ref. [31] for sequential cuts.

**First cut.** We enumerate all possible partitions of the vertices of a Feynman diagram into two nonempty sets, distinguished by being colored black or white; see fig. 5 for an example. Each diagram is evaluated according to the following rules for scalar theory. (See appendix A for a summary of our conventions.)

- Black vertices, and propagators joining two black vertices, are computed according to the usual Feynman rules.
- White vertices, and propagators joining two white vertices, are complex-conjugated with respect to the usual Feynman rules.
- Propagators joining a black and a white vertex are *cut*. They are replaced by an on-shell delta function, together with a factor of  $2\pi$  to capture the complex residue correctly, *and* a theta function restricting energy to flow in the direction *from* black

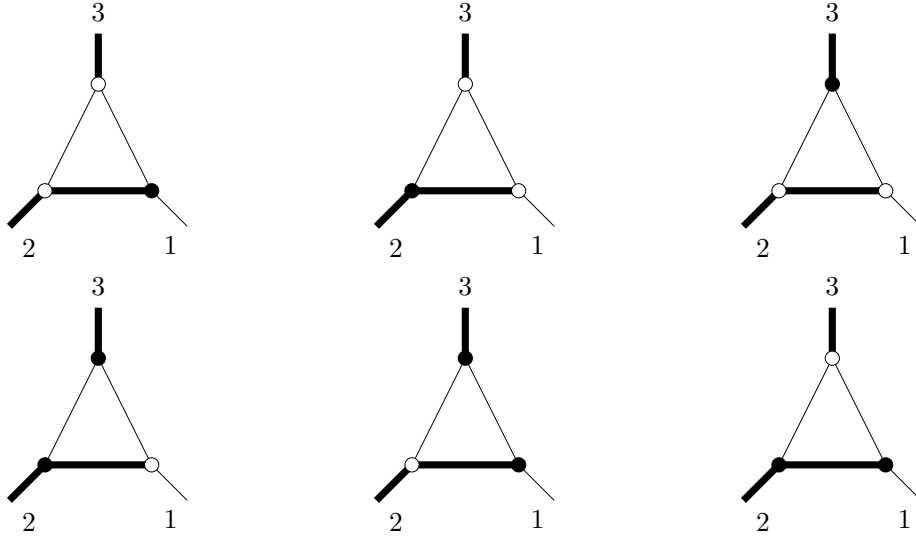


**Figure 5:** All possible cut diagrams of  $T(0, p_2^2, p_3^2; m_{12}^2, 0, 0)$ . A diagram in the top row and its corresponding diagram in the bottom row are associated to the same momentum channel, but opposite energy flow.

to white. Stated precisely, when cut, a (complex conjugated) propagator is replaced according to

$$\frac{\pm i}{p^2 - m^2 \pm i0} \longrightarrow 2\pi \delta(p^2 - m^2) \theta(p_0), \quad (4.1)$$

where we assume that the momentum vector  $p$  is directed from the black to the white vertex.

$\text{Cut}_{s_i}$  denotes the sum of all diagrams that isolate the channel  $s_i$ : if  $p$  is the sum of the momenta flowing through cut propagators from black to white, then  $p^2 = s_i$ . Although cut diagrams in a given momentum channel appear in pairs that are black/white color reversals (see fig. 5) only one can be consistent with the energies of the fixed external momenta.

We stress that these rules require that one of the two regions of the diagram (the white region in our conventions) must be computed with complex conjugated Feynman rules. In particular, this implies that the  $\pm i0$  of the invariants in the white region is reversed.

Consider a multiple-channel cut,  $\text{Cut}_{s_1, \dots, s_k} F$ . It is represented by a diagram with a color-partition of vertices for each of the cut invariants  $s_i = p_i^2$ . Assign a sequence of colors  $(c_1(v), \dots, c_k(v))$  to each vertex  $v$  of the diagram, where each  $c_i$  takes the value 0 or 1. For a given  $i$ , the colors  $c_i$  partition the vertices into two sets, such that the total momentum flowing from vertices labeled 0 to vertices labeled 1 is equal to  $p_i$ . A vertex  $v$  is finally colored according to  $c(v) \equiv \sum_{i=1}^k c_i(v) \pmod{2}$ , with black for  $c(v) = 0$  and white for  $c(v) = 1$ . The rules for evaluating a diagram are as follows (see appendix A for a summary of our conventions):

- Black vertices are computed according to the usual Feynman rules; white vertices are computed according to complex-conjugated Feynman rules.

- A propagator joining vertices  $u$  and  $v$  is uncut if  $c_i(u) = c_i(v)$  for all  $i$ . If the vertices are black, i.e.  $c(u) = c(v) = 0$ , then the propagator is computed according to the usual Feynman rules, and if the vertices are white, i.e.  $c(u) = c(v) = 1$ , then the propagator is computed according to complex-conjugated Feynman rules.
- A propagator joining vertices  $u$  and  $v$  is cut if  $c_i(u) \neq c_i(v)$  for any  $i$ . There is a theta function restricting the direction of energy flow from 0 to 1 for each  $i$  for which  $c_i(u) \neq c_i(v)$ . If different cuts impose conflicting energy flows, then the product of the theta functions is zero and the diagram gives no contribution.

We also restrict ourselves to real kinematics, both for the external and internal momenta. As a consequence, diagrams with massless on-shell three-point vertices vanish in dimensional regularization. Furthermore, the rules exclude crossed cuts and sequential cuts in which the channels are not all distinct. These last two restrictions are mentioned for completeness only, as they are not relevant in the examples studied in this paper. We refer the reader to ref. [31] for more details and examples of this set of rules. We give an example of a double cut on two external channels in fig. 4c.

For the examples considered in this paper, cut diagrams are computed in the region where the cut invariants are above their respective thresholds, all other consecutive Mandelstam invariants are below threshold, and the squares of all internal masses are positive.

## 4.2 Cut in an internal mass

To give a complete description of the coproduct of diagrams with internal masses, we must introduce a new kind of cut, a single-propagator cut, corresponding to discontinuities across branch cuts related to the internal masses. Our discussion will be in the context of one-loop diagrams, but this is solely for the simplicity of the expressions, and all the results can be straightforwardly generalized to the multi-loop case.

Let  $F$  be a one-loop planar diagram with  $n$  external legs of momentum  $p_i$ , for  $i = 1, \dots, n$ , all incoming, massive or not, and with internal masses  $m_{i,i+1}^2$  between legs  $i$  and  $i + 1$ , which we assume are all distinct. Furthermore, we define  $q_j = \sum_{i=1}^j p_i$ , for  $j = 1, \dots, n$ , so that  $q_n = 0$ . Then, according to our Feynman rules,

$$F(q_i \cdot q_j; m_{1,2}^2, \dots, m_{1,n}^2) = (-1)^n e^{\gamma_E \epsilon} \int \frac{d^{4-2\epsilon} k}{\pi^{2-\epsilon}} \prod_{i=1}^n \frac{1}{(k + q_i)^2 - m_{i,i+1}^2 + i0}. \quad (4.2)$$

The integral  $F$  is evaluated away from any branch cut in the euclidean region of the Mandelstam invariants, and for all  $m_{i,i+1}^2 > 0$ . In the same way that the Mandelstam invariants inherit an  $+i0$  prescription from the form of the propagators, we can associate a  $-i0$  prescription to the masses:

$$m_{i,i+1}^2 \rightarrow m_{i,i+1}^2 - i0.$$

Although it does not correspond to a physical region, we can analytically continue  $F$  to a region where the square of one of the masses is negative (without loss of generality, say  $m_{1,n}^2 < 0$ ), while keeping all the other squared masses positive and the Mandelstam

invariants in the euclidean region. In this region, we isolate the discontinuity associated with  $m_{1,n}^2$ :

$$\begin{aligned}
\text{Disc}_{m_{1,n}^2} F &= F(q_i \cdot q_j; m_{1,2}^2, \dots, m_{1,n}^2 - i0) - F(q_i \cdot q_j; m_{1,2}^2, \dots, m_{1,n}^2 + i0) \\
&= (-1)^n e^{\gamma_E \epsilon} \int \frac{d^{4-2\epsilon} k}{\pi^{2-\epsilon}} \left( \frac{1}{k^2 - m_{1,n}^2 + i0} - \frac{1}{k^2 - m_{1,n}^2 - i0} \right) \prod_{i=1}^{n-1} \frac{1}{(k + q_i)^2 - m_{i,i+1}^2} \\
&= (-1)^{n+1} e^{\gamma_E \epsilon} \int \frac{d^{4-2\epsilon} k}{\pi^{2-\epsilon}} (2\pi i) \delta(k^2 - m_{1,n}^2) \prod_{i=1}^{n-1} \frac{1}{(k + q_i)^2 - m_{i,i+1}^2} \\
&\equiv \text{Cut}_{m_{1,n}^2} F,
\end{aligned} \tag{4.3}$$

which shows that mass discontinuities do indeed correspond to single-particle cuts. We again stress that although we are discussing one-loop integrals, this is just for simplicity of the expressions. The same result holds for a multi-loop diagram.

Furthermore, we notice that  $F$  can also be a cut Feynman diagram as long as the propagator with mass  $m_{1,n}^2$  has not been cut previously. Cuts in internal masses can then be combined with cuts in external channels to compute sequential discontinuities in internal masses and external channels.

We can thus deduce the rules for single-propagator cuts, corresponding to mass discontinuities: we simply replace the cut propagator by a delta function, according to

$$\frac{\pm i}{p^2 - m^2 \pm i0} \rightarrow 2\pi \delta(p^2 - m^2), \tag{4.4}$$

without any condition on the energy flow or any further conjugation of other parts of the diagram. Unlike cuts in kinematic channels, the black and white colorings are unaffected by these cuts, as there is no notion of separation into two regions where one is complex-conjugated.

### 4.3 Calculation of cut diagrams

We now outline our strategy for the calculation of the cuts of the one-loop three-point functions studied in this paper. For cuts in external channels, it is a simple generalization of what is done in ref. [31], so we will be very brief. For the single-propagator cuts, we present two alternative methods. All cuts given in appendices B, C and D were obtained through the methods described here.

**Cuts in external channels.** When computing a single cut in the channel  $p_i^2$ , we work in the region where  $p_i^2$  is above its threshold, all other external channels are below threshold, and all masses are positive. We parametrize the external momenta as

$$p_i = \sqrt{p_i^2} (1, 0, \mathbf{0}_{D-2}), \quad p_j = \sqrt{p_j^2} (\alpha, \sqrt{\alpha^2 - 1}, \mathbf{0}_{D-2}), \tag{4.5}$$

where  $\alpha$  is trivial to determine in terms of the kinematic variables.

We route the loop momentum so that the propagators of momentum  $k$  and  $(p_i - k)$  are cut, and if possible the propagator of momentum  $k$  is massless. We parametrize  $k$  as

$$k = k_0(1, \beta \cos \theta, \beta \sin \theta \mathbf{1}_{D-2}), \quad (4.6)$$

where  $\theta \in [0, \pi]$ , and  $k_0, \beta > 0$ , and  $\mathbf{1}_{D-2}$  ranges over unit vectors in the dimensions transverse to  $p_i$  and  $p_j$ . If the propagator of momentum  $k$  is massless, then  $\beta = 1$ .

Using the delta function that puts the propagator of momentum  $k$  on-shell, the integration measure becomes

$$\int d^{4-2\epsilon} k \delta(k^2 - m^2) \theta(k_0) = \frac{2^{1-2\epsilon} \pi^{1-\epsilon}}{\Gamma(1-\epsilon)} \int_0^\infty dk_0 \left( \sqrt{k_0^2 - m^2} \right)^{1-2\epsilon} \int_0^1 dx (1-x)^{-\epsilon} x^{-\epsilon}, \quad (4.7)$$

in the most general case we need to consider for this paper. The  $k_0$  integral can be trivially performed using the delta function putting the propagator of momentum  $(p_i - k)$  on-shell.

The remaining uncut propagator, of momentum  $(p_j + k)$ , is linear in the  $x$  variable, and so the most complicated result we will get for the single cut of a one-loop three-point function can be written to all orders in  $\epsilon$  as a Gauss hypergeometric function, eq. (A.8), as can be seen in the several examples collected in appendices B, C and D.

If the triangle has two or three external masses (say  $p_i^2 \neq 0$  and  $p_j^2 \neq 0$ ), we can compute its sequential cuts in the external channels  $p_i^2$  and  $p_j^2$ , in the region where they are both above threshold, while the remaining external channel is below threshold and all internal masses are positive. The extra delta function makes the  $x$  integration in eq. (4.7) trivial (note, however, that it might restrict the kinematic region in which the cut is nonzero). The most complicated functions we get as a result are invariants raised to powers that are linear in  $\epsilon$ , producing powers of logarithms upon expansion in  $\epsilon$ . Again, our examples are collected in appendices B, C and D.

**Cuts in internal masses.** Cuts in internal masses are harder to compute than cuts in external channels. Here, we present two ways of computing them. Either way, we compute discontinuities, which are trivially related to cuts through eq. (4.3). The first way is a brute-force method that works in all cases considered here. The second way is more elegant, but only suitable for special configurations of the external and internal masses. Because we do not have a proof that it should work, we present it as an observation. In all cases where both can be applied we find they agree, giving evidence for the validity of the second way. We will illustrate both in the context of the triangle  $T(p_2^2, p_3^2; m_{12}^2)$ .

The first method relies on getting a Feynman parameter representation for the diagram, and then computing the discontinuity of the integrand across the branch cut associated with the internal mass. It is of course valid for any configuration of the internal and external masses. For example, we have:

$$T(p_2^2, p_3^2; m_{12}^2) = i \frac{e^{\gamma_E \epsilon} \Gamma(1+\epsilon)}{\epsilon} \int_0^1 dx \frac{(1-x)^{-\epsilon}}{m_{12}^2 + x(p_3^2 - p_2^2)} \left( (-p_3^2 x)^{-\epsilon} - (m_{12}^2 - p_2^2 x)^{-\epsilon} \right), \quad (4.8)$$

which we obtain by computing the trivial and the first non-trivial Feynman parameter integrals. We then get

$$\text{Disc}_{m_{12}^2} [(m_{12}^2 - p_2^2 x)^{-\epsilon}] = \frac{2\pi i \epsilon}{\Gamma(1-\epsilon)\Gamma(1+\epsilon)} (p_2^2 x - m_{12}^2)^{-\epsilon} \theta\left(\frac{m_{12}^2}{p_2^2} - x\right),$$

where we used  $m_{12}^2 = m_{12}^2 - i0$  and are in the region  $p_2^2 < m_{12}^2 < 0$ , to get

$$\begin{aligned} \text{Cut}_{m_{12}^2} T(p_2^2, p_3^2; m_{12}^2) &= \text{Disc}_{m_{12}^2} T(p_2^2, p_3^2; m_{12}^2) \\ &= \frac{2\pi e^{\gamma_E \epsilon}}{\Gamma(1-\epsilon)} \int_0^{m_{12}^2/p_2^2} dx (1-x)^{-\epsilon} \frac{(p_2^2 x - m_{12}^2)^{-\epsilon}}{m_{12}^2 + x(p_3^2 - p_2^2)}. \end{aligned} \quad (4.9)$$

which is trivial to compute to any desired accuracy in  $\epsilon$ .

The second way only works if there is a massive external leg non-adjacent to the massive internal leg being cut. More precisely, in our notation, if we look at the cut in the internal propagator of mass  $m_{ij}^2$ , we need  $p_k^2 \neq 0$ . We can then compute a three-propagator cut corresponding to  $\text{Cut}_{p_k^2, m_{ij}^2}$  in the region where  $m_{ij}^2 < 0$  and  $p_k^2$  is above threshold. This is trivial to evaluate. The single-propagator cut is finally obtained through dispersive integration in the  $p_k^2$ -channel of the three-propagator cut. This is not guaranteed to work a priori, because we have no proof that the  $m_{ij}^2$  discontinuity function has a dispersive representation. However, it does give the correct answer in all the cases we have considered. The reason why this method is not valid for any configuration of internal and external masses is because there is no sequential cut associated to an external mass and an internal mass if they are adjacent.

For our example, we have  $(i, j, k) = (1, 2, 3)$ . The three-propagator cut is computed in the region where  $p_3^2 > 0$  and  $m_{12}^2 < 0$  and is given by

$$\text{Cut}_{m_{12}^2, p_3^2} T(p_2^2, p_3^2; m_{12}^2) = -\frac{4\pi^2 i e^{\gamma_E \epsilon}}{\Gamma(1-\epsilon)} \frac{(p_3^2)^{-\epsilon} (-m_{12}^2)^{-\epsilon}}{(p_3^2 - p_2^2)^{1-\epsilon}} (p_3^2 + m_{12}^2 - p_2^2)^{-\epsilon} \theta(p_3^2 + m_{12}^2 - p_2^2), \quad (4.10)$$

Through a standard dispersive integral, see e.g. the brief discussion in ref. [31], we obtain

$$\begin{aligned} \text{Cut}_{m_{12}^2} T(p_2^2, p_3^2; m_{12}^2) &= \text{Disc}_{m_{12}^2} T(p_2^2, p_3^2; m_{12}^2) \\ &= -2\pi \frac{e^{\gamma_E \epsilon}}{\Gamma(1-\epsilon)} (-m_{12}^2)^{-\epsilon} \int_0^\infty \frac{ds}{s - p_3^2} \frac{s^{-\epsilon}}{(s - p_2^2)^{1-2\epsilon}} (s + m_{12}^2 - p_2^2)^{-\epsilon}. \end{aligned} \quad (4.11)$$

The integral is trivial to compute at any order in  $\epsilon$ , and matches the result obtained in eq. (4.9).

In appendices B, C and D, we collect several examples of cuts in massive internal legs. Whenever possible, the cuts were computed in each of the two ways described above, and the results agreed.

## 5 Relations among discontinuities

In this section, we explain how to relate cuts and coproduct entries, via their separate relations to discontinuities across branch cuts. This allows us to give a diagrammatic interpretation of coproduct entries. We generalize the relations presented in ref. [31] to diagrams with massive propagators. The generalization is straightforward, aside from two points regarding the  $i0$  prescription: *i*) when combining channel and mass discontinuities, the  $\pm i0$  associated to the masses is determined once all channel cuts have been taken; *ii*) the precise determination of how the  $\pm i0$  prescription propagates from invariants to symbol letters is slightly more complicated than in the absence of internal masses. After establishing the general relations, we give examples to illustrate these points.

### 5.1 Cut diagrams and discontinuities

The rules for evaluating cut diagrams are designed to compute their discontinuities. For single cuts in internal masses, the relation is straightforward as can be seen from eq. (4.3). For cuts in external channels, there are some subtleties which we now review.

The original relation for the first cut in an external channel follows from the largest time equation [3–5], and it takes the form

$$\text{Disc}_s F = -\text{Cut}_s F. \quad (5.1)$$

For sequential cuts in external channels, it was argued in ref. [31] that the relation could be generalized so that  $\text{Cut}_{s_1, \dots, s_k} F$  captures discontinuities through the relation

$$\text{Cut}_{s_1, \dots, s_k} F = (-1)^k \text{Disc}_{s_1, \dots, s_k} F, \quad (5.2)$$

where  $\text{Cut}_{s_1, \dots, s_k} F$  is to be computed according to the rules given above for multiple cuts.

Eq. (5.2), like eq. (5.1), is valid in a specific kinematic region. As mentioned in the previous section,  $\text{Cut}_{s_1, \dots, s_k} F$  is evaluated in the region where  $s_1, \dots, s_k$  are above their respective thresholds, the remaining external channels are below their thresholds, and all internal masses are positive. On the right-hand side, we proceed step by step according to the definition in eq. (3.4): each  $\text{Disc}_{s_1, \dots, s_i}$  is evaluated after analytic continuation to the same region in which  $\text{Cut}_{s_1, \dots, s_i} F$  is evaluated.

The relation between cuts in internal masses and discontinuities is trivial. For a single cut, the relation is given in eq. (4.3). It can be straightforwardly generalized as

$$\text{Cut}_{m_1^2, \dots, m_k^2} F = \text{Disc}_{m_1^2, \dots, m_k^2} F. \quad (5.3)$$

We can now combine cuts in internal masses and external channels through

$$\text{Cut}_{s_1, \dots, s_l, m_1^2, \dots, m_k^2} F = (-1)^l \text{Disc}_{s_1, \dots, s_l, m_1^2, \dots, m_k^2} F. \quad (5.4)$$

In order for eq. (5.4) to produce the correct signs, the  $\pm i0$  associated to the internal masses on the right hand side are determined from the cut diagram in which all  $l$  of the channel cuts have been taken. (We recall that according to our rules, channel cuts imply

complex conjugation of certain regions of the diagram, which affects the  $i0$ -prescription of the internal propagators. Hence we make it a rule to take channel discontinuities before mass discontinuities.) Furthermore, on the right hand side, we take a specific order of the listed invariants. Indeed, while sequential cuts are independent of the order in which the invariants are listed, the correspondences to Disc are derived in sequence so that the right-hand side of eq. (5.4) takes a different form when channels and masses on the left-hand side are permuted. Thus, eq. (5.4) implies relations among the different  $\text{Disc}_{s_1, \dots, s_l, m_1^2, \dots, m_k^2} F$ .

We note one restriction: the cut integrals reproduce sequential discontinuities through the above relations only if each additional invariant in the subscript—whether a momentum channel or a mass—introduces at least one new cut propagator in the Feynman diagrams. For example, we would not consider  $\text{Cut}_{p_1^2, m_{1,2}^2}$  of a one-loop triangle, since the propagator of mass  $m_{1,2}^2$  was already cut in the first step,  $\text{Cut}_{p_1^2}$ .

In section 5.4 we make these relations concrete in the context of specific examples.

### 5.1.1 A limit on sequential mass cuts

Suppose that two massive propagators are attached to the same external massive leg of a one-loop integral, as for example in fig. 1d. Then the double discontinuity in those two internal masses will vanish. Let us now see why this is the case. Without loss of generality, we consider the cut in  $m_{1,2}^2$  of  $\text{Cut}_{m_{1,n}^2} F$  as given in eq. (4.3). The integral with cuts of the two propagators of masses  $m_{1,n}^2$  and  $m_{1,2}^2$ , which is given by

$$(-1)^n \int \frac{d^{4-2\epsilon} k}{\pi^{2-\epsilon}} (2\pi i)^2 \delta(k^2 - m_{1,n}^2) \delta((k+p_1)^2 - m_{1,2}^2) \prod_{i=2}^{n-1} \frac{1}{(k+q_i)^2 - m_{i,i+1}^2}, \quad (5.5)$$

can be used for either of the cut integrals  $\text{Cut}_{m_{1,n}^2, m_{1,2}^2} F$  or  $\text{Cut}_{p_1^2} F$ , depending on the kinematic region where it is evaluated. If  $p_1^2 \neq 0$ , then the uncut integral  $F$  has a branch cut in  $p_1^2$ . As a consequence of the largest time equation, the integral  $\text{Cut}_{p_1^2} F$  is proportional to the discontinuity of  $F$  across this branch cut [3, 4]. In particular, the discontinuity is zero when we are below the threshold of  $p_1^2$ , which can be realized either for  $m_{1,2}^2, m_{1,n}^2 > 0$  or  $m_{1,2}^2, m_{1,n}^2 < 0$ , and in this case the integral eq. (5.5) vanishes as well.

Now, the double-cut integral  $\text{Cut}_{m_{1,n}^2, m_{1,2}^2} F$  must be evaluated in the region where  $m_{1,2}^2, m_{1,n}^2 < 0$  and all other invariants are below their thresholds. Since  $p_1^2$ , in particular, is below its threshold, the integral vanishes by the argument given above. We will see an example of this type of vanishing double cut in  $T(p_1^2, 0, 0; m_{1,2}^2, 0, m_{1,3}^2)$  in Section 5.4.3.

However, if  $p_1^2 = 0$ , then  $F$  has no branch cut associated with this external channel, and the largest time equation does not give any constraint on the result of eq. (5.5). In this case, the double discontinuity on the masses  $m_{1,2}^2$  and  $m_{1,n}^2$  can indeed be nonzero. We will see an example of this type of nonvanishing double cut in  $T(p_1^2, 0, 0; m_{1,2}^2, m_{2,3}^2, 0)$  in Section 5.4.1.

### 5.1.2 Sequential cuts of triangle diagrams

In the examples studied in this paper, we are restricted to  $k = 2$  in eq. (5.2), since after a sequence of two cuts in external channels, all three propagators are cut. Because

triangle diagrams must have at least one external massive channel, the above considerations restrict us to at most two cuts in internal masses. It follows that the maximum value for  $k$  in eq. (5.3) is also 2. This is consistent with the transcendental weight of the functions being two.

## 5.2 Coproduct and discontinuities

In Section 3, we defined the operation  $\text{Disc}_{s_1, \dots, s_k}$ . We also argued that the coproduct is a natural tool to study the discontinuity of polylogarithms. We now make the relation between the coproduct and discontinuities precise.

We start by defining the operation  $\delta_{x_1, \dots, x_k}$  on the coproduct. Given the symbol alphabet  $\mathcal{A}$ , we can write the  $(1, 1, \dots, 1, n-k)$  component of the coproduct of  $F$  as

$$\underbrace{\Delta_{1,1,\dots,1,n-k}}_{k \text{ times}} F = \sum_{(x_{i_1}, \dots, x_{i_k}) \in \mathcal{A}^k} \log x_{i_1} \otimes \dots \otimes \log x_{i_k} \otimes g_{x_{i_1}, \dots, x_{i_k}}. \quad (5.6)$$

Then, our truncation operation is defined to be

$$\delta_{x_{j_1}, \dots, x_{j_k}} F \cong \sum_{(x_{i_1}, \dots, x_{i_k}) \in \mathcal{A}^k} \delta_{i_1 j_1} \dots \delta_{i_k j_k} g_{x_{i_1}, \dots, x_{i_k}}. \quad (5.7)$$

The congruence symbol indicates that  $\delta_{x_{j_1}, \dots, x_{j_k}} F$  is defined only modulo  $\pi$ ; this is an intrinsic ambiguity due to the nature of the Hopf algebra of multiple polylogarithms. If  $F$  contains overall numerical factors of  $\pi$ , they should be factored out before performing this operation and then reinstated.

In ref. [31], it was shown how the discontinuity of any element of the Hopf algebra is captured by the operation  $\delta$  as defined in eq. (5.7). This relies on the relation

$$\text{Disc } F \cong \mu [(\text{Disc} \otimes \text{id})(\Delta_{1,n-1} F)], \quad (5.8)$$

where  $\mu$  is a linear map,  $\mu : \mathcal{H} \otimes \mathcal{H} \rightarrow \mathcal{H}$ , such that  $\mu(a \otimes b) = a \cdot b$ , for  $a, b \in \mathcal{H}$ . Eq. (5.8) is a direct consequence of the relation between the coproduct and discontinuity operator presented in ref. [30]. The whole discussion of ref. [31] in the context of massless internal propagators generalizes straightforwardly to diagrams with massive propagators, so we will simply review it briefly here.

The relation between sequential discontinuities and entries of the coproduct is

$$\text{Disc}_{r_1, \dots, r_k} F \cong \Theta \sum_{(x_1, \dots, x_k) \in \mathcal{A}^k} \left( \prod_{i=1}^k a_i(r_i, x_i) \right) \delta_{x_1, \dots, x_k} F, \quad (5.9)$$

where the sum is taken over ordered sequences  $(x_1, \dots, x_k)$  of  $k$  letters, and the  $r_i$  can be either internal masses or external channels. The congruence symbol in eq. (5.9) indicates that the right-hand side only captures terms whose coproduct is nonvanishing, and it therefore holds modulo  $(2\pi i)^{k+1}$ . The schematic factor  $\Theta$  expresses the restriction to the kinematic region where the left-hand side will be compared with  $\text{Cut}$ . The factors  $a_i(r_i, x_i)$  are the discontinuities of real-valued logarithms after analytic continuation from  $R_{i-1}$ , the

region where the  $(i - 1)$ -th cut is taken, to the region  $R_i$ , the region where the  $i$ -th cut is taken. Specifically,

$$a_i(r_i, x_i) = \text{Disc}_{r_i; R_i} \left[ \left[ \log(\pm x_i) \right] \right]_{R_{i-1}}, \quad (5.10)$$

where the double bracket means that the sign should be chosen so that the argument of the logarithm is positive in the region  $R_{i-1}$ . In section 5.4 we make these relations concrete in the context of specific examples.

Eq. (5.9) is valid independently of the order in which the discontinuities are taken. However, because for massive internal propagators the relation between Disc and Cut have the correct signs only if discontinuities on channels are taken first—see the discussion below eq. (5.4)—we will in general impose the same constraint in eq. (5.9). Furthermore, we observe that it is more complicated to identify the sign of the imaginary part of the symbol letters  $x_i$  inherited from the  $\pm i0$  prescription of the invariants. We discuss how we overcome this difficulty in the following subsection.

### 5.2.1 $\pm i0$ -prescription of symbol letters

In most examples considered in this paper, it is simple to determine the sign of the  $i0$ -prescription of a given symbol letter once we know the prescription of the invariant to which it is associated and the kinematical region in which we are working. Indeed, whenever the symbol letters are linear combinations of invariants, this is a trivial problem. However, we observe that in more complicated cases there is an ambiguity in the sign of the imaginary part of some symbol letters. We need to resolve this ambiguity, because this sign is needed to obtain the correct sign in eq. (5.9).

The simplest case where we observe this problem is the triangle with three external masses and one internal mass,  $T(p_1^2, p_2^2, p_3^2; m_{12}^2, 0, 0)$ ; see table 3. For instance, when considering the double cut first in  $p_2^2$  and then in  $p_1^2$ , we need to determine the sign of the imaginary part of  $\bar{z} - \mu_{12}$ , as inherited from the prescription of the second cut invariant,  $p_1^2 - i0$ . One can easily check that this sign is the same as the sign of the quantity

$$\frac{\bar{z}(1 - \bar{z}) - \mu_{12}(z - \bar{z})}{z - \bar{z}}.$$

which can be either positive or negative in the region where the double cut is computed,

$$z > 1, \quad 0 < \bar{z} < 1, \quad 0 < \mu_{12} < 1, \quad \bar{z} - \mu_{12} > 0.$$

If the imaginary part of  $\bar{z} - \mu_{12}$  is negative, then we are in the subregion

$$z > 1, \quad 0 < \bar{z} < 1, \quad \frac{\bar{z}(1 - \bar{z})}{z - \bar{z}} < \mu_{12} < \bar{z},$$

and if it is positive, in the subregion

$$z > 1, \quad 0 < \bar{z} < 1, \quad 0 < \mu_{12} < \frac{\bar{z}(1 - \bar{z})}{z - \bar{z}}.$$

We note that if we are in the first situation we cannot smoothly take the internal mass ( $\mu_{12}$ ) to zero. However, if we are in the second situation, corresponding to a positive imaginary

part of  $\bar{z} - \mu_{12}$ , we can take  $\mu_{12}$  to zero without any problem, which is naturally a desirable property. We thus associate a positive imaginary part to the symbol letter  $\bar{z} - \mu_{12}$ . We can confirm this is indeed the correct result by considering the same double cut in the opposite order, where there are no sign ambiguities. We treat this example in detail in section 5.4.

All other cases where we have found sign ambiguities can be solved in the same way: *we always require being in a kinematic region where massless limits can be taken smoothly*. Furthermore, we have found in all of our examples of multiple cuts that there is always an ordering of the cuts where there is no ambiguity. We have then verified that any possible ambiguities were correctly lifted through the method just described.

### 5.3 Cuts and coproduct

Having related cuts to discontinuities in section 5.1 and discontinuities to coproduct entries in section 5.2, it is now straightforward to relate cuts to coproduct entries. Combining the relations eq. (5.4) and eq. (5.9), we arrive at:

$$\text{Cut}_{s_1, \dots, s_l, m_1^2, \dots, m_k^2} F \cong \ominus \sum_{(x_1, \dots, x_l, y_1, \dots, y_k) \in \mathcal{A}^{k+l}} (-1)^l \left( \prod_{i=1}^l a_i(s_i, x_i) \prod_{j=1}^k a_j(m_j^2, y_j) \right) \delta_{x_1, \dots, x_l, y_1, \dots, y_k} F. \quad (5.11)$$

We recall that on the left-hand side the  $s_i$  and the  $m_j^2$  may be written in any order, and correspondingly permuted on the right-hand side, but we require that we act first with all the  $s_i$  and then with the  $m_j^2$ . It is not obvious that permutations of the sets  $\{s_i\}$  and  $\{m_j^2\}$  give equivalent results on the right-hand side, but this property follows from the commutativity of cuts. It implies nontrivial relations among coproduct entries.

### 5.4 Examples

We now illustrate eqs. (5.4), (5.9) and (5.11) with different examples of triangles with internal masses, by comparing the result of the direct computation of the cuts to what is predicted by the relation between Disc and  $\delta$ . We have selected examples that highlight the features specific to diagrams with internal masses, and will not cover all diagrams listed in appendices B, C and D. All remaining cases can be treated in the same way, and we have checked that they do satisfy the expected relations.

#### 5.4.1 $T(p_1^2, 0, 0; m_{12}^2, m_{23}^2, 0)$

In this example, we illustrate iterated cuts in internal masses and iterated cuts in one external channel and one internal mass. Expressions for the integral, its symbol and cuts can be found in appendix B.3. The symbol alphabet can be found in table 1. The euclidean region, which we denote by  $R_0$ , is

$$R_0 : \quad m_{12}^2 > 0, \quad m_{23}^2 > 0, \quad p_1^2 < m_{12}^2. \quad (5.12)$$

**Single cuts:** For the single cut in the invariant  $r$ , where  $r \in \{p_1^2, m_{12}^2, m_{23}^2\}$ , we will move away from the euclidean region and into region  $R_1^r$ . These regions are, respectively,

$$\begin{aligned} R_1^{p_1^2} &: & m_{12}^2 > 0, & & m_{23}^2 > 0, & & p_1^2 > m_{12}^2, \\ R_1^{m_{12}^2} &: & m_{12}^2 < 0, & & m_{23}^2 > 0, & & p_1^2 < m_{12}^2, \\ R_1^{m_{23}^2} &: & m_{12}^2 > 0, & & m_{23}^2 < 0, & & p_1^2 < m_{12}^2. \end{aligned} \quad (5.13)$$

Recalling the prescriptions  $p_1^2 + i0$  and  $m_{ij}^2 - i0$ , we can compute the coefficients  $a_1(r, x_1)$  as defined in eq. (5.10). They are computed respectively in  $R_1^{p_1^2}$ ,  $R_1^{m_{12}^2}$  and  $R_1^{m_{23}^2}$ , and turn out to be equal. We find:

$$a_1(p_1^2, m_{12}^2 - p_1^2) = a_1(m_{12}^2, m_{12}^2) = a_1(m_{23}^2, m_{23}^2) = -2\pi i.$$

We then get:

$$\begin{aligned} \text{Cut}_{p_1^2} T &= -\text{Disc}_{p_1^2} T \cong -\frac{2\pi}{p_1^2} \Theta \delta_{m_{12}^2 - p_1^2} \mathcal{T} = \frac{2\pi}{p_1^2} \log \left( 1 - \frac{m_{12}^2 - p_1^2}{m_{23}^2} \right), \\ \text{Cut}_{m_{12}^2} T &= \text{Disc}_{m_{12}^2} T \cong \frac{2\pi}{p_1^2} \Theta \delta_{m_{12}^2} \mathcal{T} = -\frac{2\pi}{p_1^2} \log \left( \frac{m_{23}^2}{m_{23}^2 - m_{12}^2} \right), \\ \text{Cut}_{m_{23}^2} T &= \text{Disc}_{m_{23}^2} T \cong \frac{2\pi}{p_1^2} \Theta \delta_{m_{23}^2} \mathcal{T} = \frac{2\pi}{p_1^2} \log \left( 1 - \frac{p_1^2}{m_{12}^2 - m_{23}^2} \right), \end{aligned} \quad (5.14)$$

which are consistent with the results in appendix B.3. All relations for single cuts follow the same pattern, so we will simply list them without further details in the remaining examples.

**Double cuts:** According to our rules, there are two different cuts to consider:  $\text{Cut}_{p_1^2, m_{23}^2}$  and  $\text{Cut}_{m_{12}^2, m_{23}^2} = \text{Cut}_{m_{23}^2, m_{12}^2}$ . We start with  $\text{Cut}_{p_1^2, m_{23}^2}$ , for which we go from the region  $R_1^{p_1^2}$  to the region

$$R_2^{p_1^2, m_{23}^2} : \quad m_{12}^2 > 0, \quad m_{23}^2 < 0, \quad p_1^2 > m_{12}^2. \quad (5.15)$$

Given our conventions for multiple cuts, we now have the prescription  $m_{23}^2 + i0$ . Then,

$$a_2(m_{23}^2, m_{23}^2) = 2\pi i, \quad a_2(m_{23}^2, p_1^2 + m_{23}^2 - m_{12}^2) = 2\pi i \theta(m_{12}^2 - p_1^2 - m_{23}^2),$$

where we have only listed the coefficients leading to nonzero contributions. We finally find

$$\begin{aligned} \text{Cut}_{p_1^2, m_{23}^2} T &= -\text{Disc}_{p_1^2, m_{23}^2} T \\ &\cong -\frac{4\pi^2 i}{p_1^2} \Theta \left[ \delta_{m_{12}^2 - p_1^2, m_{23}^2} + \theta(m_{12}^2 - p_1^2 - m_{23}^2) \delta_{m_{12}^2 - p_1^2, m_{12}^2 - p_1^2 - m_{23}^2} \right] \mathcal{T} \\ &= -\frac{4\pi^2 i}{p_1^2} \theta(m_{23}^2 + p_1^2 - m_{12}^2), \end{aligned} \quad (5.16)$$

which matches the result of the direct calculation in B.3. Interestingly, even the theta functions are correctly reproduced, which is a feature observed in all our examples. We

recall that when computing multiple cuts in external channels and internal masses, we insist on taking the discontinuity first in the external invariant, and then in the mass. It can easily be checked that if we had taken the opposite order, we would have had the opposite sign in the above equation.

We now consider the double cut in the internal masses. This is an example of the behavior described in section 5.1.1, where a double cut in internal masses attached to the same external massless leg is nonzero. We only give details for one order of the invariants, first  $m_{12}^2$  and then  $m_{23}^2$ . The opposite order can be done in exactly the same way.

To compute  $\text{Cut}_{m_{12}^2, m_{23}^2}$ , we must go from  $R_1^{m_{12}^2}$  to

$$R_2^{m_{12}^2, m_{23}^2} : \quad m_{12}^2 < 0, \quad m_{23}^2 < 0, \quad p_1^2 < m_{12}^2.$$

Because mass cuts do not require complex conjugation of any region of the diagram, we still have the prescription  $m_{23}^2 - i0$ . The coefficients  $a_2(m_{23}^2, x_2)$  giving nonzero contributions are

$$a_2(m_{23}^2, m_{23}^2) = -2\pi i, \quad a_2(m_{23}^2, m_{23}^2 - m_{12}^2) = -2\pi i \theta(m_{12}^2 - m_{23}^2).$$

We then find

$$\begin{aligned} \text{Cut}_{m_{12}^2, m_{23}^2} T &= \text{Disc}_{m_{12}^2, m_{23}^2} T \\ &= -\frac{4\pi^2 i}{p_1^2} \Theta \left[ \delta_{m_{12}^2, m_{23}^2} + \theta(m_{12}^2 - m_{23}^2) \delta_{m_{12}^2, m_{23}^2 - m_{12}^2} \right] \mathcal{T} \\ &= \frac{4\pi^2 i}{p_1^2} \theta(m_{12}^2 - p_1^2 - p_{23}^2) \theta(m_{23}^2 - m_{12}^2), \end{aligned} \quad (5.17)$$

which matches the result of the direct calculation in B.3. Taking the discontinuities in the opposite order, we would have found

$$\begin{aligned} \text{Cut}_{m_{23}^2, m_{12}^2} T &= \text{Disc}_{m_{23}^2, m_{12}^2} T \\ &= -\frac{4\pi^2 i}{p_1^2} \Theta \left[ \theta(p_1^2 + m_{23}^2 - m_{12}^2) \delta_{m_{23}^2, m_{12}^2 - p_1^2 - m_{23}^2} \right. \\ &\quad \left. + \theta(m_{23}^2 - m_{12}^2) \delta_{m_{23}^2, m_{23}^2 - m_{12}^2} \right] \mathcal{T} \\ &= \frac{4\pi^2 i}{p_1^2} \theta(m_{12}^2 - p_1^2 - p_{23}^2) \theta(m_{23}^2 - m_{12}^2), \end{aligned} \quad (5.18)$$

which also matches the direct calculation.

We finish this example with a comment. As mentioned previously, for triangle integrals we cannot set up a double cut in an external momentum and an internal mass attached to it, like  $p_1^2$  and  $m_{12}^2$  in this example, because there is no additional propagator to cut at the second stage. Correspondingly, if we were to attempt to relate Disc and the coproduct for this double cut as in the above exercise, we would be stuck when taking the second discontinuity, as the  $\pm i0$  prescription of the second invariant is not well-defined. Thus, even in this case, there is no conflict among Cut, Disc and the coproduct.

### 5.4.2 $T(0, p_2^2, p_3^2; m_{12}^2, 0, 0)$

In this example, we illustrate iterated cuts in external channels, and we give another example of iterated cuts in one external channel and one internal mass. Expressions for the integral, its symbol and cuts can be found in appendix C.2. The symbol alphabet can be found in table 2. The euclidean region, which we denote  $R_0$  (we reuse the same notation as above for all examples, since there is no ambiguity and to avoid having too many indices), is

$$R_0 : \quad m_{12}^2 > 0, \quad p_2^2 < m_{12}^2, \quad p_3^2 < 0. \quad (5.19)$$

The single discontinuities are treated as above and obey the expected relations, so we will not go through the derivation. For double discontinuities, we consider two different double cuts:  $\text{Cut}_{p_3^2, m_{12}^2}$  and  $\text{Cut}_{p_2^2, p_3^2} = \text{Cut}_{p_3^2, p_2^2}$ . The first one is very similar to what we did before so we will not address it in detail here. The second one is a new kind. In particular, we will show that both orders of taking the discontinuities give the same result.

$(p_2^2, p_3^2)$ : We must analytically continue the function from

$$R_1^{p_2^2} : \quad m_{12}^2 > 0, \quad p_2^2 > m_{12}^2, \quad p_3^2 < 0, \quad (5.20)$$

to

$$R_2^{p_2^2, p_3^2} : \quad m_{12}^2 > 0, \quad p_2^2 > m_{12}^2, \quad p_3^2 > 0. \quad (5.21)$$

In this region, the nonvanishing coefficients  $a_2(p_3^2, x_2)$  are

$$a_2(p_3^2, p_3^2) = 2\pi i, \quad a_2(p_3^2, p_2^2 - m_{12}^2 - p_3^2) = 2\pi i \theta(m_{12}^2 - p_2^2 + p_3^2).$$

We then find

$$\begin{aligned} \text{Cut}_{p_2^2, p_3^2} T &= \text{Disc}_{p_2^2, p_3^2} T \\ &\cong \frac{4\pi^2 i}{p_2^2 - p_3^2} \Theta \left[ \delta_{p_2^2 - m_{12}^2, p_3^2} + \theta(m_{12}^2 - p_2^2 + p_3^2) \delta_{p_2^2 - m_{12}^2, p_2^2 - m_{12}^2 - p_3^2} \right] \mathcal{T} \\ &= \frac{4\pi^2 i}{p_2^2 - p_3^2} \theta(p_2^2 - m_{12}^2 - p_3^2). \end{aligned} \quad (5.22)$$

$(p_3^2, p_2^2)$ : We now start in the region

$$R_1^{p_3^2} : \quad m_{12}^2 > 0, \quad p_2^2 < m_{12}^2, \quad p_3^2 < 0 \quad (5.23)$$

and go to the same region  $R_2^{p_3^2, p_2^2}$  as above. The coefficients  $a_2(p_2^2, x_2)$  are

$$a_2(p_2^2, m_{12}^2 - p_2^2 + p_3^2) = 2\pi i \theta(p_2^2 - m_{12}^2 - p_3^2)$$

and thus

$$\begin{aligned} \text{Cut}_{p_3^2, p_2^2} T &= \text{Disc}_{p_3^2, p_2^2} T \\ &\cong \frac{4\pi^2 i}{p_2^2 - p_3^2} \Theta \left[ \theta(p_2^2 - m_{12}^2 - p_3^2) \delta_{p_3^2, m_{12}^2 - p_2^2 + p_3^2} \right] \mathcal{T} \\ &= \frac{4\pi^2 i}{p_2^2 - p_3^2} \theta(p_2^2 - m_{12}^2 - p_3^2), \end{aligned} \quad (5.24)$$

as above.

As expected, the two orderings of taking discontinuities match the direct calculation of the double cut.

### 5.4.3 $T(p_1^2, 0, 0; m_{12}^2, 0, m_{13}^2)$

In this example, we show how the relations between discontinuities and the coproduct generalize when we must use variables such as the ones defined in eq. (2.7) to get a symbol with rational letters. In particular, we hope to make clearer the discussion below eq. (3.5). We also illustrate the discussion in section 5.1.1: as predicted, we show that the double cut in the two internal masses vanishes.

Expressions for the integral, its symbol, and its cuts can be found in appendix B.4. The symbol alphabet can be found in table 1. The euclidean region is

$$R_0 : \quad m_{12}^2 > 0, \quad m_{13}^2 > 0, \quad p_1^2 < \left( \sqrt{m_{12}^2} + \sqrt{m_{13}^2} \right)^2. \quad (5.25)$$

To simplify our discussion, we will restrict the euclidean region to the subregion  $R_{0*}$ , defined by

$$R_{0*} : \quad m_{12}^2 > 0, \quad m_{13}^2 > 0, \quad p_1^2 < 0 \quad \Rightarrow \quad \bar{w}_1 < 0, \quad w_1 > 1. \quad (5.26)$$

Our discussion would be similar if we had started from the other subregion of the euclidean region.

**Single cuts:** For the single cut in the invariant  $r$ , with  $r \in \{p_1^2, m_{12}^2, m_{23}^2\}$ , we will move away from the euclidean region and into region  $R_1^r$ . These three regions are

$$\begin{aligned} R_1^{p_1^2} : \quad & m_{12}^2 > 0, \quad m_{13}^2 > 0, \quad p_1^2 > \left( \sqrt{m_{12}^2} + \sqrt{m_{13}^2} \right)^2 \quad \Rightarrow \quad 0 < \bar{w}_1 < w_1 < 1, \\ R_1^{m_{12}^2} : \quad & m_{12}^2 < 0, \quad m_{13}^2 > 0, \quad p_1^2 < 0 \quad \Rightarrow \quad 0 < \bar{w}_1 < 1 < w_1, \\ R_1^{m_{13}^2} : \quad & m_{12}^2 > 0, \quad m_{13}^2 < 0, \quad p_1^2 < 0 \quad \Rightarrow \quad \bar{w}_1 < 0 < w_1 < 1. \end{aligned} \quad (5.27)$$

For the discontinuity in the  $p_1^2$  channel, we first note that, in region  $R_1^{p_1^2}$ ,  $p_1^2 + i0$  implies  $w_1 + i0$  and  $\bar{w}_1 - i0$ . Then, the nonzero coefficients  $a_1(p_1^2, x_1)$  are

$$a_1(p_1^2, \bar{w}_1) = 2\pi i, \quad a_1(p_1^2, 1 - w_1) = 2\pi i. \quad (5.28)$$

The relation between Cut, Disc and the coproduct is

$$\begin{aligned} \text{Cut}_{p_1^2} T &= -\text{Disc}_{p_1^2} T \cong \frac{2\pi}{p_1^2} \Theta [\delta_{\bar{w}_1} + \delta_{1-w_1}] \mathcal{T} \\ &= \frac{2\pi}{p_1^2} \left( \log \left( \frac{w_1}{1-w_1} \right) - \log \left( \frac{\bar{w}_1}{1-\bar{w}_1} \right) \right). \end{aligned} \quad (5.29)$$

Similarly, for the discontinuity in the mass  $m_{12}^2$ , we note that, in region  $R_1^{m_{12}^2}$ ,  $m_{12}^2 - i0$  implies  $w_1 + i0$  and  $\bar{w}_1 + i0$ . The nonzero coefficients  $a_1(m_{12}^2, x_1)$  are

$$a_1(m_{12}^2, \bar{w}_1) = -2\pi i, \quad (5.30)$$

and we then find

$$\text{Cut}_{m_{12}^2} T = \text{Disc}_{m_{12}^2} T \cong \frac{2\pi}{p_1^2} \Theta \delta_{\bar{w}_1} \mathcal{T} = \frac{2\pi}{p_1^2} \log \left( \frac{w_1}{w_1 - 1} \right). \quad (5.31)$$

Finally, for the discontinuity in the mass  $m_{13}^2$ , we note that, in region  $R_1^{m_{13}^2}$ ,  $m_{13}^2 - i0$  implies  $w_1 - i0$  and  $\bar{w}_1 - i0$ . The nonzero coefficients  $a_1(m_{13}^2, x_1)$  are

$$a_1(m_{13}^2, 1 - w_1) = -2\pi i, \quad (5.32)$$

and we then find

$$\text{Cut}_{m_{13}^2} T = \text{Disc}_{m_{13}^2} T \cong \frac{2\pi}{p_1^2} \Theta \delta_{1-w_1} \mathcal{T} = -\frac{2\pi}{p_1^2} \log \left( \frac{-\bar{w}_1}{1 - \bar{w}_1} \right). \quad (5.33)$$

We finish the discussion of these single cuts with three comments. First, we note that eqs. (5.29), (5.31) and (5.33) reproduce the direct calculation of the cuts, as expected. Second, we have confirmed eq. (3.5) as, in that form, we can indeed read the correct (symbol of the) discontinuity across the branch cut of each of the invariants appearing in the first entry. Finally, we have shown that writing the symbol in the special form of eq. (3.5) is not necessary or even natural from the point of view of the relations between Disc and  $\delta$ , as the relations are formulated in terms of individual symbol letters and not some particular combination of them. In other cases where similar variables are needed, we prefer to present the most compact expression of the symbol.

**Double cuts:** The only double cut we can consider is the double cut in the internal masses. Since the two masses are connected to an external massive leg, we claimed in section 5.1.1 that these double cuts should vanish. Indeed, this two-propagator cut can only be interpreted as a  $p_1^2$  channel cut, which vanishes when evaluated in the region where the double mass discontinuity should be computed.

The double cut  $\text{Cut}_{m_{12}^2, m_{13}^2} T = \text{Cut}_{m_{13}^2, m_{12}^2} T$  is computed in the region

$$R_2^{m_{12}^2, m_{13}^2} : \quad m_{12}^2 < 0, \quad m_{13}^2 < 0, \quad p_1^2 < \left( \sqrt{m_{12}^2} + \sqrt{m_{13}^2} \right)^2. \quad (5.34)$$

In terms of the variables  $w_1$  and  $\bar{w}_1$ , this region is split into two disconnected subregions  $R_{2a}^{m_{12}^2, m_{13}^2}$  and  $R_{2b}^{m_{12}^2, m_{13}^2}$ ,

$$R_{2a}^{m_{12}^2, m_{13}^2} : \quad \bar{w}_1 < w_1 < 0, \quad R_{2b}^{m_{12}^2, m_{13}^2} : \quad 1 < \bar{w}_1 < w_1. \quad (5.35)$$

For  $\text{Cut}_{m_{12}^2, m_{13}^2} T$ , we start in region  $R_1^{m_{12}^2}$ . In  $R_{2a}^{m_{12}^2, m_{13}^2}$ ,  $m_{13}^2 - i0$  implies  $w_1 + i0$ , and the nonvanishing coefficients  $a_2(m_{13}^2, x_2)$  are

$$a_2(m_{13}^2, w_1) = 2\pi i, \quad a_2(m_{13}^2, 1 - w_1) = 2\pi i.$$

We then get

$$\text{Cut}_{m_{12}^2, m_{13}^2} T = \text{Disc}_{m_{12}^2, m_{13}^2} T \cong -\frac{4\pi^2 i}{p_1^2} \Theta [\delta_{\bar{w}_1, w_1} + \delta_{\bar{w}_1, 1-w_1}] \mathcal{T} = 0. \quad (5.36)$$

In  $R_{2b}^{m_{12}^2, m_{13}^2}$ , all the coefficients  $a_2(m_{13}^2, x_2)$  vanish so that we again find

$$\text{Cut}_{m_{12}^2, m_{13}^2} T = \text{Disc}_{m_{12}^2, m_{13}^2} T = 0. \quad (5.37)$$

For  $\text{Cut}_{m_{13}^2, m_{12}^2} T$ , we start in region  $R_1^{m_{13}^2}$ . In  $R_{2a}^{m_{12}^2, m_{13}^2}$ , all the coefficients  $a_2(m_{13}^2, x_2)$  vanish and we get

$$\text{Cut}_{m_{13}^2, m_{12}^2} T = \text{Disc}_{m_{12}^2, m_{13}^2} T = 0. \quad (5.38)$$

In  $R_{2b}^{m_{12}^2, m_{13}^2}$ ,  $m_{12}^2 - i0$  implies  $\bar{w}_1 + i0$ . The nonvanishing coefficients  $a_2(m_{13}^2, x_2)$  are

$$a_2(m_{12}^2, \bar{w}_1) = 2\pi i, \quad a_2(m_{12}^2, 1 - \bar{w}_1) = 2\pi i$$

and we get

$$\text{Cut}_{m_{13}^2, m_{12}^2} T = \text{Disc}_{m_{12}^2, m_{13}^2} T \cong \frac{4\pi^2 i}{p_1^2} \Theta [\delta_{1-w_1, \bar{w}_1} + \delta_{1-w_1, 1-\bar{w}_1}] \mathcal{T} = 0. \quad (5.39)$$

We thus find consistent results in all subregions and for either order of the discontinuities: for all cases, the result of the double discontinuity is zero. As already mentioned, this result illustrates the discussion in [5.1.1](#).

#### 5.4.4 $T(p_1^2, p_2^2, p_3^2; m_{12}^2, 0, 0)$

With our last example, we come back to the case mentioned in section [5.2.1](#) to show that we have lifted the ambiguity of the imaginary part of some symbol letters correctly.

The relations among cuts, discontinuities and the coproduct in this example are straightforward to obtain. Indeed, the nonzero internal mass is a simple generalization of the example studied in ref. [\[31\]](#). We give the full set of relations for cuts in external channels, to verify that the procedure described in section [5.2.1](#) to fix this ambiguity does indeed give the correct result. We will not present cuts in the internal mass here, because we have already given several examples of this type of discontinuity, and they would not teach us anything new.

To get rational symbol letters, we use the variables defined in eq. [\(2.4\)](#), and also define as usual  $\mu_{12} = m_{12}^2/p_1^2$ . Expressions for the integral, its symbol, and its cuts can be found in appendix [D.2](#). The symbol alphabet can be found in table [3](#). The regions where single cuts are computed are

$$\begin{aligned} R_1^{p_1^2} &: p_1^2 > m_{12}^2, & p_2^2 < 0, & p_3^2 < 0, & m_{12}^2 > 0, \\ R_1^{p_2^2} &: p_1^2 < 0, & p_2^2 > m_{12}^2, & p_3^2 < 0, & m_{12}^2 > 0, \\ R_1^{p_3^2} &: p_1^2 < 0, & p_2^2 < 0, & p_3^2 > 0, & m_{12}^2 > 0. \end{aligned} \quad (5.40)$$

We note that these regions are not the complete regions in which single cuts are nonzero. For instance, in  $R_1^{p_1^2}$  we could have allowed  $0 < p_2^2 < m_{12}^2$ . This complicates the discussion in terms of the  $z$  and  $\bar{z}$  variables, and does not teach us anything new, so in this discussion we restrict the cut regions to the subregions defined above. In terms of  $z$ ,  $\bar{z}$  and  $\mu_{12}$ , they are

$$\begin{aligned}
R_1^{p_1^2} &: z > 1, \quad \bar{z} < 0, \quad 0 < \mu_{12} < 1, \quad z - \mu_{12} > 0, \quad \bar{z} - \mu_{12} < 0, \quad z\bar{z} - \mu_{12} < 0 \\
R_1^{p_2^2} &: 0 < z < 1, \quad \bar{z} < 0, \quad \mu_{12} < 0, \quad z - \mu_{12} > 0, \quad \bar{z} - \mu_{12} < 0, \quad z\bar{z} - \mu_{12} < 0 \\
R_1^{p_3^2} &: z > 1, \quad 0 < \bar{z} < 1, \quad \mu_{12} < 0, \quad z - \mu_{12} > 0, \quad \bar{z} - \mu_{12} > 0, \quad z\bar{z} - \mu_{12} > 0.
\end{aligned} \tag{5.41}$$

For single cuts, knowing that  $p_i^2 = p_i^2 + i0$ , there is no ambiguity in determining the sign of the imaginary part of the relevant symbol letters in the relevant kinematic region. We then find

$$\begin{aligned}
\text{Cut}_{p_1^2} T &= -\text{Disc}_{p_1^2} T \cong \frac{2\pi}{p_1^2(z - \bar{z})} \Theta [\delta_{1-z} + \delta_{\mu_{12}} + \delta_{z\bar{z} - \mu_{12}}] \mathcal{T} \\
&= -\frac{2\pi}{p_1^2(z - \bar{z})} \Theta \delta_{1 - \mu_{12}} \mathcal{T}, \\
\text{Cut}_{p_2^2} T &= -\text{Disc}_{p_2^2} T \cong -\frac{2\pi}{p_1^2(z - \bar{z})} \Theta \delta_{z\bar{z} - \mu_{12}} \mathcal{T}, \\
\text{Cut}_{p_3^2} T &= -\text{Disc}_{p_3^2} T \cong -\frac{2\pi}{p_1^2(z - \bar{z})} \Theta \delta_{1-z} \mathcal{T}.
\end{aligned} \tag{5.42}$$

For the  $p_1^2$  channel cut, we used the fact that there is no branch point at  $p_1^2 = 0$  to find a simpler relation.

The double cuts are computed in the regions

$$\begin{aligned}
R_2^{p_1^2, p_2^2} &: p_1^2 > m_{12}^2, \quad p_2^2 > m_{12}^2, \quad p_3^2 < 0, \quad m_{12}^2 > 0, \\
R_1^{p_1^2, p_3^2} &: p_1^2 > m_{12}^2, \quad p_2^2 < 0, \quad p_3^2 > 0, \quad m_{12}^2 > 0, \\
R_1^{p_2^2, p_3^2} &: p_1^2 < 0, \quad p_2^2 > m_{12}^2, \quad p_3^2 > 0, \quad m_{12}^2 > 0.
\end{aligned} \tag{5.43}$$

We leave it as an exercise to determine the sign of the symbol letters and their imaginary parts in each of these regions. This is straightforward for all double discontinuities, except for  $\text{Cut}_{p_2^2, p_1^2} T$ , in which case the imaginary part of  $\bar{z} - \mu_{12}$  does not have a definite sign in the cut region. We showed how this issue could be addressed in section 5.2.1, where we also mentioned we could check we had the correct result by comparing  $\text{Cut}_{p_2^2, p_1^2} T$  and  $\text{Cut}_{p_1^2, p_2^2} T$ .

The full set of relations among cuts, discontinuities and coproducts is

$$\begin{aligned}
\text{Cut}_{p_1^2, p_2^2} T &= \text{Disc}_{p_1^2, p_2^2} T \cong \frac{4\pi^2 i}{p_1^2(z - \bar{z})} \Theta \delta_{1-\mu_{12}, \bar{z}-\mu_{12}} \mathcal{T}, \\
\text{Cut}_{p_2^2, p_1^2} T &= \text{Disc}_{p_2^2, p_1^2} T \cong -\frac{4\pi^2 i}{p_1^2(z - \bar{z})} \Theta [\delta_{z\bar{z}-\mu_{12}, 1-z} + \delta_{z\bar{z}-\mu_{12}, \bar{z}} + \delta_{z\bar{z}-\mu_{12}, \bar{z}-\mu_{12}}] \mathcal{T}, \\
\text{Cut}_{p_1^2, p_3^2} T &= \text{Disc}_{p_1^2, p_3^2} T \cong \frac{4\pi^2 i}{p_1^2(z - \bar{z})} \Theta \delta_{1-\mu_{12}, 1-z} \mathcal{T}, \\
\text{Cut}_{p_3^2, p_1^2} T &= \text{Disc}_{p_3^2, p_1^2} T \cong -\frac{4\pi^2 i}{p_1^2(z - \bar{z})} \Theta \delta_{1-z, \bar{z}-\mu_{12}} \mathcal{T}, \\
\text{Cut}_{p_2^2, p_3^2} T &= \text{Disc}_{p_2^2, p_3^2} T \cong \frac{4\pi^2 i}{p_1^2(z - \bar{z})} \Theta \delta_{z\bar{z}-\mu_{12}, 1-z} \mathcal{T}, \\
\text{Cut}_{p_3^2, p_2^2} T &= \text{Disc}_{p_3^2, p_2^2} T \cong \frac{4\pi^2 i}{p_1^2(z - \bar{z})} \Theta \delta_{1-z, \bar{z}-\mu_{12}} \mathcal{T}.
\end{aligned} \tag{5.44}$$

Using these results and the expressions given in appendix D.2, we indeed verify that  $\text{Cut}_{p_1^2, p_2^2} T = \text{Cut}_{p_2^2, p_1^2} T$ . We have also checked that all the relations are satisfied for all pairs of external channels.

## 6 Reconstruction of Feynman integrals via the coproduct

A major motivation for computing cut integrals is that they contain a great deal of information, sometimes sufficient to reconstruct the original uncut integral, which can be harder to compute directly. The relations between cuts and coproducts suggest that the Hopf algebra can be used as a tool in this reconstruction. In this section, we show how this works in the case of the massive triangles.

In [31] it was shown that for the one-loop triangle and the three-point two-loop ladder diagrams with three external and no internal masses, the symbol of the uncut pure transcendental functions could be reconstructed through simple algebraic manipulations starting from the symbol of a single channel cut. Two strategies were presented there: in the first one, the symbol was reconstructed by adding the simplest terms necessary to satisfy the first-entry and integrability conditions; in the second one, an ansatz with undetermined coefficients was constructed and then constrained using the symmetries obeyed by the function along with the integrability and first-entry conditions. In both cases, the symbol was completely fixed and could then be integrated to get the full uncut Feynman integrals.

We now show how similar manipulations can be used to reconstruct the symbol of triangles with internal masses. We then comment on how to recover information invisible to the symbol to get the full uncut function. As in [31], we focus on *finite* triangles, because the reconstruction procedure works for the full integral but not necessarily for individual terms in the  $\epsilon$  expansion.

The reconstruction procedure detailed below requires knowledge of the symbol alphabet. In the presence of internal masses, we observe that some symbol letters appear only in mass cuts, and not in any of the channel cuts. Compared to the massless case, then,

we need to add more rules to be able to construct the full symbol starting from a channel cut. Nevertheless, we see that channel cuts highly constrain the full function. Indeed, we prefer to start from channel cuts rather than mass cuts, based on the idea that dispersive representations of Feynman diagrams are written in terms of channel discontinuities. In practice, we have found reconstruction from channel cuts to be more straightforward and successful, so that is what we present here.

In this section, we exclude from our discussion the triangle with three internal masses and three external massive legs, because it does not have a rational symbol alphabet. Indeed, although in principle we see no obstacle to reconstructing the symbol through a similar procedure, the complexity of the symbol letters does not lead so directly to clean linear relations when imposing integrability of the symbol ansatz.

### 6.1 Constructing and constraining an ansatz for the symbol

The observation that a single unitarity cut suffices to reconstruct the symbol of a Feynman integral is not surprising, given its representation as a dispersion integral [5, 31, 50, 51]. In this representation, a Feynman integral is written as an integral over its discontinuity across a branch cut, integrated along the branch cut itself. In our reconstruction procedure, the knowledge of the discontinuity is replaced by the knowledge of the cut, and the knowledge of the integration region by that of the first-entry condition.

Our general strategy is the following. We observe that the symbol alphabets of the scalar triangles we are investigating follow a pattern. With some experience, we are able to write an ansatz for their symbol, in terms of unknown numerical coefficients. Then, by imposing the knowledge of one channel cut, the first-entry condition, the integrability condition, the absence of trivial terms (of the form  $x \otimes x$ ) and the symmetries of the function, we are able to fix all of the unknown coefficients. We now give more specific rules for each of the steps just mentioned.

We start by explaining how to build the ansatz. First, we note that if the diagram is a function of  $n$  invariants, the pure functions concerned in this section are functions of  $n - 1$  dimensionless variables only. For concreteness, we always choose to normalize our variables by an external invariant. The procedure starts by listing the possible first entries. These are completely fixed by the first-entry condition; see sec. 3. Listing the second entries is more difficult than listing the first entries. It can however be done based on the knowledge of a cut integral, and, for the letters that do not appear in channel cuts, by the empirical observations we list below.

**Listing the second entries:** We always start from a single cut in an external channel. We observe the presence of the following terms in the set of second entries:

- All letters of the symbol alphabet of the channel cut taken as the known starting point.
- Differences of internal masses, or their equivalents in terms of  $w_1$  and  $\bar{w}_1$ ; see eq. (2.9).
- For triangles with two external invariants, ratios of external invariants. In our examples, this is just  $p_2^2/p_3^2$ . For the examples with three external massive channels

where we must use the variables  $z$  and  $\bar{z}$  (see (2.4)), this condition is replaced by the presence of the letters  $z$ ,  $\bar{z}$ ,  $(1 - z)$  and  $(1 - \bar{z})$ .

The terms generated through the above rules are added as cofactors of all the first entries, each multiplied by an undetermined numerical coefficient. For the first entry corresponding to the cut assumed to be known, these coefficients are of course fixed by the cut result. For the other first entries, they must be determined from additional considerations, according to the procedure we now describe.

**Fixing the coefficients:** We fix all coefficients according to the following steps:

- 1) We discard integrable terms of the form  $x \otimes x$ , as they are not needed in order to construct a minimal integrable symbol.
- 2) Since the first-entry condition involves the original Mandelstam invariants, the dimensionless variables appearing in the symbol should be expanded when imposing this condition. Notably, we sometimes normalize the invariants by a variable  $p_i^2$  with a nonzero mass threshold, so that  $p_i^2$  should not ultimately appear as a first entry by itself, although it shows up superficially in the expansion of the dimensionless variables. Thus, all of the second-entry cofactors of this  $p_i^2$  should combine to give zero.
- 3) We use the integrability condition, eq. (1.5), to fix the remaining parameters.

These three rules are already highly constraining and indeed sufficient for most examples. If they are not, in particular in cases where we use the  $z$ ,  $\bar{z}$ ,  $w_1$ , and  $\bar{w}_1$  variables, they can be complemented by the following:

- 4) Impose antisymmetry under  $z \leftrightarrow \bar{z}$  and symmetry under  $w_1 \leftrightarrow \bar{w}_1$ . Indeed, the Feynman integrals are functions of the invariants only and must thus be symmetric under these transformations. When  $z$  and  $\bar{z}$  are necessary, there is an antisymmetric rational prefactor, and so the pure function must be antisymmetric as well.
- 5) If there is a symmetry under the exchange of the legs with momenta  $p_2$  and  $p_3$ , impose symmetry under the simultaneous transformations  $z \rightarrow 1 - \bar{z}$ ,  $\bar{z} \rightarrow 1 - z$ ,  $w_1 \rightarrow 1 - \bar{w}_1$ ,  $\bar{w}_1 \rightarrow 1 - w_1$ .

We now illustrate these rules in some examples. The example in appendix B.1 is trivial and the one in appendix B.2 divergent, so we will not address them. The next-simplest example is  $T(p_1^2, 0, 0; m_{12}^2, m_{23}^2, 0)$ —see appendix B.3—and we now show how to construct the ansatz for this case. We normalize the internal masses by  $p_1^2$ , giving the dimensionless variables  $m_{12}^2/p_1^2 \equiv \mu_{12}$  and  $m_{23}^2/p_1^2 \equiv \mu_{23}$ , and we assume knowledge of the  $p_1^2$  cut, eq. (B.13). Applying the rules given above for writing the ansatz, we get

$$\begin{aligned}
& (\mu_{12} - 1) \otimes [(\mu_{23} - 1 - \mu_{12}) - \mu_{23}] \\
& + \mu_{12} \otimes [a_1(\mu_{23} - 1 - \mu_{12}) + a_2\mu_{23} + a_3(\mu_{12} - \mu_{23})] \\
& + \mu_{23} \otimes [b_1(\mu_{23} - 1 - \mu_{12}) + b_2\mu_{23} + b_3(\mu_{12} - \mu_{23})]
\end{aligned} \tag{6.1}$$

Our task is now to fix the coefficients  $a_i$  and  $b_i$ . In this case, using rules 1), 2) and 3) above fixes all coefficients, and we reproduce the symbol in eq. (B.12).

An example of similar complexity is the triangle  $T(0, p_2^2, p_3^2; m_{12}^2, 0, 0)$ , appendix C.2. We choose to normalize by  $p_2^2$ , and define the variables  $m_{12}^2/p_2^2 \equiv \mu$  and  $p_3^2/p_2^2 \equiv u$ . We assume knowledge of the  $p_2^2$  cut, eq. (C.8). According to the above steps, the general ansatz for the symbol reads:

$$\begin{aligned} & (\mu - 1) \otimes \{u + \mu - (\mu + u - 1)\} \\ & u \otimes \{a_1 u + a_2 \mu + a_3(\mu + u - 1)\} \\ & + \mu \otimes \{b_1 u + b_2 \mu + b_3(\mu + u - 1)\} \end{aligned} \quad (6.2)$$

Our task is now to fix the coefficients  $a_i$  and  $b_i$ . As in the previous example, rules 1), 2) and 3) are sufficient and we reproduce the symbol in eq. (C.7).

As a final example of our rules to build the ansatz, we look at the most complicated case we address,  $T(p_1^2, p_2^2, p_3^2; m_{12}^2, 0, m_{13}^2)$ , given in appendix D.3. This requires using the variables  $z, \bar{z}, w_1$  and  $\bar{w}_1$ . We assume knowledge of the  $p_1^2$  cut, eq. (D.13). Following our rules, the ansatz is

$$\begin{aligned} & w_1(1 - \bar{w}_1) \otimes \left[ (z - w_1) - (z - \bar{w}_1) - (\bar{z} - w_1) + (\bar{z} - \bar{w}_1) \right] \\ & + (z\bar{z} - w_1\bar{w}_1) \otimes \left[ a_1(z - w_1) + a_2(z - \bar{w}_1) + a_3(\bar{z} - w_1) + a_4(\bar{z} - \bar{w}_1) \right. \\ & \quad \left. + a_5 z + a_6 \bar{z} + a_7(1 - z) + a_8(1 - \bar{z}) + a_9(w_1\bar{w}_1 - (1 - w_1)(1 - \bar{w}_1)) \right] \\ & + ((1 - z)(1 - \bar{z}) - (1 - w_1)(1 - \bar{w}_1)) \otimes \left[ a_i \rightarrow b_i \right] + w_1\bar{w}_1 \otimes \left[ a_i \rightarrow c_i \right] \\ & + (1 - w_1)(1 - \bar{w}_1) \otimes \left[ a_i \rightarrow d_i \right], \end{aligned} \quad (6.3)$$

and we must now determine the coefficients  $a_i, b_i, c_i$  and  $d_i$ . Interestingly, also for this case all we need are rules 1), 2) and 3) to fix all coefficients.

For all remaining examples, building the ansatz can be done in a similar way as illustrated above. We now list the rules we must apply to fix the coefficients of the ansatz of the remaining examples (for all cases, we assume knowledge of the  $p_1^2$  cut):

- $T(p_1^2, 0, 0; m_{12}^2, 0, m_{13}^2)$ , appendix B.4. Rules 1), 2) and 3) are sufficient.
- $T(p_1^2, 0, 0; m_{12}^2, m_{23}^2, m_{13}^2)$ , appendix B.5. Rules 1), 2), 3), 4) and 5) are needed.
- $T(p_1^2, p_2^2, p_3^2; m_{12}^2, 0, 0)$ , appendix D.2. Rules 1), 2) and 3) are sufficient.

## 6.2 Reconstructing the full function from the symbol

We now explain how we integrate the symbol to get the full function. Although integrating a symbol is in general an unsolved problem, it is a simple problem for weight two functions where a complete basis is even known to exist in terms of classical polylogarithms, see e.g. [36]. Once we have found a function that matches our symbol, all that remains to be done is fixing terms that are invisible to the symbol, in our case weight one functions multiplied by  $\pi$  and terms proportional to  $\zeta_2$ .

Powers of  $\pi$  are typically generated by analytic continuation and appear multiplied by  $i$ . Working in the Euclidean region where the function is real and away from any branch cut avoids this problem.

To fix the terms proportional to  $\zeta_2$ , we can use two strategies. The first, which always works, is to evaluate the integrated symbol numerically at a single point and compare it to a numerically integrated Feynman parametrization of the diagram. The difference must be a rational number multiplied by  $\zeta_2$ , which completely determines our function. Alternatively, when possible, we can use the symmetries of the diagram to check if terms proportional to  $\zeta_2$  are allowed.

As examples, consider  $T(p_1^2, 0, 0; 0, m_{23}^2, 0)$  and  $T(p_1^2, p_2^2, p_3^2; m_{12}^2, 0, 0)$ . In the first case, there is no symmetry consideration to fix terms proportional to  $\zeta_2$ , and we must thus rely on numerical comparisons. In the second example, there is a rational prefactor antisymmetric under  $z \leftrightarrow \bar{z}$ , and thus the pure function must be antisymmetric under this transformation (the full function must be symmetric). This forbids the existence of terms proportional to  $\zeta_2$ .

## 7 Discussion

In this paper we have studied the analytic structure of one-loop three-point Feynman integrals with different configurations of internal and external masses. More specifically, we have investigated the structure revealed by the unitarity cuts of triangle integrals with massive internal legs, by establishing a relation between cut diagrams and specific entries of the coproduct of these integrals. This generalizes the results of [31], where only diagrams with massless propagators were considered.

The main conclusions of our investigations are the following. First, the first-entry condition has to be generalized. Indeed, for diagrams without internal masses the first-entry condition simply requires that the first entries of the coproduct must be external invariants. When internal masses are present, this is modified in two ways: we can either have external channels minus their threshold or internal masses themselves as the first entry. Stated more generally, the first entries are (arguments of) logarithms with branch points at the boundaries of the Euclidean region.

Second, we have generalized our cutting rules to correctly capture all the discontinuities of diagrams with internal masses. For discontinuities in external channels, the results of [31] can be used without modification. For discontinuities in internal masses, we must define new cutting rules incorporating single-propagator cuts. We have also discussed our strategy to compute the integrals obtained after applying our cutting rules. As also argued in [31], we observe that calculating cuts is a good way to identify appropriate variables for each diagram. Even in the case of the fully massive triangle, where we were not able to find a rational symbol alphabet, computing the individual cuts still points to useful variables.

Third, we have established our relations between discontinuities and cuts, eq. (5.4), and between discontinuities and coproduct entries, eq. (5.9). These are then combined to relate cuts to coproduct entries, eq. (5.11), which is the central result of the paper. The relations we have obtained are mostly a straightforward generalization of the ones in

[31], aside from the restriction that when computing multiple discontinuities in external channels and in internal masses, we should first take the discontinuities in the external channels and then in the external masses (failure to do so leads to wrong overall signs). We have illustrated our relations in several examples (in section 5.4).

Finally, we have shown how channel cuts highly constrain the symbol of triangles with internal masses. Indeed, we are able to completely constrain a general ansatz for the symbol of each triangle (except the fully massive triangle) using the knowledge of a single channel cut, the integrability condition and the symmetries of the functions. However, building the ansatz is more complicated than in the absence of internal masses [31], and we have had to postulate rules that determine how to construct symbol letters not appearing in channel cuts. These rules are obtained empirically and are specific to the class of diagrams we are studying. Once the symbol is known, we explain how to reconstruct the function by fixing terms invisible to the symbol. It would be very interesting to see whether reconstruction can also be done starting from cuts in internal masses.

While some of the relations we present are justified on firmer grounds, such as the relation between coproduct entries and discontinuities, others are conjectures that generalize well established results. For instance, the relation between multiple cuts and discontinuities is a generalization of the largest time equation, which relates single cuts and discontinuities. While we believe we have given ample evidence for the validity of all our relations, it would be good to have proofs.

We have restricted our examples to one-loop scalar triangle diagrams with different mass configurations. However, we believe that several of our conclusions generalize in a straightforward manner to more complicated diagrams, provided they can still be written in terms of multiple polylogarithms. Indeed, the discussion of sections 3, 4 and 5 is completely general. Studying diagrams with more external legs and of higher loop order would certainly be interesting: our expectation is that the complications arising in such configurations are mostly related to the increase of the number of external channels, and that the treatment of internal masses can be done along the same lines as what is presented here. Of course, the larger number of scales in the problem will lead to more complicated symbol alphabets, but we believe that computing the cuts of such diagrams would help find the most convenient choice of variables.

More generally, we believe that a better understanding of the analytic structure of Feynman diagrams is fundamental to develop more efficient computational methods. Supported by the results of this paper, we believe that the coproduct of the Hopf algebra of multiple polylogarithms is an appropriate tool to tackle this problem.

## Acknowledgments

It is a pleasure to thank Øyvind Almelid, Claude Duhr, Einan Gardi, David Kosower, and Alexander Ochirov for helpful discussions. Special thanks to Claude Duhr for the use of his Mathematica package `PolyLogTools`, and to Claude Duhr and Einan Gardi for comments on the manuscript. Figures were created with the help of `TikZ` [52]. S.A. is supported by Fundação para a Ciência e a Tecnologia, Portugal, through a doctoral degree fellow-

ship (SFRH/BD/69342/2010). S.A. and R.B. were supported by the Research Executive Agency (REA) of the European Union under the Grant Agreement number PITN-GA-2010-264564 (LHCPhenoNet). S.A. acknowledges the hospitality of the *Centre National de la recherche scientifique* (CNRS) and the Institute for Theoretical Physics (IPhT) of the CEA during the early stages of this work. H.G. thanks the Higgs Centre for Theoretical Physics at the University of Edinburgh and especially the School of Mathematics of Trinity College Dublin for their hospitality.

## A Feynman rules and definitions

Our conventions for the Feynman rules of the scalar diagrams we consider are:

- Vertex:

$$\bullet = i \quad (\text{A.1})$$

- Complex conjugated vertex:

$$\circ = -i \quad (\text{A.2})$$

- Propagator:

$$\bullet\text{---}\bullet = \frac{i}{p^2 - m^2 + i0} \quad (\text{A.3})$$

Massive (massless) propagators are drawn with a thick (thin) line.

- Complex conjugated propagator:

$$\circ\text{---}\circ = \frac{-i}{p^2 - m^2 - i0} \quad (\text{A.4})$$

Massive (massless) propagators are drawn with a thick (thin) line.

- Cut propagator for cut in an external channel:

$$\circ\text{---}\bullet = \bullet\text{---}\circ = \bullet\text{---}\bullet = \circ\text{---}\circ = 2\pi \delta(p^2 - m^2) \quad (\text{A.5})$$

There is a theta function restricting the direction of energy flow in a cut propagator. For single cuts, our convention is that energy flows from black to white. For multiple cuts, there are separate color labels for each cut—see section 4 for details. There can be multiple thin dotted lines indicating cuts on the same propagator without changing its value. However, each thin dotted line implies complex conjugation of a region of the diagram.

- Cut propagator for cut in an internal mass:

$$\bullet\text{---}\text{---}\bullet = \circ\text{---}\text{---}\circ = 2\pi \delta(p^2 - m^2) \quad (\text{A.6})$$

- Loop factor for loop momentum  $k$ :

$$\left(\frac{e^{\gamma_E \epsilon}}{\pi^{2-\epsilon}}\right) \int d^{4-2\epsilon} k. \quad (\text{A.7})$$

Results for triangles and their cuts often involve the Gauss hypergeometric function  ${}_2F_1$  and one of its generalizations, the  $F_1$  Appell function. They have the Euler-type integral representations

$${}_2F_1(\alpha, \beta; \gamma; z) = \frac{\Gamma(\gamma)}{\Gamma(\beta)\Gamma(\gamma-\beta)} \int_0^1 dt t^{\beta-1} (1-t)^{\gamma-\beta-1} (1-tz)^{-\alpha} \quad (\text{A.8})$$

for  $\Re \gamma > \Re \beta > 0$ , and

$$F_1(\alpha; \beta, \beta'; \gamma; x; y) = \frac{\Gamma(\gamma)}{\Gamma(\alpha)\Gamma(\gamma-\alpha)} \int_0^1 dt \frac{t^{\alpha-1} (1-u)^{\gamma-\alpha-1}}{(1-tx)^\beta (1-ty)^{\beta'}} \quad (\text{A.9})$$

for  $\Re \gamma > \Re \alpha > 0$ .

## B One-mass triangles

We give explicit expressions for the triangles with one external massive channel that are used as examples in this paper. For all the examples given, we have computed the uncut triangles both through standard Feynman parametrization and through a dispersive integral, and verified agreement of the expressions. Divergent integrals were compared with the results given in ref.[53]. For all triangles with one external massive channel considered in the following subsections, we separate the rational prefactor from the pure transcendental function according to the relation

$$T(p_1^2, 0, 0; m_{12}^2, m_{23}^2, m_{13}^2) = \frac{i}{p_1^2} \mathcal{T}(p_1^2, 0, 0; m_{12}^2, m_{23}^2, m_{13}^2), \quad (\text{B.1})$$

where the internal masses are generic and can be zero. Before expansion in the dimensional regularization parameter  $\epsilon$ , the results will often involve the functions  ${}_2F_1$  and  $F_1$  defined in eqs. (A.8) and (A.9).

### B.1 $T(p_1^2, 0, 0; 0, m_{23}^2, 0)$

The triangle of fig. 1a is given by:

$$\begin{aligned} T(p_1^2, 0, 0; 0, m_{23}^2, 0) &= \frac{ie^{\gamma_E \epsilon}}{\epsilon} \left[ \frac{(-p_1^2)^{-\epsilon}}{m_{23}^2} \frac{\Gamma(1+\epsilon)\Gamma^2(1-\epsilon)}{\Gamma(2-2\epsilon)} {}_2F_1\left(1, 1-\epsilon; 2-2\epsilon; -\frac{p_1^2}{m_{23}^2}\right) \right. \\ &\quad \left. - (m_{23}^2)^{-1-\epsilon} \frac{\Gamma(1+\epsilon)\Gamma(1-\epsilon)}{\Gamma(2-\epsilon)} {}_2F_1\left(1, 1; 2-\epsilon; -\frac{p_1^2}{m_{23}^2}\right) \right] \\ &= \frac{i}{p_1^2} \left( \text{Li}_2\left(\frac{m_{23}^2 + p_1^2}{m_{23}^2}\right) - \frac{\pi^2}{6} \right) + \mathcal{O}(\epsilon). \end{aligned} \quad (\text{B.2})$$

The symbol is

$$\mathcal{S}[\mathcal{T}(p_1^2, 0, 0; 0, m_{23}^2, 0)] = m_{23}^2 \otimes \left(\frac{m_{23}^2 + p_1^2}{m_{23}^2}\right) - p_1^2 \otimes \left(\frac{m_{23}^2 + p_1^2}{m_{23}^2}\right) + \mathcal{O}(\epsilon). \quad (\text{B.3})$$

### B.1.1 Single cuts

The cut in the external channel  $p_1^2$  is

$$\begin{aligned} \text{Cut}_{p_1^2} T(p_1^2, 0, 0; 0, m_{23}^2, 0) &= 2\pi \frac{e^{\gamma_E \epsilon} \Gamma(1-\epsilon)}{\Gamma(2-2\epsilon)} \frac{(p_1^2)^{-\epsilon}}{p_1^2 + m_{23}^2} {}_2F_1\left(1, 1-\epsilon; 2-2\epsilon; \frac{p_1^2}{p_1^2 + m_{23}^2}\right) \\ &= -\frac{2\pi}{p_1^2} \log\left(\frac{m_{23}^2}{p_1^2 + m_{23}^2}\right) + \mathcal{O}(\epsilon). \end{aligned} \quad (\text{B.4})$$

The cut in the internal mass  $m_{23}^2$  is

$$\begin{aligned} \text{Cut}_{m_{23}^2} T(p_1^2, 0, 0; 0, m_{23}^2, 0) &= \frac{2\pi e^{\gamma_E \epsilon}}{\Gamma(2-\epsilon)} \frac{(-m_{23}^2)^{-\epsilon}}{p_1^2 + m_{23}^2} {}_2F_1\left(1, 1-\epsilon; 2-\epsilon; \frac{p_1^2}{p_1^2 + m_{23}^2}\right) \\ &= \frac{2\pi}{p_1^2} \log\left(\frac{m_{23}^2 + p_1^2}{m_{23}^2}\right) + \mathcal{O}(\epsilon). \end{aligned} \quad (\text{B.5})$$

### B.1.2 Double cuts

The double cut in the external channel  $p_1^2$  and the internal mass  $m_{23}^2$  is

$$\begin{aligned} \text{Cut}_{p_1^2, m_{23}^2} T(p_1^2, 0, 0; 0, m_{23}^2, 0) &= -4\pi^2 i \frac{e^{\gamma_E \epsilon}}{\Gamma(1-\epsilon)} \frac{(p_1^2)^{-1+\epsilon} (-m_{23}^2)^{-\epsilon}}{(p_1^2 + m_{23}^2)^\epsilon} \theta(p_1^2 + m_{23}^2) \\ &= -\frac{4\pi^2 i}{p_1^2} \theta(p_1^2 + m_{23}^2) + \mathcal{O}(\epsilon). \end{aligned} \quad (\text{B.6})$$

## B.2 $T(p_1^2, 0, 0; m_{12}^2, 0, 0)$

The triangle of fig. 1b is given by:

$$\begin{aligned} T(p_1^2, 0, 0; m_{12}^2, 0, 0) &= -i \frac{e^{\gamma_E \epsilon} \Gamma(1+\epsilon)}{\epsilon(1-\epsilon)} (m_{12}^2)^{-1-\epsilon} {}_2F_1\left(1, 1+\epsilon; 2-\epsilon; \frac{p_1^2}{m_{12}^2}\right) \\ &= \frac{i}{p_1^2} \left[ \frac{1}{\epsilon} \log\left(1 - \frac{p_1^2}{m_{12}^2}\right) - \text{Li}_2\left(\frac{p_1^2}{m_{12}^2}\right) - \log^2\left(1 - \frac{p_1^2}{m_{12}^2}\right) \right. \\ &\quad \left. - \log(m_{12}^2) \log\left(1 - \frac{p_1^2}{m_{12}^2}\right) \right] + \mathcal{O}(\epsilon). \end{aligned} \quad (\text{B.7})$$

The symbol is

$$\begin{aligned} \mathcal{S} [\mathcal{T}(p_1^2, 0, 0; m_{12}^2, 0, 0)] &= \frac{1}{\epsilon} \frac{m_{12}^2 - p_1^2}{m_{12}^2} + m_{12}^2 \otimes \frac{m_{12}^2 (m_{12}^2 - p_1^2)}{p_1^2} \\ &\quad + (m_{12}^2 - p_1^2) \otimes \frac{p_1^2}{(m_{12}^2 - p_1^2)^2} + \mathcal{O}(\epsilon). \end{aligned} \quad (\text{B.8})$$

### B.2.1 Single cuts

The cut in the external channel  $p_1^2$  is

$$\begin{aligned} \text{Cut}_{p_1^2} T(p_1^2, 0, 0; m_{12}^2, 0, 0) &= -2\pi \frac{e^{\gamma_E \epsilon} \Gamma(1-\epsilon)}{\epsilon \Gamma(1-2\epsilon)} \frac{(p_1^2 - m_{12}^2)^{-2\epsilon}}{(p_1^2)^{1-\epsilon}} \\ &= -\frac{2\pi}{p_1^2 \epsilon} - \frac{2\pi}{p_1^2} (\log(p_1^2) - 2 \log(p_1^2 - m_{12}^2)) + \mathcal{O}(\epsilon). \end{aligned} \quad (\text{B.9})$$

The cut in the internal mass  $m_{12}^2$  is

$$\begin{aligned} \text{Cut}_{m_{12}^2} T(p_1^2, 0, 0; m_{12}^2, 0, 0) &= -\frac{2\pi e^{\gamma_E \epsilon}}{\epsilon \Gamma(1-\epsilon)} \frac{(-m_{12}^2)^{-\epsilon}}{p_1^2} {}_2F_1\left(1, \epsilon; 1-\epsilon; \frac{m_{12}^2}{p_1^2}\right) \\ &= -\frac{2\pi}{p_1^2 \epsilon} + \frac{2\pi}{p_1^2} \left( \log(m_{12}^2 - p_1^2) + \log\left(\frac{-m_{12}^2}{-p_1^2}\right) \right) + \mathcal{O}(\epsilon). \end{aligned} \quad (\text{B.10})$$

### B.2.2 Double cuts

The double cut in the external channel  $p_1^2$  and the internal mass  $m_{12}^2$  is zero.

### B.3 $T(p_1^2, 0, 0; m_{12}^2, m_{23}^2, 0)$

The triangle of fig. 1c is given by:

$$\begin{aligned} T(p_1^2, 0, 0; m_{12}^2, m_{23}^2, 0) &= i \frac{e^{\gamma_E \epsilon} \Gamma(1+\epsilon)}{\epsilon(1-\epsilon)(m_{12}^2 - m_{23}^2)} \left[ (m_{23}^2)^{-\epsilon} {}_2F_1\left(1, 1; 2-\epsilon; \frac{p_1^2}{m_{12}^2 - m_{23}^2}\right) \right. \\ &\quad \left. - (m_{12}^2)^{-\epsilon} F_1\left(1; 1, \epsilon; 2-\epsilon; \frac{p_1^2}{m_{12}^2 - m_{23}^2}; \frac{p_1^2}{m_{12}^2}\right) \right] \\ &= \frac{i}{p_1^2} \left[ \text{Li}_2\left(\frac{m_{12}^2}{m_{23}^2}\right) - \text{Li}_2\left(\frac{m_{12}^2 - p_1^2}{m_{23}^2}\right) \right. \\ &\quad \left. - \log\left(1 - \frac{m_{12}^2 - p_1^2}{m_{23}^2}\right) \log\left(1 - \frac{p_1^2}{m_{12}^2}\right) \right. \\ &\quad \left. + \log\left(\frac{m_{23}^2}{m_{12}^2}\right) \log\left(1 - \frac{p_1^2}{m_{12}^2 - m_{23}^2}\right) \right] + \mathcal{O}(\epsilon). \end{aligned} \quad (\text{B.11})$$

The symbol is

$$\begin{aligned} \mathcal{S}[T(p_1^2, 0, 0; m_{12}^2, m_{23}^2, 0)] &= m_{12}^2 \otimes \left(\frac{m_{12}^2 - m_{23}^2}{m_{23}^2}\right) + m_{23}^2 \otimes \left(1 - \frac{p_1^2}{m_{12}^2 - m_{23}^2}\right) \\ &\quad - (m_{12}^2 - p_1^2) \otimes \left(1 - \frac{m_{12}^2 - p_1^2}{m_{23}^2}\right) + \mathcal{O}(\epsilon). \end{aligned} \quad (\text{B.12})$$

### B.3.1 Single cuts

The cut in the external channel  $p_1^2$  is

$$\begin{aligned} \text{Cut}_{p_1^2} T(p_1^2, 0, 0; m_{12}^2, m_{23}^2, 0) &= \\ &= 2\pi \frac{e^{\gamma_E \epsilon} \Gamma(1-\epsilon)}{\Gamma(2-2\epsilon)} \frac{(p_1^2 - m_{12}^2)^{1-2\epsilon}}{m_{23}^2 (p_1^2)^{1-\epsilon}} {}_2F_1\left(1, 1-\epsilon; 2-2\epsilon; \frac{m_{12}^2 - p_1^2}{m_{23}^2}\right) \\ &= \frac{2\pi}{p_1^2} \log\left(1 - \frac{m_{12}^2 - p_1^2}{m_{23}^2}\right) + \mathcal{O}(\epsilon). \end{aligned} \quad (\text{B.13})$$

The cut in the internal mass  $m_{12}^2$  is

$$\begin{aligned}
\text{Cut}_{m_{12}^2} T(p_1^2, 0, 0; m_{12}^2, m_{23}^2, 0) &= \\
&= -\frac{2\pi}{p_1^2} \frac{e^{\gamma_E \epsilon}}{\Gamma(2-\epsilon)} \frac{(-m_{12}^2)^{1-\epsilon}}{m_{12}^2 - m_{23}^2} F_1 \left( 1; 1, \epsilon; 2-\epsilon; \frac{m_{12}^2}{m_{12}^2 - m_{23}^2}; \frac{m_{12}^2}{p_1^2} \right) \\
&= -\frac{2\pi}{p_1^2} \log \left( \frac{m_{23}^2}{m_{23}^2 - m_{12}^2} \right) + \mathcal{O}(\epsilon) .
\end{aligned} \tag{B.14}$$

The cut in the internal mass  $m_{23}^2$  is

$$\begin{aligned}
\text{Cut}_{m_{23}^2} T(p_1^2, 0, 0; m_{12}^2, m_{23}^2, 0) &= \\
&= -2\pi \frac{e^{\gamma_E \epsilon}}{\Gamma(2-\epsilon)} \frac{(-m_{23}^2)^{-\epsilon}}{m_{12}^2 - m_{23}^2} {}_2F_1 \left( 1, 1; 2-\epsilon; \frac{p_1^2}{m_{12}^2 - m_{23}^2} \right) \\
&= \frac{2\pi}{p_1^2} \log \left( 1 - \frac{p_1^2}{m_{12}^2 - m_{23}^2} \right) + \mathcal{O}(\epsilon) .
\end{aligned} \tag{B.15}$$

### B.3.2 Double cuts

The double cut in the external channel  $p_1^2$  and internal mass  $m_{23}^2$  is

$$\begin{aligned}
\text{Cut}_{p_1^2, m_{23}^2} T(p_1^2, 0, 0; m_{12}^2, m_{23}^2, 0) &= -4\pi^2 i \frac{e^{\gamma_E \epsilon}}{\Gamma(1-\epsilon)} \frac{(p_1^2)^{-1+\epsilon} (-m_{23}^2)^{-\epsilon}}{(p_1^2 - m_{12}^2 + m_{23}^2)^\epsilon} \theta(p_1^2 - m_{12}^2 + m_{23}^2) \\
&= -\frac{4\pi^2 i}{p_1^2} \theta(p_1^2 - m_{12}^2 + m_{23}^2) + \mathcal{O}(\epsilon) .
\end{aligned} \tag{B.16}$$

The double cut in the two internal masses is

$$\begin{aligned}
\text{Cut}_{m_{12}^2, m_{23}^2} T(p_1^2, 0, 0; m_{12}^2, m_{23}^2, 0) &= -4\pi^2 i \frac{e^{\gamma_E \epsilon}}{\Gamma(1-\epsilon)} \frac{(-p_1^2)^{-1+\epsilon} (-m_{23}^2)^{-\epsilon}}{(m_{12}^2 - p_1^2 - m_{23}^2)^\epsilon} \theta(m_{12}^2 - p_1^2 - m_{23}^2) \\
&\quad \theta(m_{23}^2 - m_{12}^2) \\
&= \frac{4\pi^2 i}{p_1^2} \theta(m_{12}^2 - p_1^2 - m_{23}^2) \theta(m_{23}^2 - m_{12}^2) + \mathcal{O}(\epsilon) .
\end{aligned} \tag{B.17}$$

#### B.4 $T(p_1^2, 0, 0; m_{12}^2, 0, m_{13}^2)$

The triangle of fig. 1d is given by:

$$\begin{aligned}
T(p_1^2, 0, 0; m_{12}^2, 0, m_{13}^2) &= i \frac{e^{\gamma_E \epsilon} \Gamma(1 + \epsilon)}{\epsilon(1 - \epsilon)} (-p_1^2)^{-1 - \epsilon} \left[ \frac{(w_1 - \bar{w}_1)^{-\epsilon}}{(1 - \bar{w}_1)} \right. \\
&\quad \left( \frac{(w_1 - 1)^{1 - \epsilon}}{w_1} F_1 \left( 1 - \epsilon; 1, \epsilon; 2 - \epsilon; \frac{w_1 - 1}{w_1(1 - \bar{w}_1)}; \frac{w_1 - 1}{w_1 - \bar{w}_1} \right) \right. \\
&\quad \left. - w_1^{-\epsilon} F_1 \left( 1 - \epsilon; 1, \epsilon; 2 - \epsilon; \frac{1}{1 - \bar{w}_1}; \frac{w_1}{w_1 - \bar{w}_1} \right) \right) \\
&\quad \left. - \frac{((w_1 - 1)(1 - \bar{w}_1))^{-\epsilon}}{w_1 \bar{w}_1} {}_2F_1 \left( 1, 1 - \epsilon; 2 - \epsilon; \frac{1}{w_1 \bar{w}_1} \right) \right] \\
&= \frac{i}{p_1^2} \log \left( \frac{w_1}{w_1 - 1} \right) \log \left( \frac{-\bar{w}_1}{1 - \bar{w}_1} \right) + \mathcal{O}(\epsilon) .
\end{aligned} \tag{B.18}$$

The symbol is

$$\mathcal{S} [T(p_1^2, 0, 0; m_{12}^2, 0, m_{13}^2)] = \left( \frac{w_1}{1 - w_1} \right) \otimes \left( \frac{\bar{w}_1}{1 - \bar{w}_1} \right) + \left( \frac{\bar{w}_1}{1 - \bar{w}_1} \right) \otimes \left( \frac{w_1}{1 - w_1} \right) + \mathcal{O}(\epsilon) . \tag{B.19}$$

##### B.4.1 Single cuts

The cut in the external channel  $p_1^2$  is

$$\begin{aligned}
\text{Cut}_{p_1^2} T(p_1^2, 0, 0; m_{12}^2, 0, m_{13}^2) &= \\
&= -2\pi \frac{e^{\gamma_E \epsilon} \Gamma(1 - \epsilon)}{\Gamma(2 - 2\epsilon)} (p_1^2)^{-1 - \epsilon} \frac{(w_1 - \bar{w}_1)^{1 - 2\epsilon}}{\bar{w}_1(w_1 - 1)} {}_2F_1 \left( 1, 1 - \epsilon; 2 - 2\epsilon; \frac{w_1 - \bar{w}_1}{\bar{w}_1(w_1 - 1)} \right) \\
&= \frac{2\pi}{p_1^2} \left( \log \left( \frac{w_1}{1 - w_1} \right) - \log \left( \frac{\bar{w}_1}{1 - \bar{w}_1} \right) \right) + \mathcal{O}(\epsilon) .
\end{aligned} \tag{B.20}$$

The cut in the internal mass  $m_{12}^2$  is

$$\begin{aligned}
\text{Cut}_{m_{12}^2} T(p_1^2, 0, 0; m_{12}^2, 0, m_{13}^2) &= \\
&= -2\pi \frac{e^{\gamma_E \epsilon} (-p_1^2)^{-1 - \epsilon}}{\Gamma(2 - \epsilon) (w_1 - 1)} \bar{w}_1^{-\epsilon} (w_1 - \bar{w}_1)^{-\epsilon} F_1 \left( 1 - \epsilon; 1, \epsilon; 2 - \epsilon; \frac{1}{1 - w_1}; \frac{-\bar{w}_1}{w_1 - \bar{w}_1} \right) \\
&= \frac{2\pi}{p_1^2} \log \left( \frac{w_1}{w_1 - 1} \right) + \mathcal{O}(\epsilon) .
\end{aligned} \tag{B.21}$$

The cut in the internal mass  $m_{13}^2$  is

$$\begin{aligned}
& \text{Cut}_{m_{13}^2} T(p_1^2, 0, 0; m_{12}^2, 0, m_{13}^2) = \\
& = -2\pi \frac{e^{\gamma_E \epsilon} (-p_1^2)^{-1-\epsilon}}{\Gamma(2-\epsilon)} \left[ -\frac{((1-w_1)(1-\bar{w}_1))^{-\epsilon}}{w_1 \bar{w}_1} {}_2F_1\left(1, 1-\epsilon; 2-\epsilon; \frac{1}{w_1 \bar{w}_1}\right) \right. \\
& \quad \left. + \frac{(1-w_1)^{1-\epsilon} (w_1 - \bar{w}_1)^{-\epsilon}}{w_1 (\bar{w}_1 - 1)} F_1\left(1-\epsilon; 1, \epsilon; 2-\epsilon; \frac{1-w_1}{w_1 (\bar{w}_1 - 1)}; \frac{w_1 - 1}{w_1 - \bar{w}_1}\right) \right] \\
& = -\frac{2\pi}{p_1^2} \log\left(\frac{-\bar{w}_1}{1-\bar{w}_1}\right) + \mathcal{O}(\epsilon) .
\end{aligned} \tag{B.22}$$

#### B.4.2 Double cuts

All double cuts are zero.

#### B.5 $T(p_1^2, 0, 0; m_{12}^2, m_{23}^2, m_{13}^2)$

The triangle of fig. 1e is given by<sup>6</sup>:

$$\begin{aligned}
& T(p_1^2, 0, 0; m_{12}^2, m_{23}^2, m_{13}^2) \\
& = i \frac{e^{\gamma_E \epsilon} \Gamma(1+\epsilon)}{\epsilon} (-p_1^2)^{-1-\epsilon} \left[ \frac{(w_1 - \bar{w}_1)^{-\epsilon}}{(1-\epsilon)(\mu_{23} + w_1(1-\bar{w}_1))} \right. \\
& \quad \left( (w_1 - 1)^{1-\epsilon} F_1\left(1-\epsilon; 1, \epsilon; 2-\epsilon; \frac{w_1 - 1}{\mu_{23} + w_1(1-\bar{w}_1)}; \frac{w_1 - 1}{w_1 - \bar{w}_1}\right) \right. \\
& \quad \left. - w_1^{1-\epsilon} F_1\left(1-\epsilon; 1, \epsilon; 2-\epsilon; \frac{w_1}{\mu_{23} + w_1(1-\bar{w}_1)}; \frac{w_1}{w_1 - \bar{w}_1}\right) \right) \\
& \quad \left. - \frac{(-\mu_{23})^{-\epsilon}}{w_1 \bar{w}_1 - \mu_{23}} F_1\left(1; 1, \epsilon; 2; \frac{1}{w_1 \bar{w}_1 - \mu_{23}}; \frac{\mu_{23} + (w_1 - 1)(1 - \bar{w}_1)}{\mu_{23}}\right) \right] \\
& = \frac{i}{p_1^2} \left[ \log\left(\frac{w_1}{w_1 - 1}\right) \log\left(\frac{-\bar{w}_1}{1 - \bar{w}_1}\right) - G\left(1, 0, \frac{\mu_{23}}{(w_1 - 1)(\bar{w}_1 - 1)}\right) \right. \\
& \quad \left. + G\left(1, 0, \frac{\mu_{23}}{w_1(\bar{w}_1 - 1)}\right) + G\left(1, 0, \frac{\mu_{23}}{(w_1 - 1)\bar{w}_1}\right) \right. \\
& \quad \left. - G\left(1, 0, \frac{\mu_{23}}{w_1 \bar{w}_1}\right) \right] + \mathcal{O}(\epsilon) .
\end{aligned} \tag{B.23}$$

<sup>6</sup>We wrote the result in terms of harmonic polylogarithms for simplicity. It has a longer expression in terms of classical polylogarithms which can be easily obtained using

$$G(1, 0, x) = \text{Li}_2(x) + \log(1-x) \log(x) .$$

The symbol is

$$\begin{aligned}
\mathcal{S} [\mathcal{T}(p_1^2, 0, 0; m_{12}^2, m_{23}^2, m_{13}^2)] &= \mu_{23} \otimes \frac{(\mu_{23} + w_1(1 - \bar{w}_1))(\mu_{23} + \bar{w}_1(1 - w_1))}{(\mu_{23} - w_1\bar{w}_1)(\mu_{23} - (1 - w_1)(1 - \bar{w}_1))} \\
&+ w_1 \otimes \frac{\mu_{23} - w_1\bar{w}_1}{\mu_{23} + w_1(1 - \bar{w}_1)} + \bar{w}_1 \otimes \frac{\mu_{23} - w_1\bar{w}_1}{\mu_{23} + \bar{w}_1(1 - w_1)} \\
&+ (1 - w_1) \otimes \frac{\mu_{23} - (1 - w_1)(1 - \bar{w}_1)}{\mu_{23} + \bar{w}_1(1 - w_1)} \\
&+ (1 - \bar{w}_1) \otimes \frac{\mu_{23} - (1 - w_1)(1 - \bar{w}_1)}{\mu_{23} + w_1(1 - \bar{w}_1)} + \mathcal{O}(\epsilon) .
\end{aligned} \tag{B.24}$$

### B.5.1 Single cuts

The cut in the external channel  $p_1^2$  is

$$\begin{aligned}
\text{Cut}_{p_1^2} T(p_1^2, 0, 0; m_{12}^2, m_{23}^2, m_{13}^2) &= \\
&= -2\pi \frac{e^{\gamma_E \epsilon} \Gamma(1 - \epsilon)}{\Gamma(2 - 2\epsilon)} (p_1^2)^{-1 - \epsilon} \frac{(w_1 - \bar{w}_1)^{1 - 2\epsilon}}{\bar{w}_1(w_1 - 1) - \mu_{23}} {}_2F_1 \left( 1, 1 - \epsilon; 2 - 2\epsilon; \frac{w_1 - \bar{w}_1}{\bar{w}_1(w_1 - 1) - \mu_{23}} \right) \\
&= \frac{2\pi}{p_1^2} \log \left( \frac{\mu_{23} + w_1(1 - \bar{w}_1)}{\mu_{23} + \bar{w}_1(1 - w_1)} \right) + \mathcal{O}(\epsilon) .
\end{aligned} \tag{B.25}$$

The cut in the internal mass  $m_{12}^2$  is

$$\begin{aligned}
\text{Cut}_{m_{12}^2} T(p_1^2, 0, 0; m_{12}^2, m_{23}^2, m_{13}^2) &= \\
&= \frac{2\pi e^{\gamma_E \epsilon} (-p_1^2)^{-1 - \epsilon} \bar{w}_1^{1 - \epsilon} (w_1 - \bar{w}_1)^{-\epsilon}}{\Gamma(2 - \epsilon) \mu_{23} - \bar{w}_1(w_1 - 1)} F_1 \left( 1 - \epsilon; 1, \epsilon; 2 - \epsilon; \frac{\bar{w}_1}{\mu_{23} - \bar{w}_1(w_1 - 1)}; \frac{-\bar{w}_1}{w_1 - \bar{w}_1} \right) \\
&= \frac{2\pi}{p_1^2} \log \left( \frac{\mu_{23} - w_1\bar{w}_1}{\mu_{23} + \bar{w}_1(1 - w_1)} \right) + \mathcal{O}(\epsilon) .
\end{aligned} \tag{B.26}$$

The cut in the internal mass  $m_{23}^2$  is

$$\begin{aligned}
\text{Cut}_{m_{23}^2} T(p_1^2, 0, 0; m_{12}^2, m_{23}^2, m_{13}^2) &= \\
&= 2\pi \frac{e^{\gamma_E \epsilon}}{\Gamma(1 - \epsilon)} \frac{(-p_1^2)^{-1 - \epsilon}}{1 - \epsilon} \mu_{23}^{1 - \epsilon} \frac{{}_2F_1 \left( 1, 1; 2 - \epsilon; \frac{\mu_{23}}{(\mu_{23} - (1 - w_1)(1 - \bar{w}_1))(w_1\bar{w}_1 - \mu_{23})} \right)}{(\mu_{23} - (1 - w_1)(1 - \bar{w}_1))(w_1\bar{w}_1 - \mu_{23})} \\
&= \frac{2\pi}{p_1^2} \log \left( \frac{(\mu_{23} + w_1(1 - \bar{w}_1))(\mu_{23} + \bar{w}_1(1 - w_1))}{(\mu_{23} - w_1\bar{w}_1)(\mu_{23} - (1 - w_1)(1 - \bar{w}_1))} \right) \\
&+ \mathcal{O}(\epsilon) .
\end{aligned} \tag{B.27}$$

The cut in the internal mass  $m_{13}^2$  is

$$\begin{aligned}
\text{Cut}_{m_{13}^2} T(p_1^2, 0, 0; m_{12}^2, m_{23}^2, m_{13}^2) &= \\
&= -2\pi \frac{e^{\gamma_E \epsilon}}{\Gamma(2-\epsilon)} (-p_1^2)^{-1-\epsilon} \left[ \frac{(1-w_1)^{1-\epsilon} (w_1-\bar{w}_1)^{-\epsilon}}{w_1(\bar{w}_1-1) - \mu_{23}} \right. \\
&\quad \left. F_1 \left( 1-\epsilon; 1, \epsilon; 2-\epsilon; \frac{1-w_1}{w_1(\bar{w}_1-1) - \mu_{23}}; \frac{w_1-1}{w_1-\bar{w}_1} \right) \right. \\
&\quad \left. - \frac{((1-w_1)(1-\bar{w}_1))^{1-\epsilon} {}_2F_1 \left( 1, 1-\epsilon; 2-\epsilon; \frac{(1-w_1)(1-\bar{w}_1)}{(w_1(\bar{w}_1-1) - \mu_{23})(\bar{w}_1(w_1-1) - \mu_{23})} \right)}{(w_1(\bar{w}_1-1) - \mu_{23})(\bar{w}_1(w_1-1) - \mu_{23})} \right] \\
&= \frac{2\pi}{p_1^2} \log \left( \frac{\mu_{23} - (1-w_1)(1-\bar{w}_1)}{\mu_{23} + \bar{w}_1(1-w_1)} \right) + \mathcal{O}(\epsilon) .
\end{aligned} \tag{B.28}$$

### B.5.2 Double cuts

The double cut in the external channel  $p_1^2$  and internal mass  $m_{23}^2$  is

$$\begin{aligned}
\text{Cut}_{p_1^2, m_{23}^2} T(p_1^2, 0, 0; m_{12}^2, m_{23}^2, m_{13}^2) &= -4\pi^2 i \frac{e^{\gamma_E \epsilon}}{\Gamma(1-\epsilon)} (p_1^2)^{-1-\epsilon} (\bar{w}_1(w_1-1) - \mu_{23})^{-\epsilon} \\
&\quad (-w_1(\bar{w}_1-1) + \mu_{23})^{-\epsilon} \theta(\bar{w}_1(w_1-1) - \mu_{23}) \\
&\quad \theta(-w_1(\bar{w}_1-1) + \mu_{23}) \\
&= -\frac{4\pi^2 i}{p_1^2} \theta(\bar{w}_1(w_1-1) - \mu_{23}) \theta(-w_1(\bar{w}_1-1) + \mu_{23}) \\
&\quad + \mathcal{O}(\epsilon) .
\end{aligned} \tag{B.29}$$

The double cut in the internal masses  $m_{12}^2$  and  $m_{23}^2$  is

$$\begin{aligned}
\text{Cut}_{m_{12}^2, m_{23}^2} T(p_1^2, 0, 0; m_{12}^2, m_{23}^2, m_{13}^2) &= -4\pi^2 i \frac{e^{\gamma_E \epsilon}}{\Gamma(1-\epsilon)} (-p_1^2)^{-1-\epsilon} \theta(w_1\bar{w}_1 - \mu_{23}) \\
&\quad (\mu_{23} - (w_1\bar{w}_1 - \mu_{23})(\mu_{23} - (1-w_1)(1-\bar{w}_1)))^{-\epsilon} \\
&\quad \theta(\mu_{23} - (w_1\bar{w}_1 - \mu_{23})(\mu_{23} - (1-w_1)(1-\bar{w}_1))) \\
&= \frac{4\pi^2 i}{p_1^2} \theta(w_1\bar{w}_1 - \mu_{23}) \\
&\quad \theta(\mu_{23} - (w_1\bar{w}_1 - \mu_{23})(\mu_{23} - (1-w_1)(1-\bar{w}_1))) \\
&\quad + \mathcal{O}(\epsilon) .
\end{aligned} \tag{B.30}$$

The double cut in the internal masses  $m_{13}^2$  and  $m_{23}^2$  is

$$\begin{aligned}
\text{Cut}_{m_{13}^2, m_{23}^2} T(p_1^2, 0, 0; m_{12}^2, m_{23}^2, m_{13}^2) &= -4\pi^2 i \frac{e^{\gamma_E \epsilon}}{\Gamma(1-\epsilon)} (-p_1^2)^{-1-\epsilon} \theta((1-w_1)(1-\bar{w}_1) - \mu_{23}) \\
&\quad (\mu_{23} - (w_1 \bar{w}_1 - \mu_{23})(\mu_{23} - (1-w_1)(1-\bar{w}_1)))^{-\epsilon} \\
&\quad \theta(\mu_{23} - (w_1 \bar{w}_1 - \mu_{23})(\mu_{23} - (1-w_1)(1-\bar{w}_1))) \\
&= \frac{4\pi^2 i}{p_1^2} \theta((1-w_1)(1-\bar{w}_1) - \mu_{23}) \\
&\quad \theta(\mu_{23} - (w_1 \bar{w}_1 - \mu_{23})(\mu_{23} - (1-w_1)(1-\bar{w}_1))) \\
&\quad + \mathcal{O}(\epsilon) .
\end{aligned} \tag{B.31}$$

All other double cuts are zero.

## C Two-mass triangles

We give explicit expressions for the triangles with two external massive channels that are used as examples in this paper. For all the examples given, we have computed the uncut triangles both through standard Feynman parametrization and through a dispersive integral, and verified agreement of the expressions. Divergent integrals were compared with the results given in ref. [53]. For all triangles with two external massive channels considered in the following subsections, we separate the rational prefactor from the pure transcendental function according to the relation

$$T(0, p_2^2, p_3^2; m_{12}^2, m_{23}^2, m_{13}^2) = \frac{i}{p_2^2 - p_3^2} \mathcal{T}(0, p_2^2, p_3^2; m_{12}^2, m_{23}^2, m_{13}^2), \tag{C.1}$$

where the internal masses are generic and can be zero. Before expansion in the dimensional regularization parameter  $\epsilon$ , the results will often involve the functions  ${}_2F_1$  and  $F_1$  defined in eqs. (A.8) and (A.9).

### C.1 $T(0, p_2^2, p_3^2; 0, m_{23}^2, 0)$

The triangle of fig. 2a is given by:

$$\begin{aligned}
T(0, p_2^2, p_3^2; 0, m_{23}^2, 0) &= i \frac{e^{\gamma_E \epsilon} \Gamma(1+\epsilon)}{\epsilon(1-\epsilon)} \frac{(m_{23}^2)^{-\epsilon}}{p_2^2 - p_3^2} \left[ \frac{p_2^2}{p_2^2 - m_{23}^2} {}_2F_1 \left( 1, 1-2\epsilon; 2-\epsilon; \frac{p_2^2}{p_2^2 - m_{23}^2} \right) \right. \\
&\quad \left. - \frac{p_3^2}{p_3^2 - m_{23}^2} {}_2F_1 \left( 1, 1-2\epsilon; 2-\epsilon; \frac{p_3^2}{p_3^2 - m_{23}^2} \right) \right] \\
&= \frac{i}{p_2^2 - p_3^2} \left[ \frac{1}{\epsilon} \log \left( \frac{m_{23}^2 - p_2^2}{m_{23}^2 - p_3^2} \right) + \text{Li}_2 \left( \frac{p_2^2}{p_2^2 - m_{23}^2} \right) - \text{Li}_2 \left( \frac{p_3^2}{p_3^2 - m_{23}^2} \right) \right. \\
&\quad \left. - \frac{1}{2} \log^2 (m_{23}^2 - p_2^2) + \frac{1}{2} \log^2 (m_{23}^2 - p_3^2) \right] + \mathcal{O}(\epsilon) .
\end{aligned} \tag{C.2}$$

The symbol is

$$\begin{aligned} \mathcal{S} [\mathcal{T}(0, p_2^2, p_3^2; 0, m_{23}^2, 0)] &= \frac{1}{\epsilon} \frac{m_{23}^2 - p_2^2}{m_{23}^2 - p_3^2} + m_{23}^2 \otimes \frac{p_3^2(m_{23}^2 - p_2^2)}{p_2^2(m_{23}^2 - p_3^2)} + (m_{23}^2 - p_2^2) \otimes \frac{p_2^2}{(m_{23}^2 - p_2^2)^2} \\ &\quad - (m_{23}^2 - p_3^2) \otimes \frac{p_3^2}{(m_{23}^2 - p_3^2)^2} + \mathcal{O}(\epsilon). \end{aligned} \tag{C.3}$$

### C.1.1 Single cuts

The cut in the external channel  $p_2^2$  is

$$\begin{aligned} \text{Cut}_{p_2^2} T(0, p_2^2, p_3^2; 0, m_{23}^2, 0) &= -2\pi \frac{e^{\gamma_E \epsilon} \Gamma(1 - \epsilon)}{\epsilon \Gamma(1 - 2\epsilon)} \frac{(p_2^2)^\epsilon (p_2^2 - m_{23}^2)^{-2\epsilon}}{p_2^2 - p_3^2} \\ &= -\frac{2\pi}{\epsilon(p_2^2 - p_3^2)} - \frac{2\pi}{p_2^2 - p_3^2} [\log(p_2^2) - 2 \log(p_2^2 - m_{23}^2)] + \mathcal{O}(\epsilon). \end{aligned} \tag{C.4}$$

The cut in the external channel  $p_3^2$  is trivial to obtain from the symmetry of the function. The cut in the internal mass  $m_{23}^2$  is

$$\begin{aligned} \text{Cut}_{m_{23}^2} T(0, p_2^2, p_3^2; 0, m_{23}^2, 0) &= -\frac{\pi e^{\gamma_E \epsilon}}{\epsilon \Gamma(1 - \epsilon)} \frac{\Gamma(1 + 2\epsilon)}{p_2^2 - p_3^2} \left\{ \frac{\Gamma(1 - \epsilon)}{\Gamma(1 + \epsilon)} (-p_2^2)^{-\epsilon} \left(1 - \frac{m_{23}^2}{p_2^2}\right)^{-2\epsilon} \right. \\ &\quad \left. - \frac{(-p_2^2)^{-\epsilon}}{\Gamma(1 + 2\epsilon)} {}_2F_1\left(\epsilon, 2\epsilon; 1 + 2\epsilon; 1 - \frac{m_{23}^2}{p_2^2}\right) - (p_2^2 \leftrightarrow p_3^2) \right\} \\ &= \frac{2\pi}{p_2^2 - p_3^2} \left[ \log\left(\frac{-p_3^2}{m_{23}^2 - p_3^2}\right) - \log\left(\frac{-p_2^2}{m_{23}^2 - p_2^2}\right) \right] + \mathcal{O}(\epsilon). \end{aligned} \tag{C.5}$$

### C.1.2 Double cuts

All double cuts are zero.

### C.2 $T(0, p_2^2, p_3^2; m_{12}^2, 0, 0)$

The triangle of fig. 2b is given by:

$$\begin{aligned} T(0, p_2^2, p_3^2; m_{12}^2, 0, 0) &= i \frac{e^{\gamma_E \epsilon} \Gamma(1 + \epsilon)}{\epsilon} \left[ \frac{(-p_3^2)^{-\epsilon} \Gamma^2(1 - \epsilon)}{m_{12}^2 \Gamma(2 - 2\epsilon)} {}_2F_1\left(1, 1 - \epsilon; 2 - 2\epsilon; \frac{p_2^2 - p_3^2}{m_{12}^2}\right) \right. \\ &\quad \left. - \frac{(m_{12}^2)^{-1 - \epsilon}}{1 - \epsilon} F_1\left(1; 1, \epsilon; 2 - \epsilon; \frac{p_2^2 - p_3^2}{m_{12}^2}; \frac{p_2^2}{m_{12}^2}\right) \right] \\ &= \frac{i}{(p_2^2 - p_3^2)} \left[ \text{Li}_2\left(\frac{p_2^2}{m_{12}^2}\right) - \text{Li}_2\left(\frac{p_2^2 - m_{12}^2}{p_3^2}\right) + \frac{1}{2} \log^2\left(-\frac{p_3^2}{m_{12}^2}\right) \right. \\ &\quad \left. - \log\left(\frac{p_2^2 - m_{12}^2}{p_3^2}\right) \log\left(\frac{m_{12}^2 - p_2^2 + p_3^2}{p_3^2}\right) + \frac{\pi^2}{3} \right] + \mathcal{O}(\epsilon). \end{aligned} \tag{C.6}$$

The symbol is

$$\begin{aligned} \mathcal{S}[\mathcal{T}(0, p_2^2, p_3^2; m_{12}^2, 0, 0)] &= m_{12}^2 \otimes \left( \frac{p_2^2}{p_3^2} \right) + p_3^2 \otimes \left( \frac{m_{12}^2 - p_2^2 + p_3^2}{m_{12}^2} \right) \\ &+ (m_{12}^2 - p_2^2) \otimes \left( \frac{-p_3^2 m_{12}^2}{p_2^2(p_2^2 - m_{12}^2 - p_3^2)} \right) + \mathcal{O}(\epsilon). \end{aligned} \quad (\text{C.7})$$

### C.2.1 Single cuts

The cut in the external channel  $p_2^2$  is

$$\begin{aligned} \text{Cut}_{p_2^2} T(0, p_2^2, p_3^2; m_{12}^2, 0, 0) &= \\ &= -2\pi \frac{e^{\gamma_E \epsilon} \Gamma(1 - \epsilon)}{\Gamma(2 - 2\epsilon)} \frac{(p_2^2 - m_{12}^2)^{1-2\epsilon}}{(p_2^2)^{-\epsilon} m_{12}^2 p_3^2} {}_2F_1 \left( 1, 1 - \epsilon; 2 - 2\epsilon; \frac{(p_2^2 - p_3^2)(p_2^2 - m_{12}^2)}{m_{12}^2 p_3^2} \right) \\ &= \frac{2\pi}{p_2^2 - p_3^2} \left( \log \left( \frac{p_2^2}{m_{12}^2} \right) + \log \left( \frac{p_2^2 - m_{12}^2 - p_3^2}{-p_3^2} \right) \right) + \mathcal{O}(\epsilon). \end{aligned} \quad (\text{C.8})$$

The cut in the external channel  $p_3^2$  is

$$\begin{aligned} \text{Cut}_{p_3^2} T(0, p_2^2, p_3^2; m_{12}^2, 0, 0) &= \\ &= -2\pi \frac{e^{\gamma_E \epsilon} \Gamma(1 - \epsilon)}{\Gamma(2 - 2\epsilon)} \frac{(p_3^2)^{-\epsilon}}{p_2^2 - p_3^2 - m_{12}^2} {}_2F_1 \left( 1, 1 - \epsilon; 2 - 2\epsilon; \frac{p_2^2 - p_3^2}{p_2^2 - p_3^2 - m_{12}^2} \right) \\ &= \frac{2\pi}{p_2^2 - p_3^2} (\log(m_{12}^2) - \log(m_{12}^2 - p_2^2 + p_3^2)) + \mathcal{O}(\epsilon). \end{aligned} \quad (\text{C.9})$$

The cut in the internal mass  $m_{12}^2$  is

$$\begin{aligned} \text{Cut}_{m_{12}^2} T(0, p_2^2, p_3^2; m_{12}^2, 0, 0) &= \\ &= \frac{2\pi e^{\gamma_E \epsilon}}{\Gamma(2 - \epsilon)} \frac{(m_{12}^2 - p_2^2)^{-\epsilon}}{p_3^2} \left( \frac{m_{12}^2}{p_2^2} \right)^{-\epsilon} F_1 \left( 1 - \epsilon; 1, \epsilon; 2 - \epsilon; \frac{p_3^2 - p_2^2}{p_3^2}; \frac{m_{12}^2}{m_{12}^2 - p_2^2} \right) \\ &= \frac{2\pi}{p_2^2 - p_3^2} (\log(-p_2^2) - \log(-p_3^2)) + \mathcal{O}(\epsilon). \end{aligned} \quad (\text{C.10})$$

### C.2.2 Double cuts

The double cut in the external channels  $p_2^2$  and  $p_3^2$  is

$$\begin{aligned} \text{Cut}_{p_2^2, p_3^2} T(0, p_2^2, p_3^2; m_{12}^2, 0, 0) &= \frac{4\pi^2 i e^{\gamma_E \epsilon}}{\Gamma(1 - \epsilon)} \frac{(p_3^2)^{-\epsilon} (p_2^2 - p_3^2 - m_{12}^2)^{-\epsilon}}{(m_{12}^2)^\epsilon (p_2^2 - p_3^2)^{1-2\epsilon}} \theta(p_2^2 - p_3^2 - m_{12}^2) \\ &= \frac{4\pi^2 i}{p_2^2 - p_3^2} \theta(p_2^2 - p_3^2 - m_{12}^2) + \mathcal{O}(\epsilon). \end{aligned} \quad (\text{C.11})$$

The double cut in the external channel  $p_3^2$  and the internal mass  $m_{12}^2$  is

$$\begin{aligned} \text{Cut}_{p_3^2, m_{12}^2} T(0, p_2^2, p_3^2; m_{12}^2, 0, 0) &= -4\pi^2 i \frac{e^{\gamma_E \epsilon}}{\Gamma(1 - \epsilon)} \frac{(p_3^2)^{-\epsilon} (-m_{12}^2)^{-\epsilon}}{(p_3^2 - p_2^2)^{1-\epsilon}} (p_3^2 + m_{12}^2 - p_2^2)^{-\epsilon} \\ &\quad \theta(p_3^2 + m_{12}^2 - p_2^2) \\ &= \frac{4\pi^2 i}{p_2^2 - p_3^2} \theta(p_3^2 + m_{12}^2 - p_2^2). \end{aligned} \quad (\text{C.12})$$

The double cut in the external channel  $p_2^2$  and the internal mass  $m_{12}^2$  is zero.

## D Three-mass triangles

We now present expressions for triangles with three external massive legs. We start by describing how we computed the triangles with one or two massive propagators, for which we give a very simple expression that allows us to evaluate the diagrams very easily to arbitrary order in  $\epsilon$ . Our method does not work for the case with three massive propagators, where we were not able to find a rational parametrization, and we rely on the result in ref. [54]. We will comment further on the choice of variables for this example in section D.4 below. For the cases treated in this section we will not compute mass discontinuities, as they do not add anything to what we have already illustrated in the context of previous examples. We separate the rational prefactor from the pure transcendental function according to the relation

$$T(p_1^2, p_2^2, p_3^2; m_{12}^2, m_{23}^2, m_{13}^2) = \frac{i}{p_1^2(z - \bar{z})} \mathcal{T}(p_1^2, p_2^2, p_3^2; m_{12}^2, m_{23}^2, m_{13}^2), \quad (\text{D.1})$$

where the internal masses are generic and can be zero.

### D.1 Computation of $T(p_1^2, p_2^2, p_3^2; m_{12}^2, 0, 0)$ and $T(p_1^2, p_2^2, p_3^2; m_{12}^2, 0, m_{13}^2)$

Triangles with two external masses are easily computed with standard techniques to arbitrary order in  $\epsilon$ . However, that is no longer the case for triangles with three external masses [49]. In ref. [31], the triangle with three external masses and massless internal propagators was easily computable to arbitrary order in  $\epsilon$  through a double dispersion integral over its double cut. We now show this is also possible when there are one or two massive propagators. In the following, we will use the variables

$$\alpha \bar{\alpha} = x = \frac{s_2}{p_1^2}, \quad (1 - \alpha)(1 - \bar{\alpha}) = y = \frac{s_3}{p_1^2},$$

where  $s_2$  and  $s_3$  are integration variables in dispersion relations.

We will use the shorthand  $T(p_i^2; m_{jk}^2)$  for any of the three-mass triangles. We now proceed as in ref. [31]:

$$\begin{aligned} T(p_i^2; m_{jk}^2) &= -\frac{1}{(2\pi i)^2} \int_{c_2} \frac{ds_2}{s_2 - p_2^2} \int_{c_3} \frac{ds_3}{s_3 - p_3^2} \left( \text{Cut}_{p_2^2, p_3^2} T(p_i^2; m_{jk}^2) \right) \Big|_{p_2^2=s_2, p_3^2=s_3} \\ &= \frac{i}{4\pi^2 p_1^2} \int_{c_\alpha} d\alpha \int_{c_{\bar{\alpha}}} d\bar{\alpha} \frac{\left( \text{Cut}_{p_2^2, p_3^2} \mathcal{T}(p_i^2; m_{jk}^2) \right) \Big|_{z=\alpha, \bar{z}=\bar{\alpha}}}{(\alpha \bar{\alpha} - z \bar{z})((1 - \alpha)(1 - \bar{\alpha}) - (1 - z)(1 - \bar{z}))}. \end{aligned} \quad (\text{D.2})$$

The only difference between the triangles with one and two massive propagators are the integration contours  $c_2$  and  $c_3$ , and  $c_\alpha$  and  $c_{\bar{\alpha}}$ . For the case with one internal mass,

$$c_2 = [m_{12}^2, \infty), \quad c_3 = [0, \infty) \quad \text{and} \quad c_\alpha = [1, \infty), \quad c_{\bar{\alpha}} = (-\infty, \mu_{12}],$$

and for the case with two internal masses,

$$c_2 = [m_{12}^2, \infty), \quad c_3 = [m_{13}^2, \infty) \quad \text{and} \quad c_\alpha = [w_1, \infty), \quad c_{\bar{\alpha}} = (-\infty, \bar{w}_1].$$

For either case, the functions  $\left(\text{Cut}_{p_2^2, p_3^2} \mathcal{T}(p_i^2; m_{jk}^2)\right)\Big|_{z=\alpha, \bar{z}=\bar{\alpha}}$  are given by powers of logarithms whose arguments are linear in both  $\alpha$  and  $\bar{\alpha}$ . The integral in eq. (D.2) is thus trivial to solve in terms of polylogarithms to the desired order in  $\epsilon$ . The change of variables

$$\beta = \frac{a_\beta}{\alpha} \quad \gamma = \frac{1 - a_\gamma}{1 - \bar{\alpha}},$$

where  $a_\beta = 1$  or  $w_1$  and  $a_\gamma = \mu_{12}$  or  $\bar{w}_1$  respectively for the cases with one and two internal massive propagators, makes the integration particularly simple to perform. The results for the finite terms of these two triangles, given below in eqs. (D.4) and (D.11), were computed with this method, and checked to agree with the result in ref. [54]. In our method, as mentioned above, higher orders in  $\epsilon$  become trivial to compute.

## D.2 $T(p_1^2, p_2^2, p_3^2; m_{12}^2, 0, 0)$

The triangle of fig. 3a is given by

$$T(p_1^2, p_2^2, p_3^2; m_{12}^2, 0, 0) = \frac{i}{p_1^2(z - \bar{z})} \mathcal{T}(p_1^2, z, \bar{z}, \mu_{12}), \quad (\text{D.3})$$

where  $\mathcal{T}(p_1^2, z, \bar{z}, \mu_{12})$  is a pure function given by

$$\begin{aligned} \mathcal{T}(p_1^2, z, \bar{z}, \mu_{12}) = & G(1, z, \mu_{12}) + G\left(1, \frac{\mu_{12}}{z}, \bar{z}\right) - G\left(1, \frac{\mu_{12}}{\bar{z}}, z\right) - G(1, \bar{z}, \mu_{12}) \\ & - \text{Li}_2(z) + \text{Li}_2(\bar{z}) + \log(1 - z) \log\left(1 - \frac{\mu_{12}}{z}\right) \\ & + \log\left(1 - \frac{1}{\mu_{12}}\right) \log\left(\frac{1 - z}{1 - \bar{z}}\right) - \log(1 - \bar{z}) \log\left(1 - \frac{\mu_{12}}{\bar{z}}\right) \\ & + \log(1 - \mu_{12}) \log\left(\frac{z(1 - \bar{z})(\bar{z} - \mu_{12})}{\bar{z}(1 - z)(z - \mu_{12})}\right) + \mathcal{O}(\epsilon). \end{aligned} \quad (\text{D.4})$$

The symbol of its finite part is

$$\begin{aligned} \mathcal{S}[\mathcal{T}(p_1^2, z, \bar{z}, \mu_{12})] = & \mu_{12} \otimes \frac{\bar{z}(z - \mu_{12})}{z(\bar{z} - \mu_{12})} + (1 - z)(1 - \bar{z}) \otimes \frac{(z - \mu_{12})}{(\bar{z} - \mu_{12})} \\ & + (z\bar{z} - \mu_{12}) \otimes \frac{z(1 - \bar{z})(\bar{z} - \mu_{12})}{\bar{z}(1 - z)(z - \mu_{12})} \\ & + (1 - \mu_{12}) \otimes \frac{(1 - z)(\bar{z} - \mu_{12})}{(1 - \bar{z})(z - \mu_{12})}. \end{aligned} \quad (\text{D.5})$$

### D.2.1 Single cuts

The cut in the  $p_1^2$  channel is

$$\begin{aligned} \text{Cut}_{p_1^2} T(p_1^2, p_2^2, p_3^2; m_{12}^2, 0, 0) = & -2\pi \frac{e^{\gamma_E \epsilon} \Gamma(1 - \epsilon)}{\Gamma(2 - 2\epsilon)} (p_1^2)^{-1 - \epsilon} \frac{(1 - \mu_{12})^{1 - 2\epsilon}}{(1 - z)(\mu_{12} - \bar{z})} \\ & {}_2F_1\left(1, 1 - \epsilon, 2 - 2\epsilon, \frac{(1 - \mu_{12})(z - \bar{z})}{(1 - z)(\mu_{12} - \bar{z})}\right) \\ = & \frac{2\pi}{p_1^2(z - \bar{z})} \log\left(\frac{(1 - \bar{z})(z - \mu_{12})}{(z - 1)(\mu_{12} - \bar{z})}\right) + \mathcal{O}(\epsilon). \end{aligned} \quad (\text{D.6})$$

The cut in the  $p_2^2$  channel is

$$\begin{aligned}
\text{Cut}_{p_2^2} T(p_1^2, p_2^2, p_3^3; m_{12}^2, 0, 0) &= -2\pi \frac{e^{\gamma_E \epsilon} \Gamma(1-\epsilon)}{\Gamma(2-2\epsilon)} (-p_1^2)^{-1-\epsilon} \frac{(\mu_{12} - z\bar{z})^{1-2\epsilon} (-z\bar{z})^\epsilon}{\bar{z}(1-z)(z-\mu_{12})} \\
&\quad {}_2F_1\left(1, 1-\epsilon; 2-2\epsilon; \frac{(z-\bar{z})(\mu_{12}-z\bar{z})}{\bar{z}(1-z)(z-\mu_{12})}\right) \\
&= \frac{2\pi}{p_1^2(z-\bar{z})} \log\left(\frac{-\bar{z}(1-z)(z-\mu_{12})}{z(1-\bar{z})(\mu_{12}-\bar{z})}\right) + \mathcal{O}(\epsilon).
\end{aligned} \tag{D.7}$$

The cut in the  $p_3^2$  channel is

$$\begin{aligned}
\text{Cut}_{p_3^2} T(p_1^2, p_2^2, p_3^3; m_{12}^2, 0, 0) &= -2\pi \frac{e^{\gamma_E \epsilon} \Gamma(1-\epsilon)}{\Gamma(2-2\epsilon)} (-p_1^2)^{-1-\epsilon} \frac{((z-1)(1-\bar{z}))^{-\epsilon}}{\mu_{12}-\bar{z}} \\
&\quad {}_2F_1\left(1, 1-\epsilon; 2-2\epsilon; \frac{z-\bar{z}}{\mu_{12}-\bar{z}}\right) \\
&= \frac{2\pi}{p_1^2(z-\bar{z})} \log\left(\frac{\mu_{12}-\bar{z}}{\mu_{12}-z}\right) + \mathcal{O}(\epsilon).
\end{aligned} \tag{D.8}$$

### D.2.2 Double cuts

The double cut in the  $p_i^2$  and  $p_j^2$  channels is

$$\begin{aligned}
\text{Cut}_{p_i^2, p_j^2} T(p_1^2, p_2^2, p_3^3; m_{12}^2, 0, 0) &= 4\pi^2 i \Theta_{ij} \frac{e^{\gamma_E \epsilon}}{\Gamma(1-\epsilon)} ((-1)^a p_1^2)^{-1-\epsilon} (z-\bar{z})^{-1+2\epsilon} \\
&\quad ((z-1)(1-\bar{z})(\bar{z}-\mu_{12})(z-\mu_{12}))^{-\epsilon} \\
&= \frac{4\pi^2 i}{p_1^2(z-\bar{z})} (-1)^a \Theta_{ij} + \mathcal{O}(\epsilon),
\end{aligned} \tag{D.9}$$

where  $a = 0$  for  $(i, j) = (1, 2)$  or  $(1, 3)$ , and  $a = 1$  for  $(i, j) = (2, 3)$ . The theta functions are

$$\begin{aligned}
\Theta_{12} &= \theta(z-1)\theta(1-\bar{z})\theta(z-\mu_{12})\theta(\bar{z}-\mu_{12}) \\
\Theta_{13} &= \theta(1-z)\theta(1-\bar{z})\theta(z-\mu_{12})\theta(\mu_{12}-\bar{z}) \\
\Theta_{23} &= \theta(z-1)\theta(1-\bar{z})\theta(z-\mu_{12})\theta(\mu_{12}-\bar{z}).
\end{aligned}$$

### D.3 $T(p_1^2, p_2^2, p_3^3; m_{12}^2, 0, m_{13}^2)$

The triangle of fig. 3b is given by

$$T(p_1^2, p_2^2, p_3^3; m_{12}^2, 0, m_{13}^2) = \frac{i}{p_1^2(z-\bar{z})} \mathcal{T}(p_1^2, z, \bar{z}, w_1, \bar{w}_1), \tag{D.10}$$

where  $\mathcal{T}(p_1^2, z, \bar{z}, w_1, \bar{w}_1)$  is a pure function given by

$$\begin{aligned}
\mathcal{T}(p_1^2, z, \bar{z}, w_1, \bar{w}_1) = & G\left(\frac{w_1}{z}, \frac{w_1(\bar{w}_1 - 1)}{\bar{w}_1 + (1-z)(1-\bar{z}) - 1}, 1\right) + G\left(\frac{w_1}{\bar{z}}, w_1, 1\right) \\
& - G\left(\frac{w_1}{\bar{z}}, \frac{w_1(\bar{w}_1 - 1)}{\bar{w}_1 + (1-z)(1-\bar{z}) - 1}, 1\right) - G\left(\frac{w_1}{z}, w_1, 1\right) \\
& - \text{Li}_2\left(\frac{z\bar{z}}{w_1\bar{w}_1}\right) - G\left(\frac{w_1}{z}, \frac{w_1\bar{w}_1}{z\bar{z}}, 1\right) - G\left(\bar{w}_1, \frac{w_1\bar{w}_1}{\bar{z}}, z\right) \\
& + \log\left(1 - \frac{1}{\bar{w}_1}\right) \log\left(\frac{w_1 - z}{w_1 - \bar{z}}\right) + \log\left(1 - \frac{\bar{z}}{w_1}\right) \log\left(1 - \frac{z}{\bar{w}_1}\right) \\
& + \mathcal{O}(\epsilon).
\end{aligned} \tag{D.11}$$

The symbol of its finite part is

$$\begin{aligned}
\mathcal{S}[\mathcal{T}(p_1^2, z, \bar{z}, w_1, \bar{w}_1)] = & (z\bar{z} - w_1\bar{w}_1) \otimes \frac{z(w_1 - \bar{z})(\bar{w}_1 - \bar{z})}{\bar{z}(w_1 - z)(\bar{w}_1 - z)} \\
& + ((1-z)(1-\bar{z}) - (1-w_1)(1-\bar{w}_1)) \otimes \frac{(1-\bar{z})(w_1 - z)(\bar{w}_1 - z)}{(1-z)(w_1 - \bar{z})(\bar{w}_1 - \bar{z})} \\
& + (1-w_1) \otimes \frac{(1-z)(w_1 - \bar{z})}{(1-\bar{z})(w_1 - z)} + w_1 \otimes \frac{\bar{z}(w_1 - z)}{z(w_1 - \bar{z})} \\
& + (1-\bar{w}_1) \otimes \frac{(1-z)(\bar{w}_1 - \bar{z})}{(1-\bar{z})(\bar{w}_1 - z)} + \bar{w}_1 \otimes \frac{\bar{z}(\bar{w}_1 - z)}{z(\bar{w}_1 - \bar{z})}.
\end{aligned} \tag{D.12}$$

### D.3.1 Single cuts

The cut in the  $p_1^2$  channel is

$$\begin{aligned}
\text{Cut}_{p_1^2} T(p_1^2, p_2^2, p_3^3; m_{12}^2, 0, m_{13}^2) = & -2\pi \frac{e^{\gamma_E \epsilon} \Gamma(1-\epsilon)}{\Gamma(2-2\epsilon)} (p_1^2)^{-1-\epsilon} \frac{(w_1 - \bar{w}_1)^{1-2\epsilon}}{(z - w_1)(\bar{z} - \bar{w}_1)} \\
& {}_2F_1\left(1, 1-\epsilon, 2-2\epsilon, \frac{(z-\bar{z})(w_1 - \bar{w}_1)}{(z-w_1)(\bar{z}-\bar{w}_1)}\right) \\
= & \frac{2\pi}{p_1^2(z-\bar{z})} \log\left(\frac{(z-\bar{w}_1)(w_1 - \bar{z})}{(\bar{w}_1 - \bar{z})(z-w_1)}\right) + \mathcal{O}(\epsilon).
\end{aligned} \tag{D.13}$$

The cut in the  $p_2^2$  channel is

$$\begin{aligned}
\text{Cut}_{p_2^2} T(p_1^2, p_2^2, p_3^3; m_{12}^2, 0, m_{13}^2) = & 2\pi \frac{e^{\gamma_E \epsilon} \Gamma(1-\epsilon)}{\Gamma(2-2\epsilon)} (-p_1^2)^{-1-\epsilon} \frac{(-z\bar{z})^\epsilon (w_1\bar{w}_1 - z\bar{z})^{1-2\epsilon}}{\bar{z}(w_1 - z)(z - \bar{w}_1)} \\
& {}_2F_1\left(1, 1-\epsilon, 2-2\epsilon, \frac{(z-\bar{z})(w_1\bar{w}_1 - z\bar{z})}{\bar{z}(w_1 - z)(z - \bar{w}_1)}\right) \\
= & \frac{2\pi}{p_1^2(z-\bar{z})} \log\left(\frac{-\bar{z}(z-\bar{w}_1)(w_1 - z)}{z(w_1 - \bar{z})(\bar{w}_1 - \bar{z})}\right) + \mathcal{O}(\epsilon).
\end{aligned} \tag{D.14}$$

The cut in the  $p_3^2$  channel is

$$\begin{aligned}
\text{Cut}_{p_3^2} T(p_1^2, p_2^2, p_3^3; m_{12}^2, 0, m_{13}^2) &= -2\pi \frac{e^{\gamma_E \epsilon} \Gamma(1-\epsilon)}{\Gamma(2-2\epsilon)} (p_1^2)^{-1-\epsilon} \frac{u_3^\epsilon (u_3 - \mu_{13})^{1-2\epsilon}}{(\bar{z}-1)(z-\bar{w}_1)(z-w_1)} \\
&\quad {}_2F_1 \left( 1, 1-\epsilon, 2-2\epsilon, \frac{(z-\bar{z})(u_3 - \mu_{13})}{(\bar{z}-1)(z-\bar{w}_1)(z-w_1)} \right) \\
&= \frac{2\pi}{p_1^2(z-\bar{z})} \log \left( \frac{(z-1)(\bar{z}-\bar{w}_1)(w_1-\bar{z})}{(1-\bar{z})(z-\bar{w}_1)(z-w_1)} \right) + \mathcal{O}(\epsilon).
\end{aligned} \tag{D.15}$$

### D.3.2 Double cuts

The double cut in the  $p_i^2$  and  $p_j^2$  channels is

$$\begin{aligned}
\text{Cut}_{p_i^2, p_j^2} T(p_1^2, p_2^2, p_3^3; m_{12}^2, 0, m_{13}^2) &= 4\pi^2 i \Theta_{ij} \frac{e^{\gamma_E \epsilon}}{\Gamma(1-\epsilon)} \left( (-1)^a p_1^2 \right)^{-1-\epsilon} (z-\bar{z})^{-1+2\epsilon} \\
&\quad \left( (z-w_1)(\bar{z}-\bar{w}_1)(z-\bar{w}_1)(\bar{z}-\bar{w}_1) \right)^{-\epsilon} \\
&= \frac{4\pi^2 i}{p_1^2(z-\bar{z})} (-1)^a \Theta_{ij} + \mathcal{O}(\epsilon),
\end{aligned} \tag{D.16}$$

where  $a = 0$  for  $(i, j) = (1, 2)$  or  $(1, 3)$ , and  $a = 1$  for  $(i, j) = (2, 3)$ . The theta functions are

$$\begin{aligned}
\Theta_{12} &= \theta(z-w_1)\theta(w_1-\bar{z})\theta(z-\bar{w}_1)\theta(\bar{z}-\bar{w}_1) \\
\Theta_{13} &= \theta(w_1-z)\theta(w_1-\bar{z})\theta(z-\bar{w}_1)\theta(\bar{w}_1-\bar{z}) \\
\Theta_{23} &= \theta(z-w_1)\theta(w_1-\bar{z})\theta(z-\bar{w}_1)\theta(\bar{w}_1-\bar{z}).
\end{aligned}$$

### D.4 $T(p_1^2, p_2^2, p_3^3; m_{12}^2, m_{23}^2, m_{13}^2)$

For the triangle of fig. 3c we take the expression from ref. [54], adjusted to match our conventions:

$$T(p_1^2, p_2^2, p_3^3; m_{12}^2, m_{23}^2, m_{13}^2) = \frac{i}{p_1^2(z-\bar{z})} \mathcal{T}(p_1^2, p_2^2, p_3^2; m_{12}^2, m_{23}^2, m_{13}^2), \tag{D.17}$$

where

$$\mathcal{T}(p_1^2, p_2^2, p_3^2; m_{12}^2, m_{23}^2, m_{13}^2) = \sum_{i=1}^3 \sum_{\sigma=\pm} \left[ \text{Li}_2 \left( \frac{y_{0i}-1}{y_{i\sigma}} \right) - \text{Li}_2 \left( \frac{y_{0i}}{y_{i\sigma}} \right) \right]. \tag{D.18}$$

The  $y_{0i}$  and  $y_{i\pm}$  are given by

$$\begin{aligned}
y_{0i} &= \frac{-1}{2u_i \sqrt{\lambda_z}} \left[ u_i(u_i - u_{i+1} - u_{i-1} + 2\mu_{i-1, i+1} - \mu_{i, i+1} - \mu_{i-1, i}) \right. \\
&\quad \left. - (u_{i+1} - u_{i-1})(\mu_{i-1, i} - \mu_{i, i+1}) - \sqrt{\lambda_z}(u_i - \mu_{i-1, i} + \mu_{i, i+1}) \right], \\
y_{i\pm} &= y_{0i} - \frac{1}{2u_i} \left[ u_i - \mu_{i-1, i} + \mu_{i, i+1} \pm \sqrt{\lambda_i} \right].
\end{aligned} \tag{D.19}$$

Here, the indices  $i \pm 1$  are defined cyclically. The variables  $u_i, \mu_{ij}$  are defined in eq. (2.3), and the  $\lambda_i$  for  $i = z, 1, 2, 3$  are defined in eqs. (2.5), (2.8) and (2.10).

To get as close as possible to a rational symbol alphabet, we use the variables  $z, \bar{z}, w_1, \bar{w}_1$  and  $\mu_{23}$ , which are adapted to the  $p_1^2$  channel. Since this triangle is fully symmetric, it is easy to choose variables adapted to any of the other two channels. However, given our choice, square roots of  $\lambda_2 \equiv \lambda(u_2, \mu_{12}, \mu_{23})$  and  $\lambda_3 \equiv \lambda(u_3, \mu_{13}, \mu_{23})$  make an unavoidable appearance. Written in a form where the first entries may be readily identified with the three channel thresholds and the three internal masses, the symbol of the triangle is

$$\begin{aligned}
\mathcal{S} [\mathcal{T} (p_1^2, z, \bar{z}, w_1, \bar{w}_1, \mu_{23})] = & w_1 (1 - \bar{w}_1) \otimes \frac{T_{1-}}{T_{1+}} + \frac{1}{2} \left( -z\bar{z} + w_1\bar{w}_1 - \sqrt{\lambda_2} + \mu_{23} \right) \otimes \frac{T_{2-}}{T_{2+}} \\
& + \frac{1}{2} \left( \bar{z}z - z - \bar{z} - w_1\bar{w}_1 + w_1 + \bar{w}_1 + \sqrt{\lambda_3} - \mu_{23} \right) \otimes \frac{T_{3-}}{T_{3+}} \\
& + w_1\bar{w}_1 \otimes \frac{T_{2+}}{(-z)T_{1-}} + (1 - w_1)(1 - \bar{w}_1) \otimes \frac{(z-1)T_{1+}}{T_{3-}} \\
& + 4\mu_{23} \otimes \frac{zT_{3+}}{(1-z)T_{2-}}.
\end{aligned} \tag{D.20}$$

The  $T_{i\pm}$  are given by the general formula

$$\begin{aligned}
T_{i\pm} = & -u_i(-u_i + u_{i+1} + u_{i-1} + \mu_{i,i+1} + \mu_{i,i-1} - 2\mu_{i+1,i-1}) \\
& + (u_{i+1} - u_{i-1})(\mu_{i,i+1} - \mu_{i,i-1}) \pm \sqrt{\lambda_z \lambda_i}.
\end{aligned} \tag{D.21}$$

In particular, we have

$$\begin{aligned}
T_{1\pm} = & -2(z\bar{z} + w_1\bar{w}_1 - \mu_{23}) + (w_1 + \bar{w}_1)(z + \bar{z}) \pm (w_1 - \bar{w}_1)(z - \bar{z}) \\
T_{2\pm} = & (z\bar{z} + w_1\bar{w}_1 - \mu_{23})(z + \bar{z}) - 2z\bar{z}(w_1 + \bar{w}_1) \pm (z - \bar{z})\sqrt{\lambda_2} \\
T_{3\pm} = & z^2(1 - \bar{z}) + \bar{z}^2(1 - z) + (w_1 + \bar{w}_1)(2z\bar{z} - z - \bar{z}) \\
& + (\mu_{23} - w_1\bar{w}_1)(z + \bar{z} - 2) \pm (z - \bar{z})\sqrt{\lambda_3}.
\end{aligned}$$

We note that  $T_{1\pm}$  can be written in a simpler form, but where the  $\pm$  notation is less clear:

$$\begin{aligned}
T_{1+} = & 2(\mu_{23} - (w_1 - \bar{z})(\bar{w}_1 - z)) \\
T_{1-} = & 2(\mu_{23} - (w_1 - z)(\bar{w}_1 - \bar{z})).
\end{aligned} \tag{D.22}$$

Since the triangle depends on the external momenta through the invariants, it depends on  $z$  and  $\bar{z}$  only through the symmetric combinations  $u_2 = z\bar{z}$ ,  $u_3 = (1-z)(1-\bar{z})$ . Therefore, once we have removed the rational prefactor, the symbol above is antisymmetric under the exchange  $z \leftrightarrow \bar{z}$ . However, we note that this antisymmetry is not superficially apparent in the last three terms.

#### D.4.1 Single cuts

As mentioned in section 2, for the triangle with three external and three internal masses we must be very careful with the choice of variables. We now show how it is possible to

choose variables such that each of the single cuts has a rational alphabet. However, unlike what happens for all other configurations of masses, for each cut we must choose different variables. For instance, in eq. (D.20) we chose variables that rationalize the symbol of the  $p_1^2$  cut (indeed, the  $T_{1\pm}$  are rational, as seen in eq. (D.22)). In this section, we give the cut results in terms of two slightly different sets of variables: either we normalize invariants by the same invariant associated with the channel being cut, or by a different invariant. Our notation is that  $p_i^2$  is the channel used for normalization, and  $p_j^2$  is the cut channel in the case where it is different.

We start with variables where we cut in the same channel we normalize by, namely  $p_i^2$ . To be more precise, the variables we choose are

$$\begin{aligned} z &= \frac{1 + u_j - u_k + \sqrt{\lambda(1, u_j, u_k)}}{2}, & \bar{z} &= \frac{1 + u_j - u_k - \sqrt{\lambda(1, u_j, u_k)}}{2}, \\ w_i &= \frac{1 + \mu_{ij} - \mu_{jk} + \sqrt{\lambda(u_j, \mu_{ij}, \mu_{jk})}}{2}, & \bar{w}_i &= \frac{1 + \mu_{ij} - \mu_{jk} - \sqrt{\lambda(u_j, \mu_{ij}, \mu_{jk})}}{2}, \end{aligned} \quad (\text{D.23})$$

related to the invariants through

$$\begin{aligned} z\bar{z} &= u_j = \frac{p_j^2}{p_i^2}, & (1-z)(1-\bar{z}) &= u_k = \frac{p_k^2}{p_i^2}, & \mu_{jk} &= \frac{m_{jk}^2}{p_i^2}, \\ w_i\bar{w}_i &= \mu_{ij} = \frac{m_{ij}^2}{p_i^2}, & (1-w_i)(1-\bar{w}_i) &= \mu_{ik} = \frac{m_{ik}^2}{p_i^2}. \end{aligned} \quad (\text{D.24})$$

This is a slight abuse of notation, as strictly speaking the  $z$  and  $\bar{z}$  variables are different for each  $i$ . For  $i = 1$ , these are the variables defined in 2.4 and 2.7 and the ones used for eq. (D.20).

In terms of these variables, the single cut in the  $p_i^2$  channel is

$$\begin{aligned} \text{Cut}_{p_i^2} T(p_1^2, p_2^2, p_3^2; m_{12}^2, m_{23}^2, m_{13}^2) &= -2\pi \frac{e^{\gamma_E} \Gamma(1-\epsilon)}{\Gamma(2-2\epsilon)} (p_i^2)^{-1-\epsilon} \frac{(w_i - \bar{w}_i)^{1-2\epsilon}}{(z - w_i)(\bar{z} - \bar{w}_i) - \mu_{jk}} \\ &{}_2F_1 \left( 1, 1-\epsilon; 2-2\epsilon; \frac{(z-\bar{z})(w_i - \bar{w}_i)}{(z-w_i)(\bar{z}-\bar{w}_i) - \mu_{jk}} \right) \\ &= \frac{2\pi}{p_i^2(z-\bar{z})} \log \left( \frac{(w_i - \bar{z})(\bar{w}_i - z) - \mu_{jk}}{(w_i - z)(\bar{w}_i - \bar{z}) - \mu_{jk}} \right) + \mathcal{O}(\epsilon). \end{aligned} \quad (\text{D.25})$$

Setting  $(i, j, k) = (1, 2, 3)$  and comparing with eq. (D.20), we see that the expected relation between cuts and coproduct entries holds.

Requiring that we normalize invariants by the channel being cut might be too restrictive. We now show how to define variables that do not have this requirement, but in terms of which the symbol alphabet is still rational. We define

$$\begin{aligned} z &= \frac{1 + u_j - u_k + \sqrt{\lambda(1, u_j, u_k)}}{2}, & \bar{z} &= \frac{1 + u_j - u_k - \sqrt{\lambda(1, u_j, u_k)}}{2}, \\ w_j &= \frac{u_j + \mu_{ij} - \mu_{jk} + \sqrt{\lambda(u_j, \mu_{ij}, \mu_{jk})}}{2}, & \bar{w}_j &= \frac{u_j + \mu_{ij} - \mu_{jk} - \sqrt{\lambda(u_j, \mu_{ij}, \mu_{jk})}}{2}, \end{aligned} \quad (\text{D.26})$$

related to the invariants through slightly more complicated relations,

$$\begin{aligned} z\bar{z} = u_j = \frac{p_j^2}{p_i^2}, \quad (1-z)(1-\bar{z}) = u_k = \frac{p_k^2}{p_i^2}, \quad \mu_{ik} = \frac{m_{ik}^2}{p_i^2}, \\ w_j\bar{w}_j = u_j\mu_{ij} = u_j \frac{m_{ij}^2}{p_i^2}, \quad (u_j - w_j)(u_j - \bar{w}_j) = u_j\mu_{jk} = u_j \frac{m_{jk}^2}{p_i^2}. \end{aligned} \quad (\text{D.27})$$

As above, there is a slight abuse of notation in the definition of the  $z$  and  $\bar{z}$  variables.

In terms of these variables, the single cut in the  $p_j^2$  channel is

$$\begin{aligned} \text{Cut}_{p_j^2} T(p_1^2, p_2^2, p_3^2; m_{12}^2, m_{23}^2, m_{13}^2) &= -2\pi \frac{e^{\gamma_E} \Gamma(1-\epsilon)}{\Gamma(2-2\epsilon)} (-p_i^2)^{-1-\epsilon} \frac{(-z\bar{z})^\epsilon (w_j - \bar{w}_j)^{1-2\epsilon}}{(z-w_j)(\bar{z}-\bar{w}_j) - z\bar{z}\mu_{ik}} \\ &\quad {}_2F_1\left(1, 1-\epsilon; 2-2\epsilon; \frac{(z-\bar{z})(w_j - \bar{w}_j)}{(z-w_j)(\bar{z}-\bar{w}_j) - z\bar{z}\mu_{ik}}\right) \\ &= \frac{2\pi}{p_i^2(z-\bar{z})} \log\left(\frac{z\bar{z}\mu_{ik} - (z-w_j)(\bar{z}-\bar{w}_j)}{z\bar{z}\mu_{ik} - (z-\bar{w}_j)(\bar{z}-w_j)}\right) + \mathcal{O}(\epsilon). \end{aligned} \quad (\text{D.28})$$

As promised, the symbol letters are rational.

#### D.4.2 Double cuts

We now give the results for the double cuts in terms of the two sets of variables. For the variables in eq. (D.23), we compute the double cut in channels  $p_i^2$  and  $p_j^2$ . It is given by

$$\begin{aligned} \text{Cut}_{p_i^2, p_j^2} T(p_1^2, p_2^2, p_3^2; m_{12}^2, m_{23}^2, m_{13}^2) &= \frac{4\pi^2 i e^{\gamma_E}}{\Gamma(1-\epsilon)} \frac{(p_i^2)^{-1-\epsilon}}{(z-\bar{z})^{1-2\epsilon}} (\mu_{jk} - (z-w_i)(\bar{z}-\bar{w}_i))^{-\epsilon} \\ &\quad ((z-\bar{w}_i)(\bar{z}-w_i) - \mu_{jk})^{-\epsilon} \Theta_{ij}, \end{aligned} \quad (\text{D.29})$$

where

$$\Theta_{ij} = \theta(\mu_{jk} - (z-w_i)(\bar{z}-\bar{w}_i)) \theta((z-\bar{w}_i)(\bar{z}-w_i) - \mu_{jk}).$$

For the variables of eq. (D.26), we compute the double cut in channels  $p_j^2$  and  $p_k^2$ . It is given by

$$\begin{aligned} \text{Cut}_{p_j^2, p_k^2} T(p_1^2, p_2^2, p_3^2; m_{12}^2, m_{23}^2, m_{13}^2) &= \frac{4\pi^2 i e^{\gamma_E}}{\Gamma(1-\epsilon)} \frac{(-p_i^2)^{-1-\epsilon}}{(-z\bar{z})^{-\epsilon}(z-\bar{z})^{1-2\epsilon}} \Theta_{jk} \\ &\quad \frac{(z\bar{z}\mu_{ik} - (z-w_j)(\bar{z}-\bar{w}_j))^{-\epsilon}}{((z-\bar{w}_j)(\bar{z}-w_j) - z\bar{z}\mu_{ik})^\epsilon}, \end{aligned} \quad (\text{D.30})$$

where

$$\Theta_{jk} = \theta((z-\bar{w}_j)(\bar{z}-w_j) - z\bar{z}\mu_{ik}) \theta(z\bar{z}\mu_{ik} - (z-w_j)(\bar{z}-\bar{w}_j)).$$

## References

- [1] L. Landau, *On analytic properties of vertex parts in quantum field theory*, *Nucl.Phys.* **13** (1959) 181–192.
- [2] R. Cutkosky, *Singularities and discontinuities of Feynman amplitudes*, *J.Math.Phys.* **1** (1960) 429–433.
- [3] G. 't Hooft and M. Veltman, *DIAGRAMMAR*, *NATO Adv.Study Inst.Ser.B Phys.* **4** (1974) 177–322.
- [4] M. Veltman, *Diagrammatica: The Path to Feynman rules*, *Cambridge Lect.Notes Phys.* **4** (1994) 1–284.
- [5] E. Remiddi, *Dispersion Relations for Feynman Graphs*, *Helv.Phys.Acta* **54** (1982) 364.
- [6] Z. Bern, L. J. Dixon, D. C. Dunbar, and D. A. Kosower, *One loop n point gauge theory amplitudes, unitarity and collinear limits*, *Nucl.Phys.* **B425** (1994) 217–260, [[hep-ph/9403226](#)].
- [7] Z. Bern, L. J. Dixon, D. C. Dunbar, and D. A. Kosower, *Fusing gauge theory tree amplitudes into loop amplitudes*, *Nucl.Phys.* **B435** (1995) 59–101, [[hep-ph/9409265](#)].
- [8] R. Britto, F. Cachazo, and B. Feng, *Generalized unitarity and one-loop amplitudes in N=4 super-Yang-Mills*, *Nucl.Phys.* **B725** (2005) 275–305, [[hep-th/0412103](#)].
- [9] R. Britto, E. Buchbinder, F. Cachazo, and B. Feng, *One-loop amplitudes of gluons in SQCD*, *Phys.Rev.* **D72** (2005) 065012, [[hep-ph/0503132](#)].
- [10] E. I. Buchbinder and F. Cachazo, *Two-loop amplitudes of gluons and octa-cuts in N=4 super Yang-Mills*, *JHEP* **0511** (2005) 036, [[hep-th/0506126](#)].
- [11] P. Mastrolia, *On Triple-cut of scattering amplitudes*, *Phys.Lett.* **B644** (2007) 272–283, [[hep-th/0611091](#)].
- [12] C. Anastasiou, R. Britto, B. Feng, Z. Kunszt, and P. Mastrolia, *D-dimensional unitarity cut method*, *Phys.Lett.* **B645** (2007) 213–216, [[hep-ph/0609191](#)].
- [13] D. Forde, *Direct extraction of one-loop integral coefficients*, *Phys.Rev.* **D75** (2007) 125019, [[0704.1835](#)].
- [14] E. Nigel Glover and C. Williams, *One-Loop Gluonic Amplitudes from Single Unitarity Cuts*, *JHEP* **0812** (2008) 067, [[0810.2964](#)].
- [15] P. Mastrolia, *Double-Cut of Scattering Amplitudes and Stokes' Theorem*, *Phys.Lett.* **B678** (2009) 246–249, [[0905.2909](#)].
- [16] S. Caron-Huot, *Loops and trees*, *JHEP* **1105** (2011) 080, [[1007.3224](#)].
- [17] D. A. Kosower and K. J. Larsen, *Maximal Unitarity at Two Loops*, *Phys.Rev.* **D85** (2012) 045017, [[1108.1180](#)].
- [18] H. Johansson, D. A. Kosower, and K. J. Larsen, *Two-Loop Maximal Unitarity with External Masses*, *Phys.Rev.* **D87** (2013), no. 2 025030, [[1208.1754](#)].
- [19] M. Søgaard, *Global Residues and Two-Loop Hepta-Cuts*, *JHEP* **1309** (2013) 116, [[1306.1496](#)].
- [20] M. Søgaard and Y. Zhang, *Unitarity Cuts of Integrals with Doubled Propagators*, *JHEP* **1407** (2014) 112, [[1403.2463](#)].

- [21] M. Caffo, H. Czyz, S. Laporta, and E. Remiddi, *The Master differential equations for the two loop sunrise selfmass amplitudes*, *Nuovo Cim.* **A111** (1998) 365–389, [[hep-th/9805118](#)].
- [22] S. Müller-Stach, S. Weinzierl, and R. Zayadeh, *A Second-Order Differential Equation for the Two-Loop Sunrise Graph with Arbitrary Masses*, *Commun.Num.Theor.Phys.* **6** (2012) 203–222, [[1112.4360](#)].
- [23] L. Adams, C. Bogner, and S. Weinzierl, *The two-loop sunrise graph with arbitrary masses*, [1302.7004](#).
- [24] S. Bloch and P. Vanhove, *The elliptic dilogarithm for the sunset graph*, [1309.5865](#).
- [25] E. Remiddi and L. Tancredi, *Schouten identities for Feynman graph amplitudes; the Master Integrals for the two-loop massive sunrise graph*, [1311.3342](#).
- [26] L. Adams, C. Bogner, and S. Weinzierl, *The two-loop sunrise graph in two space-time dimensions with arbitrary masses in terms of elliptic dilogarithms*, *J.Math.Phys.* **55** (2014), no. 10 102301, [[1405.5640](#)].
- [27] A. B. Goncharov, *Multiple polylogarithms and mixed Tate motives*, [math/0103059](#).
- [28] A. Goncharov, *Galois symmetries of fundamental groupoids and noncommutative geometry*, *Duke Math.J.* **128** (2005) 209, [[math/0208144](#)].
- [29] A. B. Goncharov, M. Spradlin, C. Vergu, and A. Volovich, *Classical Polylogarithms for Amplitudes and Wilson Loops*, *Phys.Rev.Lett.* **105** (2010) 151605, [[1006.5703](#)].
- [30] C. Duhr, *Hopf algebras, coproducts and symbols: an application to Higgs boson amplitudes*, *JHEP* **1208** (2012) 043, [[1203.0454](#)].
- [31] S. Abreu, R. Britto, C. Duhr, and E. Gardi, *From multiple unitarity cuts to the coproduct of Feynman integrals*, *JHEP* **1410** (2014) 125, [[1401.3546](#)].
- [32] D. Gaiotto, J. Maldacena, A. Sever, and P. Vieira, *Pulling the straps of polygons*, *JHEP* **1112** (2011) 011, [[1102.0062](#)].
- [33] K. T. Chen, *Iterated path integrals*, *Bull. Amer. Math. Soc.* **83** (1977) 831.
- [34] A. B. Goncharov, *Multiple polylogarithms, cyclotomy and modular complexes*, *Math.Res.Lett.* **5** (1998) 497–516, [[1105.2076](#)].
- [35] A. Goncharov, *A simple construction of Grassmannian polylogarithms*, [0908.2238](#).
- [36] C. Duhr, H. Gangl, and J. R. Rhodes, *From polygons and symbols to polylogarithmic functions*, *JHEP* **1210** (2012) 075, [[1110.0458](#)].
- [37] C. Duhr, *Mathematical aspects of scattering amplitudes*, [1411.7538](#).
- [38] J. M. Henn, *Multiloop integrals in dimensional regularization made simple*, *Phys.Rev.Lett.* **110** (2013) 251601, [[1304.1806](#)].
- [39] J. M. Henn, A. V. Smirnov, and V. A. Smirnov, *Analytic results for planar three-loop four-point integrals from a Knizhnik-Zamolodchikov equation*, *JHEP* **1307** (2013) 128, [[1306.2799](#)].
- [40] J. M. Henn and V. A. Smirnov, *Analytic results for two-loop master integrals for Bhabha scattering I*, *JHEP* **1311** (2013) 041, [[1307.4083](#)].
- [41] J. M. Henn, A. V. Smirnov, and V. A. Smirnov, *Evaluating single-scale and/or non-planar diagrams by differential equations*, [1312.2588](#).

- [42] S. Caron-Huot and J. M. Henn, *Iterative structure of finite loop integrals*, *JHEP* **1406** (2014) 114, [[1404.2922](#)].
- [43] T. Gehrmann, A. von Manteuffel, L. Tancredi, and E. Weihs, *The two-loop master integrals for  $q\bar{q} \rightarrow VV$* , *JHEP* **1406** (2014) 032, [[1404.4853](#)].
- [44] F. Caola, J. M. Henn, K. Melnikov, A. V. Smirnov, and V. A. Smirnov, *Two-loop helicity amplitudes for the production of two off-shell electroweak bosons in quark-antiquark collisions*, *JHEP* **1411** (2014) 041, [[1408.6409](#)].
- [45] M. Argeri, S. Di Vita, P. Mastrolia, E. Mirabella, J. Schlenk, *et al.*, *Magnus and Dyson Series for Master Integrals*, [1401.2979](#).
- [46] A. Grozin, J. M. Henn, G. P. Korchemsky, and P. Marquard, *The three-loop cusp anomalous dimension in QCD*, [1409.0023](#).
- [47] Z. Bern, E. Herrmann, S. Litsey, J. Stankowicz, and J. Trnka, *Logarithmic Singularities and Maximally Supersymmetric Amplitudes*, [1412.8584](#).
- [48] F. C. Brown, *Multiple zeta values and periods of moduli spaces  $\mathfrak{M}_{0,n}$* , *Annales Sci.Ecole Norm.Sup.* **42** (2009) 371, [[math/0606419](#)].
- [49] F. Chavez and C. Duhr, *Three-mass triangle integrals and single-valued polylogarithms*, *JHEP* **1211** (2012) 114, [[1209.2722](#)].
- [50] W. van Neerven, *Dimensional Regularization Of Mass And Infrared Singularities In Two Loop On-Shell Vertex Functions*, *Nucl.Phys.* **B268** (1986) 453.
- [51] P. Ball, V. M. Braun, and H. G. Dosch, *Form-factors of semileptonic D decays from QCD sum rules*, *Phys.Rev.* **D44** (1991) 3567–3581.
- [52] T. Tantau, *The TikZ and PGF Packages*.
- [53] R. K. Ellis and G. Zanderighi, *Scalar one-loop integrals for QCD*, *JHEP* **0802** (2008) 002, [[0712.1851](#)].
- [54] A. Denner, *Techniques for calculation of electroweak radiative corrections at the one loop level and results for W physics at LEP-200*, *Fortsch.Phys.* **41** (1993) 307–420, [[0709.1075](#)].

# Appendix D

## Second paper

# Non-Gaussian eccentricity fluctuations

Hanna Grönqvist,<sup>1</sup> Jean-Paul Blaizot,<sup>1</sup> and Jean-Yves Ollitrault<sup>1</sup>

<sup>1</sup>*Institut de physique théorique, Université Paris Saclay, CNRS, CEA, F-91191 Gif-sur-Yvette, France*  
(Dated: April 26, 2016)

We study the fluctuations of the anisotropy of the energy density profile created in a high-energy collision at the LHC. We show that the anisotropy in harmonic  $n$  has generic non-Gaussian fluctuations. We argue that these non-Gaussianities have a universal character for small systems such as p+Pb collisions, but not for large systems such as Pb+Pb collisions where they depend on the underlying non-Gaussian statistics of the initial density profile. We generalize expressions for the eccentricity cumulants  $\varepsilon_2\{4\}$  and  $\varepsilon_3\{4\}$  previously obtained within the independent-source model to a general fluctuating initial density profile.

## I. INTRODUCTION

Anisotropic flow in heavy-ion collisions [1] can be simply understood as the hydrodynamic response to spatial anisotropy in the initial state [2]. The largest components of anisotropic flow are elliptic flow,  $v_2$ , and triangular flow,  $v_3$ . In hydrodynamics, both are determined to a good approximation by linear response [3–5] to the eccentricity  $\varepsilon_2$  [6] and triangularity  $\varepsilon_3$  [7, 8] of the initial energy density profile. As a consequence, the probability distribution of anisotropic flow [9] directly constrains the initial geometry [10, 11].

The fluctuations of the initial anisotropy  $\varepsilon_n$  (with  $n = 2, 3$ ) are to a first approximation Gaussian [12, 13]. When the anisotropy is solely due to fluctuations (that is, with the notable exception of  $v_2$  in non-central nucleus-nucleus collision, which is mostly driven by the eccentricity in the reaction plane), non-Gaussianities can be measured directly using higher-order cumulants of the distribution of  $v_n$ , for instance the order 4 cumulant  $v_n\{4\}$ . Non-Gaussian flow fluctuations have first been seen through  $v_3\{4\}$  in Pb-Pb collisions [14, 15]. Similar non-Gaussianities are seen in initial-state models of  $\varepsilon_3$  [16].  $v_2\{4\}$  has also been measured in p-Pb collisions [17, 18], and is also predicted by standard initial-state models [19].

The question therefore arises as to what non-Gaussianities can tell us about the density fluctuations in the initial state: do they reveal interesting features of the dynamics, or are they the result of some general constraints? It has been pointed out for instance that the condition  $|\varepsilon_n| \leq 1$  alone generates a universal non-Gaussian component [20], which matches recent measurements of higher-order cumulants  $v_2\{6\}$  and  $v_2\{8\}$  in p-Pb collisions [21]. On the other hand, this is known to be only approximate. General analytic results about the statistics of  $\varepsilon_n$  can be obtained within a simple model where the initial density profile is a superposition of pointlike, independent sources [22]. Non-gaussianities arise typically as corrections to the central limit [23]. Expressions of  $\varepsilon_2\{4\}$  [24] and  $\varepsilon_3\{4\}$  [25] reveal a non-trivial dependence on the initial density profile, thus breaking the universal behavior just mentioned, as will be illustrated in Sec. III.

The goal of this paper is to assess more precisely what the non-Gaussianity of anisotropy fluctuations may tell us about the initial density profile and its fluctuations, thereby extending the study initiated in Ref. [26]. For simplicity, we restrict ourselves to the case of central collisions, i.e.  $b = 0$ , where initial anisotropies are solely due to fluctuations. In the next section we recall general definitions of eccentricities and the cumulant of their probability distribution. Then in Sec. III, we review known results from the independent source model. In Sec. IV, we carry out a perturbative analysis for a general fluctuating density distribution, assuming that the fluctuations are small and uncorrelated. In Sec. V, these perturbative results are compared with full Monte Carlo simulations in order to assess the validity of the perturbative expansion. Conclusions are presented in Sec. VI. Technical material is gathered in several appendices.

## II. INITIAL ANISOTROPIES

We first recall the definitions of the anisotropy  $\varepsilon_n$  and of the cumulants  $\varepsilon_n\{2\}$  and  $\varepsilon_n\{4\}$ . We denote by  $\rho(z)$  the energy density in a given event, where  $z = x + iy$  is the complex coordinate in the transverse plane. The complex Fourier anisotropies [8, 27] are defined by

$$\varepsilon_n = \frac{\int_z z^n \rho(z)}{\int_z |z|^n \rho(z)}, \quad (1)$$

where we use the short hand  $\int_z = \int dx dy$  for the integration over the transverse plane. The definition (1) assumes that the center of the density lies at the origin. In an arbitrary coordinate system, one must replace  $z$  with  $z - z_0$ , where  $z_0 = \int_z z \rho(z) / \int_z \rho(z)$  is the center of the distribution. We refer to this correction as to the “recentering” correction.

The density  $\rho(z)$  fluctuates event to event, which entails fluctuations of the eccentricities  $\varepsilon_n$ . There is therefore an associated probability distribution of  $|\varepsilon_n|$ , that can, in principle, be determined from experiments. Experimental observables involve even moments of this distribution, which are conveniently combined into cumulants. The first 2 cumulants  $\varepsilon_n\{2\}$  and  $\varepsilon_n\{4\}$  are defined

as [28, 29]:

$$\begin{aligned}\varepsilon_n\{2\}^2 &\equiv \langle |\varepsilon_n|^2 \rangle \\ \varepsilon_n\{4\}^4 &\equiv 2\langle |\varepsilon_n|^2 \rangle^2 - \langle |\varepsilon_n|^4 \rangle,\end{aligned}\quad (2)$$

where angular brackets denote averages over events in a given centrality class.

If the anisotropy is solely due to fluctuations, and if the distribution of eccentricity fluctuations is Gaussian [12],  $\varepsilon_n\{4\}$  vanishes. Thus a non-vanishing  $\varepsilon_n\{4\}$  directly reflects the non-Gaussianity of eccentricity fluctuations. The observation of a positive  $v_2\{4\}$  in proton-nucleus collisions [17, 18] (where the initial anisotropies are mostly due to fluctuations, and  $v_2 \propto \varepsilon_2$  in every event) shows that  $\varepsilon_2\{4\}^4 > 0$ , and similarly, the observation of positive  $v_3\{4\}$  [14, 15] in nucleus-nucleus collisions, at all centralities, shows that  $\varepsilon_3\{4\}^4 > 0$ .

As already stated, our goal is to see what these results tell us about the fluctuations of the density  $\rho(z)$ . The task is complicated by the fact that the relation between density and eccentricity fluctuations is not a direct one, because the relation (1) between  $\rho(z)$  and  $\varepsilon_n$  is non linear. Also, the same relation (1) shows that  $\rho(z) > 0$  ensures that  $|\varepsilon_n| \leq 1$ . This puts a constraint on the allowed range of local density fluctuations. Our efforts will mostly focus on the relations between the cumulants of the density fluctuations and those of the eccentricity fluctuations. Our study is limited to  $\varepsilon_n\{2\}$  and  $\varepsilon_n\{4\}$ , but higher-order cumulants such as  $\varepsilon_n\{6\}$  could be studied in a similar way.

### III. IDENTICAL SOURCES

We first recall known analytical results obtained within a simple model where the energy density is represented by a sum of identical, pointlike sources, much as in a Monte Carlo Glauber simulation [30]:

$$\rho(z) = \sum_{i=1}^N \delta(z - z_i). \quad (3)$$

The positions  $z_i$  of the sources,  $i = 1, \dots, N$ , are independent random variables with probability  $p(z_i)$  ( $\int_z p(z) = 1$ ) and  $N \geq 2$  is fixed. With this normalization, the total energy is  $\int_z \rho(z) = N$ . It is dimensionless. Since the sources are independent, the statistics of the fluctuations of  $\rho(z)$  is formally equivalent to that of the density fluctuations of a two-dimensional ideal gas of  $N$  particles with an average density profile  $\langle \rho(z) \rangle = Np(z)$ . Inserting Eq. (3) into (1), one obtains

$$\varepsilon_n = \frac{\sum_{i=1}^N (z_i - z_0)^n}{\sum_{i=1}^N |z_i - z_0|^n}, \quad (4)$$

where  $z_0 = (1/N) \sum_{i=1}^N z_i$  is the center of the distribution. Throughout this paper, we assume for simplicity that  $\langle \rho(z) \rangle$  has radial symmetry and depends only on

$r \equiv |z|$ , that is, we consider collisions at zero impact parameter. The anisotropy  $\varepsilon_n$  still differs from zero in general because the number of sources  $N$  is finite ( $N$  controls the strength of the fluctuations, which vanishes as  $N \rightarrow \infty$ ). The non linear dependence between  $\rho(z)$  and  $\varepsilon_n$  is reflected here in a non linear dependence of  $\varepsilon_n$  on the position of the sources. This makes the analytical calculation of the distribution of  $\varepsilon_n$  difficult for an arbitrary  $p(z_i)$ .

#### A. An exact result

In the particular case where the average density profile is Gaussian,  $p(z_i) \propto \exp(-|z_i|^2/R_0^2)$ , the probability distribution of  $\varepsilon_2$  can be calculated exactly [20, 31], and the first cumulants are<sup>1</sup>

$$\begin{aligned}\varepsilon_2\{2\} &= \sqrt{\frac{2}{N}} \\ \varepsilon_2\{4\} &\equiv \left( \frac{16}{N^2(N+2)} \right)^{1/4}.\end{aligned}\quad (5)$$

In the limiting case  $N = 2$ , the energy consists of two pointlike spots, therefore  $|\varepsilon_2| = 1$  for all events, which implies  $\varepsilon_2\{2\} = \varepsilon_2\{4\} = 1$ .

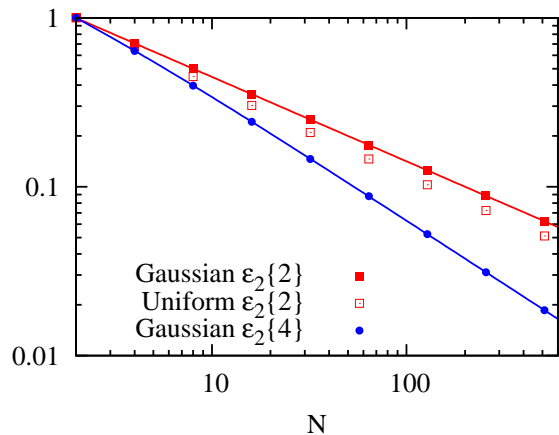


FIG. 1. (Color online) Closed symbols: values of  $\varepsilon_2\{2\}$  and  $\varepsilon_2\{4\}$  obtained in a Monte Carlo simulation of the Gaussian independent-source model. Lines: exact result given by Eq. (5). Open squares display, for sake of comparison, the values of  $\varepsilon_2\{2\}$  for a uniform average density profile (Sec. III B). Statistical errors are smaller than symbols.

Both  $\varepsilon_2\{2\}$  and  $\varepsilon_2\{4\}$  vanish in the limit  $N \rightarrow \infty$ , as expected since the average density profile is isotropic.

<sup>1</sup> The exact result in Ref. [31] is derived without the recentering correction. However, it can be shown that the recentering correction amounts to replacing  $N$  with  $N - 1$ .

$\varepsilon_2\{4\}$  decreases faster than  $\varepsilon_2\{2\}$  because eccentricity fluctuations become more and more Gaussian in the limit of large  $N$ . As we shall see below, the scaling laws  $\varepsilon_2\{2\} \propto N^{-1/2}$  and  $\varepsilon_2\{4\} \propto N^{-3/4}$  are general, in the source model, for fluctuation-dominated eccentricities in the limit  $N \gg 1$  [23].

The identical source model can easily be implemented through Monte Carlo simulations, by sampling the positions of the source  $z_i$  according to the distribution  $p(z)$ , for a large number of events. Numerical results are shown in Fig. 1. They are compatible with the exact result for all  $N$ , as they should.

Eliminating  $N$  between the two equations (5), one obtains the following relation between  $\varepsilon_2\{2\}$  and  $\varepsilon_2\{4\}$ :

$$\varepsilon_2\{4\} = \varepsilon_2\{2\}^{3/2} \left( \frac{2}{1 + \varepsilon_2\{2\}^2} \right)^{1/4}. \quad (6)$$

It has been conjectured [20] that this relation holds to a good approximation for all models of initial conditions, and also for  $\varepsilon_3$ . However, we shall see on explicit examples that this is not always the case.

### B. Perturbative results

More general results, i.e., valid for an arbitrary average density profile  $p(z)$  and when  $N \gg 1$ , have been obtained for  $\varepsilon_2$  [24] and  $\varepsilon_3$  [25], by treating fluctuations as a small parameter, as we shall explain later. To leading order in  $1/N$ , one obtains for  $n = 2, 3$

$$\begin{aligned} \varepsilon_n\{2\}^2 &= \frac{1}{N} \frac{\langle r^{2n} \rangle}{\langle r^n \rangle^2} \\ \varepsilon_n\{4\}^4 &= \frac{1}{N^3} \left( -\frac{8\langle r^{2n} \rangle^3}{\langle r^n \rangle^6} + \frac{8\langle r^{3n} \rangle \langle r^{2n} \rangle}{\langle r^n \rangle^5} \right. \\ &\quad \left. - \frac{\langle r^{4n} \rangle}{\langle r^n \rangle^4} + \frac{2\langle r^{2n} \rangle^2}{\langle r^n \rangle^4} \right), \end{aligned} \quad (7)$$

where angular brackets denote average values taken with  $p(z)$  (or, equivalently, the average density profile  $\langle \rho(z) \rangle$ ), and  $r \equiv |z|$ .

Note that  $\varepsilon_n\{4\}^4$  is the sum of two positive and two negative terms, and there are typically large cancellations. For a 2-dimensional Gaussian average density profile, for instance,  $\langle r^{2k} \rangle = k! R_0^{2k}$  and Eq. (7) yields for  $n = 2$ :

$$\begin{aligned} \varepsilon_2\{2\}^2 &= \frac{2}{N} \\ \varepsilon_2\{4\}^4 &= \frac{1}{N^3} (-64 + 96 - 24 + 8) = \frac{16}{N^3}, \end{aligned} \quad (8)$$

in agreement with the exact result (5) for  $N \gg 1$ .

For a generic average density profile  $\langle \rho(r) \rangle$ , the relative magnitudes of the four terms in the expression of  $\varepsilon_n\{4\}^4$ , Eq. (7), may vary. The Cauchy-Schwarz inequality  $\langle xy \rangle^2 \leq \langle x^2 \rangle \langle y^2 \rangle$  with  $x = r^{n/2}$  and  $y = r^{3n/2}$  proves that the second term is always larger than the first term (in absolute magnitude). The first term is itself at least

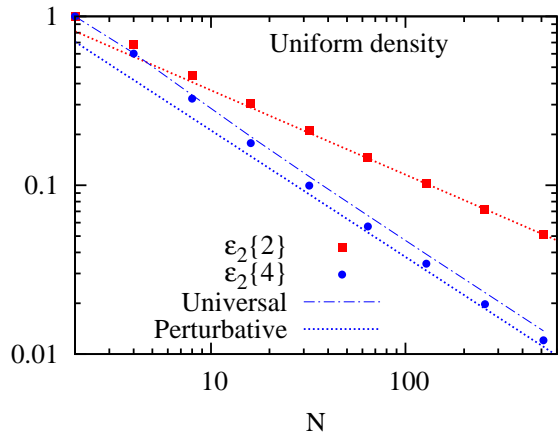


FIG. 2. (Color online) Same as Fig. 1 for a uniform density distribution in a disk. Symbols are values obtained in a Monte Carlo simulation, and dotted lines are straight lines corresponding to the perturbative formulas (9). Dash-dotted line, labeled “Universal”: value of  $\varepsilon_2\{4\}$  derived using Eq. (6), where  $\varepsilon_2\{2\}$  in the right-hand side is taken from the Monte Carlo result.

four times larger than the fourth term. But the magnitude of the third term may vary significantly, so that the sign of  $\varepsilon_n\{4\}^4$  may be negative if the density decreases slowly for large  $r$ . Therefore the observation that  $\varepsilon_n\{4\}^4 > 0$  in experiments provides nontrivial information.

In order to illustrate the sensitivity of  $\varepsilon_n$  to  $\langle \rho(r) \rangle$ , we carry out simulations with a uniform average density profile,  $\langle \rho(r) \rangle = \theta(R_0 - r)$ . Figure 1 shows that  $\varepsilon_2\{2\}$  is slightly smaller than with a Gaussian profile. This is confirmed by the analytic formulas Eq. (7): The moments are given by  $\langle r^{2k} \rangle = R_0^{2k}/(k+1)$  and one has

$$\begin{aligned} \varepsilon_2\{2\}^2 &= \frac{4}{3N} \\ \varepsilon_2\{4\}^4 &= \frac{368}{135N^3}. \end{aligned} \quad (9)$$

Comparison with Eq. (8) reveals that  $\varepsilon_2\{2\}^2$  is smaller by a factor  $\frac{2}{3}$ . Figure 2 shows that Monte Carlo results converge to the perturbative values (9) for large  $N$  as expected.

The fact that the anisotropies depend on the average density profile  $p(z)$  implies that the relation between  $\varepsilon_n\{4\}$  and  $\varepsilon_n\{2\}$  is not universal: Eq. (6) cannot always hold, as we have already indicated. Yet, as can be seen in Fig. 2, it accounts reasonably well for numerical results at all  $N$ , and is particularly accurate for small  $N$  where it gives a much better result than the asymptotic formula (9).

In Sec. IV, the perturbative result Eq. (7) will be generalized to an arbitrary initial density profile. We shall be able to assign a physical interpretation to each of the four terms in the perturbative expansion of  $\varepsilon_n\{4\}^4$ , namely:

- The first term arises from the non linear relation, Eq. (1), between the eccentricity and the density  $\rho(z)$ . Due to this nonlinearity, even when  $\rho(z)$  has a Gaussian distribution, the distribution of  $\varepsilon_n$  can be non-Gaussian.
- The second and third term arise from the genuine non-Gaussianity of the distribution of  $\rho(z)$ , that is, they are related respectively to the cumulants of order three and four of the density distribution.
- The fourth term is due to energy conservation, namely, the constraint that the total energy  $N$  should be exactly the same for all events.

#### IV. GENERALIZATION TO AN ARBITRARY FLUCTUATING DENSITY PROFILE

We now generalize the results of Sec. III B to an arbitrary (typically continuous) density profile  $\rho(z)$ . We write  $\rho(z) = \langle \rho(z) \rangle + \delta\rho(z)$ , where  $\langle \rho(z) \rangle$  is the density averaged over events and  $\delta\rho(z)$  the fluctuation. In addition, we no longer consider the total energy  $E = \int_z \rho(z)$  a dimensionless quantity, as in the identical source model.

##### A. Small fluctuations

Radial symmetry implies  $\int_z z^n \langle \rho(z) \rangle = 0$  and Eq. (1) can be rewritten as

$$\varepsilon_n = \frac{\int_z z^n \delta\rho(z)}{\int_z r^n \langle \rho(z) \rangle + \int_z r^n \delta\rho(z)}, \quad (10)$$

where we have neglected the recentering correction. We introduce the shorthand notation, for any function of  $z$ :

$$\begin{aligned} \delta f &\equiv \frac{1}{\langle E \rangle} \int_z f(z) \delta\rho(z) \\ \langle f \rangle &\equiv \frac{1}{\langle E \rangle} \int_z f(z) \langle \rho(z) \rangle, \end{aligned} \quad (11)$$

where  $\langle E \rangle$  is the average total energy:

$$\langle E \rangle = \int_z \langle \rho(z) \rangle. \quad (12)$$

With this notation, Eq. (10) can be rewritten as

$$\varepsilon_n = \frac{\delta z^n}{\langle r^n \rangle + \delta r^n} = \frac{\delta z^n}{\langle r^n \rangle} \left( 1 + \frac{\delta r^n}{\langle r^n \rangle} \right)^{-1}. \quad (13)$$

We expect  $\delta z^n / \langle r^n \rangle$  and  $\delta r^n / \langle r^n \rangle$  in Eq. (13) to be small for a large system and accordingly we treat them in a perturbative expansion. The size fluctuation  $\delta r^n$  can be neglected to leading order [13], but must be taken into account at next-to-leading order, by expanding Eq. (13) in powers of  $\delta r^n$ . One thus obtains for the moments:

$$|\varepsilon_n|^2 \simeq \frac{\delta z^n \delta \bar{z}^n}{\langle r^n \rangle^2} \left( 1 - 2 \frac{\delta r^n}{\langle r^n \rangle} + 3 \frac{(\delta r^n)^2}{\langle r^n \rangle^2} + \dots \right)$$

$$|\varepsilon_n|^4 \simeq \frac{(\delta z^n)^2 (\delta \bar{z}^n)^2}{\langle r^n \rangle^4} \left( 1 - 4 \frac{\delta r^n}{\langle r^n \rangle} + 10 \frac{(\delta r^n)^2}{\langle r^n \rangle^2} + \dots \right). \quad (14)$$

To perform the average over events, one is then led to evaluate averages of products of  $\delta f$ 's. For instance, a 2-point average is of the form:

$$\langle \delta f \delta g \rangle = \frac{1}{\langle E \rangle^2} \int_{z_1, z_2} f(z_1) g(z_2) \langle \delta\rho(z_1) \delta\rho(z_2) \rangle. \quad (15)$$

More generally, terms of order  $n$  in the fluctuations involve  $n$ -point functions of the density field,  $\langle \delta\rho(z_1) \dots \delta\rho(z_n) \rangle$ . We now derive the general form of these  $n$ -point functions.

##### B. Locality and cumulants

We assume that that fluctuations are correlated only over distances much shorter than any other scale of interest [13]. A consequence of this locality hypothesis is that the energy  $E$  contained in a transverse area  $S$  much larger than the typical area  $\sigma$  of a local fluctuation has almost Gaussian fluctuations. This is seen by decomposing the area  $S$  in a large number  $S/\sigma$  of independent subareas, and applying the central limit theorem. However, the condition  $E > 0$  induces non-Gaussianities that are visible when the relative fluctuations become sizable. In particular, the probability is likely to have positive skew, as illustrated in Fig. 3. Skewness is proportional to the third cumulant of the energy distribution.

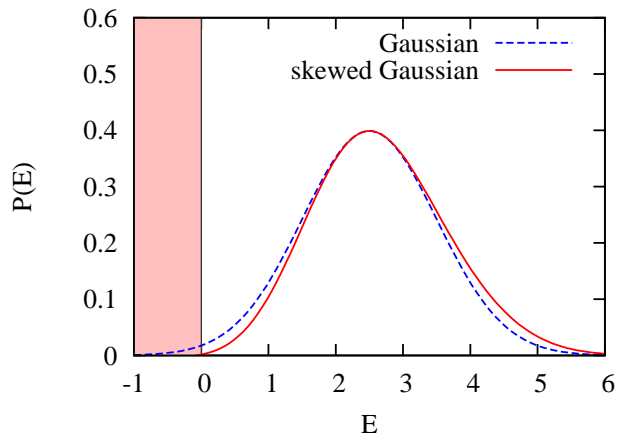


FIG. 3. (Color online) Sketch of the probability of the energy  $E$  in a given area. The Gaussian (dashed line) extends into the forbidden region  $E < 0$  (shaded area). Significant improvement is obtained by skewing the Gaussian (solid line).

Consider now two areas  $S_1$  and  $S_2$  large compared to  $\sigma$  but small compared to the total area of the system. Let  $E_1$  and  $E_2$  denote the energies in these two different

areas. The absence of correlations between fluctuations beyond an area of size  $\sigma$  implies that  $E_1$  and  $E_2$  are independent variables. Denoting by  $E = E_1 + E_2$  the sum, one obtains for arbitrary  $k$ :

$$\ln\langle e^{kE} \rangle = \ln\langle e^{kE_1} \rangle + \ln\langle e^{kE_2} \rangle. \quad (16)$$

This function of  $k$  is called the generating function of cumulants. The cumulant of order  $n$ , denoted by  $\kappa_n$ , is obtained by expanding to a given order  $k^n$ .

$$\ln\langle e^{kE} \rangle = \sum_{n=1}^{+\infty} \frac{k^n}{n!} \kappa_n \quad (17)$$

Eq. (16) shows that cumulants of the sum are sums of individual cumulants to all orders.

The additivity property Eq. (16) implies that cumulants of the energy in a cell scale like the transverse area  $S$  of the cell. Therefore we denote by  $\kappa_n(z) \equiv \kappa_n/S$  the density of the cumulant per unit transverse area at point  $z$ . At this point we note that all quantities that we are interested in are integrals of functions that are smooth on the scale of  $S$ . This allows us to abandon all reference to  $S$  and use a completely local formalism. A general definition of  $\kappa_n(z)$  is given in Appendix A using the formalism of functional integrals. The first cumulant  $\kappa_1(z)$  is the average value of the energy density,  $\kappa_1(z) = \langle \rho(z) \rangle$ . The second cumulant  $\kappa_2(z)$  is the variance. The magnitude of fluctuations is controlled by  $\kappa_2(z)$ .

The identical source model of Sec. III. does not satisfy the locality condition Eq. (16) because the total energy  $N$  is fixed by construction, which introduces a long-range correlation. One recovers Eq. (16) if  $N$  is allowed to fluctuate according to a Poisson distribution, as shown in Appendix C. In this case, all cumulants are equal:  $\kappa_n(z) = \langle N \rangle p(z)$ , where  $\langle N \rangle$  is the average value of  $N$ . In the general case, one can define an effective number of sources as follows [13]:

$$N_{\text{eff}} \equiv \frac{(\int_z \kappa_1(z))^2}{\int_z \kappa_2(z)}, \quad (18)$$

which coincides with  $\langle N \rangle$  for identical sources.

Cumulants of order 3 and higher vanish for a Gaussian distribution. The cumulants  $\kappa_3(z)$  and  $\kappa_4(z)$  correspond to the skewness and kurtosis, respectively.

### C. $n$ -point functions

We show in Appendix A that the 2-point function is:

$$\langle \delta\rho(z_1)\delta\rho(z_2) \rangle = \kappa_2(z_1)\delta(z_1 - z_2), \quad (19)$$

where  $\kappa_2(z)$  parametrizes the variance of the energy density at point  $z$ . Inserting Eq. (19) into Eq. (15), one obtains

$$\langle \delta f \delta g \rangle = \frac{1}{\langle E \rangle^2} \int_z f(z)g(z)\kappa_2(z), \quad (20)$$

where  $\langle E \rangle = \int_z \kappa_1(z)$  (Eq. (12)). The order of magnitude of the relative fluctuation is  $\langle \delta f \delta g \rangle / \langle f \rangle \langle g \rangle \sim 1/N_{\text{eff}}$ , which means that the typical order of magnitude of relative fluctuations  $\delta f / \langle f \rangle$  in a given event is  $1/\sqrt{N_{\text{eff}}}$ .

Higher-order averages are computed in a similar way, as discussed in Appendix A. In particular, the non-Gaussian character of energy fluctuations results in non-trivial 3-point averages:

$$\langle \delta f \delta g \delta h \rangle = \frac{1}{\langle E \rangle^3} \int_z f(z)g(z)h(z)\kappa_3(z). \quad (21)$$

This quantity is of order  $1/N_{\text{eff}}^2$ . In a given event,  $\delta f \delta g \delta h$  is of order  $1/N_{\text{eff}}^{3/2}$ , but after averaging over events, the result is smaller by a factor  $1/\sqrt{N_{\text{eff}}}$ . Thus 3 and 4-point averages contribute to the same order. More generally, orders  $2n - 1$  and  $2n$  both give contributions of order  $1/N_{\text{eff}}^n$ . This implies that the expansions of  $\langle |\varepsilon_n|^2 \rangle$  or  $\langle |\varepsilon_n|^4 \rangle$  are eventually in powers of  $1/N_{\text{eff}}$  rather than  $1/\sqrt{N_{\text{eff}}}$ . It also implies that the terms proportional to  $\delta r^n$  and  $(\delta r^n)^2$  in Eq. (14), even though they appear to be of different orders by naive power counting, both contribute at the same (next-to-leading) order.

The fourth-order moment in Eq. (14) involves terms up to order 6 in the fluctuations. 4-point averages and higher can be reduced using Wick's theorem (Eqs. (A6) and (A8)) which breaks them into a sum of products of lower-order terms and a connected part, which is much smaller and vanishes for Gaussian fluctuations.

### D. Perturbative results

It is now a straightforward exercise to evaluate the moments of the distribution of  $|\varepsilon_n|$  by averaging Eq. (14) over events, keeping terms up to next-to-leading order.

We use radial symmetry (which implies that  $\kappa_n(z)$  only depends on  $|z|$ ) to eliminate terms such as  $\langle \delta z^n \delta r^n \rangle$  or  $\langle (\delta z^n)^2 \rangle$ . The nontrivial contractions are

$$\begin{aligned} a &\equiv \frac{\langle \delta z^n \delta \bar{z}^n \rangle}{\langle r^n \rangle^2} \\ a' &\equiv \frac{\langle (\delta r^n)^2 \rangle}{\langle r^n \rangle^2} \\ b &\equiv \frac{\langle \delta z^n \delta \bar{z}^n \delta r^n \rangle}{\langle r^n \rangle^3} \\ c &\equiv \frac{\langle (\delta z^n)^2 (\delta \bar{z}^n)^2 \rangle_c}{\langle r^n \rangle^4}, \end{aligned} \quad (22)$$

where the subscript  $c$  in the last line denotes the connected part, defined in Appendix A by Eq. (A5). We have scaled by powers of  $\langle r^n \rangle$  so as to obtain dimensionless quantities. Then  $a$ ,  $a'$ ,  $b$  and  $c$  are of order  $1/N_{\text{eff}}$ ,  $1/N_{\text{eff}}$ ,  $1/N_{\text{eff}}^2$  and  $1/N_{\text{eff}}^3$ , respectively. Using Eqs. (20),

(21) and (A7), one obtains

$$\begin{aligned} a &= a' = \frac{\int_z r^{2n} \kappa_2(z)}{\left(\int_z r^n \kappa_1(z)\right)^2} \\ b &= \frac{\int_z r^{3n} \kappa_3(z)}{\left(\int_z r^n \kappa_1(z)\right)^3} \\ c &= \frac{\int_z r^{4n} \kappa_4(z)}{\left(\int_z r^n \kappa_1(z)\right)^4}. \end{aligned} \quad (23)$$

Since one expects cumulants to be positive to all orders, these quantities are all positive. Both  $b$  and  $c$  result from the non-Gaussianity of density fluctuations, i.e., they are proportional to averages of the cumulants  $\kappa_3(z)$  and  $\kappa_4(z)$ , respectively. The moments (14) can be simply expressed in terms of these elementary building blocks using Wick's theorem (Eqs. (A6) and (A8)):

$$\begin{aligned} \langle |\varepsilon_n|^2 \rangle &= a - 2b + 3aa' \\ \langle |\varepsilon_n|^4 \rangle &= 2a^2 + c - 16ab + 20a^2a', \end{aligned} \quad (24)$$

where the first term in each line is the leading order term, and the next terms are the next-to-leading corrections. The leading-order result for  $\varepsilon_n\{2\}$  has already been obtained in Ref. [13], namely:

$$\varepsilon_n\{2\}^2 \equiv \langle |\varepsilon_n|^2 \rangle = a = \frac{\int_z r^{2n} \kappa_2(z)}{\left(\int_z r^n \kappa_1(z)\right)^2}. \quad (25)$$

Terms of order  $1/N_{\text{eff}}^2$  cancel in the 4-cumulant (2):

$$\varepsilon_n\{4\}^4 = -8a^2a' + 8ab - c, \quad (26)$$

where we have kept all terms of order  $1/N_{\text{eff}}^3$ , which is the leading non-trivial order for this quantity. This equation is one of the main results of this article. Together with Eq. (23), it expresses the non-Gaussianity of eccentricity fluctuations in terms of the statistical properties of the underlying density field, in the regime where the perturbative expansion is valid.

We can check the result for identical, pointlike sources where  $\kappa_n(z) = \langle N \rangle p(z)$ . Eq. (23) then reduces to

$$\begin{aligned} a &= a' = \frac{1}{\langle N \rangle} \frac{\langle r^{2n} \rangle}{\langle r^n \rangle^2} \\ b &= \frac{1}{\langle N \rangle^2} \frac{\langle r^{3n} \rangle}{\langle r^n \rangle^3} \\ c &= \frac{1}{\langle N \rangle^3} \frac{\langle r^{4n} \rangle}{\langle r^n \rangle^4}. \end{aligned} \quad (27)$$

Inserting these expressions into Eq. (26), one recovers the first three terms in Eq. (7), if one replaces  $N$  with  $\langle N \rangle$ . The missing (fourth) term is due to energy conservation (i.e., the condition that  $N$  is fixed), which breaks locality. As shown in Appendix C, the missing term appears as a contribution to  $c$ .

We now discuss the case of a general density  $\rho(x)$ . If density fluctuations were Gaussian,  $b$  and  $c$  would vanish, which would result in  $\varepsilon_n\{4\}^4 < 0$ . The only positive contribution is the second term in Eq. (26), which

originates from the third cumulant of the density fluctuations.<sup>2</sup> Therefore the observation of a positive  $v_n\{4\}$  in experiments is by itself a clear indication that the density field has positive skew.

For simplicity, we have neglected energy conservation and the recentering correction. Energy conservation is important in practice because experimental analyses are essentially done at fixed energy: Experiments use as a proxy for impact parameter an observable dubbed ‘‘centrality’’ which is typically based on the multiplicity seen in a detector [32], which is strongly correlated with the total energy. Therefore one can essentially consider that the total energy  $E = \int_z \rho(z)$  is fixed in a narrow centrality class. This imposes a constraint on the density fluctuations, which modifies the expressions of  $a'$ ,  $b$  and  $c$ , as discussed in Appendix D. However, the numerical effect on eccentricity cumulants often turns out to be small, as the numerical study presented in the next section will show. As for the effect of the recentering correction, it is discussed in detail in Appendix E. It brings additional terms to Eq. (24), but these terms cancel in  $\varepsilon_n\{4\}^4$  so that Eq. (26) is unchanged.

## V. MONTE CARLO SIMULATIONS

In this section we present results of numerical simulations. Our goal is twofold. First, we want to assess the domain of validity of the results obtained in Sec. IV: How large must the system be for the expansion in powers of fluctuations to be valid? Second, we want to go beyond the identical source model of Sec. III and test the perturbative results in a more general situation where cumulants of the density  $\kappa_n(z)$  depend on the order  $n$ . This will be achieved by weighing the sources differently so that they are no longer identical, as discussed in Appendix B. All the Monte Carlo simulations in this section are done with a Gaussian average density profile, as in Sec. III A.

### A. Identical sources

The first set of simulations is similar to that discussed in Sec. III A. The only difference is that the number of sources  $N$  is no longer fixed but follows a Poisson distribution,<sup>3</sup> so that we can apply Eq. (27). Note that the Monte Carlo simulation uses a Lagrangian specification of the density field, by sampling the position of each source, while the derivation of Sec. IV C use a Eulerian point of view, by specifying the correlators of the

<sup>2</sup> Energy conservation also gives a positive contribution, but it is typically much smaller

<sup>3</sup> Note that  $\varepsilon_2$  is undefined for  $N = 0, 1$ , therefore we only consider values of  $\langle N \rangle$  large enough that  $N = 0, 1$  have probability close to 0.

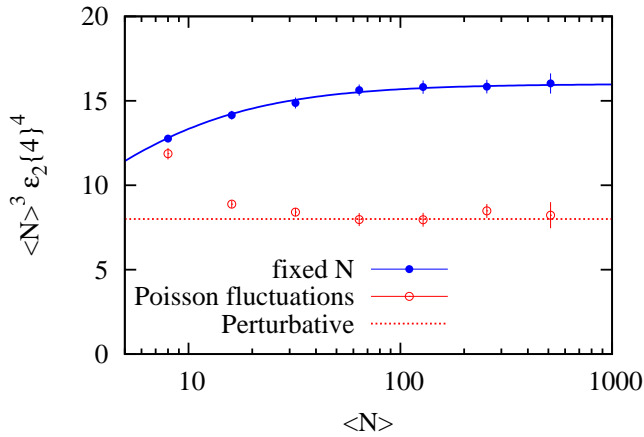


FIG. 4. (Color online)  $\langle N \rangle^3 \varepsilon_2\{4\}^2$  versus  $\langle N \rangle$ . Closed symbols: fixed  $N$ , as in Fig. 1. Full line: exact result (5). Open symbols: Poisson fluctuations. Dotted line: Perturbative result Eq. (28).

density at given points. Both Lagrangian and Eulerian descriptions are equivalent, as shown in Appendix C.

For a Gaussian density profile, Eqs. (26) and (27) give

$$\varepsilon_n\{4\}^4 = \frac{8}{\langle N \rangle^3}. \quad (28)$$

Comparison with Eq. (8) shows that the lack of energy conservation decreases  $\varepsilon_n\{4\}^4$  by a factor 2. One sees in Fig. 4 that Monte Carlo results quickly converge to the perturbative result (28) for large  $\langle N \rangle$ . The effect of energy conservation is smaller for smaller  $\langle N \rangle$ .

### B. Negative binomial fluctuations

In order to test the perturbative results of Sec. IV in the more general case where cumulants differ, we allow for a simple generalization of Eq. (3), by letting the energy of each source fluctuate:

$$\rho(z) = \sum_{i=1}^N w_i \delta(z - z_i), \quad (29)$$

where  $w_i > 0$  is the energy of source  $i$ , and  $N$  is still distributed according to a Poisson distribution to ensure locality. We assume for simplicity that the fluctuations in the position ( $z_i$ ) and the strength ( $w_i$ ) are uncorrelated. Then  $\rho(z)$  can be viewed as the density of a polydisperse ideal gas, which generalizes the monodisperse case of Sec. III. While the cumulants of the density are all equal for identical sources, they differ in general for weighted sources:  $\kappa_n(z) = \langle w^n \rangle \langle N \rangle p(z)$  (see Appendices B and C). Inserting this expression into Eq. (23), one finds that weights are taken into account by replacing  $r^n$  with  $w r^n$  everywhere in Eqs. (27).

The fluctuations of the weights increase eccentricity fluctuations [36, 37]. Thus, the effective number of sources as defined by Eq. (18) is:

$$N_{\text{eff}} \equiv \frac{\langle w \rangle^2}{\langle w^2 \rangle} \langle N \rangle. \quad (30)$$

It is smaller than  $\langle N \rangle$  if  $w$  fluctuates.

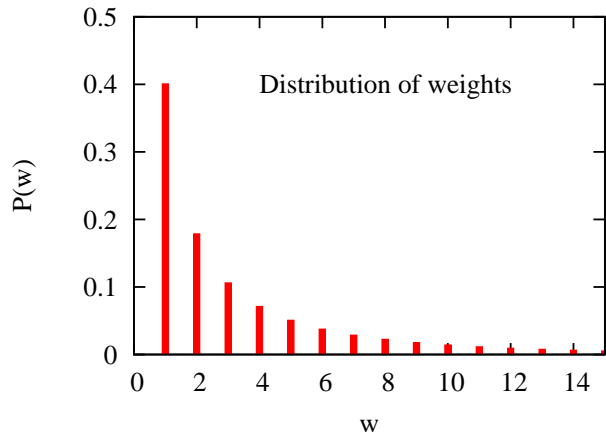


FIG. 5. (Color online) Probability distribution of the energy of a single source, corresponding to Eq. (31) with  $p = 0.892$ .

For simplicity again, we assume that  $w$  is an integer, so that it represents a multiplicity rather than an energy. The probability distribution  $P(w)$  used in our calculations is displayed in Fig. 5. It is chosen in such a way that the total multiplicity  $\sum_{i=1}^N w_i$  follows a negative binomial distribution, in line with observations in high-energy physics experiments [33, 34]. As shown in Appendix F, this is satisfied if each  $w_i$  follows a logarithmic distribution:

$$P(w) = -\frac{1}{\ln(1-p)} \frac{p^w}{w}. \quad (31)$$

This distribution depends on a single parameter  $p$ , which lies between 0 and 1. The limit  $p \rightarrow 0$  corresponds to identical sources,  $w = 1$ . The larger  $p$ , the wider the distribution. Throughout this paper, we use the value  $p = 0.892$  corresponding to multiplicity fluctuations at LHC energies [35]. With this distribution, Eq. (30) gives

$$N_{\text{eff}} = -\frac{p}{\ln(1-p)} \langle N \rangle. \quad (32)$$

With the chosen value of  $p$ ,  $N_{\text{eff}} \approx 0.4 \langle N \rangle$ . When weights are taken into account, Eq. (27) is replaced with (F5). These equations show that  $N_{\text{eff}}$  reflects incompletely the fluctuations of the density: in particular, for a given  $N_{\text{eff}}$ , the non-Gaussian contractions  $b$  and  $c$  increase with  $p$ , because cumulants increase rapidly with order. Inserting Eqs. (F5) into Eqs. (24) and (26), one obtains for a

Gaussian density profile:

$$\begin{aligned}\varepsilon_2\{2\}^2 &= \frac{2}{N_{\text{eff}}} - \frac{12p}{N_{\text{eff}}^2} + \mathcal{O}\left(\frac{1}{N_{\text{eff}}^3}\right) \\ \varepsilon_2\{4\}^4 &= \frac{8(1-3p^2)}{N_{\text{eff}}^3} + \mathcal{O}\left(\frac{1}{N_{\text{eff}}^4}\right).\end{aligned}\quad (33)$$

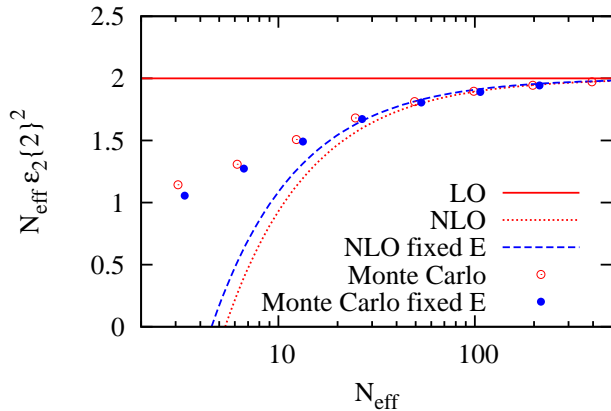


FIG. 6. (Color online)  $N_{\text{eff}}\varepsilon_2\{2\}^2$  versus  $N_{\text{eff}}$ . Symbols are results of Monte Carlo calculations, with (closed symbols) and without (open symbols) energy conservation. They are slightly shifted right and left, respectively, so that they do not overlap. The full line is the leading order perturbative result, the dotted and dashed lines are the next-to-leading perturbative results, with (Eq. (34)) and without (Eq. (33)) energy conservation.

Figure 6 displays Monte Carlo results for  $\varepsilon_2\{2\}$  together with the leading order and next-to-leading order perturbative results, Eq. (33). The convergence of the numerical results to the asymptotic result is slower than for identical sources (see Figs. 2 and 4). The large magnitude of the next-to-leading order correction and the fact that it overestimates the correction are signs that the perturbative expansion diverges for small values of  $N_{\text{eff}}$ .

Figure 7 displays our results for  $\varepsilon_2\{4\}^4$ . The perturbative result Eq. (33) is negative. On the other hand, Monte Carlo simulations return a positive  $\varepsilon_2\{4\}^4$  result for  $N_{\text{eff}}$  up to  $\sim 100$ , again showing that the convergence of the perturbative expansion is very slow. For values of  $N_{\text{eff}}$  smaller than 20, the universal scaling, Eq. (6), gives a rather accurate result, but becomes poorer as  $N_{\text{eff}}$  increases.

### C. Energy conservation

Finally, we study the combined effect of negative binomial fluctuations and energy conservation. In the Monte Carlo simulations, this is done by generating events with arbitrary energies and keeping only those which have the

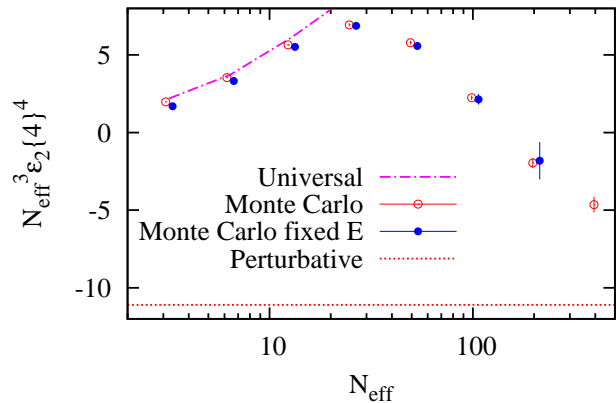


FIG. 7. (Color online)  $N_{\text{eff}}^3\varepsilon_2\{4\}^4$  versus  $N_{\text{eff}}$ . Symbols are results of Monte Carlo calculations, with (closed symbols) and without (open symbols) energy conservation. As in the previous figure, they are slightly shifted to the left or to the right. Dotted line: perturbative result (33). Dash-dotted line: Eq. (6), where  $\varepsilon_2\{2\}$  in the right-hand side is taken from the Monte Carlo simulation.

exact same energy<sup>4</sup>  $E = \sum_{i=1}^N w_i$ . This procedure is time consuming, in particular for large systems, which is the reason why our results with energy conservation, shown in Figs. 6 and 7, do not go as high in  $N_{\text{eff}}$  as results without energy conservation. Numerical results show that energy conservation has a very small effect for all  $N_{\text{eff}}$ . This was not a priori expected: we have seen indeed that, for identical sources, energy conservation decreases  $\varepsilon_2\{4\}^4$  by a factor 2 (see Fig. 4).

Energy conservation modifies the  $n$ -point functions of the density field  $\rho(z)$ , as shown in Appendix D. As a consequence, the values of  $a'$ ,  $b$ ,  $c$  are changed, and Eq. (23) is replaced with (D9). With logarithmic weights, energy conservation modifies Eq. (F5) into Eq. (F6), and the first of Eqs. (33) is replaced with

$$\varepsilon_2\{2\}^2 = \frac{2}{N_{\text{eff}}} - \frac{8p+2}{N_{\text{eff}}^2} + \mathcal{O}\left(\frac{1}{N_{\text{eff}}^3}\right).\quad (34)$$

The corresponding change is very modest, as can be seen in Fig. 6. Furthermore, it turns out that the recentering correction, discussed in Appendix E, cancels the effect of energy conservation for a Gaussian density profile, so that the full next-to-leading order expression with both energy conservation and recentering is again Eq. (33).

We have not derived the modification of  $\varepsilon_2\{4\}^4$  due to energy conservation: it involves the connected 4-point function, whose modifications due to energy conservation are more complicated. However, the results displayed

<sup>4</sup> In our case, the energy is an integer. We fix it to the integer closest to the mean energy.

in Fig. 7 suggest that this modification may be of little relevance in practice.

## VI. DISCUSSION

We have studied the non-Gaussianity of eccentricity fluctuation by means of Monte Carlo simulations and perturbative calculations. While all the numerical results shown in this paper are for  $\varepsilon_2$ , we have checked that conclusions also hold for the triangularity  $\varepsilon_3$ . We have generalized the perturbative calculation of Ref. [24] to an arbitrary energy density profile, under the sole assumption that density fluctuations at different points are uncorrelated.

When a perturbative expansion, which relies of the smallness of the local density fluctuations, is valid, we have obtained evidence that the non-Gaussianity of eccentricity fluctuations largely originates from the non-Gaussianity of density fluctuations. More specifically, the skewness and kurtosis of density fluctuations give positive and negative contributions to  $\varepsilon_n\{4\}^4$ , respectively. While the condition that the energy is positive naturally generates such non-Gaussianities, their magnitude is not universal but depends on the higher order cumulants of the density distribution. In particular, the sign of  $\varepsilon_n\{4\}^4$  is not universal, and can be negative in the presence of large (negative binomial) fluctuations of the multiplicity.

However, Monte Carlo simulations suggest that the convergence of the perturbative series can be very slow, and that results for a few hundred sources (corresponding to the number of participants in a central nucleus-nucleus collisions [26]) may vary significantly from the perturbative result. This makes it difficult to draw too definite conclusions from the present study. For small systems, on the other hand, we find that the universal statistics proposed in Ref. [20] is generally a good approximation. The observation that this universal statistics is also compatible with experimental results on elliptic flow in proton-nucleus collisions [21] therefore further supports the conclusion that elliptic flow in these systems originates from the initial eccentricity  $\varepsilon_2$ .

## ACKNOWLEDGEMENTS

This work is supported by the European Research Council under the Advanced Investigator Grant ERC-AD-267258.

### Appendix A: Cumulants and $n$ -point functions

In this Appendix we use functional methods to obtain the connected  $n$ -point functions and the cumulants  $\kappa_n(z)$  introduced in Sec. IV C. The generating functional of mo-

ments is defined as:

$$\mathcal{Z}\{j(z)\} \equiv \left\langle \exp \left( \int_z j(z)\rho(z) \right) \right\rangle. \quad (\text{A1})$$

The  $n$ -point functions, such as the 2-point function  $\langle \rho(z_1)\rho(z_2) \rangle$ , are obtained by differentiating  $\mathcal{Z}$  twice with respect to the auxiliary source  $j(z)$  and setting  $j$  to 0. *Connected*  $n$ -point functions are obtained by differentiating  $\ln \mathcal{Z}$ , e.g.:

$$\begin{aligned} \langle \rho(z_1)\rho(z_2) \rangle_c &= \langle \delta\rho(z_1)\delta\rho(z_2) \rangle \\ &= \frac{\delta^2 \ln \mathcal{Z}\{j(z)\}}{\delta j(z_1)\delta j(z_2)} \Big|_{j=0}. \end{aligned} \quad (\text{A2})$$

Assuming that density fluctuations at different points are uncorrelated entails that the contributions of different points to  $\mathcal{Z}\{j(z)\}$  factorize, therefore  $\ln \mathcal{Z}\{j(z)\}$  can be written as an integral over  $z$  of a function, which can itself be expanded in a power series

$$\ln \mathcal{Z}\{j(z)\} = \int_z \sum_{n=1}^{+\infty} \frac{j(z)^n}{n!} \kappa_n(z). \quad (\text{A3})$$

This equation provides a formal definition of the cumulants  $\kappa_n(z)$ . Successive differentiations of Eq. (A3) with respect to  $j(z)$  yield connected  $n$ -point functions. The 2-point function is Eq. (19). The connected 3-point and 4-point functions are given by:

$$\begin{aligned} \langle \rho(z_1)\rho(z_2)\rho(z_3) \rangle_c &= \langle \delta\rho(z_1)\delta\rho(z_2)\delta\rho(z_3) \rangle \\ &= \kappa_3(z_1)\delta(z_1 - z_2)\delta(z_1 - z_3), \end{aligned} \quad (\text{A4})$$

and

$$\begin{aligned} \langle \rho(1)\rho(2)\rho(3)\rho(4) \rangle_c &= \langle \delta\rho(1)\delta\rho(2)\delta\rho(3)\delta\rho(4) \rangle \\ &\quad - \langle \delta\rho(1)\delta\rho(2) \rangle \langle \delta\rho(3)\delta\rho(4) \rangle \\ &\quad - \langle \delta\rho(1)\delta\rho(3) \rangle \langle \delta\rho(2)\delta\rho(4) \rangle \\ &\quad - \langle \delta\rho(1)\delta\rho(4) \rangle \langle \delta\rho(2)\delta\rho(3) \rangle \\ &= \kappa_4(z_1)\delta_{12}\delta_{13}\delta_{14}, \end{aligned} \quad (\text{A5})$$

where  $\delta\rho(i)$  stands for  $\delta\rho(z_i)$ ,  $\delta_{12}$  for  $\delta(z_1 - z_2)$ , etc. The higher-order cumulants  $\kappa_3(z)$  and  $\kappa_4(z)$  express the non-Gaussian character of the initial energy density distribution.

Using Eq. (A5), 4-point averages can be decomposed as:

$$\begin{aligned} \langle \delta f \delta g \delta h \delta k \rangle &= \langle \delta f \delta g \rangle \langle \delta h \delta k \rangle \\ &\quad + \langle \delta f \delta h \rangle \langle \delta g \delta k \rangle \\ &\quad + \langle \delta f \delta k \rangle \langle \delta g \delta h \rangle \\ &\quad + \langle fghk \rangle_c, \end{aligned} \quad (\text{A6})$$

where the first three terms in the right-hand side, which are given by Wick's theorem, are of order  $1/N_{\text{eff}}^2$ , while the last term is a non-Gaussian correction, of order  $1/N_{\text{eff}}^3$ :

$$\langle fghk \rangle_c = \frac{1}{\langle E \rangle^4} \int_z f(z)g(z)h(z)k(z)\kappa_4(z). \quad (\text{A7})$$

Higher order  $n$ -point functions can be expanded using Wick's theorem in a similar way. In particular, the 5-point function gets contributions from 2 and 3 point functions.

$$\begin{aligned} \langle \delta f \delta g \delta h \delta k \delta l \rangle &= \langle \delta f \delta g \rangle \langle \delta h \delta k \delta l \rangle \\ &\quad + \text{permutations (10 terms)} \\ &\quad + \langle fghkl \rangle_c, \end{aligned} \quad (\text{A8})$$

where the various contractions are of order  $1/N_{\text{eff}}^3$ , while the connected part is of order  $1/N_{\text{eff}}^4$ .

## Appendix B: Cumulants of local sources

We derive here the expressions of the cumulants for identical, pointlike sources, starting with the case where each source has unit energy. Consider the distribution of energy  $E$  in an infinitesimal transverse area  $S$ . This area contains a source with probability  $\alpha \ll 1$ . The energy  $E$  in the area is 0 with probability  $1 - \alpha$  and 1 with probability  $\alpha$ , therefore

$$\langle e^{kE} \rangle = 1 - \alpha + \alpha e^k, \quad (\text{B1})$$

and the generating function of cumulants is simply

$$\ln \langle e^{kE} \rangle = \alpha (e^k - 1). \quad (\text{B2})$$

Using Eq. (17) and expanding to order  $k^n$ , one obtains

$$\kappa_n = \alpha. \quad (\text{B3})$$

All cumulants are equal and positive. If, in addition, locality is assumed, this result is generalized to an arbitrary area by dividing it into infinitesimal areas and using the fact that cumulants are additive.

We assume that the numbers of sources in two separate areas are independent variables. This in turn implies that the total number of sources  $N$  follows a Poisson distribution.

The independent source model can be generalized by allowing the energy of each source  $w$  to fluctuate with a probability  $P(w)$ . The previous results hold with the replacement of  $e^k$  with  $\langle e^{wk} \rangle$  in Eqs. (B1) and (B2), where brackets denote an average taken with respect to  $P(w)$ . Eq. (B3) is then replaced by

$$\kappa_n = \alpha \langle w^n \rangle. \quad (\text{B4})$$

Cumulants are no longer equal, but still positive.

## Appendix C: Identical sources

We derive the connected  $n$ -point functions of the density for the identical source model. We insert  $\rho(z)$  from Eq. (3) into the generating functional (A1):

$$\mathcal{Z} \{j(z)\} = \left\langle \prod_{i=1}^N \exp(j(z_i)) \right\rangle$$

$$= \sum_{N=0}^{+\infty} p_N \left( \int_z p(z) e^{j(z)} \right)^N, \quad (\text{C1})$$

where  $p_N$  is the probability of having  $N$  sources and  $p(z)$  is the probability distribution of a source in the transverse plane. We now study two versions of the independent source model: the case where  $N$  follows a Poisson distribution, and the case where  $N$  is fixed.

If  $N$  follows a Poisson distribution, then  $p_N = e^{-\langle N \rangle} \langle N \rangle^N / N!$ . By resumming the series in Eq. (C1), one obtains

$$\ln \mathcal{Z} \{j(z)\} = \langle N \rangle \left( \int_z p(z) e^{j(z)} - 1 \right). \quad (\text{C2})$$

This equation is of the type (A3) with  $\kappa_n(z) = \langle N \rangle p(z)$ . Connected  $n$ -point functions are therefore local, and cumulants  $\kappa_n(z)$  are all equal.

For fixed  $N$ , Eq. (C1) yields

$$\ln \mathcal{Z} \{j(z)\} \equiv N \ln \left( \int_z p(z) e^{j(z)} \right). \quad (\text{C3})$$

Thus the connected  $n$ -point functions to all orders are proportional to  $N$ . Successive differentiations with respect to  $j$  give:

$$\langle \rho(z) \rangle = N p(z) \quad (\text{C4})$$

and

$$\langle \delta \rho(z_1) \delta \rho(z_2) \rangle = N (p(z_1) \delta(z_1 - z_2) - p(z_1) p(z_2)). \quad (\text{C5})$$

The first term in the right-hand side of Eq. (C5) is a local correlation. The second term is a disconnected term: this term results from the constraint  $\sum_z \delta \rho(z) = 0$ : the integral over  $z$  of Eq. (C5) is 0.

The connected 3-point and 4-point functions are

$$\begin{aligned} \langle \delta \rho(z_1) \delta \rho(z_2) \delta \rho(z_3) \rangle &= N p(z_1) \delta(z_1 - z_2) \delta(z_1 - z_3) \\ &\quad - N p(z_1) p(z_2) \delta(z_2 - z_3) \\ &\quad - N p(z_2) p(z_3) \delta(z_3 - z_1) \\ &\quad - N p(z_3) p(z_1) \delta(z_1 - z_2) \\ &\quad + 2N p(z_1) p(z_2) p(z_3). \end{aligned} \quad (\text{C6})$$

and

$$\begin{aligned} \langle \rho(1) \rho(2) \rho(3) \rho(4) \rangle_c &= N p(1) \delta_{12} \delta_{13} \delta_{14} \\ &\quad - N (p(1) \delta_{12} \delta_{13} p(4) + \dots) \\ &\quad - N (p(1) \delta_{12} p(3) \delta_{34} + \dots) \\ &\quad + 2N (p(1) \delta_{12} p(3) p(4) + \dots) \\ &\quad - 6N p(1) p(2) p(3) p(4), \end{aligned} \quad (\text{C7})$$

where  $\delta \rho(i)$  stands for  $\delta \rho(z_i)$ , where  $\delta_{12}$  stands for  $\delta(z_1 - z_2)$ , etc., and where  $+\dots$  means that one should average over all permutations, which yield 4, 3 and 6 terms respectively for the 2nd, 3rd and 4th lines of Eq. (C7). The integral over  $z_1$  is zero because of energy conservation.

After inserting Eqs. (C5), (C6) and (C7) into the definitions of  $a$ ,  $a'$ ,  $b$  and  $c$ , Eq. (22), one finds that the condition that  $N$  is fixed modifies Eq. (27) into

$$\begin{aligned} a &= \frac{1}{\langle N \rangle} \frac{\langle r^{2n} \rangle}{\langle r^n \rangle^2} \\ a' &= \frac{1}{\langle N \rangle} \left( \frac{\langle r^{2n} \rangle}{\langle r^n \rangle^2} - 1 \right) \\ b &= \frac{1}{\langle N \rangle^2} \left( \frac{\langle r^{3n} \rangle}{\langle r^n \rangle^3} - \frac{\langle r^{2n} \rangle}{\langle r^n \rangle^2} \right) \\ c &= \frac{1}{\langle N \rangle^3} \left( \frac{\langle r^{4n} \rangle - 2\langle r^{2n} \rangle^2}{\langle r^n \rangle^4} \right). \end{aligned} \quad (\text{C8})$$

The first coefficient  $a$  is unchanged. The modifications of  $a'$  and  $b$  cancel in the combination  $-aa' + b$  entering the expression of  $\varepsilon_n\{4\}$ , Eq. (26). The modification of  $c$ , which produces the last term in Eq. (7), is due to the 3rd line of Eq. (C7).

#### Appendix D: Energy conservation

We now derive the expressions of connected  $n$ -point functions for an arbitrary density profile  $\rho(z)$  when the total energy is fixed. Similar results have been obtained for momentum conservation [38, 39]. We denote by  $\mathcal{Z}_E\{j(z)\}$  the generating function corresponding to a fixed energy  $E$ :

$$\mathcal{Z}_E\{j(z)\} \equiv \frac{\langle \exp(\int_z j(z)\rho(z)) \delta(E - \int_z \rho(z)) \rangle}{\langle \delta(E - \int_z \rho(z)) \rangle}. \quad (\text{D1})$$

It is normalized so that  $\mathcal{Z}_E\{j=0\} = 1$ . Using the integral representation of the Dirac distribution,  $\delta(x) = \frac{1}{2\pi} \int e^{-ikx} dk$ , one can express  $\mathcal{Z}_E$  in terms of  $\mathcal{Z}$  using Eq. (A1):

$$\mathcal{Z}_E\{j(z)\} = \frac{\int_{-\infty}^{+\infty} \exp(-ikE) \mathcal{Z}\{j(z) + ik\} dk}{\int_{-\infty}^{+\infty} \exp(-ikE) \mathcal{Z}\{ik\} dk}. \quad (\text{D2})$$

The integral over  $k$  in the numerator is evaluated using the saddle point method. The saddle point  $k_0$  is obtained by truncating the cumulant expansion Eq. (A3) to order 2, inserting it into (D2), and differentiating the exponent with respect to  $k$ :

$$ik_0 = \frac{E - \int_z \kappa_1(z) - \int_z j(z)\kappa_2(z)}{\int_z \kappa_2(z)}. \quad (\text{D3})$$

In the saddle point approximation, the integral in the numerator of Eq. (D2) is obtained by evaluating the integrand at  $k = k_0$ . One thus obtains

$$\begin{aligned} \ln \mathcal{Z}_E\{j(z)\} &= -ik_0 E + \int_z (j(z) + ik_0)\kappa_1(z) \\ &\quad + \frac{1}{2} \int_z (j(z) + ik_0)^2 \kappa_2(z), \end{aligned} \quad (\text{D4})$$

where we have left out the contribution of the denominator which is independent of  $j$ . The connected

$n$ -point functions are then obtained by differentiating  $\ln \mathcal{Z}_E\{j(z)\}$  at  $j = 0$ . The one-point function is the average value of the density:

$$\langle \rho(z_1) \rangle = \kappa_1(z_1) + \frac{E - \int_z \kappa_1(z)}{\int_z \kappa_2(z)} \kappa_2(z_1). \quad (\text{D5})$$

The first term in the right-hand side of Eq. (D5) is the average value of  $\rho(z)$  in the absence of energy conservation, while the second term is the correction due to energy conservation. This equation means that the energy excess  $E - \int_z \kappa_1(z)$  is distributed in the transverse plane proportionally to the variance  $\kappa_2(z)$ .

The 2-point function (19) becomes:

$$\langle \delta\rho(z_1)\delta\rho(z_2) \rangle = \kappa_2(z_1)\delta(z_1 - z_2) - \frac{\kappa_2(z_1)\kappa_2(z_2)}{\int_z \kappa_2(z)}. \quad (\text{D6})$$

Note that it does not involve the value of  $E$ . One can check that the right-hand side vanishes upon integration over  $z_1$ , as expected from the condition of energy conservation which implies  $\int_z \delta\rho(z) = 0$ .

The connected 3-point function is obtained by expanding the generating functional  $\mathcal{Z}_E$  to first order in the higher-order cumulants  $\kappa_3$ . The only effect of energy conservation is to replace  $j(z)$  by  $j(z) + ik_0$ , or (since the constant term drops upon differentiation) through the substitution

$$j(z) \rightarrow j(z) - \frac{\int_{z'} j(z')\kappa_2(z')}{\int_{z'} \kappa_2(z')}. \quad (\text{D7})$$

Eq. (A4) becomes:

$$\begin{aligned} \langle \delta\rho(z_1)\delta\rho(z_2)\delta\rho(z_3) \rangle &= \kappa_3(z_1)\delta(z_1 - z_2)\delta(z_1 - z_3) \\ &\quad - \frac{\kappa_3(z_1)\delta(z_1 - z_2)\kappa_2(z_3) + \text{perm.}}{\int_z \kappa_2(z)} \\ &\quad + \frac{\kappa_3(z_1)\kappa_2(z_2)\kappa_2(z_3) + \text{perm.}}{(\int_z \kappa_2(z))^2} \\ &\quad - \frac{\int \kappa_3}{(\int \kappa_2)^3} \kappa_2(z_1)\kappa_2(z_2)\kappa_2(z_3) \end{aligned} \quad (\text{D8})$$

The second and third lines must be summed over circular permutations of  $z_1, z_2, z_3$ . One may again check that the right-hand side vanishes upon integration over  $z_1$ . Note that the three-point function involves cumulants of two different orders  $\kappa_2$  and  $\kappa_3$ , and that it is linear in  $\kappa_3$ . This linearity is due to the fact that we evaluate the non-Gaussianity to first (linear) order. In the case of identical sources, where  $\kappa_3(z) = \kappa_2(z)$ , one recovers Eq. (C6). Note that the 2-point function and 3-point functions do not involve  $E$ . The correlations are not changed by triggering on the tail of the distribution, that is, on ultracentral collisions.

Energy conservation modifies Eqs. (22) to

$$a = \frac{\int_z r^{2n} \kappa_2(z)}{(\int_z r^n \kappa_1(z))^2}$$

$$a' = \frac{\int_z r^{2n} \kappa_2(z)}{\left(\int_z r^n \kappa_1(z)\right)^2} - \frac{\left(\int_z r^n \kappa_2(z)\right)^2}{\left(\int_z r^n \kappa_1(z)\right)^2 \int_z \kappa_2(z)}$$

$$b = \frac{\int_z r^{3n} \kappa_3(z)}{\left(\int_z r^n \kappa_1(z)\right)^3} - \frac{\int_z r^{2n} \kappa_3(z) \int_z r^n \kappa_2(z)}{\left(\int_z r^n \kappa_1(z)\right)^3 \int_z \kappa_2(z)}, \quad (\text{D9})$$

Note that the expression of  $a$  is unchanged, so that the leading order anisotropy (25) is not affected by energy conservation. For identical sources, where  $\kappa_n(z)$  is independent of the order  $n$ , Eq. (D9) reduces to Eq. (C8). We have not derived the modified expression of  $c$ , which involves the connected 4-point function.

### Appendix E: Recentering correction

We discuss here the effect of the recentering correction on perturbative results. Our discussion is limited to  $\varepsilon_2$  for simplicity. The recentering correction arises from the requirement that the coordinate system be centered in every event. When one takes it into account, Eq. (13) is replaced by [25]

$$\varepsilon_2 = \frac{\delta z^2 - (\delta z)^2}{\langle r^2 \rangle} \left( 1 + \frac{\delta r^2}{\langle r^2 \rangle} - \frac{\delta z \delta \bar{z}}{\langle r^2 \rangle} \right)^{-1}. \quad (\text{E1})$$

In order to evaluate the moment  $\langle |\varepsilon_2|^2 \rangle$  to next-to-leading order in the fluctuations, as in Sec. IV D, we must keep all terms of order 3 and 4 in the fluctuations. The recentering correction introduces new nontrivial contractions, in addition to those defined in Eq. (22):

$$d \equiv \frac{\langle (\delta z)^2 (\delta \bar{z})^2 \rangle}{\langle r^2 \rangle^2} = \frac{2 \left( \int_z r^2 \kappa_2(z) \right)^2}{\langle E \rangle^2 \left( \int_z r^2 \kappa_1(z) \right)^2}$$

$$e \equiv \frac{\langle \delta z^2 \delta \bar{z}^2 \delta z \delta \bar{z} \rangle}{\langle r^2 \rangle^3} = \frac{\int_z r^4 \kappa_2(z) \int_z r^2 \kappa_2(z)}{\langle E \rangle \left( \int_z r^2 \kappa_1(z) \right)^3}$$

$$f \equiv \frac{\langle \delta z^2 (\delta \bar{z})^2 \rangle}{\langle r^2 \rangle^2} = \frac{\int_z r^4 \kappa_3(z)}{\langle E \rangle \left( \int_z r^2 \kappa_1(z) \right)^2}, \quad (\text{E2})$$

which are all of order  $1/N_{\text{eff}}^2$  according to the power counting of Sec. IV C. The first of Eqs. (24) becomes

$$\langle |\varepsilon_2|^2 \rangle = a - 2b + 3aa' + d + 2e - 2f. \quad (\text{E3})$$

Let us check the validity of these additional terms in the particular case of identical sources. For identical sources, all cumulants are equal and the energy  $E$  is just the number of sources  $N$ , therefore  $e = f$  and  $d = 2/\langle N \rangle^2$ . For a Gaussian density profile, the exact results are  $\langle |\varepsilon_2|^2 \rangle = 2/N$  with recentering and  $\langle |\varepsilon_2|^2 \rangle = 2/(N+1)$  without recentering. The recentering correction is therefore  $2/N - 2/(N+1) \simeq 2/N^2$ , in agreement with our perturbative estimate for large  $N$ .

We have checked that the recentering correction does not affect the result (26), i.e., it does contribute to  $\varepsilon_2\{4\}^4$  to order  $1/N^3$ .

### Appendix F: Logarithmic weights

In this section, we explain how to choose the weights, in an independent-source model, in such a way that the distribution of the total energy is a negative binomial. The negative binomial distribution is

$$P_{NBD}(w) = \binom{w+k-1}{w} p^w (1-p)^k, \quad (\text{F1})$$

where  $p$  and  $k$  are two parameters, with  $0 \leq p < 1$  and  $k > 0$ . If two variables  $w_1$  and  $w_2$  are both distributed according to  $P_{NBD}(w)$ , then the sum  $w_1 + w_2$  also follows a negative binomial distribution with the same  $p$  and  $k \rightarrow 2k$ . Thus  $p$  is an intensive quantity and  $k$  an extensive quantity. In limit of a small area, defined by  $k \rightarrow 0$ , Eq. (F1) reduces to

$$P_{NBD}(0) = 1 + k \ln(1-p)$$

$$P_{NBD}(w) = k \frac{p^w}{w} \text{ for } w \geq 1. \quad (\text{F2})$$

The probability of finding a source within the small area is defined as

$$\alpha \equiv 1 - P_{NBD}(0) = \sum_{w=1}^{+\infty} P_{NBD}(w) = -k \ln(1-p). \quad (\text{F3})$$

This equation gives  $k$  as a function of  $\alpha$ . Inserting into the second line of Eq. (F2), One obtains  $P_{NBD}(w) = \alpha P(w)$  for  $w \geq 1$ , where  $P(w)$  is the distribution of  $w$  for a single source, given by Eq. (31).

The moments of the distribution  $P(w)$  can be calculated analytically. One obtains

$$\frac{\langle w^2 \rangle}{\langle w \rangle^2} = \frac{-\ln(1-p)}{p}$$

$$\frac{\langle w^3 \rangle}{\langle w \rangle^3} = \left( \frac{-\ln(1-p)}{p} \right)^2 (1+p)$$

$$\frac{\langle w^4 \rangle}{\langle w \rangle^4} = \left( \frac{-\ln(1-p)}{p} \right)^3 (1+4p+p^2). \quad (\text{F4})$$

The cumulants of the energy density are proportional to the moments of  $w$  as shown in Appendix B:  $\kappa_n(z) = \langle N \rangle \langle w^n \rangle p(z)$ . Inserting the above expressions into Eq. (23), one obtains

$$a = a' = \frac{1}{N_{\text{eff}}} \frac{\langle r^{2n} \rangle}{\langle r^n \rangle^2}$$

$$b = \frac{(1+p)}{N_{\text{eff}}^2} \frac{\langle r^{3n} \rangle}{\langle r^n \rangle^3}$$

$$c = \frac{(1+4p+p^2)}{N_{\text{eff}}^3} \frac{\langle r^{4n} \rangle}{\langle r^n \rangle^4}, \quad (\text{F5})$$

where  $N_{\text{eff}}$  is defined by Eq. (32). Eqs. (F5) reduces to Eqs. (27) in the limit  $p \rightarrow 0$ , as expected. Inserting Eq. (F5) into Eqs. (24) and (26), one obtains Eq. (33).

With energy conservation taken into account, one uses Eq. (D9) instead of Eq. (23):

$$a = \frac{1}{N_{\text{eff}}} \frac{\langle r^{2n} \rangle}{\langle r^n \rangle^2}$$

$$\begin{aligned}
a' &= \frac{1}{N_{\text{eff}}} \left( \frac{\langle r^{2n} \rangle}{\langle r^n \rangle^2} - 1 \right) & e &= \frac{1}{N_{\text{eff}}^2} \frac{\langle r^4 \rangle}{\langle r^2 \rangle^2} \\
b &= \frac{(1+p)}{N_{\text{eff}}^2} \left( \frac{\langle r^{3n} \rangle}{\langle r^n \rangle^3} - \frac{\langle r^{2n} \rangle}{\langle r^n \rangle^2} \right). & f &= \frac{1+p}{N_{\text{eff}}^2} \frac{\langle r^4 \rangle}{\langle r^2 \rangle^2}.
\end{aligned} \tag{F6}$$

We finally consider the effect of the recentering correction. With logarithmic weights, Eqs. (E2) become

$$d = \frac{2}{N_{\text{eff}}^2}$$

Inserting Eqs. (F7) and (F6) into Eqs. (E3), one finds that the contribution to  $\varepsilon_2\{2\}^2$  from recentering exactly cancels the contribution from energy conservation for a Gaussian density profile.

- 
- [1] U. Heinz and R. Snellings, *Ann. Rev. Nucl. Part. Sci.* **63**, 123 (2013) [arXiv:1301.2826 [nucl-th]].
- [2] M. Luzum and H. Petersen, *J. Phys. G* **41**, 063102 (2014) [arXiv:1312.5503 [nucl-th]].
- [3] F. G. Gardim, J. Noronha-Hostler, M. Luzum and F. Grassi, *Phys. Rev. C* **91**, no. 3, 034902 (2015) [arXiv:1411.2574 [nucl-th]].
- [4] H. Niemi, G. S. Denicol, H. Holopainen and P. Huovinen, *Phys. Rev. C* **87**, no. 5, 054901 (2013) [arXiv:1212.1008 [nucl-th]].
- [5] F. G. Gardim, F. Grassi, M. Luzum and J. Y. Ollitrault, *Phys. Rev. C* **85**, 024908 (2012) [arXiv:1111.6538 [nucl-th]].
- [6] B. Alver *et al.* [PHOBOS Collaboration], *Phys. Rev. Lett.* **98**, 242302 (2007) [nucl-ex/0610037].
- [7] B. Alver and G. Roland, *Phys. Rev. C* **81**, 054905 (2010) Erratum: [*Phys. Rev. C* **82**, 039903 (2010)] [arXiv:1003.0194 [nucl-th]].
- [8] D. Teaney and L. Yan, *Phys. Rev. C* **83**, 064904 (2011) [arXiv:1010.1876 [nucl-th]].
- [9] G. Aad *et al.* [ATLAS Collaboration], *JHEP* **1311**, 183 (2013) [arXiv:1305.2942 [hep-ex]].
- [10] T. Renk and H. Niemi, *Phys. Rev. C* **89**, no. 6, 064907 (2014) [arXiv:1401.2069 [nucl-th]].
- [11] L. Yan, J. Y. Ollitrault and A. M. Poskanzer, *Phys. Lett. B* **742**, 290 (2015) [arXiv:1408.0921 [nucl-th]].
- [12] S. A. Voloshin, A. M. Poskanzer, A. Tang and G. Wang, *Phys. Lett. B* **659**, 537 (2008) [arXiv:0708.0800 [nucl-th]].
- [13] J. P. Blaizot, W. Broniowski and J. Y. Ollitrault, *Phys. Lett. B* **738**, 166 (2014) [arXiv:1405.3572 [nucl-th]].
- [14] K. Aamodt *et al.* [ALICE Collaboration], *Phys. Rev. Lett.* **107**, 032301 (2011) [arXiv:1105.3865 [nucl-ex]].
- [15] S. Chatrchyan *et al.* [CMS Collaboration], *Phys. Rev. C* **89**, no. 4, 044906 (2014) [arXiv:1310.8651 [nucl-ex]].
- [16] R. S. Bhalerao, M. Luzum and J. Y. Ollitrault, *J. Phys. G* **38**, 124055 (2011) [arXiv:1106.4940 [nucl-ex]].
- [17] G. Aad *et al.* [ATLAS Collaboration], *Phys. Lett. B* **725**, 60 (2013) [arXiv:1303.2084 [hep-ex]].
- [18] S. Chatrchyan *et al.* [CMS Collaboration], *Phys. Lett. B* **724**, 213 (2013) [arXiv:1305.0609 [nucl-ex]].
- [19] P. Bozek and W. Broniowski, *Phys. Rev. C* **88**, no. 1, 014903 (2013) [arXiv:1304.3044 [nucl-th]].
- [20] L. Yan and J. Y. Ollitrault, *Phys. Rev. Lett.* **112**, 082301 (2014) [arXiv:1312.6555 [nucl-th]].
- [21] V. Khachatryan *et al.* [CMS Collaboration], *Phys. Rev. Lett.* **115**, no. 1, 012301 (2015) [arXiv:1502.05382 [nucl-ex]].
- [22] R. S. Bhalerao and J. Y. Ollitrault, *Phys. Lett. B* **641**, 260 (2006) [nucl-th/0607009].
- [23] S. Floerchinger and U. A. Wiedemann, *JHEP* **1408**, 005 (2014) [arXiv:1405.4393 [hep-ph]].
- [24] B. Alver *et al.*, *Phys. Rev. C* **77**, 014906 (2008) [arXiv:0711.3724 [nucl-ex]].
- [25] R. S. Bhalerao, M. Luzum and J. Y. Ollitrault, *Phys. Rev. C* **84**, 054901 (2011) [arXiv:1107.5485 [nucl-th]].
- [26] J. P. Blaizot, W. Broniowski and J. Y. Ollitrault, *Phys. Rev. C* **90**, no. 3, 034906 (2014) [arXiv:1405.3274 [nucl-th]].
- [27] Z. Qiu and U. W. Heinz, *Phys. Rev. C* **84**, 024911 (2011) [arXiv:1104.0650 [nucl-th]].
- [28] N. Borghini, P. M. Dinh and J. Y. Ollitrault, *Phys. Rev. C* **64**, 054901 (2001) [nucl-th/0105040].
- [29] M. Miller and R. Snellings, *nucl-ex/0312008*.
- [30] M. L. Miller, K. Reygers, S. J. Sanders and P. Steinberg, *Ann. Rev. Nucl. Part. Sci.* **57**, 205 (2007) [nucl-ex/0701025].
- [31] J. Y. Ollitrault, *Phys. Rev. D* **46**, 229 (1992).
- [32] B. Abelev *et al.* [ALICE Collaboration], *Phys. Rev. C* **88**, no. 4, 044909 (2013) [arXiv:1301.4361 [nucl-ex]].
- [33] A. Giovannini and L. Van Hove, *Z. Phys. C* **30**, 391 (1986).
- [34] F. Gelis, T. Lappi and L. McLerran, *Nucl. Phys. A* **828**, 149 (2009) [arXiv:0905.3234 [hep-ph]].
- [35] I. Kozlov, M. Luzum, G. Denicol, S. Jeon and C. Gale, arXiv:1405.3976 [nucl-th].
- [36] A. Dumitru and Y. Nara, *Phys. Rev. C* **85**, 034907 (2012) [arXiv:1201.6382 [nucl-th]].
- [37] B. Schenke, P. Tribedy and R. Venugopalan, *Phys. Rev. C* **86**, 034908 (2012) [arXiv:1206.6805 [hep-ph]].
- [38] N. Borghini, P. M. Dinh and J. Y. Ollitrault, *Phys. Rev. C* **62**, 034902 (2000) [nucl-th/0004026].
- [39] N. Borghini, *Eur. Phys. J. C* **30**, 381 (2003) [hep-ph/0302139].

# Appendix E

## Third paper

# Hydrodynamical noise and Gubser flow

Li Yan<sup>\*</sup> and Hanna Grönqvist<sup>†</sup>

*Institut de Physique Théorique,  
Université Paris Saclay, CEA,  
CNRS, F-91191 Gif-sur-Yvette, France*

## Abstract

Hydrodynamical noise is introduced on top of Gubser's analytical solution to viscous hydrodynamics. With respect to the ultra-central collision events of Pb-Pb, p-Pb and p-p at the LHC energies, we solve the evolution of noisy fluid systems and calculate the radial flow velocity correlations. We show that the absolute amplitude of the hydrodynamical noise is determined by the multiplicity of the collision event. The evolution of azimuthal anisotropies, which is related to the generation of harmonic flow, receives finite enhancements from hydrodynamical noise. Although it is strongest in the p-p systems, the effect of hydrodynamical noise on flow harmonics is found to be negligible, especially in the ultra-central Pb-Pb collisions. For the short-range correlations, hydrodynamical noise contributes to the formation of a near-side peak on top of the correlation structure originated from initial state fluctuations. The shape of the peak is affected by the strength of hydrodynamical noise, whose height and width grow from the Pb-Pb system to the p-Pb and p-p systems.

arXiv:1511.07198v2 [nucl-th] 16 Mar 2016

---

<sup>\*</sup> [li.yan@cea.fr](mailto:li.yan@cea.fr)

<sup>†</sup> [hanna.gronqvist@cea.fr](mailto:hanna.gronqvist@cea.fr)

## I. INTRODUCTION

One of the recent focuses on relativistic heavy-ion collisions carried out at the Large Hadron Collider (LHC) and Relativistic Heavy-Ion Collider (RHIC) lies in small colliding systems, including p-p and p-Pb at the LHC [1–6], d-Au and  $^3\text{He-Au}$  at RHIC [7, 8]. Especially in the collision events with sufficiently high multiplicity, it has been noticed that observables related to multi-particle correlations are consistent with a medium collective expansion scenario [6, 9, 10]. Relativistic hydrodynamics is a natural candidate to simulate and investigate the collective expansion of a QCD medium, even in small colliding systems [11–17]. However, applying viscous hydrodynamics to small colliding systems is challenged by a couple of factors. First, the applicability of viscous hydrodynamics is constrained by the convergence of gradient expansion, which is normally quantified by Knudsen number  $\text{Kn}$ . In smaller systems, the smaller system size leads to a larger value of  $\text{Kn}$  and the applicability of hydrodynamics is deteriorated accordingly [18]. Second, although hydrodynamical noise was introduced long ago by Landau and Lifshitz [19, 20], and was recently generalized to relativistic systems by Kapusta, Müller and Stephanov [21], it is neglected in most of the present hydrodynamic simulations. Since hydrodynamical noise is generically associated with dissipations and expected to be more pronounced in small systems, its influence in the small colliding systems needs to be clarified. The purpose of this work is to quantitatively estimate the effects of thermal noise in Pb-Pb, p-Pb and p-p collisions at the LHC energies, in order to test the applicability of *noisy* and *viscous* hydrodynamics in these systems.

Instead of more explicit numerical simulations of hydrodynamics with thermal noise [22, 23], this work resorts to an analytical solution of viscous hydrodynamics given by Gubser and Yarom [24, 25], known as the Gubser flow. By doing so, the inclusion of thermal noise in hydrodynamics is simplified dramatically both theoretically and numerically. Although Gubser flow is not as realistic as being required for heavy-ion collisions, it mimics the expansion of a hot conformal medium after its thermalization. Therefore, as one preliminary work on hydrodynamical noise, we will restrict ourselves to the initial stage of heavy-ion collisions. We will not address hadronization and freeze-out.

This paper is organized as follows. The theoretical framework of viscous hydrodynamics and hydrodynamical noise is discussed on a general ground in Section II. In Section III we briefly review Gubser flow, then thermal noise is introduced into Gubser’s solution in Section IV in parallel to the case of 1+1D Bjorken flow [21]. In order to estimate the effects of hydrodynamical noise with respect to the Pb-Pb, p-Pb and p-p systems, we solve the noisy Gubser flow in Section V, with discussions in terms of formal solutions presented in Section VA and numerical simulations in Section VB. Summary and conclusions are given in Section VI.

## II. HYDRODYNAMICS AND HYDRODYNAMICAL FLUCTUATIONS

In this section and throughout this work, we work with a metric signature that is mostly positive  $(-, +, +, +)$ , thereby the flow velocity  $u^\mu$  is normalized as  $u^2 = -1$ , and the projection operator  $\Delta^{\mu\nu}$  is defined as  $\Delta^{\mu\nu} = u^\mu u^\nu + g^{\mu\nu}$ . Tensor indices within angular brackets are transverse, traceless and symmetric, while tensor indices inside parentheses are symmetric. Except being specified as in Section VA, we also use angular brackets around a quantity to denote ensemble average, which is defined as the average over simulation events with respect to the same initial condition.

The evolution of quark-gluon plasma in heavy-ion collisions can be well described by relativistic hydrodynamics, together with an equation of state (EOS) originated from lattice QCD. Neglecting baryon number conservation, hydrodynamics regarding heavy-ion collisions is formulated as the conservation of energy-momentum,

$$d_\mu T^{\mu\nu} = 0, \quad (2.1)$$

where we have taken  $d_\mu$  to indicate the covariant derivative and  $T^{\mu\nu}$  is the energy-momentum tensor. In the Landau frame,

$$T^{\mu\nu} = \epsilon u^\mu u^\nu + \mathcal{P} \Delta^{\mu\nu} + \Pi^{\mu\nu}, \quad (2.2)$$

with dissipative effects characterized by the stress tensor  $\Pi^{\mu\nu}$ . Viscous hydrodynamics generally takes a form of gradient expansion,

$$\Pi^{\mu\nu} = -\eta \sigma^{\mu\nu} - \zeta \Delta^{\mu\nu} \nabla \cdot u + O(\nabla^2), \quad (2.3)$$

where  $\sigma^{\mu\nu} = 2\nabla^{\langle\mu} u^{\nu\rangle}$  and  $\nabla^\mu \equiv \Delta^{\mu\nu} d_\nu$ .  $\Pi^{\mu\nu}$  has a determined form up to first order in the expansion, which is known as the Navier-Stokes hydrodynamics. Throughout this work we shall only consider conformal fluids with linear equation of state  $\epsilon = 3\mathcal{P}$ , while bulk viscous effects are ignored by taking bulk viscosity  $\zeta = 0$ . When applying hydrodynamics to heavy-ion collision,  $\Pi^{\mu\nu}$  in Eq. (2.3) can be practically treated as one dynamical quantity, and accordingly Eq. (2.3) is recognized as its equation of motion.

A standard way of introducing thermal noise in hydrodynamics was suggested by Landau and Lifshitz [19, 20] for the first order dissipative hydrodynamics, and extended to the framework of relativistic hydrodynamics by Kapusta, Müller and Stephanov [21]. If one associates for each thermodynamical quantity with a fluctuation term which characterizes thermal noise, e.g., temperature, energy density and pressure are expressed as (suffix ‘0’ indicates ensemble-averaged quantity.)

$$T(x) = T_0(x) + \delta T(x), \quad (2.4a)$$

$$\epsilon(x) = \epsilon_0(x) + \delta \epsilon(x), \quad (2.4b)$$

$$\mathcal{P}(x) = \mathcal{P}_0(x) + \delta \mathcal{P}(x), \quad (2.4c)$$

and so for each dynamical quantity in the fluid system,

$$u^\mu(x) = u_0^\mu(x) + \delta u^\mu(x), \quad (2.5a)$$

$$\Pi^{\mu\nu}(x) = \Pi_0^{\mu\nu}(x) + S^{\mu\nu}(x). \quad (2.5b)$$

Note that the hydrodynamical noise term  $S^{\mu\nu}$  is introduced with respect to  $\Pi^{\mu\nu}$ . One thus arrives at a new expression for the energy-momentum tensor,

$$T^{\mu\nu} = T_0^{\mu\nu} + \delta T^{\mu\nu}. \quad (2.6)$$

$T_0^{\mu\nu}$  in Eq. (2.6) indicates contributions from ensemble-averaged hydro quantities, while  $\delta T^{\mu\nu}$  is determined by thermal fluctuations. Apart from cases, such as those where phase transition plays an significant role in the system evolution (cf. [26]), which is beyond the scope of this work, thermal fluctuations are relatively small variables. Accordingly, one can treat thermal fluctuations perturbatively with respect to the background evolution  $d_\mu T_0^{\mu\nu} =$

0. To the first order in fluctuations, hydro equations of motion for fluctuations  $d_\mu \delta T^{\mu\nu} = 0$  are linearized and lead to

$$\delta w D u_\alpha + w \delta u^\mu d_\mu u_\alpha + (Dw + w \partial \cdot u) \delta u_\alpha + \nabla_\alpha \delta \mathcal{P} + w D \delta u_\alpha + d_\mu (\delta \Pi_\alpha^\mu + S_\alpha^\mu) = 0 \quad (2.7a)$$

$$D \delta \epsilon + \delta w \partial \cdot u + d_\mu (w \delta u^\mu) + w \delta u^\alpha D u_\alpha - u^\alpha d_\mu (\delta \Pi_\alpha^\mu + S_\alpha^\mu) = 0 \quad (2.7b)$$

where  $w = \epsilon + \mathcal{P}$  is the enthalpy density.  $\delta \Pi^{\mu\nu}$  in Eqs. (2.7) is a term induced by  $\delta T$  and  $\delta u^\mu$ . Without the hydrodynamical noise term  $S^{\mu\nu}$ , Eqs. (2.7) also describe the hydro evolution of initial state fluctuations to linear order. In Eqs. (2.7) and in the following, we ignore the suffix ‘0’ for the ensemble-averaged quantities for simplicity, when confusions do not arise.

When the system is in thermal equilibrium, two-point autocorrelations of these fluctuations in Eqs. (2.4) and  $\delta u^\mu$  are known to be local in space and time, with correlation strength constrained by thermodynamical variables in equilibrium [19, 20]. Autocorrelations of thermal quantities are related with each other through the equation of state. When the system is out-of-equilibrium and driven by hydrodynamics, especially when dissipation is taken into account, the autocorrelation of these fluctuations must be determined with respect to that of hydrodynamical noise  $S^{\mu\nu}$ , according to the fluctuation-dissipation theorem,

$$\langle S^{\mu\nu}(x_1) S^{\alpha\beta}(x_2) \rangle = (\gamma^{\mu\nu\alpha\beta} + \gamma^{\alpha\beta\mu\nu}) \delta^{(4)}(x_1 - x_2), \quad (2.8)$$

where the Onsager coefficient  $\gamma^{\mu\nu\alpha\beta}$  relates the symmetric tensor  $\nabla^{(\mu} u^{\nu)}/T$  to  $\Pi^{\mu\nu}$ ,

$$\Pi^{\mu\nu} = -\gamma^{\mu\nu\alpha\beta} \frac{\nabla_{(\alpha} u_{\beta)}}{T}. \quad (2.9)$$

In addition to the symmetry between pairs of indices  $(\mu\nu)$  and  $(\alpha\beta)$ , which is guaranteed by Onsager’s relation [20],  $\gamma^{\mu\nu\alpha\beta}$  is symmetric, traceless (with conformal EOS) and transverse in  $\mu$  and  $\nu$ , as well as in  $\alpha$  and  $\beta$ . It can be shown that for Navier-Stokes hydrodynamics  $\Pi^{\mu\nu} = -\eta \sigma^{\mu\nu}$  [21]<sup>1</sup>,

$$\gamma^{\mu\nu\alpha\beta} = 2T\eta \Delta^{\mu\nu\alpha\beta}, \quad (2.11)$$

with the tensor structure  $\Delta^{\mu\nu\alpha\beta}$  defined by projection operators,

$$\Delta^{\mu\nu\alpha\beta} = \frac{1}{2} [\Delta^{\mu\alpha} \Delta^{\nu\beta} + \Delta^{\mu\beta} \Delta^{\nu\alpha}] - \frac{1}{3} \Delta^{\mu\nu} \Delta^{\alpha\beta}. \quad (2.12)$$

The two-point auto-correlation determined by Eqs. (2.8) and (2.9) are characteristic only for the first order dissipative hydrodynamics, which represents white noise with correlation strength constrained by first order transport coefficients. When higher order viscous corrections are taken into account with respect to the causality, space-time dependence must be altered from a Dirac delta function and one accordingly obtains colored noise which depends also on higher order transport coefficients [27]. Although Navier-Stokes hydrodynamics suffers from causality problem, which contains superluminal modes corresponding to sufficiently large momentum. In this work, we shall only solve Navier-Stokes hydrodynamics with finite number of hydrodynamic modes, in a way that the issue of causality becomes less significant.

<sup>1</sup> Except the result shown in Eq. (2.11), when  $\zeta \neq 0$  there is an extra piece of  $\gamma_\zeta^{\mu\nu\alpha\beta}$ ,

$$\gamma_\zeta^{\mu\nu\alpha\beta} = 2T\zeta \Delta_\zeta^{\mu\nu\alpha\beta}, \quad (2.10)$$

where  $\Delta_\zeta^{\mu\nu\alpha\beta} = \frac{1}{2} \Delta^{\mu\nu} \Delta^{\alpha\beta}$  is factorized automatically in terms of the projection operator.

### III. GUBSER FLOW

In this section we briefly review some of the essential ingredients of Gubser flow, which are relevant to our present work. More details of Gubser's solution to relativistic hydrodynamics and discussions can be found in [24, 25].

Analytical solutions to viscous hydrodynamics can be achieved with respect to certain symmetry constraints, which allows one to recover the solution in a more general coordinate system by coordinate transformations. For instance, the well-known Bjorken flow relies on a Bjorken boost invariance regarding the space-time geometry in heavy-ion collisions, which is explicit if one writes the metric tensor in Milne coordinates (beam axis along  $z$ ),

$$ds^2 = -d\tau^2 + dx^2 + dy^2 + \tau^2 d\xi^2, \quad (3.1)$$

with

$$\tau = \sqrt{t^2 - z^2} \quad \text{and} \quad \xi = \frac{1}{2} \ln \frac{t+z}{t-z},$$

and one immediately finds the solution of flow velocity profile with  $u^\xi = 0$ , which then gives rise to  $v_z = z/t$  in the original space-time. Recently, Gubser and Yarom developed a new type of analytical solution by imposing rotational symmetry with respect to the beam axis [24, 25], in addition to Bjorken boost invariance. Starting from the Milne space-time Eq. (3.1), the manifold  $R^{3,1}$  is firstly transformed into  $dS_3 \times R$  via a Weyl rescaling. The following mapping,

$$\sinh \rho = -\frac{1 - q^2 \tau^2 + q^2 r^2}{2q\tau}, \quad (3.2)$$

$$\tan \theta = \frac{2qr}{1 + q^2 \tau^2 - q^2 r^2}, \quad (3.3)$$

further allows one to rewrite the metric tensor as

$$d\hat{s}^2 = -d\rho^2 + d\xi^2 + \cosh^2 \rho (d\theta^2 + \sin^2 \theta d\phi), \quad (3.4)$$

which manifests the symmetry  $SO(3) \times SO(1,1) \times \mathcal{Z}_2$ .  $\rho$  in Eq. (3.4) is interpreted as the de Sitter time.  $q$  in Eq. (3.2) is a parameter with dimension inverse of length, which characterizes the transverse size of the system. One can accordingly read off the profile of flow velocity from Eq. (3.4)

$$\hat{u}^\mu = (1, 0, 0, 0). \quad (3.5)$$

We follow the same notation in [25] that a 'hat' over a quantity indicates that the quantity is defined in the coordinate system Eq. (3.4). Although flow velocity profile in Eq. (3.5) describes a fluid cell at rest, there exists non-zero expansion rate due to the geometry,

$$\hat{\nabla} \cdot \hat{u} = 2 \tanh \rho, \quad (3.6)$$

which results in a diagonal shear tensor  $\sigma^{\mu\nu}$ ,

$$\hat{\sigma}^{\mu\nu} = \hat{P}^{\mu\nu} \frac{2}{3} \tanh \rho, \quad (3.7)$$

where  $\hat{P}^{\mu\nu}$  is a *traceless* projection operator which is identical to  $\hat{\Delta}^{\mu\nu}$  except for the  $\xi\xi$  component:  $\hat{P}^{\xi\xi} = -2\hat{\Delta}^{\xi\xi}$ . Simplification of hydro equations of motion is expected accordingly. And indeed the only non-trivial equation left from Eq. (2.1) is an equation of continuity,

$$D\hat{\epsilon} + (\hat{\epsilon} + \hat{\mathcal{P}})d_\mu\hat{u}^\mu + \nabla_{(\mu}\hat{u}_{\nu)}\hat{\Pi}^{\mu\nu} = 0, \quad (3.8)$$

which still requires solution with respect to the gradient expansion order by order. The analytical solution to Navier-Stokes hydrodynamics can be found for a conformal equation of state:  $\hat{\epsilon} = 3\hat{\mathcal{P}}$ . For instance, the energy density in the ‘hat’ system is [25]

$$\hat{\epsilon}(\rho) = (\cosh \rho)^{-\frac{8}{3}} \left[ \hat{T}_0 + \frac{1}{3}H_0F(\rho) \right]^4, \quad (3.9)$$

where  $F(\rho)$  is a function defined by the following integral

$$F(\rho) = \int_0^\rho dr (\cosh(r))^{\frac{2}{3}} \tanh^2(r), \quad (3.10)$$

and  $H_0$  is a constant proportional to  $\eta/s$  which parameterizes shear viscosity in the ‘hat’ coordinate system.  $\hat{T}_0$  is a dimensionless parameter constrained by the total multiplicity of the collision event, whose details will be given later in Section V regarding numerical simulations.

Once hydrodynamics is fully solved in the ‘hat’ coordinate system, quantities in the  $(\tau, x, y, \xi)$  system can be recovered via the following transformations,

$$\epsilon = \tau^{-4}\hat{\epsilon}, \quad (3.11a)$$

$$n = \tau^{-3}\hat{n}, \quad (3.11b)$$

$$u_\tau = \tau \left( \frac{\partial\rho}{\partial\tau}\hat{u}_\rho + \frac{\partial\theta}{\partial\tau}\hat{u}_\theta \right), \quad (3.11c)$$

$$u_\perp = \tau \left( \frac{\partial\rho}{\partial r}\hat{u}_\rho + \frac{\partial\theta}{\partial r}\hat{u}_\theta \right), \quad (3.11d)$$

$$u_{\phi_i} = \tau\hat{u}_{\phi_i}, \quad (3.11e)$$

$$u_\xi = \tau\hat{u}_\xi. \quad (3.11f)$$

It has been noticed that the gradient expansion breaks down in Gubser’s solution at early de Sitter times for Navier-Stokes hydrodynamics [25], and also at late de Sitter times if one investigates second order viscous hydrodynamics. Such constraints indicate initialization times at which the thermal system can be approximated by viscous hydrodynamics. Accordingly, regarding realistic systems in heavy-ion collisions, we shall avoid very early or late de Sitter times in our analysis.

#### IV. NOISY GUBSER FLOW

To a large extent, effects of hydrodynamical noise can be investigated analytically with respect to solvable hydro models, such as Bjorken flow in 1+1D and Gubser flow. The discussion on hydrodynamical noise with respect to Bjorken flow in 1+1D was given previously in [21], from which we generalize to the case of Gubser flow.

## A. Bjorken flow

Following the discussions in [21], for a 1+1D Bjorken's solution with respect to the Navier-Stokes hydrodynamics, the essential simplification is a factorization of the tensor structure of the two-point autocorrelation function in Eq. (2.11)

$$\Delta^{\mu\nu\alpha\beta} \propto P^{\mu\nu} P^{\alpha\beta}, \quad (4.1)$$

and one thus expects

$$S^{\mu\nu}(\tau, \xi) = w(\tau) f(\tau, \xi) P^{\mu\nu}, \quad (4.2)$$

where  $P^{\mu\nu}$  is the same tensor defined under Eq. (3.7), but now in the Milne space-time. Notice that we write the factorization in Eq. (4.2) in terms of the traceless projector  $P^{\mu\nu}$  instead of  $\Delta^{\mu\nu}$  [21], which differs by a factor of two in this particular case of Bjorken flow in 1+1D.<sup>2</sup> Generally, for a conformal fluid system,  $P^{\mu\nu}$  is preferred since  $\gamma^{\mu\nu\alpha\beta}$  is traceless in  $\mu$  and  $\nu$ . With dimension being saturated by the enthalpy density  $w(\tau)$  in Eq. (4.2) and tensor structure being represented by  $P^{\mu\nu}$ , hydrodynamical noise associated with shear viscous tensor is reduced to one unknown scalar function  $f(\tau, \xi)$ , which satisfies

$$\langle f(\tau_1, \xi_1) f(\tau_2, \xi_2) \rangle = \frac{2T(\tau_1)\eta(\tau_1)}{3A_{\perp}w^2(\tau_1)\tau_1} \delta(\tau_1 - \tau_2) \delta(\xi_1 - \xi_2). \quad (4.3)$$

$A_{\perp}$  characterizes transverse size of the system.

Noisy hydro equations of motion can be simplified with respect to the factorization. For later convenience, we expand the  $\xi$  dependence of a hydrodynamical variable into its conjugate  $k_{\xi}$ , through a Fourier transformation, e.g., temperature is

$$T(\tau, \xi) = \int \frac{dk_{\xi}}{2\pi} e^{ik_{\xi}\xi} \tilde{T}(\tau, k_{\xi}). \quad (4.4)$$

One finds that for each  $k_{\xi}$ -mode, Eqs. (2.7) can now be recast into a Langevin equation,

$$\tilde{\mathcal{V}}'(\rho, k_{\xi}) = -\tilde{\Gamma}(\rho, k_{\xi}) \tilde{\mathcal{V}}(\rho, k_{\xi}) + \tilde{\mathcal{K}}(\rho, k_{\xi}), \quad (4.5)$$

where prime indicates derivatives with respect to<sup>3</sup>  $\rho = \ln(\tau/\tau_0)$  and

$$\tilde{\mathcal{V}}(\rho) = \begin{pmatrix} \tilde{n}(\rho, k_{\xi}) \\ \tilde{\alpha}(\rho, k_{\xi}) \end{pmatrix}. \quad (4.6)$$

We follow the same notations as in [21], such that  $\tilde{n} = \int d\xi e^{ik_{\xi}\xi} \delta s/s$  stands for the relative fluctuations of entropy density, and  $\tilde{\alpha} = \int d\xi e^{ik_{\xi}\xi} \tau u^{\xi}$  the fluctuation of flow velocity along  $\xi$ .  $\tilde{\Gamma}$  is a  $2 \times 2$  matrix which is entirely determined by Bjorken's solution of hydrodynamics [21].  $\tilde{\mathcal{K}}$  incorporates  $k_{\xi}$ -mode of the random scalar function  $f(\tau, \xi)$ ,

$$\tilde{\mathcal{K}}(\rho) = \begin{pmatrix} -\tilde{f} \\ -ik_{\xi}\tilde{f} \end{pmatrix}. \quad (4.7)$$

<sup>2</sup> Since the bulk part is automatically factorized, one can simply restore the result in [21] for the  $\zeta \neq 0$  case with an extra term proportional to  $\Delta^{\alpha\beta}$

<sup>3</sup> We use the same notation  $\rho$ , which should be distinguished from the de Sitter time  $\rho$  used in the 'hat' coordinate system for Gubser flow.

It is interesting to note that the effect of thermal noise on  $\tilde{\alpha}$  vanishes for the  $k_\xi = 0$  mode.

Without transverse expansion, Bjorken flow in 1+1D is an oversimplified model regarding heavy-ion collisions. Nonetheless, it is worth analyzing, at least to a qualitative level, the effect of hydrodynamical noise. We start by rewriting Eq. (4.3) for each  $k_\xi$ -mode as,

$$\langle \tilde{f}(\tau_1, k_{\xi_1}) \tilde{f}(\tau_2, k_{\xi_2}) \rangle = \frac{\pi\nu}{A_\perp w(\tau_1)\tau_1} \delta(\tau_1 - \tau_2) \delta(k_{\xi_2} + k_{\xi_1}). \quad (4.8)$$

Despite the constant  $\nu$ , which is proportional to  $\eta/s$ ,

$$\nu = \frac{4\eta}{3s}$$

the amplitude of the autocorrelation is totally determined by the factor  $A_\perp w\tau$  in the denominator. Apparently one would expect a stronger effect of hydrodynamical noise in a system with smaller size, due to the appearance of  $A_\perp$ . However, with respect to heavy-ion collisions, parametrically one can write the factor as a whole as

$$A_\perp w(\tau)\tau \sim A_\perp \left( \frac{dE}{\tau d^2x_\perp d\xi} \right) \tau \sim \frac{dE_\perp}{dy}, \quad (4.9)$$

which is interpreted as the transverse energy deposited per rapidity, and is equivalent to the multiplicity production of one collision event. Eq. (4.8) thus demonstrates the fact that the strength of hydrodynamical noise is essentially controlled by the multiplicity, instead of transverse size of a colliding system.

## B. Gubser flow

Following the same strategy for Bjorken flow in the previous section, we generalize the discussion of hydrodynamical noise to the case of Gubser flow. Note that in the  $(\rho, \theta, \phi, \xi)$  coordinate system, flow velocity profile is essentially the same as a Bjorken's solution in 1+1D, except the fact that transverse expansion is now taken into account as well. Therefore, it is not surprising that the symmetry considered in Gubser flow leads to a similar factorization of the tensor structure in Eq. (2.11). Especially for Navier-Stokes hydrodynamics  $\hat{\Pi}^{\mu\nu} \propto \hat{P}^{\mu\nu}$ , one has

$$\hat{\Delta}^{\mu\nu\alpha\beta} \propto \hat{P}^{\mu\nu} \hat{P}^{\alpha\beta} \quad (4.10)$$

and thus the autocorrelation of hydrodynamical noise becomes

$$\langle \hat{S}^{\mu\nu}(\rho_1, \theta_1, \phi_1, \xi_1) \hat{S}^{\alpha\beta}(\rho_2, \theta_2, \phi_2, \xi_2) \rangle = \frac{\nu \hat{T} \hat{S} \hat{P}^{\mu\nu} \hat{P}^{\alpha\beta}}{2 \cosh^2 \rho_1 \sin \theta_1} \delta(\rho_1 - \rho_2) \delta(\theta_1 - \theta_2) \delta(\phi_1 - \phi_2) \delta(\xi_1 - \xi_2). \quad (4.11)$$

With the above factorization, we can accordingly write  $\hat{S}^{\mu\nu}$  in terms of  $\hat{P}^{\mu\nu}$ ,

$$\hat{S}^{\mu\nu}(\rho, \theta, \phi, \xi) = \hat{w}(\rho) \hat{f}(\rho, \theta, \phi, \xi) \hat{P}^{\mu\nu}, \quad (4.12)$$

so that the correlation function of hydrodynamical noise reduces to correlation of a dimensionless scalar function,

$$\langle \hat{f}(\rho_1, \theta_1, \phi_1, \xi_1) \hat{f}(\rho_2, \theta_2, \phi_2, \xi_2) \rangle = \frac{\nu}{2\hat{w} \cosh^2 \rho_1 \sin \theta_1} \delta(\rho_1 - \rho_2) \delta(\theta_1 - \theta_2) \delta(\phi_1 - \phi_2) \delta(\xi_1 - \xi_2). \quad (4.13)$$

Note that enthalpy density  $\hat{w}(\rho)$  is used to saturate conformal dimension, even though quantities in the ‘hat’ system are dimensionless by construction.

Accounting for the  $SO(3) \times SO(1, 1) \times \mathcal{Z}_2$ -symmetry of Gubser flow, the mode decomposition can be done with respect to spherical harmonics. In particular for the scalar function  $\hat{f}(\rho, \theta, \phi, \xi)$ , one has <sup>4</sup>

$$\hat{f}(\rho, \theta, \phi, \xi) = \sum_{l,m} \int \frac{dk_\xi}{2\pi} h_{lm}(\rho, k_\xi) Y_{lm}(\theta, \phi) e^{ik_\xi \xi}. \quad (4.14)$$

and the two-point autocorrelation of each mode can be correspondingly found as

$$\langle h_{l_1 m_1}(\rho_1, k_{\xi_1}) h_{l_2 m_2}(\rho_2, k_{\xi_2}) \rangle = \frac{\pi\nu}{\hat{w} \cosh^2 \rho_1} \delta(\rho_1 - \rho_2) \delta_{l_1 l_2} \delta_{m_1, -m_2} (-1)^{m_1} \delta(k_{\xi_1} + k_{\xi_2}). \quad (4.15)$$

A couple of comments are in order with respect to Eq. (4.15). First, it should be emphasized that hydrodynamical noise contains only scalar modes, as a direct consequence of the factorization Eq. (4.12). However, it is not generally true since the tensor structure of the hydrodynamical noise term can be more involved and leads to fluctuations in both vector and tensor modes. Second, one can parametrically estimate the effects of hydrodynamical noise in heavy-ion collisions, by examining the magnitude of correlation in Eq. (4.15), as we did previously in Section IV A for the Bjorken flow. The essential quantity that determines the strength of hydrodynamical noise is  $\hat{w}$  in the denominator, in addition to the constant parameter  $\nu$  which is proportional to  $\eta/s$ . In Gubser’s solution to hydrodynamics,  $\hat{w}$  relies solely on the parameter  $\hat{T}_0$ , which is determined by the total multiplicity, but *not system size*. Therefore, in accordance with what was noticed in Section IV A, although one usually expects the system size to play a significant role in the estimate of hydrodynamical noise, we conclude that the absolute effect of hydrodynamical noise in an expanding medium in heavy-ion collisions is dominated by *multiplicity*.

When decomposing fluctuations of hydro variables, scalar modes and vector modes must be considered with respect to spherical harmonics  $Y_{lm}$  and vector spherical harmonics  $\Phi_{lm}^i$  respectively. We expand the following independent fluctuation variables,

$$\delta\hat{T}(\rho, \theta, \phi, \xi) = \hat{T}(\rho) \sum_{l,m} \int \frac{dk_\xi}{2\pi} \delta_{lm}(\rho, k_\xi) Y_{lm}(\theta, \phi) e^{ik_\xi \xi}, \quad (4.16a)$$

$$\delta u_i(\rho, \theta, \phi, \xi) = \sum_{l,m} \int \frac{dk_\xi}{2\pi} [v_{lm}^s(\rho, k_\xi) \partial_i Y_{lm}(\theta, \phi) + v_{lm}^v(\rho, k_\xi) \Phi_{lm}^i(\theta, \phi)] e^{ik_\xi \xi}, \quad (4.16b)$$

$$\delta u_\xi(\rho, \theta, \phi, \xi) = \sum_{l,m} \int \frac{dk_\xi}{2\pi} v_{lm}^\xi(\rho, k_\xi) Y_{lm}(\theta, \phi) e^{ik_\xi \xi}, \quad (4.16c)$$

where  $i = \theta, \phi$  denotes orientations in the transverse plane. In terms of all the scalar modes ( $\delta_{lm}, v_{lm}^s, v_{lm}^\xi$ ) and vector modes  $v_{lm}^v$ , Eqs. (2.7) on top of Gubser flow take an identical form as in Eq. (4.5),

$$\tilde{\mathcal{V}}'_{lm}(\rho, k_\xi) = -\tilde{\Gamma}(l, m, \rho, k_\xi) \tilde{\mathcal{V}}_{lm}(\rho, k_\xi) + \tilde{\mathcal{K}}_{lm}(\rho, k_\xi), \quad (4.17)$$

<sup>4</sup> Our convention of spherical harmonics is

$$Y_{lm}(\theta, \phi) = \sqrt{\frac{2l+1}{4\pi} \frac{(l-m)!}{(l+m)!}} P_l^m(\cos(\theta)) e^{im\phi}.$$

with extra dependence on the transverse dimension captured by indices  $l$  and  $m$ . The prime in Eq. (4.17) indicates derivative with respect to  $\rho$ , and  $\tilde{\mathcal{V}}(\rho)$  is,

$$\tilde{\mathcal{V}}_{lm}(\rho, k_\xi) = \begin{pmatrix} \delta_{lm}(\rho, k_\xi) \\ v_{lm}^s(\rho, k_\xi) \\ v_{lm}^\xi(\rho, k_\xi) \\ v_{lm}^v(\rho, k_\xi) \end{pmatrix}. \quad (4.18)$$

We purposely assign the vector mode to be the fourth element in  $\tilde{\mathcal{V}}_{lm}$ .  $\tilde{\Gamma}(l, m, \rho, k_\xi)$  in Eq. (4.17) is a  $4 \times 4$  matrix with a rather complicated form, with its components given in [25].  $\tilde{\Gamma}$  is block-diagonalized, since vector modes and scalar modes are decoupled due to parity.  $\tilde{\mathcal{K}}_{lm}(\rho, k_\xi)$  depends on the scalar modes of hydrodynamical noise  $h_{lm}$ ,

$$\tilde{\mathcal{K}}_{lm}(\rho, k_\xi) = \begin{pmatrix} -\frac{2}{3} \tanh \rho h_{lm}(\rho, k_\xi) \\ \frac{2\hat{T}}{3\hat{T}'} \tanh \rho h_{lm}(\rho, k_\xi) \\ \frac{i4k_\xi \hat{T}}{\hat{T} + H_0 \tanh \rho} h_{lm}(\rho, k_\xi) \\ 0 \end{pmatrix}. \quad (4.19)$$

The last element in  $\tilde{\mathcal{K}}$  vanishes as it should, since hydrodynamical noise does not contribute to vector modes. Also, we notice that for the  $k_\xi = 0$  mode, the evolution of  $v_{lm}^\xi(\rho, 0)$  is insensitive to the hydrodynamical noise as well. Eq. (4.19) introduces two sources of instabilities, corresponding to the zeros of  $\hat{T}'$  and  $\hat{T} + H_0 \tanh \rho$ . As has been discussed thoroughly in [25], both sorts of instabilities have been noticed in the structure of the matrix  $\tilde{\Gamma}$  already in the case without hydrodynamical noise.

## V. SOLVING GUBSER FLOW WITH HYDRODYNAMICAL NOISE

Hydro equations of motion are coupled with the equation of state, which in general resorts to numerical solutions. When hydrodynamical noise is taken in account, in addition to the ensemble-averaged background flow, one also needs numerical simulations of stochastic equations [22, 28] regarding the random unknown tensor variables  $S^{\mu\nu}$ . However, with respect to a background Gubser flow, the tensor structure of hydrodynamical noise is well determined and has been discussed in the previous section, so that numerical simulations are largely simplified.

A general procedure of solving noisy hydrodynamics on top of Gubser flow comprises the following steps. First, one solves Eqs. (4.17) mode-by-mode, with initial conditions and parameters specified with respect to desired collision systems. Second, hydrodynamical variables, such as flow velocity and temperature, are obtained through mode summation as in Eqs. (4.16). Similar strategy has also been applied in analyses of perturbations on top of solvable hydro models [29–31]. To recover quantities in the original  $(\tau, r, \phi, \xi)$  coordinate system, one is additionally required to do a coordinate transformation according to Eqs. (3.2).

For each mode, although Eqs. (4.17) represent four-coupled equations, simplifications can be made as follows. First, as we emphasized before, the hydrodynamical evolution does not couple vector modes to scalar modes. Besides, hydrodynamical fluctuations do not contribute to vector modes. As a consequence, we shall not consider vector modes in our analysis. Second, we shall restrict ourselves to the case of  $k_\xi = 0$ . By doing so, the matrix

$\tilde{\Gamma}$  is further block-diagonalized in a way that equation of motion for  $v^\xi$  is decoupled. The third component of  $\tilde{\mathcal{K}}$  also vanishes when  $k_\xi = 0$ . Therefore, the only non-trivial equations of motion which receive extra contributions from hydrodynamical noise are the two coupled equations for the scalar modes  $\delta_{lm}$  and  $v_{lm}^s$ , with

$$\tilde{\Gamma}_{11} = \frac{H_0 \tanh^2 \rho}{3\hat{T}} \quad (5.1a)$$

$$\tilde{\Gamma}_{12} = \frac{l(l+1)\text{sech}^2 \rho [H_0 \tanh \rho - \hat{T}]}{3\hat{T}} \quad (5.1b)$$

$$\tilde{\Gamma}_{21} = \frac{2H_0 \tanh \rho}{H_0 \tanh \rho - 2\hat{T}} + 1 \quad (5.1c)$$

$$\tilde{\Gamma}_{22} = \frac{H_0 \hat{T} [-4(3l(l+1) - 10)\text{sech}^2 \rho - 16] + 6H_0^2 \tanh^3 \rho + 8\hat{T}^2 \tanh \rho}{6\hat{T} [H_0 \tanh \rho - 2\hat{T}]} \quad (5.1d)$$

Similar equations have been investigated in [31] without hydrodynamical noise. Note that all  $m$ -modes of the same index  $l$  evolve identically since there is no dependence on index  $m$  in the  $\tilde{\Gamma}$  matrix and  $\tilde{\mathcal{K}}$ .

### A. Formal solution

Before numerically solving Eqs. (4.17), we investigate qualitatively the behavior of hydrodynamical noise and its evolution. The following discussion is made ad hoc with respect to a background Gubser flow, but it can be applied to hydrodynamical noise on top of Bjorken flow as well. One can write a formal solution of Eq. (4.17) (and similarly Eq. (4.5)) in terms of a Green function,

$$\tilde{\mathcal{V}}(\rho, K) = \int_{\rho_0}^{\rho} d\rho' \tilde{\mathcal{G}}(\rho - \rho', K) \tilde{\mathcal{K}}(\rho', K) + \tilde{\mathcal{G}}(\rho - \rho_0, K) \tilde{\mathcal{V}}(\rho_0, K), \quad (5.2)$$

where  $K$  is an abbreviated notation for the conjugate variables to specify modes, i.e.,  $K = (l, m, k_\xi)$  for Gubser flow and  $K = k_\xi$  for Bjorken flow. Green function  $\tilde{\mathcal{G}}$  is determined by the following equation (note that we take  $\rho = \ln(\tau_0/\tau)$  for Bjorken flow)

$$\partial_\rho \tilde{\mathcal{G}}(\rho - \rho', K) = -\tilde{\Gamma}(\rho, K) \tilde{\mathcal{G}}(\rho - \rho', K), \quad (5.3)$$

with the initial condition

$$\tilde{\mathcal{G}}(0, K) = 1. \quad (5.4)$$

The solution of Eq. (5.3) is

$$\tilde{\mathcal{G}}(\rho - \rho', K) = \mathcal{T} \exp \left[ - \int_{\rho'}^{\rho} d\rho'' \tilde{\Gamma}(\rho'', K) \right], \quad (5.5)$$

where  $\mathcal{T}$  indicates a time ordering with respect to  $\rho$ . Except in some extreme limits, there is no simple analytical expression for the Green function  $\tilde{\mathcal{G}}$ , regarding a specified form of  $\tilde{\Gamma}$  from hydrodynamics. However, some of the behaviors of mode evolution are known qualitatively. For instance, it has been shown that viscosity damps mode evolution [25]. In particular, in the large  $l$  and small viscosity limit, one finds that  $\tilde{\mathcal{G}}(\Delta\rho) \sim \exp[-l^2 H_0 \Delta\rho]$ .

From Eq. (5.2), we notice that at any time, each mode comprises contributions from fluctuations in the initial state (the second term) and hydrodynamical noise (the first term). Especially, due to the fact that the ensemble average of one-point function of thermal fluctuations vanishes,

$$\langle \tilde{\mathcal{K}} \rangle = 0,$$

the mode evolution of the one-point function is governed by hydrodynamic response to initial state fluctuations. In heavy-ion collisions, initial state fluctuations are quantum fluctuations associated with the probability distribution of nucleons inside the colliding nucleus. Therefore, one would expect initial state fluctuations to be independent of ensemble average, and the one-point function evolution has a form of linear response

$$\langle \tilde{\mathcal{V}}(\rho, K) \rangle = \tilde{\mathcal{G}}(\rho - \rho_0, K) \langle \tilde{\mathcal{V}}(\rho_0, K) \rangle. \quad (5.6)$$

The effect of hydrodynamical noise can be investigated in terms of the evolution of two-point correlation function. The equal-time two-point correlation can be found according to Eq. (5.2)

$$\begin{aligned} \langle \tilde{\mathcal{V}}_i(\rho, K) \tilde{\mathcal{V}}_j(\rho, K') \rangle &= \int_{\rho_0}^{\rho} d\rho' \left( \tilde{\mathcal{G}}(\rho - \rho', K) \Lambda_{th}(\rho') \tilde{\mathcal{G}}^T(\rho - \rho', -K) \right)_{ij} \delta(K + K') \\ &+ \left( \tilde{\mathcal{G}}(\rho - \rho_0, K) \Lambda_{ini}(\rho_0, K, K') \tilde{\mathcal{G}}^T(\rho - \rho_0, K') \right)_{ij}, \end{aligned} \quad (5.7)$$

where subscript  $i$  indicates the  $i$ -th component of the fluctuation mode  $\tilde{\mathcal{V}}$ , and  $\delta(K + K')$  stands for

$$\delta_{l_1 l_2} \delta_{m_1, -m_2} (-1)^{m_1} \delta(k_{\xi_1} + k_{\xi_2}),$$

corresponding to the correlation of the white hydrodynamical noise on top of Gubser flow. In obtaining Eq. (5.7), we have extended the concept of ‘average’. We restrict ourselves to one specified centrality class with fixed total multiplicity, so that the average in Eq. (5.7) automatically contains average over collision events and ensemble average in each collision event,

$$\langle \dots \rangle = \frac{1}{N_{\text{collision event}}} \sum \left[ \langle \dots \rangle_{\text{ensemble}} \right]. \quad (5.8)$$

More explicitly, collision events are distinguished by their initial conditions, while ensemble events stick with the same initial condition but evolve with random hydrodynamical noise on an event-by-event basis. Therefore, we are allowed to drop the mixing between hydrodynamical noise  $\tilde{\mathcal{K}}$  at any time and initial state fluctuations  $\tilde{\mathcal{V}}(\rho_0, K)$  in the average, namely  $\langle \tilde{\mathcal{K}}(\rho, K) \tilde{\mathcal{V}}(\rho_0, K') \rangle = 0$ , which factorizes into the ensemble average of one-point function of hydrodynamical noise, and the two-point correlation in Eq. (5.7) is written again as a term from initial state fluctuations plus a term from hydrodynamical noise.

The structure of two-point autocorrelations of hydrodynamical noise is known locally in space-time, with the amplitude  $\Lambda_{th}$  fixed with respect to the form of  $\tilde{\mathcal{K}}$  given in Eq. (4.19) and the fluctuation-dissipation theorem in Eq. (4.15). Note that vector modes do not contribute. Two-point correlations of initial state fluctuations are determined by averaging over collision events, instead of ensemble average. We consider two extreme scenarios in this work. One is inspired by independent sources [32], from which two-point correlations of initial state fluctuations are expected to be local in the transverse plane, and all  $K$ -modes are initialized correspondingly with specified values. In the other scenario, we initialize with selected modes

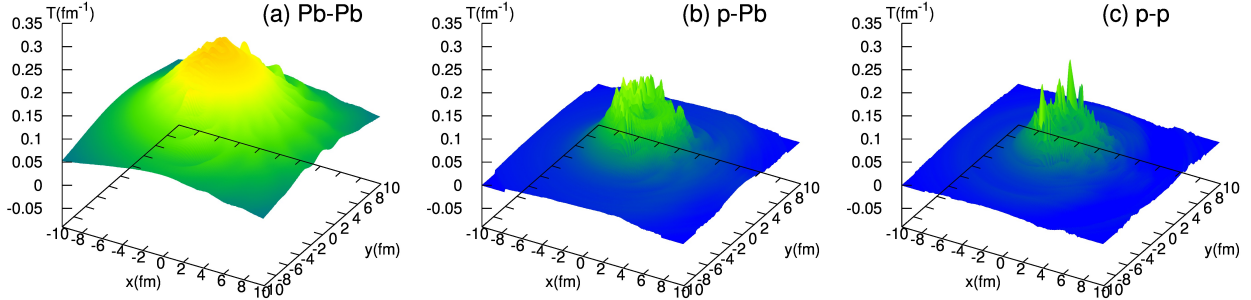


FIG. 1. (Color online) Snapshots of temperature evolution at  $\tau = 2.5$  fm of one random (a) Pb-Pb, (b) p-Pb and (c) p-p event, in units of  $\text{fm}^{-1}$ .

accounting for the  $SO(2)$  rotational symmetry in the transverse plane. Especially, we are allowed to deform initial energy density profile with a desired eccentricity. More details of these two types of initialization will be given later in the next section.

## B. Numerical simulations

We solve the two coupled equations of motion numerically on top of Gubser flow for the scalar modes  $\delta_l$  and  $v_l^s$ , with parameters  $\hat{T}_0$  and  $q$  specified with respect to ultra-central collision events of Pb-Pb, p-Pb and p-p at the LHC energies.  $\hat{T}_0$  is determined according to the event multiplicity. Following [24] and [31], we adopt the relation,

$$\hat{T}_0 = \frac{1}{f_*^{1/12}} \left( \frac{3}{16\pi} \frac{dS}{d\xi} \right)^{1/3}, \quad (5.9)$$

where the constant  $f_* = \epsilon/T^4 = 11$  is the effective degree of freedom extracted from Lattice QCD calculations, and

$$\frac{dS}{d\xi} = 7.5 \frac{dN_{ch}}{dy}. \quad (5.10)$$

$\hat{T}_0$  is found to be 7.3 for the 0~5% central PbPb collisions with  $\sqrt{s_{NN}} = 2.76$  TeV [31], corresponding to multiplicity production per rapidity  $dN_{ch}/dy \sim 1600$  [33]. For the p-Pb collisions with  $\sqrt{s_{NN}} = 5.02$  TeV [3], we take  $\hat{T}_0 = 3.1$  which leads to an estimate of  $dN_{ch}/dy \sim 150$ . Very recently, long-range correlations were measured in the ultra-central proton-proton collision events with multiplicity higher than 100 in the rapidity gap  $|y| < 2.4$  [1], for which we take  $\hat{T}_0 = 2.0$ . The parameter  $q$  constrains the finite transverse size of the fluid system. For a Pb-Pb system, we take  $q = (4.3\text{fm})^{-1}$  [24], while for both p-Pb and p-p systems we take  $q = (1.1\text{fm})^{-1}$ . In all the simulations in this work, the viscosity parameter is taken to be  $H_0 = 0.33$  [25], which corresponds to  $\eta/s = 0.134$ .

Fig. 1 displays the solved temperature distribution of one random Pb-Pb, p-Pb and p-p event at  $\tau = 2.5$  fm, without initial state fluctuations. Specifying  $\tau = 2.5$  fm for the analysis of all the three systems breaks conformal symmetry, which is however of phenomenological interest since  $\tau = 2.5$  fm is a typical time scale that all the three systems experience in the early stages of evolution. The effect of hydrodynamical noise is qualitatively captured by

the bumpiness of the temperature profile, which presents a clear trend of becoming more pronounced from the Pb-Pb system (Fig. 1(a)) to the p-p system (Fig. 1(c)). We have checked that when taking ensemble average, the bumpiness disappears in the temperature evolution, which corresponds to  $\langle \delta_l(\rho) \rangle = 0$ .

In order to quantify the effect of hydrodynamical noise, one must investigate two-point auto-correlations of hydrodynamical variables. For the sake of numerical simplicity, in this work we focus on the two-point auto-correlation of radial flow velocity  $u_r$  of the same  $\tau$  (equal time) and  $r$  (equal radius), which is determined by the equal-time two-point auto-correlations of modes  $\langle v_l^s(\rho)v_l^s(\rho) \rangle$ . We have checked that our conclusions are not changed from the analysis of other types of two-point auto-correlations, such as the auto-correlations of temperature fluctuations which depends on  $\langle \delta_l(\rho)\delta_l(\rho) \rangle$ . We thereby define the following correlation function that describes the two-point auto-correlation of radial flow velocity of the medium,

$$C_{u_r u_r}(\tau, \Delta\phi, r, \phi) = \langle u_r(\tau, r, \phi)u_r(\tau, r, \phi + \Delta\phi) \rangle - \langle u_{rb}(\tau, r)^2 \rangle. \quad (5.11)$$

Note that trivial contributions from the azimuthally symmetric background flow are subtracted in Eq. (5.11). One can further focus on the correlation structure with respect to the relative azimuthal angle  $\Delta\phi$  by integrating over  $r$  and  $\phi$ ,

$$\begin{aligned} C_{u_r u_r}(\tau, \Delta\phi) &= \int \frac{\tau r dr d\phi}{2\pi} \langle u_r(\tau, r, \phi)u_r(\tau, r, \phi + \Delta\phi) \rangle - \int \frac{\tau r dr d\phi}{2\pi} \langle u_{rb}(\tau, r)^2 \rangle \\ &= C_{u_r u_r}^T(\tau, \Delta\phi) + C_{u_r u_r}^I(\tau, \Delta\phi). \end{aligned} \quad (5.12)$$

The angular structure in Eq. (5.12) depends not only on the hydrodynamical noise, but also contains a fraction induced from initial state fluctuations, which we denote as  $C_{u_r u_r}^T$  and  $C_{u_r u_r}^I$  respectively. The significance of hydrodynamical noise in heavy-ion collisions is then captured by the relative contributions from  $C_{u_r u_r}^T$  and  $C_{u_r u_r}^I$ . Therefore, in our numerical results, we shall concentrate on the ratio between these two contributions,  $C^T/C^I$ .

It should be emphasized that the separation of two-point radial flow velocity auto-correlation into one term from initial state fluctuations and the other induced by hydrodynamical noise in Eq. (5.12) is one particular feature in our analysis, as has been demonstrated in the formal solution Eq. (5.7). In practical analysis, one is thus allowed to simulate the system evolution independently in cases with only initial state fluctuations, and in cases with only hydrodynamical fluctuations. However, in more involved studies where contributions to two-point correlations from initial state fluctuations and hydrodynamical fluctuations are not simply separable, one must carry out simulations with both sources of fluctuations considered simultaneously. In this work, we follow the conventional procedure of solving noisy hydro equations of motion, by initializing the system with initial state fluctuations in two extreme scenarios: One with a specified initial azimuthal anisotropy and the other with a Dirac delta function. By doing so, we claim that effects of hydrodynamical noise can be estimated with respect to the experimentally measured long-range and short-range correlation structures respectively.

### 1. Effects of hydrodynamical noise on long-range correlations

Long-range correlations of the observed spectra in heavy-ion collisions are associated with harmonic flow, which in turn depends on the evolution of azimuthal anisotropies of density

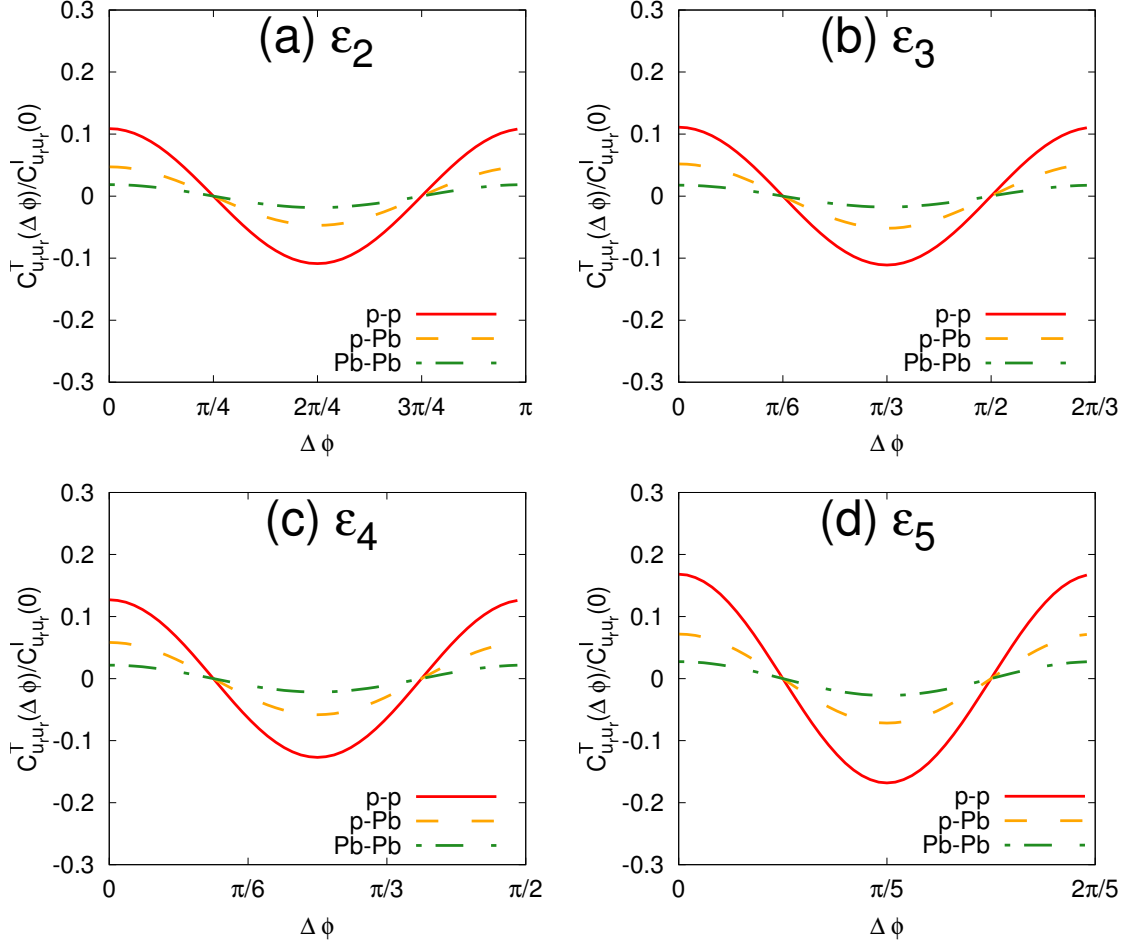


FIG. 2. (Color online) Structure of the radial flow velocity auto-correlation determined by hydrodynamical noise, depicted as the ratio between  $C_{u_r u_r}^T(\tau, \Delta\phi)$  and the magnitude of  $C_{u_r u_r}^I(\tau, \Delta\phi)$  (i.e, the absolute value of  $C_{u_r u_r}^I(\tau, \Delta\phi)$  at  $\Delta\phi = 0$ ) at  $\tau = 2.5$  fm. Results are obtained from numerical simulations of 10000 events with respect to initial condition Eq. (5.13) with an (a)  $\epsilon_2$ , (b)  $\epsilon_3$ , (c)  $\epsilon_4$  and (d)  $\epsilon_5$ , for p-p (red solid lines), p-Pb (orange dashed lines) and Pb-Pb (green dash-dotted lines) systems.

profile. For each harmonic order  $m$ , anisotropy is characterized by the so-called eccentricity  $\epsilon_m$  which represents an invariant deformation of the density profile under azimuthal rotation  $\phi \rightarrow \phi + 2\pi/m$ . Therefore, we perturb the azimuthally symmetric initial profile of Gubser flow by certain azimuthal modes. Following the discussions originated in [25], for each harmonic order  $m$ , when initial state fluctuations are characterized by the following non-zero modes <sup>5</sup>

$$\frac{\delta\hat{T}(\theta, \phi, \rho_0, \xi)}{\hat{T}(\rho_0)} = -\sqrt{\Lambda_{ini}} \left[ (-1)^m \frac{1}{\sqrt{2}} Y_{m,m}(\theta, \phi) + \frac{1}{\sqrt{2}} Y_{m,-m}(\theta, \phi) \right], \quad (5.13)$$

one accordingly realizes a density profile with a non-zero  $\epsilon_m$ . It should be emphasized that the eccentricity generated from Eq. (5.13) is closely related to the eccentricity defined in

<sup>5</sup> The  $(-1)^m$  factor in the brackets originates from our convention of spherical harmonics.

terms of cumulants with a  $r^m$  weighting [34], yet to an approximate level. More detailed analysis of Eq. (5.13) with respect to phenomenology can be found in [25]. The sign convention in Eq. (5.13) is taken so that the gradient of the deformed density is maximal along  $x$ -axis.  $\Lambda_{ini}$  in Eq. (5.13) reduces to a constant parameter to be fixed by the values of  $\varepsilon_m$  in the colliding systems. In our simulations with respect to the ultra-central Pb-Pb and p-Pb colliding systems, we take  $\varepsilon_2(\text{Pb-Pb}) \sim 0.05$  and  $\varepsilon_2(\text{p-Pb}) \sim 0.15$  at  $\tau = 0.6$  fm, which are typical values considered in phenomenological studies of heavy-ion collisions (cf. [35, 36]). For ultra-central p-p collisions, due to the smaller multiplicity production we take a larger value of initial anisotropy  $\varepsilon_2(\text{p-p}) \sim 0.2$ . We have checked that the same values of  $\Lambda_{ini}$  result in eccentricities of higher harmonics (up to  $\varepsilon_5$ ) of the similar order of magnitude in the corresponding systems.

For each of the particular deformations introduced in the initial state, we solve for the noisy Gubser flow and calculate the correlation function defined in Eq. (5.12). Since we are only interested in the effect of hydrodynamical noise on the long-range correlations, i.e., the evolution of azimuthal anisotropies, in the mode summation we ignore contributions from modes other than those of relevance to the corresponding initial anisotropies. For instance, if one calculates the evolution of ellipticity, to quantify Eq. (5.12) the mode summation only involves  $\langle (v_{2,2}^s(\rho))^2 \rangle$  and  $\langle (v_{2,-2}^s(\rho))^2 \rangle$ .

In Fig. 2, two-point auto-correlation  $C_{u_r u_r}^T(\tau, \Delta\phi)$  are plotted as a function of  $\Delta\phi$  at  $\tau = 2.5$  fm. Although the structure of  $C_{u_r u_r}^I(\Delta\phi)$  is not shown, it is worth mentioning that  $C_{u_r u_r}^I$  and  $C_{u_r u_r}^T$  share the same structures as a function of  $\Delta\phi$ , but are different in magnitudes. The periodic correlation structures shown in Fig. 2 are rooted in the azimuthal symmetries considered for each of these cases. For an initial  $\varepsilon_2$ ,  $\varepsilon_3$ ,  $\varepsilon_4$  and  $\varepsilon_5$ , correlations of radial flow velocity exhibit periodicity in  $\pi$ ,  $2\pi/3$ ,  $\pi/2$  and  $2\pi/5$  respectively. We take the ratio between  $C_{u_r u_r}^T$  and the magnitude of the correlation function  $C_{u_r u_r}^I$ , i.e.,  $C_{u_r u_r}^T(\tau, \Delta\phi)/C_{u_r u_r}^I(\tau, 0)$ , so that one is allowed to read off directly the relative change of anisotropies due to hydrodynamical noise in Fig. 2. As can be seen in Fig. 2, hydrodynamical noise results in extra contributions to the development of azimuthal anisotropies, which are getting stronger from the ultra-central Pb-Pb collision systems, to ultra-central p-Pb and p-p, and also from lower order harmonics to higher order harmonics. The increasing contribution from hydrodynamical noise according to harmonic order can be understood as follows: On one hand, hydrodynamical noise is insensitive to the harmonic order, which is subject to the independence of index  $m$  in the evolution equation (cf. Eqs. (5.1)). On the other hand, however, evolution of anisotropies of higher order harmonics suffers stronger viscous suppression. Accounting for both effects, one would expect that relatively hydrodynamical noise becomes more important for higher order harmonics. Nonetheless, the over-all magnitude of enhancement is not significant, in particular for the Pb-Pb systems in which it is less than 3%.

## 2. Effects of hydrodynamical noise on short-range correlations

For the analysis of short-range correlations, initial condition is chosen with temperature fluctuating in the transverse plane with respect to a Dirac delta function,

$$\frac{\delta\hat{T}(\rho_0, \theta, \phi, \xi)}{\hat{T}(\rho_0)} = \sqrt{\Lambda_{ini}} \times \frac{1}{\cosh \rho_0 \sin \theta} \delta(\theta - \theta_0) \delta(\phi - \phi_0). \quad (5.14)$$

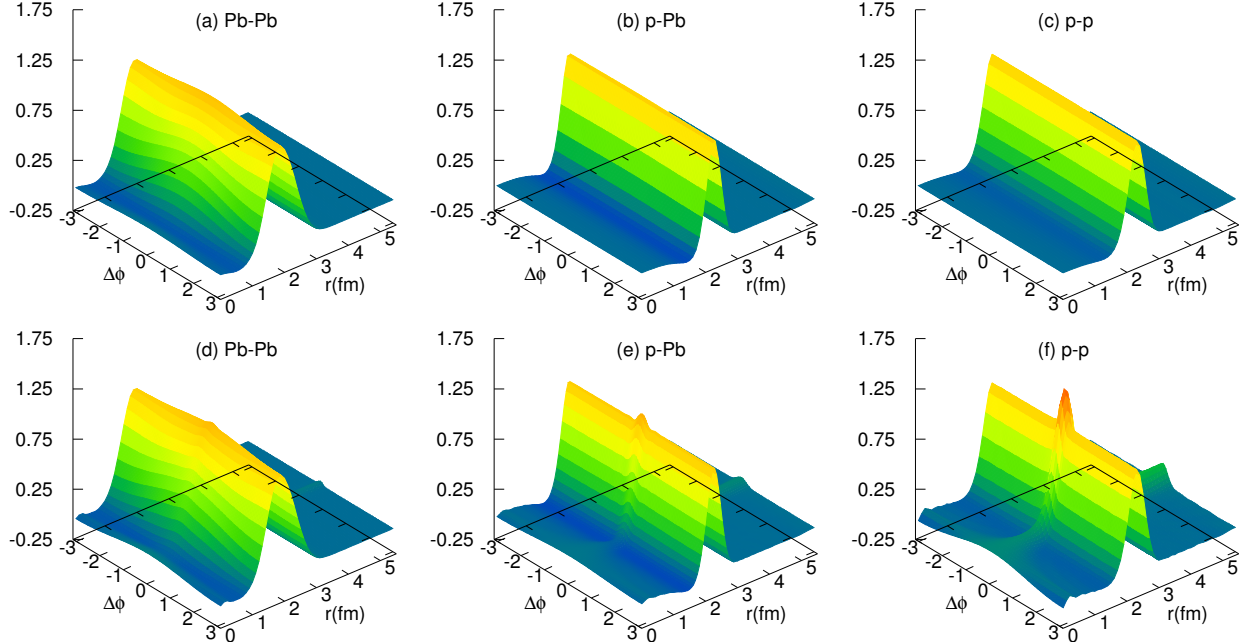


FIG. 3. (Color online) Two-point auto-correlations of radial flow velocity defined by only an integration over  $\phi$  in Eq. (5.11),  $C_{u_r u_r}(\tau, \Delta\phi, r)$ , as a function of  $r$  and  $\Delta\phi$ . Results are obtained with respect to initial condition Eq. (5.14) with  $\theta_0 = 0.2$  and  $\phi_0 = \pi$ , at  $\tau = 2.5$  fm, without hydrodynamical noise (upper row) and with hydrodynamical noise (lower row) from numerical simulations of 5000 events. To have all the three systems plotted on the same scale, magnitudes of the correlations are rescaled in a way that the height of the bump at  $|\Delta\phi| = \pi$  is equal to 1.

One may check that on an event-by-event basis, Eq. (5.14) is consistent with a Dirac delta in the transverse plane in the original Milne space-time.<sup>6</sup> The same values of  $\Lambda_{ini}$  fixed by eccentricities in the previous section are kept regarding the colliding systems under consideration. Without losing generality, we take  $\theta_0 = 0.2$  and  $\phi_0 = \pi$  throughout this work, which corresponds to a peak near the origin on the x-axis. Since higher  $l$ -modes receive stronger viscous suppression, our simulations are limited to the modes  $l < 30$ .

Fig. 3(a), (b) and (c) depict the corresponding results of the correlation function  $C_{u_r u_r}(\tau, r, \Delta\phi)$  (without  $r$  integration) in the ultra-central Pb-Pb, p-Pb and p-p colliding systems respectively without the inclusion of hydrodynamical noise, at  $\tau = 2.5$  fm. Regarding an initial density profile which is perturbed by a delta function, hydro evolution results in sound-wave propagation along with the medium expansion, which is exactly seen as a bump in the over-all structure of  $C_{u_r u_r}$ . To have the correlation functions plotted on the same scale, we have rescaled the height of the bump so that it is unity at  $|\Delta\phi| = \pi$ . This rescaling reveals a generic feature of Gubser's solution that the medium expands much faster in smaller systems p-Pb and p-p than in Pb-Pb, which however does not affect our analysis of the effect of hydrodynamical noise. The position of the sound horizon reflects hydro response to the position of the initial delta function. The shape of the bump is altered from a delta function by diffusion and dissipation. As one would expect, hydrodynamical noise affects the fine structure of the fluid system, which is then reflected as an excess around

<sup>6</sup> To see so, one must integrate over  $\theta_0$  and  $\phi_0$ , which is equivalent to average over collision events.

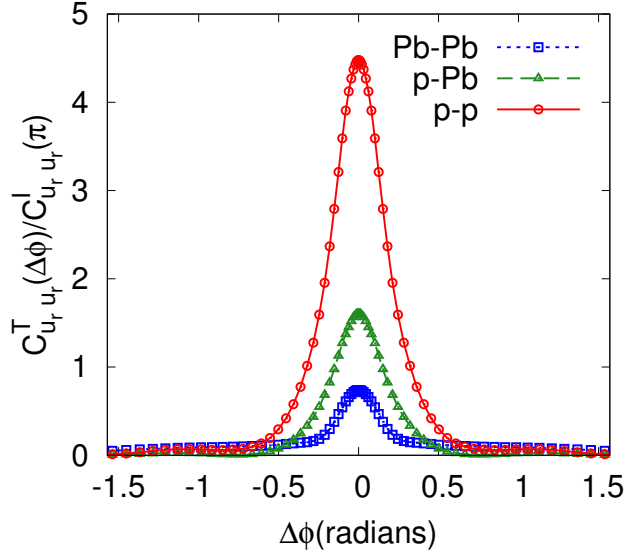


FIG. 4. (Color online) Details of the near-side peak in radial flow velocity correlations due to hydrodynamical noise, depicted in terms of the correlation function  $C_{u_r u_r}^T(\tau, \Delta\phi)$  divided by the magnitude of correlation due to initial fluctuation, i.e., value of  $C_{u_r u_r}^I(\tau, \Delta\phi)$  taken at  $|\Delta\phi| = \pi$ , with  $\tau = 2.5$  fm.

$\Delta\phi = 0$ . As seen in Fig. 3(d), (e) and (f), when hydrodynamical noise is considered in our simulations, an excess in the auto-correlation structure indeed appears at  $\Delta\phi = 0$  and persists from around origin ( $r = 0$ ) to large radii. Especially, on top of the bump structure the hydrodynamical noise leads to a near-side peak which is marginal in the Pb-Pb system as shown in Fig. 3(d), but becomes significant in p-p as shown in Fig. 3(f).

We next concentrate on the details of the near-side peak from the hydrodynamical noise in Fig. 3. To avoid overestimation of the effect of hydrodynamical noise, we limit the integration over  $r$  and  $\phi$  around the bump. Rescaled again by the magnitude of  $C_{u_r u_r}^I$  (now with  $\Delta\phi = \pi$ ), we obtain consequently the near-side peak in  $C_{u_r u_r}^T$  due to hydrodynamical noise relative to the correlation structure induced by initial state fluctuations. Results corresponding to the ultra-central Pb-Pb, p-Pb and p-p systems are shown in Fig. 4, which exhibit a clear trend in the three colliding systems. The height, as well as the width, of the peak increase from Pb-Pb, to p-Pb and p-p.

## VI. SUMMARY AND CONCLUSIONS

In this work we solved the noisy Gubser flow, by implementing hydrodynamical noise on top of Gubser's solution to Navier-Stokes hydrodynamics. Hydrodynamical noise is formulated in a standard way according to the fluctuation-dissipation relations, from which we noticed that the absolute amplitude of hydrodynamical noise in ultra-central heavy-ion collisions is essentially determined by the total multiplicity of the collision event, instead of the system size as one might have anticipated. Regarding the ultra-central Pb-Pb, p-Pb and p-p collisions carried out at the LHC energies, we quantitatively analyzed the effects of hydrodynamical noise with emphasis on long-range (evolution of azimuthal anisotropies) and short-range correlations. A clear trend of enhancement of the hydrodynamical noise

was confirmed in both cases from the Pb-Pb system, to p-Pb and p-p systems, which as we have claimed, is mostly due to the decrease of multiplicity, but not system size.

Azimuthal anisotropies receive extra contributions from the hydrodynamical noise during medium evolution, which implies an increase of harmonic flow  $v_n$ . In addition, higher order harmonics are found more sensitive to the hydrodynamical noise, which confirms the results from more sophisticated hydrodynamical simulations [23]. However, at least from our simulations for the conformal and azimuthally symmetric systems, the increase of anisotropies due to hydrodynamical noise is not significant. Especially, we expect that for the ultra-central Pb-Pb collision systems, the effect of hydrodynamical noise on harmonic flow  $v_n$  is negligibly small. On the contrary, short-range structure of the fluid system is more affected by the effect of hydrodynamical noise, which is demonstrated as the appearance of a near-side peak. It is understandable in the sense that higher order hydro modes, which correspond to the finer structure of a fluid system, are dominated by contributions from hydrodynamical noise, rather than hydro response to initial state fluctuations. We investigated in details the structure of the peak, relative to the short-range two-point flow velocity correlations induced by initial state fluctuations. We noticed that both the height and the width are enhanced when the effect of hydrodynamical noise becomes larger.

Bearing in mind that our analysis of the noisy Gubser flow is less realistic in several aspects, especially the caveat that we have no freeze-out process and there exists a gap between the two-point flow velocity correlation and the experimentally measured two-particle correlations, it is implied from our results that simulations of viscous hydrodynamics without hydrodynamical noise are reliable for the investigation of harmonic flow  $v_n$ , even in the smaller colliding systems like p-Pb. However, hydrodynamical noise must be taken into account if one studies the fine structure of the near-side two-particle correlations, which also contains informations related to the dissipative properties of the QCD medium.

## ACKNOWLEDGMENTS

We are grateful for many helpful discussions with Jean-Yves Ollitrault at different stages of this work. LY also thanks Derek Teaney and Clint Young for useful conversations. LY is funded by the European Research Council under the Advanced Investigator Grant ERC-AD-267258.

## Appendix A: Numerics

There exist several schemes for solving a stochastic differential equation numerically (cf. [37]), depending on appropriate interpretations of the stochastic integral with respect to noise. Rewriting Eqs. (4.17) as,

$$d\tilde{\mathcal{V}}(\rho) = -\tilde{\Gamma}(l, \rho)\tilde{\mathcal{V}}(\rho)d\rho + \tilde{\mathcal{K}}d\rho, \quad (\text{A1})$$

we notice that  $\tilde{\mathcal{K}}d\rho = dW_\rho$  represents an increment of Wiener process  $W_\rho$  which satisfies

$$W_{\rho_0} = 0, \quad \langle W_\rho \rangle = 0, \quad \langle (W_{\rho+\Delta\rho} - W_\rho)^2 \rangle = |\Delta\rho| \times \text{factor}. \quad (\text{A2})$$

The ‘factor’ in the above relations indicates that the correlation strength of the Wiener process is additionally determined by the amplitude of two-point autocorrelation of hydrodynamical noise in Eq. (4.15). Then for any time increase  $\Delta\rho$ , one needs to evaluate the

stochastic integral numerically, through the limit of Riemann sum,

$$\Delta W = \int_{\rho}^{\rho+\Delta\rho} \tilde{\mathcal{K}}(\rho') d\rho' = \lim_{n \rightarrow \infty} \sum_i^n \tilde{\mathcal{K}}(\bar{\rho}_i) \frac{\Delta\rho}{n}. \quad (\text{A3})$$

However, ambiguity arises when one takes  $\bar{\rho}_i = \rho + i\Delta\rho/n$  or  $\bar{\rho}_i = \rho + (i + 1/2)\Delta\rho/n$  in the sum, which corresponds to the Itô integral and the Stratonovich integral respectively. For multiplicative noise (when  $\tilde{\mathcal{K}}$  depends on  $\tilde{\mathcal{V}}$ ) these two integrals lead to different values, while for noise that is not multiplicative (when  $\tilde{\mathcal{K}}$  is independent of  $\tilde{\mathcal{V}}$ ) Itô and Stratonovich integrals coincide. Since hydrodynamical noise in our work is not multiplicative, recipes derived from either the Itô integral or the Stratonovich integral can be applied equivalently. Indeed, we have checked that the Euler-Maruyama method and the Heun's method discussed in Ref.[28] result in compatible solutions.

## Appendix B: Estimation of statistical error from ensemble average

The total number of events for the ensemble average is taken accounting for the convergence of ensemble average, as well as statistical errors of our numerical simulations. One can estimate statistical errors of ensemble averaged quantities from variance, which for the two-point correlations requires the knowledge of four-point correlations. For the hydrodynamical noise considered in the linear order, there are no generic four-point correlations despite the one from two-point auto-correlations. Therefore, the variance of any two-point correlation originated from the hydrodynamical noise is of the same order the two-point correlation itself. For instance, for the temperature modes which are completely induced by hydrodynamical noise, from Wick's theorem,

$$\langle(\delta_l)^4\rangle = 3\langle(\delta_l)^2\rangle^2, \quad (\text{B1})$$

one finds the variance

$$\text{Var}[\langle(\delta_l)^2\rangle] = \sqrt{2}\langle(\delta_l)^2\rangle, \quad (\text{B2})$$

and statistical error of  $\langle(\delta_l)^2\rangle$  is

$$\Delta\langle(\delta_l)^2\rangle = \frac{\sqrt{2}\langle(\delta_l)^2\rangle}{\sqrt{N_{\text{ensemble}}}}. \quad (\text{B3})$$

In this work, we take  $N_{\text{ensemble}} = 10000$  and  $5000$  for the investigation of long-range and short-range correlations respectively, such that relatively the statistical error of two-point correlations of hydrodynamical noise from our numerical simulations is less than 3%.

- 
- [1] CMS Collaboration (CMS), “Observation of long-range near-side two-particle correlations in pp collisions at  $\sqrt{s} = 13$  TeV,” (2015).
  - [2] Georges Aad *et al.* (ATLAS), “Observation of long-range elliptic anisotropies in  $\sqrt{s} = 13$  and 2.76 TeV  $pp$  collisions with the ATLAS detector,” (2015), [arXiv:1509.04776 \[hep-ex\]](#).
  - [3] Serguei Chatrchyan *et al.* (CMS Collaboration), “Multiplicity and transverse momentum dependence of two- and four-particle correlations in pPb and PbPb collisions,” *Phys.Lett.* **B724**, 213–240 (2013), [arXiv:1305.0609 \[nucl-ex\]](#).

- [4] Georges Aad *et al.* (ATLAS Collaboration), “Measurement of long-range pseudorapidity correlations and azimuthal harmonics in  $\sqrt{s_{NN}} = 5.02$  TeV proton-lead collisions with the ATLAS detector,” *Phys.Rev.* **C90**, 044906 (2014), [arXiv:1409.1792 \[hep-ex\]](#).
- [5] Serguei Chatrchyan *et al.* (CMS Collaboration), “Observation of long-range near-side angular correlations in proton-lead collisions at the LHC,” *Phys.Lett.* **B718**, 795–814 (2013), [arXiv:1210.5482 \[nucl-ex\]](#).
- [6] Vardan Khachatryan *et al.* (CMS), “Evidence for Collective Multiparticle Correlations in p-Pb Collisions,” *Phys. Rev. Lett.* **115**, 012301 (2015), [arXiv:1502.05382 \[nucl-ex\]](#).
- [7] Shengli Huang, “**Highlight of phenix results,**” (2014), talk at Initial Stages 2014.
- [8] A. Adare *et al.* (PHENIX Collaboration), “Quadrupole Anisotropy in Dihadron Azimuthal Correlations in Central  $d+Au$  Collisions at  $\sqrt{s_{NN}}=200$  GeV,” *Phys.Rev.Lett.* **111**, 212301 (2013), [arXiv:1303.1794 \[nucl-ex\]](#).
- [9] Adam Bzdak, Piotr Bozek, and Larry McLerran, “Fluctuation induced equality of multi-particle eccentricities for four or more particles,” *Nucl.Phys.* **A927**, 15–23 (2014), [arXiv:1311.7325 \[hep-ph\]](#).
- [10] Li Yan and Jean-Yves Ollitrault, “Universal fluctuation-driven eccentricities in proton-proton, proton-nucleus and nucleus-nucleus collisions,” *Phys.Rev.Lett.* **112**, 082301 (2014), [arXiv:1312.6555 \[nucl-th\]](#).
- [11] Igor Kozlov, Matthew Luzum, Gabriel Denicol, Sangyong Jeon, and Charles Gale, “Transverse momentum structure of pair correlations as a signature of collective behavior in small collision systems,” (2014), [arXiv:1405.3976 \[nucl-th\]](#).
- [12] Guang-You Qin and Berndt Mller, “Elliptic and triangular flow anisotropy in deuteron-gold collisions at  $\sqrt{s_{NN}} = 200$  GeV at RHIC and in proton-lead collisions at  $\sqrt{s_{NN}} = 5.02$  TeV at the LHC,” *Phys.Rev.* **C89**, 044902 (2014), [arXiv:1306.3439 \[nucl-th\]](#).
- [13] Piotr Bozek, “Collective flow in p-Pb and d-Pd collisions at TeV energies,” *Phys.Rev.* **C85**, 014911 (2012), [arXiv:1112.0915 \[hep-ph\]](#).
- [14] J.L. Nagle, A. Adare, S. Beckman, T. Koblesky, J. Orjuela Koop, *et al.*, “Exploiting Intrinsic Triangular Geometry in Relativistic He3+Au Collisions to Disentangle Medium Properties,” *Phys.Rev.Lett.* **113**, 112301 (2014), [arXiv:1312.4565 \[nucl-th\]](#).
- [15] Piotr Bozek and Wojciech Broniowski, “Collective dynamics in high-energy proton-nucleus collisions,” *Phys.Rev.* **C88**, 014903 (2013), [arXiv:1304.3044 \[nucl-th\]](#).
- [16] Piotr Bozek and Wojciech Broniowski, “Collective flow in ultrarelativistic  $^3\text{He}$ -Au collisions,” *Phys.Lett.* **B739**, 308–312 (2014), [arXiv:1409.2160 \[nucl-th\]](#).
- [17] Li Yan, “Plane correlations in small colliding systems,” *Phys. Rev.* **C91**, 064909 (2015), [arXiv:1503.00880 \[nucl-th\]](#).
- [18] H. Niemi and G. S. Denicol, “How large is the Knudsen number reached in fluid dynamical simulations of ultrarelativistic heavy ion collisions?” (2014), [arXiv:1404.7327 \[nucl-th\]](#).
- [19] D. Landau and E. Lifshitz, *Statistical Physics Part 1*, 2nd ed., Course of Theoretical Physics, Vol. 5 (Pergamon Press, 1987).
- [20] D. Landau and E. Lifshitz, *Statistical Physics Part 2*, 2nd ed., Course of Theoretical Physics, Vol. 6 (Pergamon Press, 1987).
- [21] J. I. Kapusta, B. Muller, and M. Stephanov, “Relativistic Theory of Hydrodynamic Fluctuations with Applications to Heavy Ion Collisions,” *Phys. Rev.* **C85**, 054906 (2012), [arXiv:1112.6405 \[nucl-th\]](#).
- [22] C. Young, J. I. Kapusta, C. Gale, S. Jeon, and B. Schenke, “Thermally Fluctuating Second-Order Viscous Hydrodynamics and Heavy-Ion Collisions,” *Phys. Rev.* **C91**, 044901 (2015),

- arXiv:1407.1077 [nucl-th].
- [23] K Murase and T Hirano, “Hydrodynamic fluctuations and dissipation in an integrated dynamical model,” (2015), quark Matter 2015, Kobe, Japan.
  - [24] Steven S. Gubser, “Symmetry constraints on generalizations of Bjorken flow,” *Phys.Rev.* **D82**, 085027 (2010), arXiv:1006.0006 [hep-th].
  - [25] Steven S. Gubser and Amos Yarom, “Conformal hydrodynamics in Minkowski and de Sitter spacetimes,” *Nucl.Phys.* **B846**, 469–511 (2011), arXiv:1012.1314 [hep-th].
  - [26] Misha A. Stephanov, K. Rajagopal, and Edward V. Shuryak, “Event-by-event fluctuations in heavy ion collisions and the QCD critical point,” *Phys. Rev.* **D60**, 114028 (1999), arXiv:hep-ph/9903292 [hep-ph].
  - [27] Koichi Murase and Tetsufumi Hirano, “Relativistic fluctuating hydrodynamics with memory functions and colored noises,” (2013), arXiv:1304.3243 [nucl-th].
  - [28] Clint Young, “Numerical integration of thermal noise in relativistic hydrodynamics,” *Phys. Rev.* **C89**, 024913 (2014), arXiv:1306.0472 [nucl-th].
  - [29] Stefan Floerchinger and Urs Achim Wiedemann, “Fluctuations around Bjorken Flow and the onset of turbulent phenomena,” *JHEP* **11**, 100 (2011), arXiv:1108.5535 [nucl-th].
  - [30] Nikolaos Brouzakis, Stefan Floerchinger, Nikolaos Tetradis, and Urs Achim Wiedemann, “Nonlinear evolution of density and flow perturbations on a Bjorken background,” *Phys. Rev.* **D91**, 065007 (2015), arXiv:1411.2912 [hep-ph].
  - [31] Pilar Staig and Edward Shuryak, “The Fate of the Initial State Fluctuations in Heavy Ion Collisions. II The Fluctuations and Sounds,” *Phys. Rev.* **C84**, 034908 (2011), arXiv:1008.3139 [nucl-th].
  - [32] Jean-Paul Blaizot, Wojciech Broniowski, and Jean-Yves Ollitrault, “Correlations in the Monte Carlo Glauber model,” *Phys. Rev.* **C90**, 034906 (2014), arXiv:1405.3274 [nucl-th].
  - [33] Kenneth Aamodt *et al.* (ALICE), “Centrality dependence of the charged-particle multiplicity density at mid-rapidity in Pb-Pb collisions at  $\sqrt{s_{NN}} = 2.76$  TeV,” *Phys. Rev. Lett.* **106**, 032301 (2011), arXiv:1012.1657 [nucl-ex].
  - [34] Derek Teaney and Li Yan, “Triangularity and Dipole Asymmetry in Heavy Ion Collisions,” *Phys. Rev.* **C83**, 064904 (2011), arXiv:1010.1876 [nucl-th].
  - [35] Matthew Luzum and Jean-Yves Ollitrault, “Extracting the shear viscosity of the quark-gluon plasma from flow in ultra-central heavy-ion collisions,” *Proceedings, 23rd International Conference on Ultrarelativistic Nucleus-Nucleus Collisions : Quark Matter 2012 (QM 2012)*, *Nucl. Phys.* **A904-905**, 377c–380c (2013), arXiv:1210.6010 [nucl-th].
  - [36] Adam Bzdak, Bjoern Schenke, Prithwish Tribedy, and Raju Venugopalan, “Initial state geometry and the role of hydrodynamics in proton-proton, proton-nucleus and deuteron-nucleus collisions,” *Phys. Rev.* **C87**, 064906 (2013), arXiv:1304.3403 [nucl-th].
  - [37] P. Kloeden and E. Platen, *Numerical Solutions of Stochastic Differential Equations*, 1st ed., Stochastic Modelling and Applied Probability, Vol. 23 (Springer-Verlag Berlin Heidelberg, 1992).

# Bibliography

- [1] F. Chavez and C. Duhr, *Three-mass triangle integrals and single-valued polylogarithms*, *JHEP* **1211** (2012) 114 [1209.2722].
- [2] S. Abreu, R. Britto, C. Duhr and E. Gardi, *From multiple unitarity cuts to the coproduct of Feynman integrals*, 1401.3546.
- [3] F. Gelis and B. Schenke, *Initial State Quantum Fluctuations in the Little Bang*, 1604.00335.
- [4] **ALICE** Collaboration, K. Aamodt *et. al.*, *Harmonic decomposition of two-particle angular correlations in Pb-Pb collisions at  $\sqrt{s_{NN}} = 2.76$  TeV*, *Phys. Lett.* **B708** (2012) 249–264 [1109.2501].
- [5] **CMS** Collaboration, S. Chatrchyan *et. al.*, *Centrality dependence of dihadron correlations and azimuthal anisotropy harmonics in PbPb collisions at  $\sqrt{s_{NN}} = 2.76$  TeV*, *Eur. Phys. J.* **C72** (2012) 2012 [1201.3158].
- [6] B. Schenke, P. Tribedy and R. Venugopalan, *Fluctuating Glasma initial conditions and flow in heavy ion collisions*, *Phys. Rev. Lett.* **108** (2012) 252301 [1202.6646].
- [7] H. Niemi, G. S. Denicol, H. Holopainen and P. Huovinen, *Event-by-event distributions of azimuthal asymmetries in ultrarelativistic heavy-ion collisions*, *Phys. Rev.* **C87** (2013), no. 5 054901 [1212.1008].
- [8] **ALICE** Collaboration, K. Aamodt *et. al.*, *Higher harmonic anisotropic flow measurements of charged particles in Pb-Pb collisions at  $\sqrt{s_{NN}}=2.76$  TeV*, *Phys. Rev. Lett.* **107** (2011) 032301 [1105.3865].
- [9] **CMS** Collaboration, S. Chatrchyan *et. al.*, *Multiplicity and transverse momentum dependence of two- and four-particle correlations in pPb and PbPb collisions*, *Phys. Lett.* **B724** (2013) 213–240 [1305.0609].

- [10] R. Snellings, *Elliptic Flow: A Brief Review*, *New J. Phys.* **13** (2011) 055008 [1102.3010].
- [11] B. Alver and G. Roland, *Collision geometry fluctuations and triangular flow in heavy-ion collisions*, *Phys. Rev.* **C81** (2010) 054905 [1003.0194].  
[Erratum: *Phys. Rev.*C82,039903(2010)].
- [12] S. S. Gubser and A. Yarom, *Conformal hydrodynamics in Minkowski and de Sitter spacetimes*, *Nucl. Phys.* **B846** (2011) 469–511 [1012.1314].
- [13] S. S. Gubser, *Symmetry constraints on generalizations of Bjorken flow*, *Phys. Rev.* **D82** (2010) 085027 [1006.0006].
- [14] P. Staig and E. Shuryak, *The Fate of the Initial State Fluctuations in Heavy Ion Collisions. II The Fluctuations and Sounds*, *Phys. Rev.* **C84** (2011) 034908 [1008.3139].
- [15] G. Passarino and M. J. G. Veltman, *One Loop Corrections for  $e^+ e^-$  Annihilation Into  $\mu^+ \mu^-$  in the Weinberg Model*, *Nucl. Phys.* **B160** (1979) 151.
- [16] C. Anastasiou, C. Duhr, F. Dulat, F. Herzog and B. Mistlberger, *Higgs Boson Gluon-Fusion Production in QCD at Three Loops*, *Phys. Rev. Lett.* **114** (2015) 212001 [1503.06056].
- [17] L. Landau, *On analytic properties of vertex parts in quantum field theory*, *Nucl.Phys.* **13** (1959) 181–192.
- [18] R. Cutkosky, *Singularities and discontinuities of Feynman amplitudes*, *J.Math.Phys.* **1** (1960) 429–433.
- [19] G. 't Hooft and M. Veltman, *DIAGRAMMAR*, *NATO Adv.Study Inst.Ser.B Phys.* **4** (1974) 177–322.
- [20] M. Veltman, *Diagrammatica: The Path to Feynman rules*, *Cambridge Lect.Notes Phys.* **4** (1994) 1–284.
- [21] E. Remiddi, *Dispersion Relations for Feynman Graphs*, *Helv.Phys.Acta* **54** (1982) 364.
- [22] Z. Bern, L. J. Dixon, D. C. Dunbar and D. A. Kosower, *One loop  $n$  point gauge theory amplitudes, unitarity and collinear limits*, *Nucl.Phys.* **B425** (1994) 217–260 [hep-ph/9403226].

- [23] Z. Bern, L. J. Dixon, D. C. Dunbar and D. A. Kosower, *Fusing gauge theory tree amplitudes into loop amplitudes*, *Nucl.Phys.* **B435** (1995) 59–101 [hep-ph/9409265].
- [24] R. Britto, F. Cachazo and B. Feng, *Generalized unitarity and one-loop amplitudes in  $N=4$  super-Yang-Mills*, *Nucl.Phys.* **B725** (2005) 275–305 [hep-th/0412103].
- [25] R. Britto, E. Buchbinder, F. Cachazo and B. Feng, *One-loop amplitudes of gluons in SQCD*, *Phys.Rev.* **D72** (2005) 065012 [hep-ph/0503132].
- [26] E. I. Buchbinder and F. Cachazo, *Two-loop amplitudes of gluons and octa-cuts in  $N=4$  super Yang-Mills*, *JHEP* **0511** (2005) 036 [hep-th/0506126].
- [27] P. Mastrolia, *On Triple-cut of scattering amplitudes*, *Phys.Lett.* **B644** (2007) 272–283 [hep-th/0611091].
- [28] C. Anastasiou, R. Britto, B. Feng, Z. Kunszt and P. Mastrolia, *D-dimensional unitarity cut method*, *Phys.Lett.* **B645** (2007) 213–216 [hep-ph/0609191].
- [29] D. Forde, *Direct extraction of one-loop integral coefficients*, *Phys.Rev.* **D75** (2007) 125019 [0704.1835].
- [30] E. Nigel Glover and C. Williams, *One-Loop Gluonic Amplitudes from Single Unitarity Cuts*, *JHEP* **0812** (2008) 067 [0810.2964].
- [31] P. Mastrolia, *Double-Cut of Scattering Amplitudes and Stokes' Theorem*, *Phys.Lett.* **B678** (2009) 246–249 [0905.2909].
- [32] S. Caron-Huot, *Loops and trees*, *JHEP* **1105** (2011) 080 [1007.3224].
- [33] D. A. Kosower and K. J. Larsen, *Maximal Unitarity at Two Loops*, *Phys.Rev.* **D85** (2012) 045017 [1108.1180].
- [34] H. Johansson, D. A. Kosower and K. J. Larsen, *Two-Loop Maximal Unitarity with External Masses*, *Phys.Rev.* **D87** (2013), no. 2 025030 [1208.1754].
- [35] M. Sogaard, *Global Residues and Two-Loop Hepta-Cuts*, *JHEP* **1309** (2013) 116 [1306.1496].
- [36] M. Sogaard and Y. Zhang, *Unitarity Cuts of Integrals with Doubled Propagators*, *JHEP* **1407** (2014) 112 [1403.2463].

- [37] M. Caffo, H. Czyz, S. Laporta and E. Remiddi, *The Master differential equations for the two loop sunrise selfmass amplitudes*, *Nuovo Cim.* **A111** (1998) 365–389 [[hep-th/9805118](#)].
- [38] S. Müller-Stach, S. Weinzierl and R. Zayadeh, *A Second-Order Differential Equation for the Two-Loop Sunrise Graph with Arbitrary Masses*, *Commun.Num.Theor.Phys.* **6** (2012) 203–222 [[1112.4360](#)].
- [39] L. Adams, C. Bogner and S. Weinzierl, *The two-loop sunrise graph with arbitrary masses*, [1302.7004](#).
- [40] S. Bloch and P. Vanhove, *The elliptic dilogarithm for the sunset graph*, [1309.5865](#).
- [41] E. Remiddi and L. Tancredi, *Schouten identities for Feynman graph amplitudes; the Master Integrals for the two-loop massive sunrise graph*, [1311.3342](#).
- [42] L. Adams, C. Bogner and S. Weinzierl, *The two-loop sunrise graph in two space-time dimensions with arbitrary masses in terms of elliptic dilogarithms*, *J.Math.Phys.* **55** (2014), no. 10 102301 [[1405.5640](#)].
- [43] A. B. Goncharov, *Multiple polylogarithms and mixed Tate motives*, [math/0103059](#).
- [44] A. Goncharov, *Galois symmetries of fundamental groupoids and noncommutative geometry*, *Duke Math.J.* **128** (2005) 209 [[math/0208144](#)].
- [45] A. B. Goncharov, M. Spradlin, C. Vergu and A. Volovich, *Classical Polylogarithms for Amplitudes and Wilson Loops*, *Phys.Rev.Lett.* **105** (2010) 151605 [[1006.5703](#)].
- [46] C. Duhr, *Hopf algebras, coproducts and symbols: an application to Higgs boson amplitudes*, *JHEP* **1208** (2012) 043 [[1203.0454](#)].
- [47] D. Gaiotto, J. Maldacena, A. Sever and P. Vieira, *Pulling the straps of polygons*, *JHEP* **1112** (2011) 011 [[1102.0062](#)].
- [48] R. Britto, “Introduction to scattering amplitudes.” Lectures given at the Institut de Physique Théorique, CEA, Saclay, France. URL: [http://ipht-i.cea.fr/Phocea-SPhT/ast\\_visu\\_spht.php?id\\_ast=604](http://ipht-i.cea.fr/Phocea-SPhT/ast_visu_spht.php?id_ast=604), 2011.

- [49] L. J. Dixon, *A brief introduction to modern amplitude methods*, 1310.5353.
- [50] C. Duhr, *Mathematical aspects of scattering amplitudes*, 1411.7538.
- [51] A. B. Goncharov, *Multiple polylogarithms, cyclotomy and modular complexes*, *Math.Res.Lett.* **5** (1998) 497–516 [1105.2076].
- [52] S. Abreu, *Cuts, discontinuities and the coproduct of Feynman integrals*. PhD thesis, The University of Edinburgh, 2015.
- [53] J. M. Henn, *Multiloop integrals in dimensional regularization made simple*, *Phys. Rev. Lett.* **110** (2013) 251601 [1304.1806].
- [54] J. M. Henn, A. V. Smirnov and V. A. Smirnov, *Analytic results for planar three-loop four-point integrals from a Knizhnik-Zamolodchikov equation*, *JHEP* **07** (2013) 128 [1306.2799].
- [55] J. M. Henn and V. A. Smirnov, *Analytic results for two-loop master integrals for Bhabha scattering I*, *JHEP* **11** (2013) 041 [1307.4083].
- [56] J. M. Henn, A. V. Smirnov and V. A. Smirnov, *Evaluating single-scale and/or non-planar diagrams by differential equations*, 1312.2588.
- [57] M. Argeri, S. Di Vita, P. Mastrolia, E. Mirabella, J. Schlenk *et. al.*, *Magnus and Dyson Series for Master Integrals*, 1401.2979.
- [58] S. Abreu, R. Britto and H. Grönqvist, *Cuts and coproducts of massive triangle diagrams*, *JHEP* **07** (2015) 111 [1504.00206].
- [59] R. Britto and E. Mirabella, *Single Cut Integration*, *JHEP* **01** (2011) 135 [1011.2344].
- [60] S. Abreu, “Personal notes on computing cut diagrams.” 2014.
- [61] C. Duhr, H. Gangl and J. R. Rhodes, *From polygons and symbols to polylogarithmic functions*, *JHEP* **1210** (2012) 075 [1110.0458].
- [62] **ALICE** Collaboration, M. Wilde, *Measurement of Direct Photons in pp and Pb-Pb Collisions with ALICE*, *Nucl. Phys.* **A904-905** (2013) 573c–576c [1210.5958].
- [63] R. J. Glauber, *Lectures in Theoretical Physics*. Interscience, New York, 1959. p. 315.

- [64] M. L. Miller, K. Reygers, S. J. Sanders and P. Steinberg, *Glauber modeling in high energy nuclear collisions*, *Ann. Rev. Nucl. Part. Sci.* **57** (2007) 205–243 [nucl-ex/0701025].
- [65] P. Shukla, *Glauber model for heavy ion collisions from low-energies to high-energies*, nucl-th/0112039.
- [66] P. Kovtun, D. T. Son and A. O. Starinets, *Viscosity in strongly interacting quantum field theories from black hole physics*, *Phys. Rev. Lett.* **94** (2005) 111601 [hep-th/0405231].
- [67] **BRAHMS** Collaboration, I. Arsene *et. al.*, *Quark gluon plasma and color glass condensate at RHIC? The Perspective from the BRAHMS experiment*, *Nucl. Phys.* **A757** (2005) 1–27 [nucl-ex/0410020].
- [68] **PHENIX** Collaboration, K. Adcox *et. al.*, *Formation of dense partonic matter in relativistic nucleus-nucleus collisions at RHIC: Experimental evaluation by the PHENIX collaboration*, *Nucl. Phys.* **A757** (2005) 184–283 [nucl-ex/0410003].
- [69] B. B. Back *et. al.*, *The PHOBOS perspective on discoveries at RHIC*, *Nucl. Phys.* **A757** (2005) 28–101 [nucl-ex/0410022].
- [70] **STAR** Collaboration, J. Adams *et. al.*, *Experimental and theoretical challenges in the search for the quark gluon plasma: The STAR Collaboration’s critical assessment of the evidence from RHIC collisions*, *Nucl. Phys.* **A757** (2005) 102–183 [nucl-ex/0501009].
- [71] D. Teaney and L. Yan, *Non linearities in the harmonic spectrum of heavy ion collisions with ideal and viscous hydrodynamics*, *Phys. Rev.* **C86** (2012) 044908 [1206.1905].
- [72] M. Luzum and H. Petersen, *Initial State Fluctuations and Final State Correlations in Relativistic Heavy-Ion Collisions*, *J. Phys.* **G41** (2014) 063102 [1312.5503].
- [73] J.-Y. Ollitrault, *Anisotropy as a signature of transverse collective flow*, *Phys. Rev.* **D46** (1992) 229–245.
- [74] **PHOBOS** Collaboration, B. Alver *et. al.*, *System size, energy, pseudorapidity, and centrality dependence of elliptic flow*, *Phys. Rev. Lett.* **98** (2007) 242302 [nucl-ex/0610037].

- [75] **WMAP** Collaboration, E. Komatsu *et. al.*, *Five-Year Wilkinson Microwave Anisotropy Probe (WMAP) Observations: Cosmological Interpretation*, *Astrophys. J. Suppl.* **180** (2009) 330–376 [0803.0547].
- [76] **CMS** Collaboration, V. Khachatryan *et. al.*, *Evidence for Collective Multiparticle Correlations in p-Pb Collisions*, *Phys. Rev. Lett.* **115** (2015), no. 1 012301 [1502.05382].
- [77] R. S. Bhalerao and J.-Y. Ollitrault, *Eccentricity fluctuations and elliptic flow at RHIC*, *Phys. Lett.* **B641** (2006) 260–264 [nucl-th/0607009].
- [78] R. Andrade, F. Grassi, Y. Hama, T. Kodama and O. Socolowski, Jr., *On the necessity to include event-by-event fluctuations in experimental evaluation of elliptical flow*, *Phys. Rev. Lett.* **97** (2006) 202302 [nucl-th/0608067].
- [79] **STAR** Collaboration, L. Adamczyk *et. al.*, *Third Harmonic Flow of Charged Particles in Au+Au Collisions at  $\sqrt{s_{NN}} = 200$  GeV*, *Phys. Rev.* **C88** (2013), no. 1 014904 [1301.2187].
- [80] **ATLAS** Collaboration, G. Aad *et. al.*, *Measurement of the azimuthal anisotropy for charged particle production in  $\sqrt{s_{NN}} = 2.76$  TeV lead-lead collisions with the ATLAS detector*, *Phys. Rev.* **C86** (2012) 014907 [1203.3087].
- [81] D. Teaney and L. Yan, *Triangularity and Dipole Asymmetry in Heavy Ion Collisions*, *Phys. Rev.* **C83** (2011) 064904 [1010.1876].
- [82] M. Luzum and J.-Y. Ollitrault, *Directed flow at midrapidity in heavy-ion collisions*, *Phys. Rev. Lett.* **106** (2011) 102301 [1011.6361].
- [83] E. Retinskaya, M. Luzum and J.-Y. Ollitrault, *Directed flow at midrapidity in  $\sqrt{s_{NN}} = 2.76$  TeV Pb+Pb collisions*, *Phys. Rev. Lett.* **108** (2012) 252302 [1203.0931].
- [84] S. A. Voloshin, A. M. Poskanzer, A. Tang and G. Wang, *Elliptic flow in the Gaussian model of eccentricity fluctuations*, *Phys. Lett.* **B659** (2008) 537–541 [0708.0800].
- [85] J.-P. Blaizot, W. Broniowski and J.-Y. Ollitrault, *Continuous description of fluctuating eccentricities*, *Phys. Lett.* **B738** (2014) 166–171 [1405.3572].

- [86] L. Yan and J.-Y. Ollitrault, *Universal fluctuation-driven eccentricities in proton-proton, proton-nucleus and nucleus-nucleus collisions*, *Phys. Rev. Lett.* **112** (2014) 082301 [1312.6555].
- [87] N. Borghini, P. M. Dinh and J.-Y. Ollitrault, *Flow analysis from multiparticle azimuthal correlations*, *Phys. Rev.* **C64** (2001) 054901 [nucl-th/0105040].
- [88] B. Alver *et al.*, *Importance of correlations and fluctuations on the initial source eccentricity in high-energy nucleus-nucleus collisions*, *Phys. Rev.* **C77** (2008) 014906 [0711.3724].
- [89] R. S. Bhalerao, M. Luzum and J.-Y. Ollitrault, *Understanding anisotropy generated by fluctuations in heavy-ion collisions*, *Phys. Rev.* **C84** (2011) 054901 [1107.5485].
- [90] **ALICE** Collaboration, B. Abelev *et al.*, *Centrality determination of Pb-Pb collisions at  $\sqrt{s_{NN}} = 2.76$  TeV with ALICE*, *Phys. Rev.* **C88** (2013), no. 4 044909 [1301.4361].
- [91] A. Giovannini and L. Van Hove, *Negative Binomial Multiplicity Distributions in High-Energy Hadron Collisions*, *Z. Phys.* **C30** (1986) 391.
- [92] F. Gelis, T. Lappi and L. McLerran, *Glittering Glazmas*, *Nucl. Phys.* **A828** (2009) 149–160 [0905.3234].
- [93] I. Kozlov, M. Luzum, G. Denicol, S. Jeon and C. Gale, *Transverse momentum structure of pair correlations as a signature of collective behavior in small collision systems*, 1405.3976.
- [94] K. Dusling, W. Li and B. Schenke, *Novel Collective Phenomena in High-Energy Proton-Proton and Proton-Nucleus Collisions*, 1509.07939.
- [95] P. M. Chesler, *How big are the smallest drops of quark-gluon plasma?*, 1601.01583.
- [96] **CMS** Collaboration, V. Khachatryan *et al.*, *Observation of Long-Range Near-Side Angular Correlations in Proton-Proton Collisions at the LHC*, *JHEP* **09** (2010) 091 [1009.4122].
- [97] **ALICE** Collaboration, B. Abelev *et al.*, *Long-range angular correlations on the near and away side in p-Pb collisions at  $\sqrt{s_{NN}} = 5.02$  TeV*, *Phys. Lett.* **B719** (2013) 29–41 [1212.2001].

- [98] **CMS** Collaboration, S. Chatrchyan *et. al.*, *Observation of long-range near-side angular correlations in proton-lead collisions at the LHC*, *Phys. Lett.* **B718** (2013) 795–814 [1210.5482].
- [99] **ATLAS** Collaboration, G. Aad *et. al.*, *Observation of Associated Near-Side and Away-Side Long-Range Correlations in  $\sqrt{s_{NN}}=5.02$  TeV Proton-Lead Collisions with the ATLAS Detector*, *Phys. Rev. Lett.* **110** (2013), no. 18 182302 [1212.5198].
- [100] **PHENIX** Collaboration, A. Adare *et. al.*, *Quadrupole Anisotropy in Dihadron Azimuthal Correlations in Central d+Au Collisions at  $\sqrt{s_{NN}}=200$  GeV*, *Phys. Rev. Lett.* **111** (2013), no. 21 212301 [1303.1794].
- [101] Y. Akiba *et. al.*, *The Hot QCD White Paper: Exploring the Phases of QCD at RHIC and the LHC*, 1502.02730.
- [102] B. Schenke and R. Venugopalan, *Eccentric protons? Sensitivity of flow to system size and shape in p+p, p+Pb and Pb+Pb collisions*, *Phys. Rev. Lett.* **113** (2014) 102301 [1405.3605].
- [103] C. E. Coleman-Smith and B. Müller, *Mapping the proton’s fluctuating size and shape*, *Phys. Rev.* **D89** (2014) 025019 [1307.5911].
- [104] S. Schlichting and B. Schenke, *The shape of the proton at high energies*, *Phys. Lett.* **B739** (2014) 313–319 [1407.8458].
- [105] L. D. Landau and E. M. Lifshitz, *Statistical Physics Part 1*, vol. 5. Pergamon Press, 1987.
- [106] L. D. Landau and E. M. Lifshitz, *Statistical Physics Part 2*, vol. 6. Pergamon Press, 1987.
- [107] J. I. Kapusta, B. Muller and M. Stephanov, *Relativistic Theory of Hydrodynamic Fluctuations with Applications to Heavy Ion Collisions*, *Phys. Rev.* **C85** (2012) 054906 [1112.6405].
- [108] L. Yan, “Unpublished notes on gubser and bjorken hydrodynamics.” 2015.
- [109] J.-Y. Ollitrault, *Relativistic hydrodynamics for heavy-ion collisions*, *Eur. J. Phys.* **29** (2008) 275–302 [0708.2433].

- [110] U. Heinz and R. Snellings, *Collective flow and viscosity in relativistic heavy-ion collisions*, *Ann. Rev. Nucl. Part. Sci.* **63** (2013) 123–151 [1301.2826].
- [111] L. D. Landau, *On the multiparticle production in high-energy collisions*, *Izv. Akad. Nauk Ser. Fiz.* **17** (1953) 51–64.
- [112] M. Nakahara, *Geometry, Topology and Physics*. second ed.
- [113] O. Philipsen, *The QCD equation of state from the lattice*, *Prog. Part. Nucl. Phys.* **70** (2013) 55–107 [1207.5999].
- [114] **HotQCD** Collaboration, P. Petreczky, *On trace anomaly in 2+1 flavor QCD*, *PoS LATTICE2012* (2012) 069 [1211.1678].
- [115] Y. Aoki, G. Endrodi, Z. Fodor, S. D. Katz and K. K. Szabo, *The Order of the quantum chromodynamics transition predicted by the standard model of particle physics*, *Nature* **443** (2006) 675–678 [hep-lat/0611014].
- [116] K. Dusling and T. Schäfer, *Bulk viscosity, particle spectra and flow in heavy-ion collisions*, *Phys. Rev.* **C85** (2012) 044909 [1109.5181].
- [117] W. A. Hiscock and L. Lindblom, *Stability and causality in dissipative relativistic fluids*, *Annals Phys.* **151** (1983) 466–496.
- [118] W. A. Hiscock and L. Lindblom, *Generic instabilities in first-order dissipative relativistic fluid theories*, *Phys. Rev.* **D31** (1985) 725–733.
- [119] W. Israel, *Nonstationary irreversible thermodynamics: A Causal relativistic theory*, *Annals Phys.* **100** (1976) 310–331.
- [120] W. Israel and J. M. Stewart, *Transient relativistic thermodynamics and kinetic theory*, *Annals Phys.* **118** (1979) 341–372.
- [121] R. Baier, P. Romatschke, D. T. Son, A. O. Starinets and M. A. Stephanov, *Relativistic viscous hydrodynamics, conformal invariance, and holography*, *JHEP* **04** (2008) 100 [0712.2451].
- [122] J. D. Bjorken, *Highly Relativistic Nucleus-Nucleus Collisions: The Central Rapidity Region*, *Phys. Rev.* **D27** (1983) 140–151.

- [123] M. A. Stephanov, K. Rajagopal and E. V. Shuryak, *Event-by-event fluctuations in heavy ion collisions and the QCD critical point*, *Phys. Rev. D* **60** (1999) 114028 [[hep-ph/9903292](#)].
- [124] **CMS** Collaboration, C. Collaboration, *Observation of long-range near-side two-particle correlations in pp collisions at  $\sqrt{s} = 13$  TeV*, .
- [125] G. Policastro, D. T. Son and A. O. Starinets, *The Shear viscosity of strongly coupled  $N=4$  supersymmetric Yang-Mills plasma*, *Phys. Rev. Lett.* **87** (2001) 081601 [[hep-th/0104066](#)].
- [126] **Particle Data Group** Collaboration, K. A. Olive *et. al.*, *Review of Particle Physics*, *Chin. Phys.* **C38** (2014) 090001.

**Titre :** Fluctuations dans des collisions entre particules aux hautes énergies

**Mots clés :** QCD, Intégrales de Feynman, Collisions de particules, Fluctuations, Hydrodynamique

**Résumé :** Nous étudions des fluctuations qui sont omniprésentes dans des collisions entre particules aux hautes énergies. Ces fluctuations peuvent être de nature classique ou quantique et nous allons considérer ces deux cas. D'abord, nous étudions les fluctuations quantiques qui sont présentes dans des collisions entre protons. Celles-ci sont calculables en théorie quantique des champs, et nous allons nous concentrer sur une certaine classe de diagrammes dans ce cadre. Dans un second temps nous allons étudier des fluctuations qui sont présentes dans des collisions entre particules plus lourdes que le proton. Celles-ci sont décrites par les lois quantiques de la nature qui donnent les positions des nucléons dans le noyau, ou bien des fluctuations classiques, d'origine thermique, qui affectent l'évolution hydrodynamique du milieu produit dans une collision.

Les fluctuations dans des collisions entre protons peuvent être calculées analytiquement jusqu'à un certain ordre en théorie quantique des champs. Nous allons nous concentrer sur des diagrammes à une boucle, d'une topologie donnée. Ces diagrammes aux boucles donnent des intégrales, qui typiquement sont difficiles à calculer. Nous allons démontrer comment des outils des mathématiques modernes peuvent être utilisés pour faciliter leur évaluation. En particulier, nous allons étudier des relations entre des coupures d'un diagramme, la discontinuité à travers d'un branchement et le coproduit. Nous allons démontrer comment l'intégrale originale peut être reconstruite à partir de l'information contenue dans le coproduit. Nous nous attendons à ce que ces méthodes seront utiles pour le calcul des diagrammes avec des topologies plus difficiles et ainsi aident au calcul des nouvelles amplitudes de diffusion.

A la fin, nous étudions les deux types de fluctuations qui ont lieu dans des collisions entre ions lourds. Celles-ci sont liées soit à l'état initial de la matière, soit à l'état intermédiaire produit dans une telle collision. Les fluctuations de l'état initial ont été mesurées expérimentalement, et on voit qu'elles donnent lieu à des non-Gaussianités dans le spectre final de particules. Nous allons démontrer comment ces non-Gaussianités peuvent être compris comme des positions et des énergies d'interaction aléatoires des 'sources' dans les noyaux entrant en collision. En plus, nous étudions le bruit hydrodynamique dans le milieu produit juste après une collision. Le comportement de ce milieu est celui d'un fluide à basse viscosité.



**Title :** Fluctuations in high energy particle collisions

**Keywords :** QCD, Feynman Integrals, Particle collisions, Fluctuations, Hydrodynamics

**Abstract :** We study fluctuations that are omnipresent in high-energy particle collisions. These fluctuations can be either of classical or quantum origin and we will study both. Firstly, we consider the type of quantum fluctuations that arise in proton-proton collisions. These are computable perturbatively in quantum field theory and we will focus on a specific class of diagrams in this set-up. Secondly, we will consider the fluctuations that are present in collisions between nuclei that can be heavier than protons. These are the quantum laws of nature that describe the positions of nucleons within a nucleus, but also the hydrodynamic fluctuations of classical, thermal origin that affect the evolution of the medium produced in heavy-ion collisions.

The fluctuations arising in proton-proton collisions can be computed analytically up to a certain order in perturbative quantum field theory. We will focus on one-loop diagrams of a fixed topology. Loop diagrams give rise to integrals that typically are hard to evaluate. We show how modern mathematical methods can be used to ease their computation. We will study the relations among unitarity cuts of a diagram, the discontinuity across the corresponding branch cut and the coproduct. We show how the original integral corresponding to a given diagram can be reconstructed from the information contained in the coproduct. We expect that these methods can be applied to solve more complicated topologies and help in the computation of new amplitudes in the future.

Finally, we study the two types of fluctuations arising in heavy-ion collisions. These are related either to the initial state or the intermediate state of matter produced in such collisions. The initial state fluctuations are experimentally observed to give rise to non-Gaussianities in the final-state spectra. We show how these non-Gaussianities can be explained by the random position and interaction energy of 'sources' in the colliding nuclei. Furthermore, we investigate the effect of hydrodynamical noise in the evolution of the medium produced just after a collision. This medium behaves like a fluid with a very low viscosity, and so the corresponding evolution is hydrodynamical.

